

MANCHESTER
1824

The University of Manchester

**Synesthesia – The art of seeing QCD colour:
A measurement of colour flow
in top-quark pair events**

A thesis submitted to The University of Manchester for the degree of

Doctor of Philosophy

(PhD)

in the Faculty of Science and Engineering

Fabian Wilk

2018



Particle Physics Group
School of Physics and Astronomy
Faculty of Science and Engineering



TABLE OF CONTENTS

Abstract	5
Declaration	7
Copyright	9
Acknowledgements	11
Preface	13
I Introduction	15
II Theoretical Background	17
1 The Standard Model	17
2 Top-Quark Physics	27
3 Introduction to Colour Flow	35
III The Experimental Apparatus	41
4 The Large Hadron Collider	41
5 The ATLAS Experiment	47
6 Future and Upgrades	61
IV Analysis Definitions and Tools	75
7 Simulation of Events	75
8 Event Reconstruction	81
9 Fiducial Measurements and Unfolding	91
10 Simulating Exotic Colour Flow	97
11 Modelling of Fake Lepton Background	107
V Measurements and Studies	115
12 A Measurement of Top-Quark Pair Production	115
13 Measuring Colour Flow at 13 TeV	131
14 Jet Pull and Beyond – Colour Flow in Boosted Topologies .	181
VI Conclusion	189
References	191

Abstract

Candidate	Fabian Wilk
Title	Synesthesia – The art of seeing QCD colour: A measurement of colour flow in top-quark pair events
University and Faculty	The University of Manchester Faculty of Science and Engineering School of Physics and Astronomy
Degree	Doctor of Philosophy (PhD)
Submission Date	9 th of May 2018
Resubmission Date	28 th of July 2018

In the Summer of 2015, the Large Hadron Collider resumed operation after a two-year shutdown, providing proton–proton collisions at a record energy of $\sqrt{s} = 13$ TeV. This thesis presents two measurements of data recorded by the ATLAS detector in proton–proton collisions at the LHC. The first is a measurement of the top-quark pair production cross-section. A dataset of 85 pb^{-1} recorded during an early operating period at the new centre-of-mass energy is used. The cross-section is measured in the single-lepton final state using a high-momentum electron or muon. Measured cross-section values from the two sub-channels and the combination are all consistent within their uncertainties with predictions from theoretical calculations.

The second analysis using ATLAS data is a measurement of colour flow in top-quark pair events based on a dataset of 36.1 fb^{-1} . This measurement also uses the single-lepton final state. Observables are constructed from the jet-pull vector, a momentum-weighted angular moment of a jet, which are sensitive to the colour flow in the signal event topology. Two scenarios are considered: the two jets originating from the hadronically decaying W boson and the two \mathbf{b} -tagged jets from the top-quark decays. Observables derived from the former are sensitive to colour flow of a colour singlet while those derived from the latter probe the overall top-quark pair colour-flow. The measured observables are corrected for detector effects by unfolding them to particle level. Normalised unfolded distributions are compared to theoretical predictions taken from simulation and the agreement is quantified. Good agreement between the measured data and the predictions is observed for some combinations of observables and predictions. However, none of the predictions describes data well across all measured observables. A model with exotic colour flow is also constructed. The data favours the predictions from simulation according to the Standard Model over the model with exotic colour flow.

Declaration

No portion of the work referred to in the thesis has been submitted in support of an application for another degree or qualification of this or any other university or other institute of learning.

(date and signature)

Copyright

1. The author of this thesis (including any appendices and/or schedules to this thesis) owns certain copyright or related rights in it (the “*Copyright*”) and he has given The University of Manchester certain rights to use such Copyright, including for administrative purposes.
2. Copies of this thesis, either in full or in extracts and whether in hard or electronic copy, may be made **only** in accordance with the Copyright, Designs and Patents Act 1988 (as amended) and regulations issued under it or, where appropriate, in accordance with licensing agreements which the University has from time to time. This page must form part of any such copies made.
3. The ownership of certain Copyright, patents, designs, trademarks and other intellectual property (the “*Intellectual Property*”) and any reproductions of copyright works in the thesis, for example graphs and tables (“*Reproductions*”), which may be described in this thesis, may not be owned by the author and may be owned by third parties. Such Intellectual Property and Reproductions cannot and must not be made available for use without the prior written permission of the owner(s) of the relevant Intellectual Property and/or Reproductions.
4. Further information on the conditions under which disclosure, publication and commercialisation of this thesis, the Copyright and any Intellectual Property and/or Reproductions described in it may take place is available in the University IP Policy,¹ in any relevant Thesis restriction declarations deposited in the University Library, The University Library’s regulations² and in The University’s policy on Presentation of Theses

¹ See: <http://documents.manchester.ac.uk/DocuInfo.aspx?DocID=24420>

² See: <http://www.library.manchester.ac.uk/about/regulations/>

Acknowledgements

Any endeavour as grand and glorious as the modern high-energy particle physics experiments at CERN cannot function without collaboration. My first thanks goes to all those whose contribution is small and frequently not even noted by the author but integral: the entire body of people who work and collaborate at CERN.

Yvonne, my supervisor, has been key to making this journey happen. I would like to thank her for the continuous support throughout my PhD. Often times I have strayed from the straight path and chased down some rabbit hole in search for a pretty plot or a programming challenge. Your guidance, and the annoyingly early Monday morning meetings, have been critical for keeping me on-track and I am ever grateful. Your craziness and your enthusiasm for top-quark physics and colour flow are famously contagious and have helped keep me motivated.

To Tom, who was a mentor during all stages of my PhD: your help with the colour-flow measurement was invaluable and you have always been a source of knowledge and advice. Moreover, you have helped me to stay relaxed throughout a truly annoying internal review process. Most importantly, you have provided support, reassurance, and guidance whenever I needed it.

The post-docs Ian, Jay, and Quake each deserve my gratitude for their inputs on practical and analysis matters. Both Ian and Jay had a helping hand in getting simulation samples done that only “my” colour-flow measurement needed. I would also like to thank you for helping hone the written account of my PhD.

I would like to thank the entire particle-physics group at Manchester who have made my time in Manchester and at CERN a pleasant experience. I would also like to call out a few people explicitly: specifically Diego, Pawel, and Paki whom I will miss dearly — especially when the panther calls on a Friday evening.

The people whom I have started my PhD with in Manchester have become more than colleagues. They have become friends and an integral part of the social net that has kept me happy and also sane in times of stress. I would like explicitly express my gratitude to Johnny (for the booze shared) and Ste (for the stimulating conversations).

My friend and colleague Dominik has been a constant throughout my entire academic life and I am happy to have shared the experience of being a PhD student with him both in Manchester and at CERN. Exchanging ideas with you out on the balcony was probably the most fun part of tackling an analysis problem. It appears that this will be the last leg of our professional journey we have walked together, I will miss that. But I am looking forward to having some new non-work topics to talk about.

I would like to thank my family for not giving up on a brother, son, and grandchild who all too frequent forgot to call. I am delighted that I got to show you CERN and the Geneva area. Also, I am still looking forward to having that pint in my favourite pub in Manchester.

Finally, most importantly, I would like to thank Sara. For everything.

Preface

All measured data studied in this thesis was collected by the *ATLAS* experiment. This was only made possible by the combined efforts of the members of the *ATLAS* collaboration and the members of CERN who operate the LHC. Much of the simulated data that was used for this thesis was also generated by members of the *ATLAS* collaboration. Both measured and simulated data were processed using the *ATLAS* reconstruction software. Consequently, the work presented here relies on the software and computing infrastructure provided by the *ATLAS* collaboration. The author has contributed to the *ATLAS* reconstruction software — in particular during his role as Top Derivations Software Contact — and the top working-group’s analysis software.

As part of becoming a full member of the *ATLAS* collaboration, member candidates have to become qualified as an author. This is achieved by working a fixed time on a *qualification task* that is usually related to *ATLAS* operation, upgrade, or some other type of utility function. The qualification task performed by the author of this thesis was related to studying different end-cap detector geometry designs for a future *ATLAS* detector upgrade using simulation. This is presented in Section 6.

Section 11 discusses a data-driven method which is used to model a specific type of background. This method requires parameterised efficiency factors which must be derived from data and simulation beforehand. The work presented in this thesis uses parameterisations which have been derived by Nedaa Asbah and Frédéric Derue. Furthermore, in Section 11 some figures are shown for illustrative purposes which they have provided.

Section 12 presents a measurement of the production cross-section for top-quark pairs. This measurement was performed in collaboration with a large group of *ATLAS* collaborators and published as a conference note. The measurement consists of several independent parts and the part presented in this thesis was performed in collaboration with Rafał Bielski and Tom Neep. The author’s main contributions were the overall cross-section extraction and the treatment and study of signal modelling and PDF uncertainties.

In Section 13, a measurement of colour flow in top-quark pair events is presented. This measurement was published as conference note and a paper was submitted

to EPJ C. The measurement was performed in collaboration with Tom Neep who participated as an advisor as well as an editor for the conference note and paper. While not contributing as an “analyser” by directly operating on the measured data, his help as an experienced physicist was invaluable. The author was responsible for all parts of the analysis including the editorial tasks of writing the conference note and paper.

I Introduction

Throughout the course of history, human curiosity has driven natural philosophers and scientists to seek for ever smaller building blocks of reality. Ancient philosophers invented the concept of the *atom*, an indivisible base unit of matter, and scientists went forth and found it, just to smash it in search for an even smaller base unit. This quest is led by the hope that understanding these smallest building blocks and how they interact with each other facilitates a more profound understanding of reality. By extrapolation, such knowledge would lead to a better understanding of the more accessible human scale and even the cosmic scale.

To our current best understanding, we have found the smallest indivisible particles that are the building blocks of matter. These particles and the forces that act between them are described by the *Standard Model*. Just like any other scientific theory this may not be the final answer. Indeed, there are several phenomena that cannot be explained by the theory. At the same time it has proven to be quite resilient to attempts of finding faults in its predictions.

The field of experimental high-energy particle physics uses colliders of ever increasing particle energy and density to smash quantum-scale objects in the hope of better understanding physical reality. Measurement of the remains of the particle collisions facilitates comparison with theoretical predictions in an effort to either falsify or support the theory. Production rate measurements for specific remnants are on the forefront of such studies. New physics might manifest through yet unobserved remnants or modify production rates of well-known processes.

The Standard Model is a combination of several different theories which describe distinct particles and forces. One of these is the *strong force* which is described by the theory of quantum chromodynamics (QCD) and is responsible for binding the constituents of protons and neutrons. The strong force originates from a property called *colour* which these constituents possess. Colour, which has nothing to do with the real-world colour that we know from everyday life, is in some ways similar to the familiar electric charge. However, while we can observe individual electric charges, such as for example electrons, the same is apparently not true for objects with *colour charge*. Individual colour charges are not realised in nature, instead we

I Introduction

observe composite objects where multiple colour charges cancel to a colour-neutral object — such as protons and neutrons. The hidden colour-charges are responsible for the *colour connections* that bind these constituents through the strong force. This also prompts the question how we even know that colour exists. The intrinsic colour charges, which we cannot measure directly, are predicted to affect how coloured particles interact with one another and influence the emission of radiation. Through measurement of the distributions of particle momenta and energy in the region between two colour charges, the *colour flow* can be made visible. This is not unlike synesthesia: the colour charges of QCD and particle kinematics are not directly related and seemingly live in different realms, and yet kinematic quantities make the otherwise hidden colour flow visible.

At the energy frontier of experimental particle-physics collider-experiments is the Large Hadron Collider (LHC) at CERN which resumed operation in 2015 at a newly increased centre-of-mass energy of $\sqrt{s} = 13$ TeV. Measurements of the production rate of well-known processes are usually among the first physics analyses made public when operating at a new energy frontier. A measurement of the production rate for top-quark pairs with the ATLAS experiment at this new centre-of-mass energy will be one main topic presented in this thesis. Such cross-section measurements are at the forefront of the constant attempts to disprove the Standard Model. However, they are also important for validating theoretical calculations and provide inputs to derivative work. Given the LHC's formidable performance, processes that were considered rare twenty years ago, like production of top quarks, have become commonplace: the production rate for top quarks is expected to be at the order of tens per second. As a result, more subtle effects can be investigated and studied. A measurement of colour flow in events with a top-quark pair is the main focus of the work presented in this thesis. In addition to validation of the theory and phenomenology, measuring colour flow provides important inputs for simulation tuning efforts.

This thesis is organised as follows: Chapter II discusses the general theoretical background of the presented work. The experimental apparatus that facilitates the measurements presented in this thesis is introduced in Chapter III. This chapter also includes a section that describes the planned upgrade programme with emphasis on work that the author contributed to. Chapter IV discusses definitions and tools used by the analyses and measurements presented in this thesis. The actual studies and measurements that are the primary content of this thesis are presented in Chapter V. Finally, in Chapter VI, the work presented in this thesis is summarised and brought to conclusion.

Remark: Throughout this thesis, the system of natural units, where $\hbar = c = k_B = 1$, is adopted unless stated otherwise. Electric charges are implicitly given in multiples of the elementary charge e . When referring to individual particles, final states, or decay chains, charge conjugates are implied unless otherwise stated. All natural constants and the values of particle properties are taken from [1] unless otherwise stated.

II Theoretical Background

This chapter presents the general theoretical framework and context upon which the work discussed in this thesis is based. Section 1 introduces the Standard Model of Elementary Particle Physics, which is the general theoretical framework relevant in high-energy physics. A more thorough discussion of the heaviest member of the family of elementary particles, the top quark, is presented in Section 2. Finally, in Section 3, the colour flow, which is a feature of the Standard Model and centrepiece of the work presented in this thesis, will be introduced.

1 The Standard Model

CONTENTS		
1.1	The Particle Zoo	18
1.1.1	Building Blocks of Nature	18
1.1.2	Mediators	19
1.2	The Fundamental Interactions	20
1.2.1	The Electromagnetic Interaction	20
1.2.2	The Strong Interaction	21
1.2.3	The Weak Interaction	23
1.3	The Parton Model	24

The Standard Model of Elementary Particle Physics (Standard Model or SM) [1–4] is a refined theory which has been extended and improved over the course of the last century. It is currently the most accurate theoretical description of the world of fundamental particles and the forces acting between them. Its predictions have been tested and verified by numerous measurements to astonishing levels of accuracy. However, the SM has also several known deficiencies and shortcomings such as the nature of neutrinos and the origin of their mass or its failure to explain the observed asymmetry between matter and anti-matter in the universe.

The SM is a quantum field theory, which is a theory that combines quantum mechanics and special relativity. In this formalism, particles are represented by mathematical fields and interactions are defined through a **LAGRANGE** density which operates upon the fields. It combines descriptions of three fundamental forces through the theories of *Quantum Electrodynamics* (QED), *Quantum Chromodynamics* (QCD), and the *weak force* to a comprehensive theory. Description of the fundamental forces is complemented by the **HIGGS** mechanism which adds a consistent formalism to

introduce masses to the particles defined by the SM. Gravity, the fourth fundamental force, is not described by the SM.

1.1 The Particle Zoo

The SM distinguishes between elementary and composite particles: the former are point-like, meaning they have no intrinsic substructure, whereas the latter are compound objects. Elementary particles are categorised by their spin-eigenvalue: **Fermions** — which are spin- $1/2$ particles — are the fundamental matter-particles and **Bosons** — which have integer spin — are particles that mediate particle interactions.

Particles of both groups possess further quantum numbers beyond spin. Quantum numbers that correspond to a physical charge, such as the electric charge, are of particular relevance: each particle X has an associated anti-particle \bar{X} that has the same mass but opposite values of the physical charges. A particle is its own anti-particle, $X \equiv \bar{X}$, if all physical charges are zero-valued. Figure 1 shows a graphical representation of the fundamental particles in the SM.

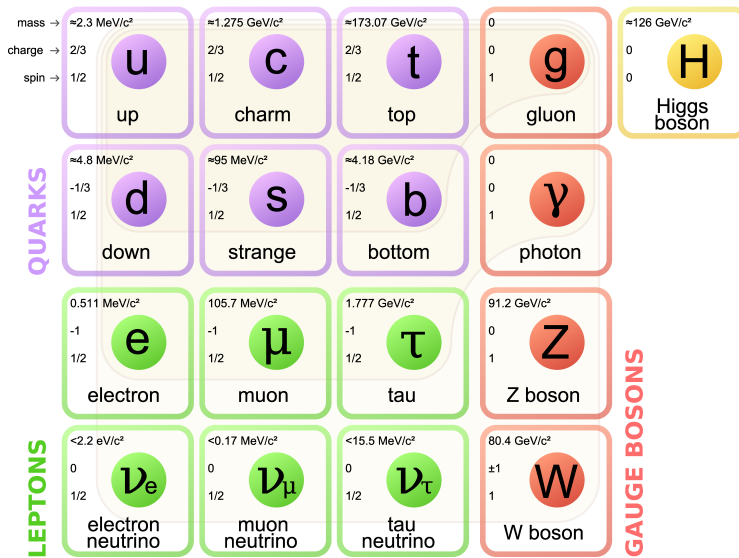


Figure 1: Graphical representation of the elementary particles in the Standard Model [5].

The elementary fermions predicted by the theory are shown in the three left-most columns while elementary bosons are shown in the right-most two columns: there are twelve fermions, each paired with an anti-particle, and five fundamentally different bosons — the gluon, two weakly interacting massive bosons, the photon, and the HIGGS boson.

1.1.1 Building Blocks of Nature

Elementary fermions are grouped into three generations, sorted by their mass, as illustrated by the three columns of fermions in Figure 1, counting from left to right. In general, fermions of the same type but different generation, that is fermions in the same row in Figure 1, have very similar properties apart from their mass. A mass

ordering is observed that facilitates the decay of particles of higher generation to those of a lower generation.

There are a total of twelve different elementary fermions, called *flavours*, in the SM. The family of fermions can be further categorised into the **Quarks** and **Leptons**, marked in purple respectively green in Figure 1. Quarks are subject to all fundamental forces while leptons do not interact according to QCD.

Fermions are sometimes called *matter particles* as they are the constituents that make up atoms and therefore everything that humans interact with in everyday life. However, only the particles of the first generation are observed as constituents of stable matter. The members of generations two and three are unstable themselves and can be created only for a short time.

§1. Leptons In the SM there are six different leptons. The charged leptons — electron e , muon μ , and tau τ — have electric charge $Q = -1$ ¹ and are each partnered to an electrically neutral neutrino. These neutrinos are named electron neutrino ν_e , muon neutrino ν_μ , and tau neutrino ν_τ .

While charged leptons are quite well-understood in the SM, the nature of neutrinos is still a source of unanswered questions: the SM predicts massless neutrinos but evidence from neutrino oscillation experiments requires neutrinos to have mass. Furthermore, because neutrinos are electrically neutral, neutrino and anti-neutrino may be the same. Many experiments studying neutrino physics are attempting to improve our understanding of the nature of neutrinos.

§2. Quarks Quarks are grouped as *up-type* quarks which have electric charge $Q = +2/3$ and *down-type* quarks with $Q = -1/3$. The up-type quarks are named *up-*, *charm-*, and *top-quark* (\mathbf{u} , \mathbf{c} , and \mathbf{t} , respectively), the down-type quarks are called *down-*, *strange-*, and *bottom-quark* (\mathbf{d} , \mathbf{s} , and \mathbf{b} , respectively). In addition to electric charge, quarks carry *colour charge*, which is the charge of the strong interaction described by QCD. The production, properties, and decay of the top quark, which is at the focus of the work presented in this thesis, will be presented in more detail in Section 2.

1.1.2 Mediators

In the SM all interactions are mediated by bosons. Four types of bosons are introduced by the fundamental interactions, these are the photon, the W and Z bosons, and the gluon; they are marked in red in Figure 1. Their properties are presented in more detail when discussing the fundamental forces in Section 1.2.

The final mediator boson of the SM — the **Higgs** boson H , marked in yellow in Figure 1 — is predicted by the *Higgs mechanism* [6–8] which was proposed in 1964.

¹ Electric charges of particles are expressed in units of the electron charge.

By *spontaneous symmetry breaking*, the HIGGS mechanism gives mass to the fermions and bosons introduced by the other parts of the SM. Unlike the other mediators of the SM, the HIGGS boson does not mediate a fundamental force but rather lets particles acquire mass through its interaction. The HIGGS boson has zero-valued electric charge. It is expected to have mass itself which it acquires through self-coupling. After a long hunt, the HIGGS boson was finally discovered in 2012 by the ATLAS and CMS experiments at the LHC [9, 10].

1.2 The Fundamental Interactions

The Standard Model covers three fundamental interactions known as the strong, weak, and electromagnetic forces. The fourth fundamental force, gravity, is not described by the standard model, which is one of its shortcomings. Finding and testing a mathematical formalism for describing quantum gravity remains a top priority for theoretical physics. Table 1 compares the coupling strengths of the fundamental forces.

Force	Relative Strength
Strong	~ 1
Electromagnetic	$\sim 10^{-3}$
Weak	$\sim 10^{-8}$
Gravity	$\sim 10^{-37}$

Table 1: Relative coupling strengths of the four fundamental forces as exerted between two fundamental particles at a distance of 1 fm [4].

The strong force has the largest relative strength, followed by the other fundamental forces included in the SM. Gravity on the other hand has a relative strength that is many orders of magnitude smaller than the other fundamental forces. Hence, for all ordinary experimental matters, gravity can be neglected in particle physics without further discussion.

Each fundamental force is mediated by at least one exchange particle which are marked in red in Figure 1. However, due to conservation of different quantum numbers only certain types of interactions (transformations between particles) are allowed. Figure 2 shows the fundamental interaction vertices of the force-carrying bosons in the SM.

1.2.1 The Electromagnetic Interaction

The electromagnetic (EM) interaction is the most easily accessible interaction, that is described by the SM, both experimentally and conceptually. It is mediated by the photon γ which is electrically neutral and massless and couples to the electric charge of its interaction partners. The theory that describes electromagnetic interactions is Quantum Electrodynamics (QED).

Figure 2b shows the fundamental SM vertex of QED as a FEYNMAN diagram where the wiggly line denotes the photon and the solid lines represent (anti-)fermions.² Since the photon couples to the electric charge, the participating fermions must be

² For a more complete introduction to the conventions used for drawing FEYNMAN diagrams see Ref. [4].

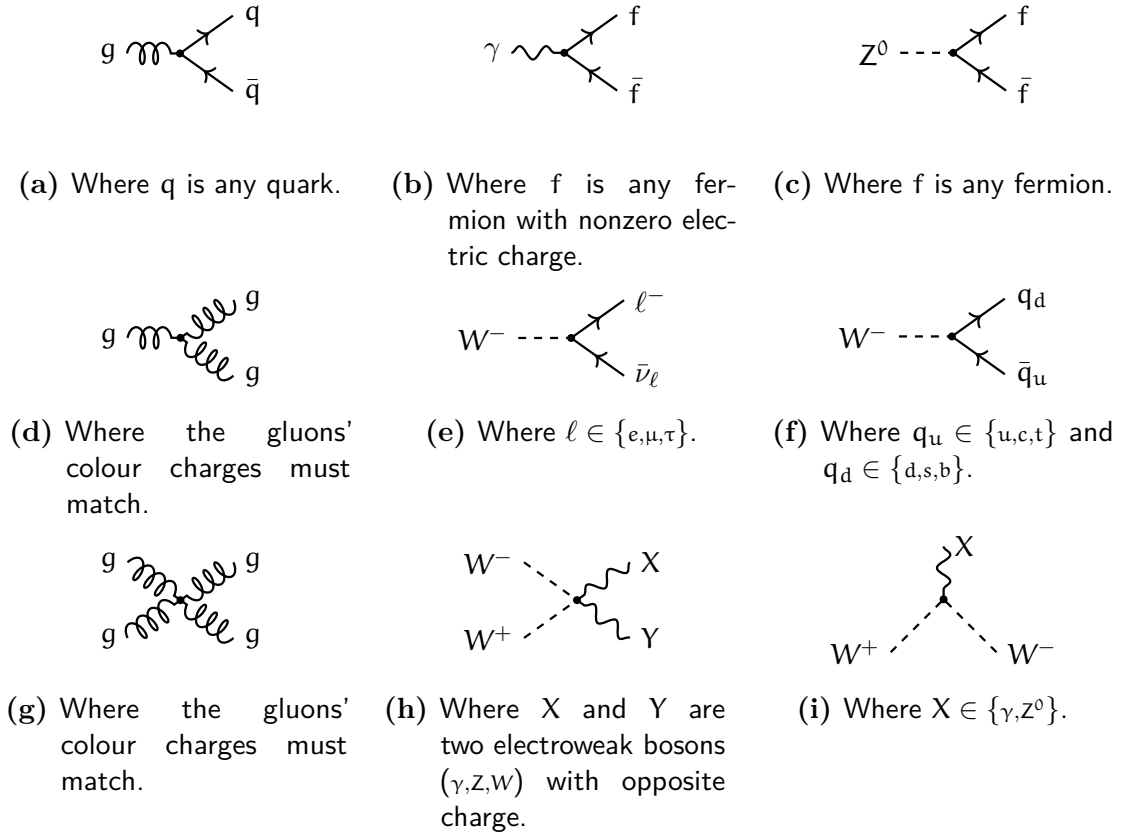


Figure 2: FEYNMAN diagrams of fundamental force-carrying interaction vertices in the Standard Model. Charge conjugates — if they exist — are implied [3, 4].

either quarks or charged leptons. Neutrinos do not participate in electromagnetic interactions. Furthermore, the fermion–anti-fermion pair must have the same flavour, i.e. the EM interaction is flavour-conserving.

1.2.2 The Strong Interaction

The dynamics of the strong force are described by Quantum Chromodynamics (QCD) [11–13]. It was developed mostly during the 1960s and 1970s and describes the interactions of quarks and gluons.

Just like QED, the theory of QCD has a massless mediator — the gluon g — which couples to a charge that is held by its interaction partners. Various experiments found that the QCD charge is in fact three-valued. In order to provide an allegory of these states, the charge is called *colour charge* and its valid states are labeled *red*, *green*, and *blue* (each with an anti-colour counterpart). Combination of a colour and anti-colour of the same type, e.g. red–anti-red, yields a colourless state as does combination of all three (anti-)colours. The QCD mediator itself carries one quantum of colour and one of anti-colour charge. As a result, it can couple to other gluons: self interaction is possible, see Figures 2d and 2g. The only known particles other than the gluon carrying colour charge are the quarks: quarks carry one quantum of colour while anti-quarks carry one quantum of anti-colour, see Figure 2a. Like the photon, the gluon only couples to quark–anti-quark pairs that have the same flavour and consequently QCD is flavour-conserving.

An important and unique feature of the strong interaction is the so-called **asymptotic freedom**: the force between two colour-connected states, i.e. two quarks, becomes asymptotically weaker as the energy increases and distance between the state decreases. Given that the distance between the states is small enough, and correspondingly the energy large enough, the quarks can be considered as *free* particles. However, as the distance grows, the coupling grows increasingly stronger. In theoretical particle-physics, calculation of the processes is typically performed through perturbative calculations which rely on the fact that the coupling constant of the interaction is small. For QCD, this is no longer true for small energies or, correspondingly, large distance scales. In practice, this problem is resolved by using the *factorisation theorem* which separates any process into high-energy components, which can use perturbative calculations, and low-energy components which must use some other model. In a more general form, this can be applied in a sequential manner. As a result, successive processes taking place at different energy scales can be calculated separately with each step only depending on the outcome, not the specifics, of the previous step.

Another unique feature of QCD is **colour confinement**: as two colour-connected quarks are moved apart, the gluon field forms a narrow tube between the two quarks, due to the gluon self-attraction, rather than spreading out uniformly [4]. Since the energy stored within the colour field increases nearly linearly, at some point it becomes energetically more favourable for the field to produce a new quark–anti-quark pair from the vacuum. Consequentially, free quarks do not exist and indeed have not been observed experimentally. Furthermore, a bound quark state (a so-called hadron) can exist only if it is a colour singlet, i.e. the sum of the colour charges of its constituents must be zero. The colour charge carried by the constituents is confined to a bound state and separating the actual charge carriers will only result in the formation of new bound states.

Compound states of quarks are either bound states of a quark and an anti-quark, called **Mesons**, or bound states composed of three quarks, called **Baryons**. Mesons are generally unstable and short-lived, whereas baryons can be very long-lived (e.g. the neutron) or even be considered stable (e.g. the proton). There is no theoretical reason which prevents more complex bound states and experimental evidence suggest they may exist, however, they are not relevant to this thesis.

The unique properties of the strong interaction give rise to a variety of experimental implications. One rather important implication is that quarks and gluons cannot be observed individually. Rather, they are observed as *jets*: short-distance, high-energy quarks and gluons individually give rise to narrowly collimated streams of particles, the jets, forming within a cone-like structure at large-scale distances.

1.2.3 The Weak Interaction

The weak interaction is the third and final fundamental force described by the SM. Unlike both QED and QCD it is mediated by massive bosons: the electrically neutral Z^0 boson and the two electrically charged W^\pm bosons. The mediators of the weak interaction couple to all types of fermions and are consequently the only part of the SM which connects the electrically- and colour-neutral neutrinos with the remainder of the particle zoo.

In the SM, the Z boson mediates neutral-current weak interactions — see Figure 2c — while the W^\pm bosons mediate charged-current weak interactions — see Figures 2e and 2f. Unlike any other boson, the W bosons couple to fermions of different flavour and consequently the charged-current weak interaction is the only non-flavour-conserving process in the SM. Since the W bosons have electric charge they can couple to the photon. Furthermore, they themselves possess the charge of the weak interaction and therefore self-interactions resulting in triple- and quartic-gauge-couplings are possible, see Figures 2h and 2i.

In the 1960s GLASHOW, SALAM, and WEINBERG proposed the model of *electroweak unification* (also called GSW theory) which fully describes electromagnetic and weak interactions of particles [14–16] in a combined theory at energies above ~ 100 GeV. Initially, the theory predicted that the coupling of the W bosons should be flavour ignorant, that is to say its strength should be equal for all flavours. However, various experiments showed discrepancies in the measured coupling strengths: universality of the weak interaction was challenged.

In 1963 CABIBBO first proposed a solution to the problem [17] which was later extended by KOBAYASHI and MASKAWA in 1973 [18]. Their theory, the so-called *CABIBBO-KOBAYASHI-MASKAWA (CKM) mechanism*, also predicted a third generation of quarks. The newly theorised particles — the bottom and top quarks — were discovered in 1977 [19] and 1995 [20, 21] respectively. The central idea of the CKM mechanism is that the flavour eigenstates of the weak interaction $|q\rangle$ are not equal to the mass eigenstates $|q'\rangle$. By multiplying a unitary, complex transformation matrix V_{CKM} ³ one can be transformed into the other. Conceptually this is a basis transformation rotating the states from one space to the other. Any charged-current vertex that couples two quarks of flavour i and j , introduces a proportionality to the CKM matrix element $V_{\text{CKM}}^{(i,j)}$ to the calculation of the transition probability. Hence, assuming that V_{CKM} is non-trivial (i.e. not the unit matrix), the *mismatch* of the quantum states of propagation and interaction results in varying coupling strengths for the different quarks. The non-zero off-diagonal matrix elements correspond to the magnitudes of the flavour-changing contributions of the charged weak current. Their

³ The so-called CABIBBO-KOBAYASHI-MASKAWA Matrix or CKM Matrix.

values are not predicted by the SM, however, unitarity of the matrix constrains the absolute values to combine to unity in each column and row.

Equation (1) shows the measured magnitudes of the CKM matrix elements as given by Ref. [1].

$$\begin{pmatrix} |V_{ud}| & |V_{us}| & |V_{ub}| \\ |V_{cd}| & |V_{cs}| & |V_{cb}| \\ |V_{td}| & |V_{ts}| & |V_{tb}| \end{pmatrix} \sim \begin{pmatrix} 0.974 & 0.225 & 0.004 \\ 0.225 & 0.974 & 0.041 \\ 0.009 & 0.040 & 0.999 \end{pmatrix} \quad (1)$$

These measurements find that the off-diagonal terms are non-zero but rather small, particularly for mixing with third-generation quarks. As a consequence, the charged-current weak interactions are not only non-flavour-conserving but also allow cross-generational coupling of quarks, albeit at a suppressed rate.

1.3 The Parton Model

Hadrons, such as the protons which are collided in the LHC accelerator, are composite particles that form as bound quark states. In addition to these real component quarks, the so-called *valence quarks*, the colour field of QCD induces a constant exchange of virtual gluons between the valence quarks inside the hadron. These gluons may split into virtual $q\bar{q}$ pairs, so-called *sea quarks* which are re-absorbed into the color field at a later stage. In the parton model [1, 22], which collectively calls the combination of all three constituent types *partons*, the constituents act like a cloud of quasi-free particles in place of the hadron. This property follows from the asymptotic freedom of QCD.

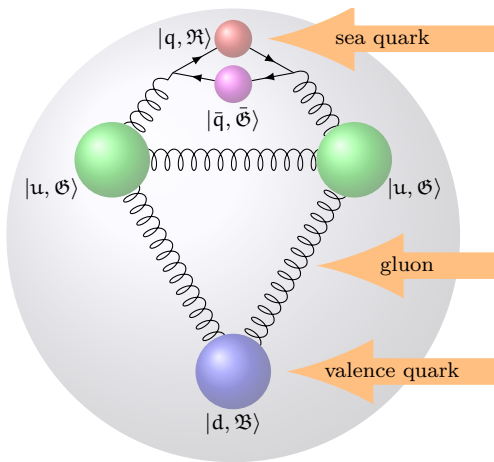


Figure 3: Illustration of parton model using a proton; large (small) spheres are valence (sea) quarks; the arrows denote possible interaction targets in hadron collisions. $\mathcal{C} \in \{\mathfrak{R}, \mathfrak{G}, \mathfrak{B}\}$ denotes colour, $\bar{\mathcal{C}} \in \{\bar{\mathfrak{R}}, \bar{\mathfrak{G}}, \bar{\mathfrak{B}}\}$ anti-colour.

Figure 3 shows an illustration of the parton model using a proton (gray sphere) as an example. Each of the partons carries only a fraction x , the so-called **BJORKEN** scaling [1, 23], of their mother hadron's momentum.⁴

This has particular relevance for particle collisions involving hadrons: the actual collision involves a parton rather than its mother hadron. Therefore, the collision partner(s) and energies are not deterministic: a collision may involve a valence or sea quark or a gluon. Furthermore,

the colliding parton will carry a (random) fraction x of the hadron momentum. Consequently, if the collision energy is relatively close to the threshold energy of a

⁴ For simplicity the discussion is restricted to one dimension, specifically the beam direction in the collision point.

given process, both partons must have large x in order for the desired process to be possible.

The probability distribution for the **BJORKEN** scaling x depends on the type of mother hadron, the type of parton, and the energy scale μ^2 of a collision. The complete set of these functions is called *parton distribution functions* (PDFs) and each function in the set describes the probability density of finding a parton of a specific type with **BJORKEN** scaling x at a scale μ^2 . Figure 4 shows a PDF set evaluated at an energy scale relevant for top-quark physics for a proton mother-particle.

Precise knowledge of the PDFs is critical in order to be able to simulate particle collisions. While they cannot be calculated perturbatively in QCD, the theory relates PDFs at lower energy scales μ^2 to those at higher scales. The distribution functions can be measured experimentally, for example, in deep inelastic scattering experiments. Such a reference point can be used to calculate the PDFs — using an appropriate parameterisation — and extrapolate them to a different energy scale. There is not one unique commonly accepted PDF prediction but rather a variety of competing PDFs based on different experimental datasets and differing parameterisations.

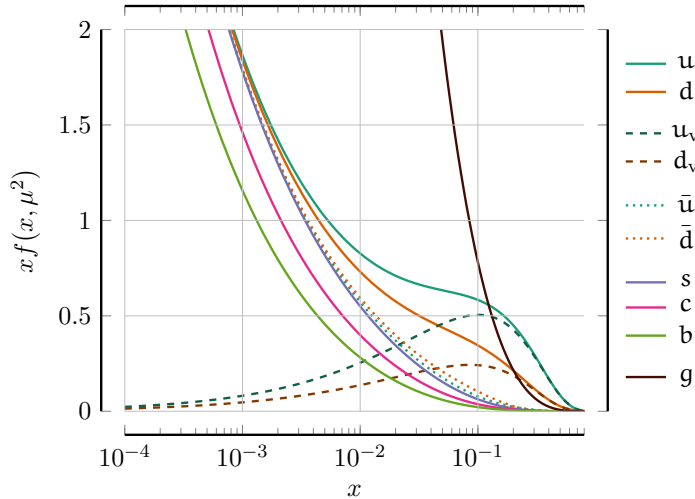


Figure 4: Parton distribution functions (PDFs) for protons at $\mu = 2 \cdot m_t \sim 2 \cdot 173 \text{ GeV}$. The valence quark contributions to u and d are labelled as u_v and d_v respectively. Sea quark contributions for these quarks are not listed separately but are equal to \bar{u} and \bar{d} respectively. Data taken from [24] using the CT10 NNLO PDFs [25].

2 Top-Quark Physics

CONTENTS		
2.1	Properties	27
2.2	Production	28
2.3	Decay	32

The following section provides a brief introduction to top-quark physics. This includes a discussion of some important top-quark properties as well as the practicalities of its production and decay.

Following the discovery of the bottom quark in 1977 [19], the search for its up-type partner was intensified [26]. Because it is significantly more massive than any other elementary fermion, it was only discovered in 1995 — almost twenty years after the b quark — by the CDF and DØ experiments at the TeVatron collider¹ [20, 21].

2.1 Properties

The top quark is an up-type quark of the third generation in the Standard Model. Therefore, it has an electric charge of $Q = +2/3$ and is the partner to the bottom quark. The most recent combination by the Particle Data Group puts the top-quark mass at

$$m_t = 173.1 \pm 0.6 \text{ GeV}, \quad (2)$$

using combined results from the ATLAS, CMS, and the TeVatron experiments [1]. A summary of direct top-quark mass measurements performed with LHC data is shown in Figure 5.

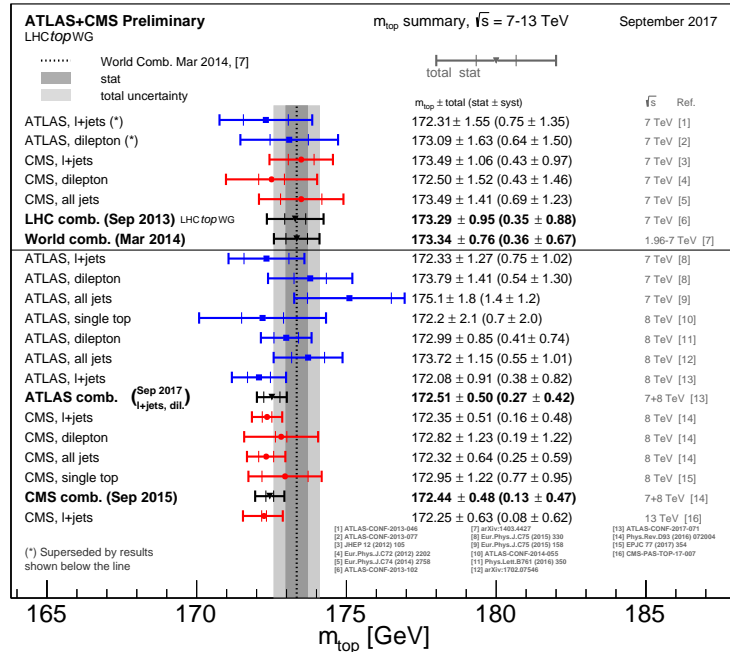


Figure 5: Summary of ATLAS and CMS direct top-quark mass measurements [27]. Results are compared with combinations of LHC measurements as well as the world combination using LHC and TeVatron measurements. Results shown below the horizontal line were produced after the LHC and world combinations were performed.

¹ The TeVatron [1] was a proton–antiproton collider operated at $\sqrt{s} = 1.8$ and 1.96 GeV centre-of-mass energy.

The top quark is a unique probe to study the SM: its mass is significantly larger than that of any other fermion — $m_t \sim 40 \times m_b$ [1] — and even exceeds that of the massive bosons. As a result, the top quark is the only fermion that may be produced on-shell and can then decay to a non-virtual electroweak boson. In many cases, higher-order processes are suppressed according to the inverse of the mass of the virtual particle, which makes top-quark contributions to virtual loops dominant. Moreover, the SM coupling of the HIGGS boson to fermions is expected to be proportional to the fermion’s mass, making the top quark an important probe for HIGGS-fermion physics.

The expected mean lifetime of the top quark in the SM, given the large top-quark mass, is predicted to be at the order of $5 \cdot 10^{-25}$ s [1, 28]. This timescale is about one order of magnitude smaller than the so-called hadronisation time, that is the timescale of the strong interaction [29, 30].² Hence, the top quark does not form hadrons before it decays, which allows the unique opportunity to study a “bare” quark untainted by hadronisation effects [29, 30]. As side effect, there are no bound states involving a top quark.

2.2 Production

Figure 6 compares predicted cross sections for various important physics processes at LHC energies for proton–(anti)proton collisions.

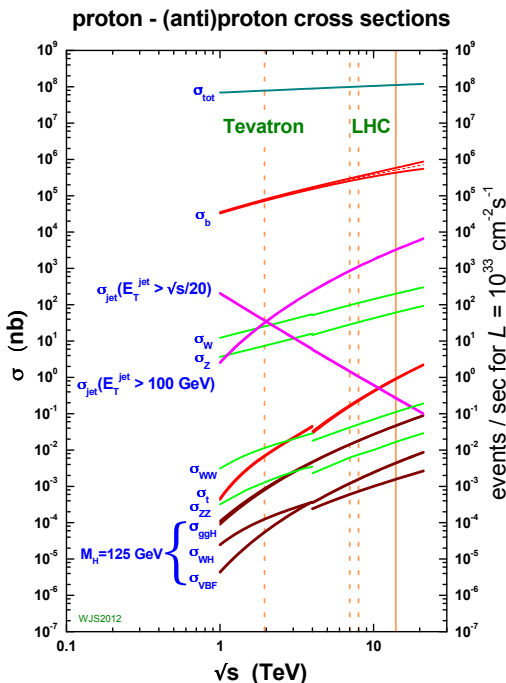


Figure 6: Cross sections for important physics processes in proton–(anti)proton collisions as a function of the centre-of-mass energy [32, 33]. For broken graphs, the left (right) piece shows $p\bar{p}$ (pp) collisions.

A strong dependence of the top-quark production rate on the collision energy can be observed — spanning about four orders of magnitude for the energy range from the Tevatron to the LHC. Even at LHC design energy, the production rate of top-quark pairs is low compared to other processes such as vector boson production. This does not mean, however, that top-quark physics is limited by statistics: the number of top quarks produced at the LHC is in the tens of millions.

Theoretical predictions are of course only one half of the picture: production cross section measurements quantify reality and can later be used to validate the accuracy of the theoretical predictions. A summary of such measurements performed by the ATLAS collaboration across a variety of processes is

² The time scale for hadronisation is $\sim 1/\Lambda_{\text{QCD}} \sim 10^{-24}$ s [31].

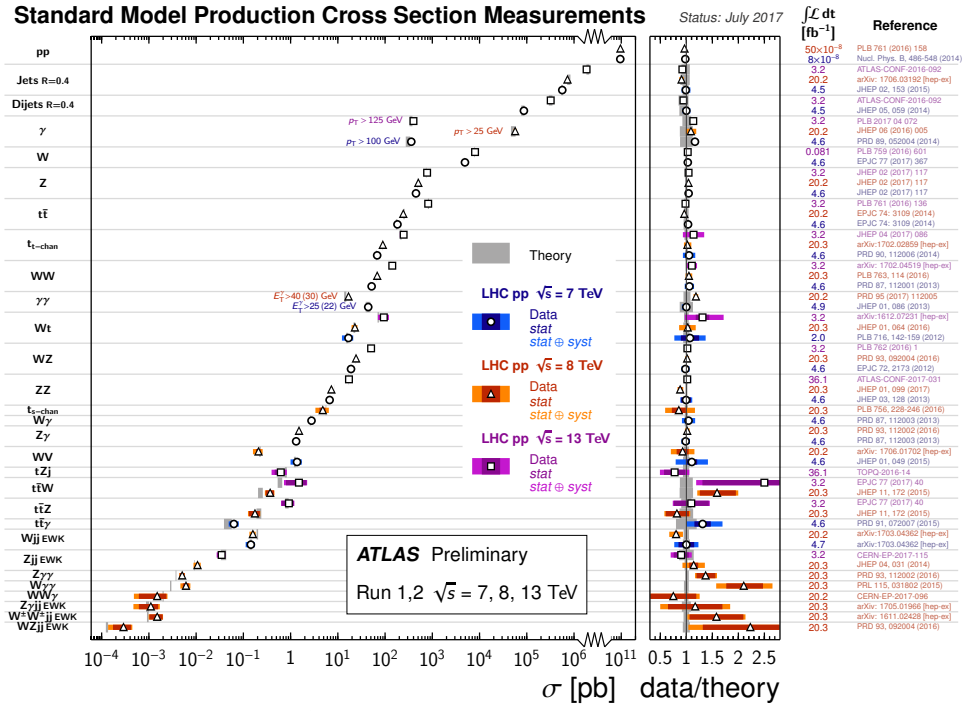


Figure 7: Detailed summary of several Standard Model total and fiducial cross section measurements performed by ATLAS [34]. The measurement results are compared to the theory predictions for the specific process.

shown in Figure 7. The different results are compared to theoretical predictions which are found to be in good agreement across a large range of processes and therefore many orders of magnitude in the production rate.

At LHC conditions, top quarks are either produced through QCD in $t\bar{t}$ pairs or through electroweak processes as single top or anti-top quarks.

§1. Pair Production At a generic proton–(anti-)proton collider the top quark can be produced as real particle in leading-order strong interactions as $t\bar{t}$ pair once the centre-of-mass energy exceeds twice the top-quark mass. Leading order FEYNMAN diagrams for top-quark pair production are shown in Figure 8. At the LHC, top-quark pairs are predominantly produced through gluon fusion.

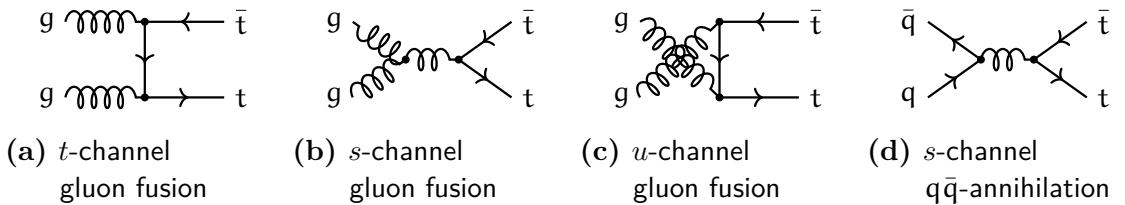


Figure 8: FEYNMAN diagrams for the leading order production mechanisms of top-quark pairs.

The top-quark pair production cross-section has been calculated to exact next-to-next-to-leading order (NNLO) in α_s including resummation of next-to-next-to-leading logarithmic soft-gluon contributions (NNLL) [35–40] which yields

$$\sigma_{t\bar{t}} = 832^{+46}_{-51} \text{ pb} \quad (3)$$

at a centre-of-mass energy of $\sqrt{s} = 13 \text{ TeV}$ and assuming a top-quark mass m_t of 172.5 GeV .³ This theoretical cross-section is calculated using the Top++ 2.0 program [41]. Figure 9 compares the measured top-quark pair production cross-section for a variety of LHC measurements as well as combinations from LHC and TeVatron data to theoretical predictions.

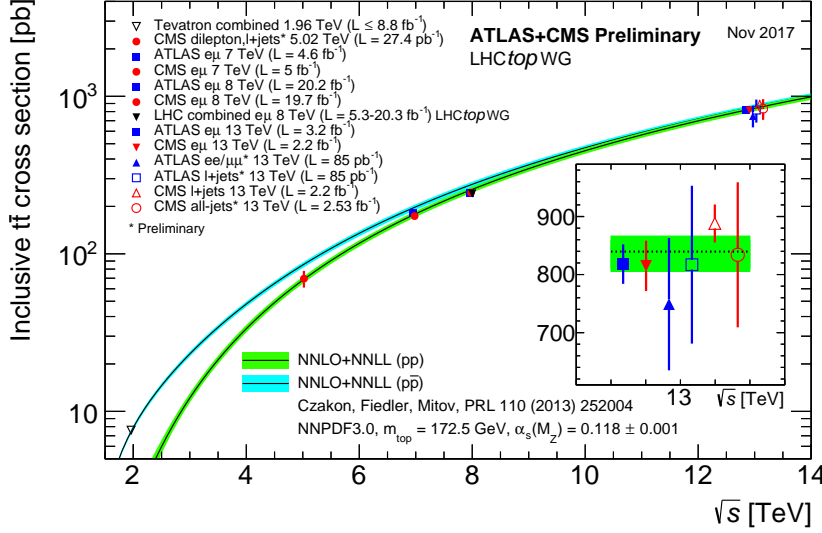


Figure 9: Summary of LHC and TeVatron measurements of top-pair production cross-section as function of centre-of-mass energy compared to NNLO+NNLL QCD prediction [27]. Measurements made at the same centre-of-mass energy are slightly offset for clarity.

§2. Single Top-Quark Production Single top quarks can be produced through electroweak interactions starting at centre-of-mass energies slightly above m_t . Observation of single top quarks was achieved by the CDF and $D\bar{O}$ experiments [42, 43] fourteen years after the discovery of the top quark in pair production.

Figure 10 shows leading order FEYNMAN diagrams for single top-quark production which is grouped into three different categories: t - and s -channel production and Wt production.

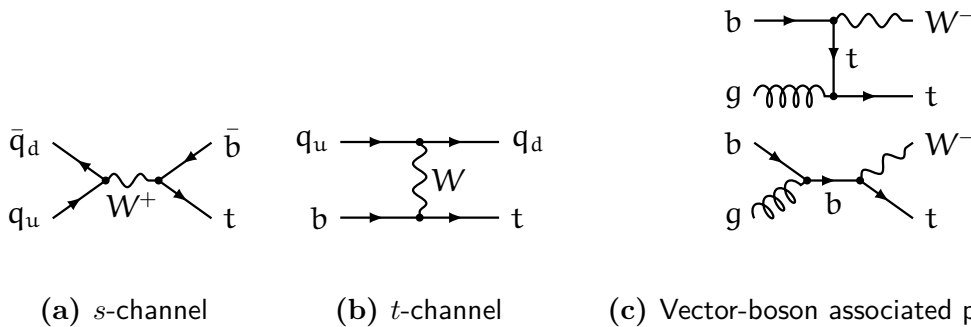


Figure 10: FEYNMAN diagrams for the leading order production mechanisms of single top quarks.

The single top-quark production cross-sections have been calculated at next-to-leading order (NLO) in α_s for the s - and t -channels and at NLO+NNLL for Wt which yields

³ The uncertainties on the theoretical cross-section reflect the impact of variations of the PDF, the strong coupling constant α_s , and the scale as well as the uncertainty on the top-quark mass on the calculation.

the cross-sections listed in Table 2. The expected total production cross-section for single top quarks is about 36 % of that calculated for pair production.

At the LHC, single top-quark production is dominated by t -channel production followed by considerable contributions from vector-boson associated (VBA) production Wt and negligible contributions from s -channel production: $\sim 75\% \sim 20\%$ and $< 5\%$ respectively, see Table 2.

Channel	Cross-section σ [pb]
t -channel	$216.99 \pm_{7.71}^{9.04}$ [44, 45]
s -channel	$10.32 \pm_{0.36}^{0.4}$ [45, 46]
Wt	71.70 ± 3.85 [45, 47]
Total	$299.01 \pm_{8.63}^{9.83}$

Table 2: Predicted production cross-sections for different single top-quark production modes in pp collisions at a centre-of-mass energy of $\sqrt{s} = 13$ TeV and assuming a top-quark mass of $m_t = 172.5$ GeV.

Figure 11 compares ATLAS measurements of the single top-quark production cross-section in all three production modes for a variety of centre-of-mass energies to the theoretical predictions.

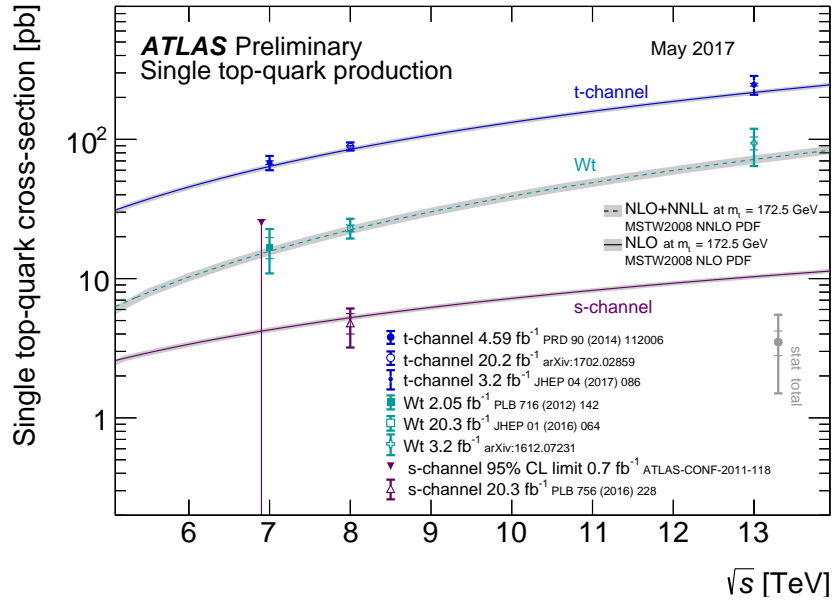


Figure 11: Summary of ATLAS measurements of the single top-quark production cross-sections in various channels as a function of the centre-of-mass energy compared to theoretical calculations based on NLO QCD and on NLO QCD complemented with NNLL resummation [27].

At leading order, the single top-quark is accompanied either by a W boson or a lighter quark, therefore, the production signature for single top events is more polluted than that of top-quark pairs. Single top-quark and $t\bar{t}$ pair production are often mutual sources of background contamination. Indeed, the dominant pair production typically contributes as a large background pollution to single-top measurements. Conversely, production of Wt can mimic a $t\bar{t}$ signal and is usually one of the main background contaminations to $t\bar{t}$ measurements in final states with at least one lepton.

Single top-quark measurements provide opportunity for a rich range of property measurements. For example, all (leading order) single top-quark production channels are sensitive to the CKM matrix element $|V_{tb}|$. In fact, single top-quark production remains the only method for a direct $|V_{tb}|$ measurement to this day [1].

Regardless, the work presented in this thesis focuses on $t\bar{t}$ production and measurements based upon this signal. Therefore, single top-quarks will be considered as background contribution for the remainder of this thesis. With the growing dataset of the LHC, rarer processes including top quarks such as associated production $t\bar{t} + X$ where $X = \{W, Z, H\}$ or even production of two $t\bar{t}$ pairs become available for study. However, like the much larger single top-quark production, these contributions are considered background to the work presented in this thesis.

2.3 Decay

Following its production, a top quark decays rapidly through the electroweak interaction. In the SM this decay follows the chain $t \rightarrow W^+ q_d$ (charge conjugates implied). Since the CKM matrix element $|V_{tb}|$ is almost unity — see Equation (1) — the top quark decays almost exclusively to a W^+ and b , as depicted in Figure 12. Contributions to $W^+ d$ or $W^+ s$ are typically only relevant for studies that specifically target the light-quark decays.⁴

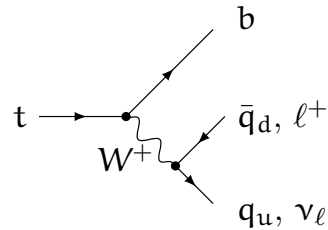


Figure 12: FEYNMAN diagram of top-quark decay (charge conjugates implied).

§1. Decay Channels Due to the top-quark’s large mass, the W boson can be produced on-shell. It then decays either hadronically, i.e. $W^+ \rightarrow q_u \bar{q}_d$, or leptonically, i.e. $W^+ \rightarrow l^+ \nu_l$ (charge conjugates implied). The charge of the W boson classifies the top quark as quark or anti-quark and, unlike that of the b/\bar{b} quark, can be measured reliably in leptonic decay modes.

Each $t\bar{t}$ pair features two such decay arms, which classify the event as **dileptonic**, **semileptonic** (also called *single lepton*, *lepton + jets*, or $l + \text{jets}$), or **allhadronic** (sometimes called *alljets*). Unlike the electron or muon, the τ lepton typically decays within the detector of a particle physics experiment. The τ is not observed directly but rather through its decay products. Since resolving this decay separately is experimentally rather challenging, τ lepton decay modes of the top-quark are typically classified by the resulting final state. The work presented in this thesis makes use of this simplification.

Figure 13 shows illustrations for the different decay topologies typically considered by $t\bar{t}$ measurements. The three channels mentioned before are shown in Figure 13 (a)–(c).

⁴ In practice, most LHC measurements — including the measurements presented in this thesis — assume $\text{Br}(t \rightarrow Wb) = 1$. This is in agreement with the measured value for $|V_{tb}|$ which is consistent with unity [1].

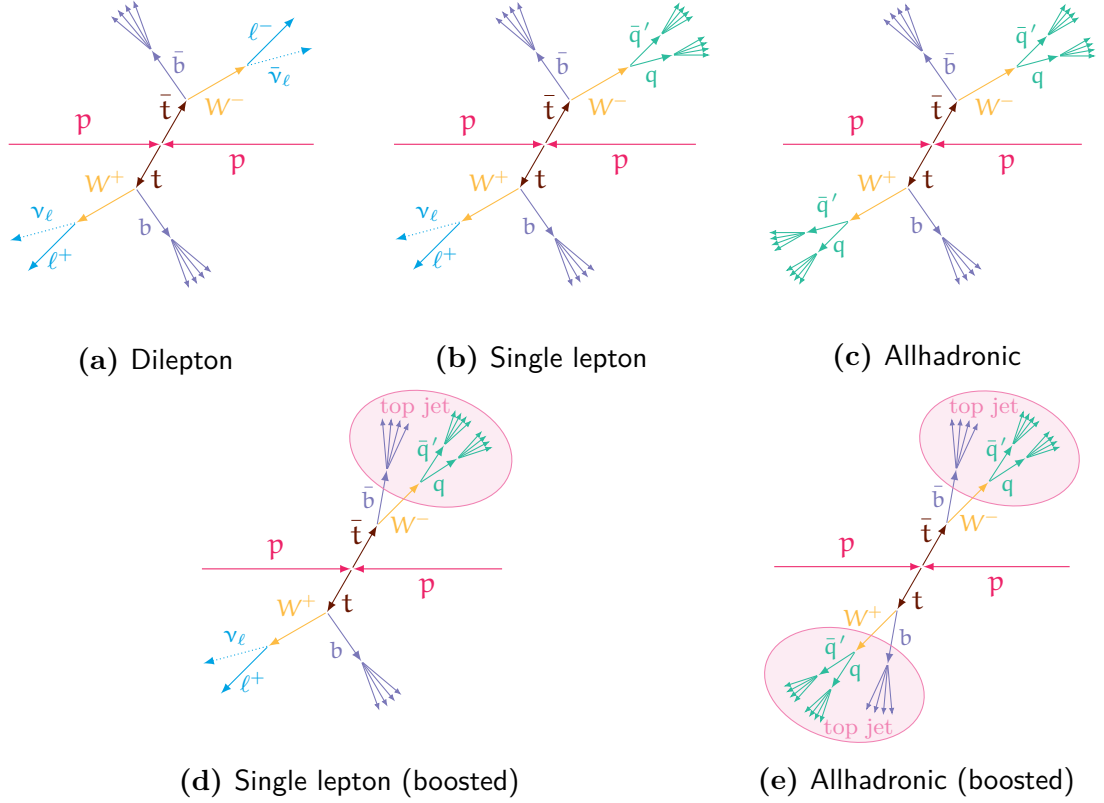


Figure 13: Illustrations of $t\bar{t}$ decay topologies typically considered by various top-quark measurements.

For final states involving at least one hadronically decaying W boson so called *boosted* topologies are considered as well; these are shown in Figure 13 (d)–(e). Boosted topologies account for the fact that if a hadronically decaying top-quark has large (transverse) momentum, and therefore **LORENTZ** boost, the jets originating from its decay products are expected to be rather collinear. As a consequence, the individual jets formed from the chain $t \rightarrow bW(\rightarrow q\bar{q}')$ are extremely close and thus resolving them individually is difficult.

§2. Branching Fractions Calculation of the approximate branching fractions for the decay channels is straightforward: a W boson decays to all of the lepton pairs with the same probability yielding three equally probable leptonic W decay modes. Since the W boson is colour neutral, there exist three different decay modes for each of the valid up- and down quark combinations ($q_u\bar{q}_d$ for a W^+) which correspond to the three colour neutral quark combinations $|\mathcal{C}\bar{\mathcal{C}}\rangle$ for $\mathcal{C} \in \{\mathfrak{R}, \mathfrak{G}, \mathfrak{B}\}$. Since the W boson is on-shell and too light to decay to $t\bar{b}$, there are two possible quark pairs, namely $u\bar{d}$ and $c\bar{s}$.⁵ Therefore, there are an additional 2×3 approximately equally probable hadronic W decay modes.

Hence, for a single W boson, the branching fraction for a leptonic decay is $1/3$ and for a hadronic decay $2/3$. Using combinatorics one can then calculate the branching fractions for the $t\bar{t}$ decay modes that are listed in Figure 14.

⁵ The mixed generation couplings can be ignored because the CKM matrix is unitary.

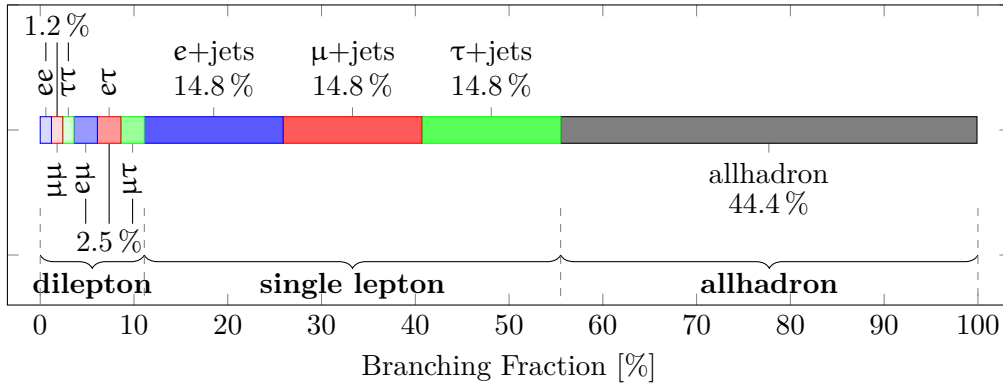


Figure 14: Decay modes of $t\bar{t}$ system and approximate branching fractions for the individual channels.

Traditionally, the single lepton final states $e + \text{jets}$ and $\mu + \text{jets}$ are considered the golden channel of top-quark physics. They have a distinctive signature with a high-momentum lepton, which reduces contamination by background sources, and the branching fraction is reasonably large, ensuring ample statistics. The dilepton final state has a very clean signature with considerably lower expected background contamination, however, its total contribution is rather small. Nevertheless, with the large datasets available at the LHC, measurements in the dilepton channel are less likely to suffer from low statistics. On the one hand, measurements in the allhadronic final state have to cope with significantly larger background contamination, on the other hand, the large branching fraction ensures a sizeable dataset. Extensive statistics may be used to leverage the large background contamination or focus on rare regions of phase space. Furthermore, the allhadronic final state is the only $t\bar{t}$ final state without neutrinos which generally escape direct detection and must be reconstructed through momentum imbalance constraints.

3 Introduction to Colour Flow

CONTENTS		
3.1	Introduction	35
3.2	Colour Flow as part of QCD	36
3.3	Historical Perspective	38

A complete measurement as well as a variety of studies of the colour flow in $t\bar{t}$ events are the centrepiece of the work presented in this thesis. In this section, colour flow will be introduced with some remarks on the theoretical background. In addition, a quick overview of previous measurements related to colour flow is presented.

3.1 Introduction

In high-energy hadron collisions, such as those at the LHC, both quarks and gluons are produced abundantly in the initial hard-scatter collision as well as the subsequent decay and event formation. However, as a result of the confining nature of Quantum Chromodynamics, a direct measurement of quarks and gluons as well as the interactions that occur between these particles is not possible. Instead, only colourless hadrons can be measured. Nevertheless, the colour charge carried by the quarks and gluons produced in the hard-scatter interaction is considered by every subsequent interaction and decay in which they participate. This colour charge “flows” from the initial state towards stable particles according to rules illustrated by Figure 15, which depicts the colour connections for relevant elementary QCD vertices. The colour charge of particles that are involved affects both strength and direction of the strong force. An approximate description of the radiation patterns in QCD is obtained through a colour-connection picture, see Ref. [48], where colour strings connect quarks and gluons of a given colour to quarks and gluons with the corresponding anti-colour. Since the overall colour charge is conserved, connections must exist between initial (coloured) particles and the components of stable colour-neutral hadrons. Emission of a gluon may “repaint” a quark before it fragments, however, its remains then have some colour connection to the fragmentation remains of the gluon.



Figure 15: QCD colour propagation rules for elementary quark-gluon vertices. Black lines denote FEYNMAN-diagram style vertices, coloured lines show QCD colour connection lines.

In an experimental apparatus, the high energy quarks and gluons of the initial hard-scatter are measured as *jets*. These are bunches of collimated hadrons that form in the time-evolution of the coloured initial particles. Colour connections between the high energy particles influence the structure of emitted radiation and also the structure of the resulting jets. For example, soft gluon radiation off a quark is

enhanced in some regions of phase space compared to others as will be discussed in more detail in the next section.

The impact of colour connections on the event shape and structure of composite objects, such as jets, is rather subtle compared to that of kinematic effects. Measuring these effects is experimentally challenging. However, providing conclusive evidence for the existence of the connections — the *colour flow* — between particles across the event is important for the validation of the theory as well as phenomenological description.

3.2 Colour Flow as part of QCD

The observer does not have direct access to QCD, instead we observe jets which form according to the rules of QCD. This jet formation process consists of multiple stages, which will be revisited again in Section 7, that differ in the energy scale of the particles involved. Colour flow has important implications for all stages of jet formation.

The colour flow of the hard-scatter event is set and fixed by the topology of said hard-scatter and follows directly from the QCD calculation of the process. This colour flow indirectly affects jet formation as it is the input to all following effects.

§1. Colour Coherence Effects At large energy scale, that is during the so-called parton shower and before hadronisation, colour flow affects jet formation through *colour coherence* in the emission pattern of gluons. Specifically, an increase of radiation is predicted along a colour connection compared to a region of phase space without such a connection as result of this coherence effect, for more details see Ref. [48]. This effect has an analogue in QED, the **CHUDAKOV** effect, which is discussed here for simplicity.

In short, the **CHUDAKOV** effect predicts that the emission of secondary photons in the process $\gamma \rightarrow e^+e^- \rightarrow e^+e^-\gamma$ — which initially is a $1 \rightarrow 2$ QED splitting process — is suppressed outside of the opening angle of the e^+e^- cone.

For a heuristic analysis,¹ consider a photon which splits into an electron-positron pair where the electron later radiates a secondary photon, see Figure 16. A splitting variable z that defines the momentum fraction passed on to the secondary photon can be introduced. Assume for simplicity that both angles θ_{ee} and $\theta_{e\gamma}$ are small. In this approximation, the transverse momentum of the radiated secondary photon is $k_{\perp} \sim zp\theta_{e\gamma}$. The secondary photon must be radiated within a timescale Δt defined by the virtuality of the intermediate electron.

¹ This is based on the approach presented in Ref. [48], a similar treatment can be found in Ref. [49].

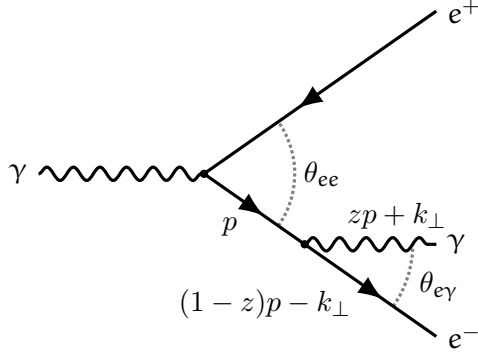


Figure 16: The CHUDAKOV effect: a soft photon from an electron cannot resolve its parent from the accompanying positron. In the FEYNMAN diagram a primary photon splits into an e^+e^- pair, the electron in turn emits a secondary photon. The virtual electron's momentum prior to emission of the photon is p which is passed on to the (real) electron and the radiated photon according to the splitting variable z ; the momentum k_\perp describes the out-of-plane component of the secondary photon and real electron relative to the virtual electron.

This timescale is related to the energy imbalance ΔE at the $e \rightarrow e\gamma$ vertex

$$\Delta E \sim k_\perp^2/zp \sim zp\theta_{e\gamma}^2 \quad (4)$$

according to the HEISENBERG uncertainty principle through $\Delta E\Delta t \sim 1$.² At the same time, the separation between the e^+e^- pair will become

$$\Delta d \sim \theta_{ee}\Delta t \sim \theta_{ee}/zp\theta_{e\gamma}^2. \quad (5)$$

A non-negligible probability for the emission of the secondary photon requires that the photon can actually resolve the electron rather than just the e^+e^- pair. If the photon cannot resolve the two fermions separately, it must act on the pair which has a net electric charge of zero and therefore implies no emission at all. The requirement translates to

$$\Delta d > \frac{\lambda}{\theta_{e\gamma}} \sim \frac{1}{zp\theta_{e\gamma}} \quad \rightarrow \quad \frac{\theta_{ee}}{zp\theta_{e\gamma}^2} > \frac{1}{zp\theta_{e\gamma}}, \quad (6)$$

where λ is the secondary photon's wavelength, which implies that $\theta_{ee} > \theta_{e\gamma}$.

Going from QED to QCD, the electric charges must be replaced by colour charges which complicates the derivation and introduces additional colour factors, see also Ref. [48]. For a generic parton without colour charge splitting into a $q\bar{q}$, i.e. for example for $e^+e^- \rightarrow \gamma \rightarrow q\bar{q}$, the effect of colour coherence is essentially the same as the CHUDAKOV effect in QED. Gluon radiation at large angles is suppressed because the gluon fails to resolve the individual quarks and instead is sensitive to the colourless initial parton.

§2. Colour Reconnection Effects In addition to colour coherence, *colour reconnection* (CR) effects are also influenced by colour flow. Contributions in the perturbative regime are expected to be negligible [51], however, non-perturbative colour reconnection impacts hadronisation. Hadronisation, which is a comparatively low energy process, is the process responsible for the formation of (colourless) hadrons out of the quarks and gluons resulting from the previous higher energy QCD processes; it will be revisited in Section 7. The QCD theory of hadronisation is

² The relation for the energy imbalance follows from $1 \rightarrow 2$ splitting considerations for the emission of a massless particle as discussed in Ref. [50].

not fully understood and no first-principles theory exists at the moment. Instead, a variety of phenomenological models, that are inspired by perturbative QCD and experimental observations, are used.

Colour reconnection effects are a result of the finite number of colour charges as well as overlaps of colour connections in space-time.³ Put simply, the overall colour charge topology of an event subtly affects hadron formation all across the event and is a form of “*cross-talk*” [54]. Ambiguities regarding the partons which belong to separate colour-singlets are a result of the small number of colour-charge values N_C — which is equal to three in the SM. CR effects are particularly relevant for topologies which involve relatively short-distance production of coloured particles from a colour-singlet parent such as $e^+e^- \rightarrow W^+W^- \rightarrow$ hadrons, see Ref. [55, 56], or the $t\bar{t} \rightarrow \ell + \text{jets}$ topology studied by the work presented in this thesis [53].⁴

For example, in the decay $t \rightarrow b\bar{u}d$ (via an intermediate W boson), the $u\bar{d}$ system may not remain as a fully separate colour-singlet due to the overlaps. Rather than showering and hadronising fully independently, some cross-talk effects occur. In general, the CR effect is suppressed with $1/N_C^2$ [53].

3.3 Historical Perspective

In the mid-1970s QCD was regarded as the only viable candidate theory to explain strong interactions [57]. A variety of then-recent observations could be explained using the theory. However, a direct proof of the existence of the gluon, the mediator of QCD, remained elusive. Eventually, it was suggested to look for widening of jets in two-jet events or even a proper three-jet structure from an e^+e^- initial state [58]. This structure emerges in $e^+e^- \rightarrow$ hadrons ($\equiv q\bar{q}$) production as the centre-of-mass energy increases [59]. Initially, as the centre-of-mass energy \sqrt{s} grows, a two-jet structure can be observed. With further increasing \sqrt{s} , a relatively low-momentum gluon may be radiated resulting in a widening of one of the quark-jets. Eventually, large-angle radiation of a gluon becomes possible and the complete three-jet structure can be observed. Based on momentum-conservation considerations, the kinematics of the three jets are expected to fall into a plane with very small amount of transverse momentum. By exploiting such event-shape features, the gluon was conclusively discovered at PETRA at a centre-of-mass energy of $\sqrt{s} = 27.4$ GeV [60–63].

Following the discovery, a variety of studies were performed to further understand the structure of the three-jet events. At its core, these measurements were precursors to modern colour flow measurements which exploit simple observables based on the

³ Sometimes this effect is also-called *colour rearrangement*. See Refs. [52, 53] for a brief overview of colour reconnection (CR) and phenomenological models as well as implications of CR for measurements at the LHC.

⁴ The reason for the relevance of the hadronic W boson decays is the expected vertex separation of ~ 0.1 fm which is significantly smaller than the typical hadronic scale of ~ 1 fm. Similarly, the top quark decays well within the hadronic scale, see Ref. [53].

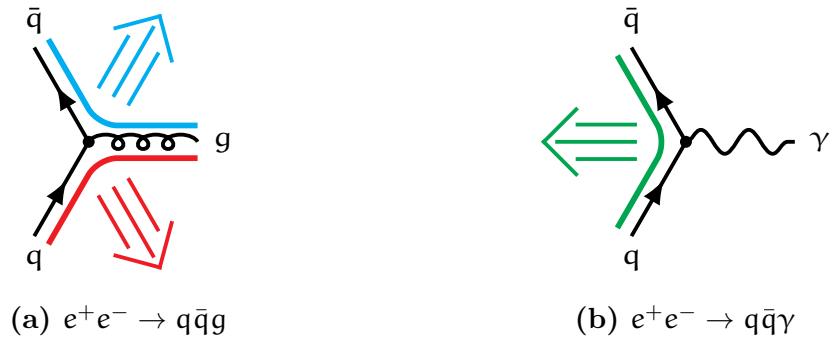


Figure 17: Illustration of decay signatures of three-particle final states used for the analyses at PETRA. For simplicity, particles are assumed to have equal absolute momentum and illustration is shown in the centre-of-mass frame. The coloured lines symbolise colour connections, the arrows directions towards which additional radiation is expected to be pulled.

event superstructure. For example, it was found that additional radiation mostly forms between the quarks and high energy gluon(s), as illustrated in Figure 17. This dependence of the observed radiation patterns on the colour flow defined by the hard partons is particularly striking when compared to $q\bar{q}\gamma$ events where the radiation is enhanced between the two quark-jets. The observed pattern, which is an excellent example of colour coherence, is a result of the fact that showering and fragmentation of quarks and gluons occurs preferentially along a colour connection.

Furthermore, the JADE collaboration compared the shape of the different jets in measured three-jet events and found that the third-leading jet in these three-jet events has a noticeably different shape compared to the leading and subleading jets or any of the jets in di-jet events [64]. In these studies it was found that the third-leading jet, the presumed gluon-jet, has a broader energy and constituent distribution than the other two jets, the presumed quark-jets. This can also be compared to the $q\bar{q}\gamma$ final state which contains exclusively quark-initiated jets. The study of jets based on whether they are initiated by fragmentation of a quark or gluon is still a relevant topic in particle physics. However, emphasis has shifted from pure discovery and study to the desire to make use of these difference in the form of classification.

In the years following the discovery of the gluon, colour coherence measurements using the three-jet topology have been performed across a range of particle colliders and centre-of-mass energies for example in e^+e^- collisions at PETRA [64, 65], PEP [66–68] and LEP [69, 70], $p\bar{p}$ collisions at the TeVatron [71–73], and pp collisions at the LHC [74].

At LEP, on-shell production of both Z and W bosons is abundant and very clean thanks to the leptonic initial state. This setup initiated a new class of colour flow measurements which make use of the colourless initial state provided in the hadronic decay modes of the electroweak bosons. In hadronic WW diboson events interconnection effects between the jets originating from the decay of different W

bosons were observed [56, 75, 76]. The ratios of particle and energy flow quantities in the interjet regions for jets either from the same or different W bosons were found to be sensitive to the modelling of the colour flow and in particular the modelling of colour reconnection effects. Colour reconnection and coherence effects were also observed using colour-singlet initial states based on hadronic Z decays [77, 78]. At the TeVatron, a measurement of the energy (distribution) surrounding high-energy jets in events selected for $W + \text{jets}$ ⁵ was found to be sensitive to the modelling of the colour flow in simulation [79].

The next evolution in colour flow measurements involved the combination of two aspects previously only used separately: information gained from the activity within a jet, the so-called *jet substructure*, can be complemented by information about the activity between different jets, the *jet superstructure*, to achieve an enhanced sensitivity. On one end, jet substructure provides sensitivity to soft radiation originating from a relatively hard scale with a comparably reduced contamination. Conversely, at the other end, jet superstructure allows to introduce sensitivity to the event topology.

The *jet pull* is a jet substructure variable built from momentum-weighted radial moments of jet constituents. It can be used to construct the *jet-pull angle* by combining the jet pull with the relative orientation of two jets within the event, which is jet superstructure information. This concept was first introduced in Ref. [80]. Both the jet pull and jet-pull angle derived from it will be revisited in Section 13.

The jet-pull angle was designed to be sensitive to the colour flow of the initiation partons of two (arbitrary) jets. Its inventors suggested that it may be used to separate dijets that originate from a colour singlet, such as a W/Z or H_{IGGS} boson, from those that come from a colour octet, such as a gluon [80, 81]. Indeed, the jet-pull angle was used for that purpose with some success at the TeVatron [82] and LHC [10, 83] in searches for the H_{IGGS} boson.⁶ The jet pull angle has also been the target of dedicated analyses both at the TeVatron [84] and the LHC [85]. In this thesis, the first analysis using the jet-pull angle at a centre-of-mass energy of $\sqrt{s} = 13 \text{ TeV}$ is presented. The existing range of observables derived from the jet-pull observable is extended — in comparison to previous analyses — in order to obtain a better understanding of the capabilities of the jet pull.

⁵ Rather than using a hadronically decaying W boson to provide a well-defined colourless initial state, this measurement balances a high- p_{T} jet in one event hemisphere against a leptonically decaying W boson. The W and its children are colourless and therefore do not influence the colour structure of the jet which is studied and can be used as a colourless reference signal on event-by-event basis.

⁶ The analyses use the pull angle observable along with many other variables as inputs to a machine learning algorithm in order to construct a signal-discriminating variable.



The Experimental Apparatus

In this chapter, the experimental apparatus used by the ATLAS collaboration will be discussed. In Section 4, the Large Hadron Collider and its general design and performance are presented. Afterwards, in Section 5 the ATLAS detector is discussed in detail. Finally, Section 6 provides a perspective of the future: the upgrade schedule and plans for the experimental apparatus are presented, as well as personal contributions by the author.

4 The Large Hadron Collider

CONTENTS	
4.1 Accelerator Design	42
4.2 Performance	44

The *Large Hadron Collider* (LHC) [86] located at the European Organization for Nuclear Research (CERN) near Geneva, Switzerland is the most powerful particle accelerator built to this day. It is designed to provide proton and ion collisions at centre-of-mass energies of up to $\sqrt{s} = 14$ TeV (for pp collisions). The accelerator is a circular accelerator with a circumference of about 27 km and is located in an underground tunnel at around 100 m to 175 m depth which previously hosted the LEP electron–positron collider from 1989 to 2000 [87]. Following the LEP shutdown and subsequent LHC approval, four of the eight existing tunnel access points were redeveloped to accommodate four new main experiments: the multipurpose experiments ATLAS [88] and CMS [89], the b-physics experiment LHCb [90], and an experiment which is designed to study interactions at extreme energy densities in collisions of heavy ions ALICE [91].

During its first operating period, known as *Run 1*, from 2010 to 2013, the LHC provided collisions at centre-of-mass energies of 7 and later 8 TeV. Subsequently, the accelerator complex and the experiments have undergone a major maintenance and upgrade program, during the so-called *Long Shutdown 1* (LS1). The next operating period, *Run 2*, started in 2015 at an increased centre-of-mass energy of 13 TeV. Run 2 is expected to last until the end of 2018, when the next phase of major maintenance and upgrades is planned.

4.1 Accelerator Design

The LHC is the final stage of a multi-staged accelerator complex [92]. Figure 18 shows a topographic map of the accelerator complex located at CERN. The stages of this accelerator chain service not only the LHC but also a variety of other experiments as shown on the map.

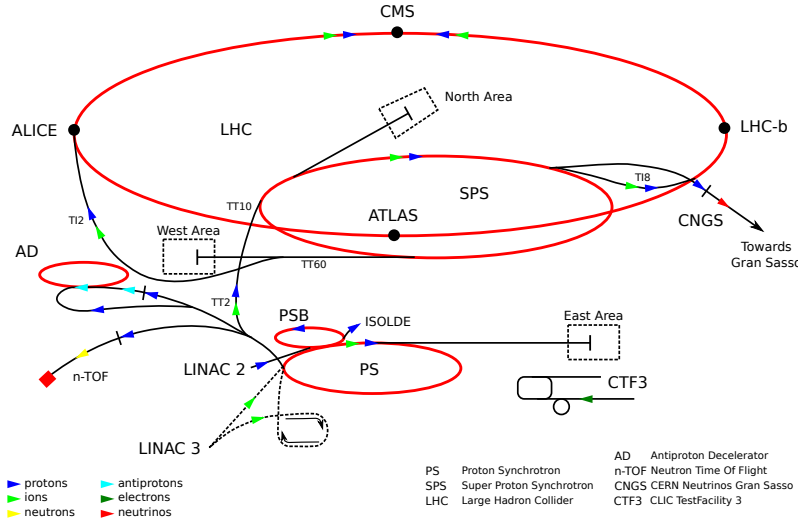


Figure 18: The CERN accelerator complex [93].

By using a multi-staged accelerator system, a more diverse range of beam energies is available to the many experiments at CERN. Furthermore, this design allows to re-use and share accelerators as well as use designs specific to the requirements at the given intermediate beam energy. Likewise, the final component, the LHC, can be tuned to the needs of the collider experiments at maximum energy. In fact, low-energy beams could not be injected and accelerated in the LHC.

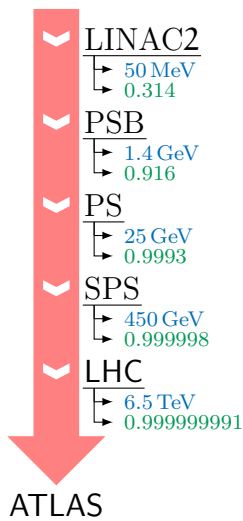


Figure 19: Accelerator chain used for pp physics at ATLAS. For each accelerator, the first number is the proton energy, the second the proton speed in units of speed of light.

Figure 19 shows the accelerator chain used for proton–proton collisions at the ATLAS experiment at the LHC. Each proton collision at the LHC starts from a bottle of hydrogen gas: hydrogen atoms are broken down, separating protons and electrons, and the protons are extracted using an electric field. These protons are injected into the LINAC2 which was commissioned in 1978. It is the only linear accelerator in the whole LHC chain and accelerates the protons to an energy of 50 MeV over a distance of about 36 m.

The protons are then transferred into the *Proton Synchrotron Booster* (PSB), a circular accelerator with a circumference of about 157 m which was commissioned in 1972. The PSB accelerates the protons to an energy of 1.4 GeV before passing them to the *Proton Synchrotron* (PS).

The PS, which was built in 1959 and is thus the oldest part of the LHC accelerator chain, has a circumference of 628 m. Acceleration in the PS takes the protons to a nominal energy of 25 GeV. In addition, the PS is also used to separate the protons into groups, so-called *bunches*, as is needed for LHC operation. From the PS, the protons are passed on to the next and penultimate stage, the *Super Proton Synchrotron* (SPS).

The SPS has a circumference of 6.9 km and accelerates the protons to the nominal LHC injection energy of 450 GeV. It was originally commissioned in 1976. In addition to being an injector for the LHC, the SPS provides protons to a number of fixed target experiments located at CERN's north area. Furthermore, its protons are used as input for the production of the neutrinos used by the CERN Neutrinos to Gran Sasso (CNGS) experiment.

Protons are transferred to the LHC using two transfer lines and are fed into its two beam pipes forming the desired contra-rotating beams. In the LHC, the two beams are accelerated to the nominal beam energy. After careful tuning of the beam energy and envelope, the beams are declared stable and brought to collision at the four interaction points. Filling of one of the LHC's rings takes about 4¹/₂ minutes, the subsequent acceleration phase in the LHC typically concludes after about 25 minutes.

The particles are not stored individually or as a single continuous stream in the LHC but rather as so-called *bunches*. A bunch typically consists of several billion protons and at nominal operation around 2000 bunches circulate the LHC per beam. The bunches are separated by a gap of 50 ns during commissioning and early data taking periods and 25 ns during nominal operation. The latter corresponds to a bunch separation of about 7.5 m, less than a third of the length of the ATLAS detector. The bunch spacing also determines the collision rate of 40 MHz. Over the course of a single run, which can last many hours, the bunch contents decline due to the collisions. Once bunch and beam properties have degraded too much or the filling of the LHC has fallen too much, the beams are dumped and a new fill is started.

Rather than being a perfect circle, the LHC consists of eight arc sections and eight straight sections which alternate. Each arc contains 154 dipole (*bending*) magnets to keep the protons on track, as well as several quadrupole (totaling at about 50 per arc) and other multipole magnets which are used for correcting the beam position and general focusing. All magnets are superconducting — in order to achieve the required field strengths of up to 8.6 T — and to enable this, they must be cooled down to about 1.9 K using fluid helium. The straight sections host the access cavities which also contain the detectors operated by the main LHC experiments.

Heavy Ion Runs In addition to pp operation, the LHC spends some time each year producing Pb-Pb and p-Pb collision, the so-called heavy ion runs. As the

heavy-ion physics programme is not relevant to the work presented in this thesis, the corresponding dataset and the specific requirements for its operation are not discussed any further.

4.2 Performance

A measure of the performance of an accelerator is the number of collisions at an interaction point, which can be expressed as *instantaneous luminosity* \mathcal{L} . This quantity describes the number of interactions that occur per second and unit area, it is expressed in units of $[\text{cm}^{-2} \text{s}^{-1}]$.

For a physics measurement, the total dataset size is more relevant. It is quantified by the *integrated luminosity* $\mathcal{L}_{\text{Int}} := \int \mathcal{L} dt$. In practice, this quantity is expressed in inverse barns with $1 \text{ b}^{-1} \equiv 1 \cdot 10^{24} \text{ cm}^{-2}$ with typical values for the LHC being of order $1 \text{ fb}^{-1} \equiv 1000 \text{ pb}^{-1} \equiv 1 \cdot 10^{39} \text{ cm}^{-2}$. For a given process \mathcal{L}_{Int} can be used to calculate the expected number of collisions that are attributed to the process in question using the relation $N = \sigma \cdot \mathcal{L}_{\text{Int}}$, where σ is the cross-section of that process.

The expected instantaneous luminosity can be calculated from beam parameters using

$$\mathcal{L} = \frac{N_B n_b^2 f_{\text{Rev}}}{4\pi\sigma_x\sigma_y}, \quad (7)$$

where N_B is the number of bunches, n_b is the number of particles per bunch, f_{Rev} is the beam revolution frequency,¹ and σ_x and σ_y are the beam widths assuming that the beams have a **GAUSSIAN** profile. This assumes that the two beams have equal filling characteristics and profiles. In practice, the beams do not collide head-on but rather under a small angle. While this reduces the expected luminosity it improves accelerator performance because it makes re-use of the non-scattered parts of each beam more straightforward. The luminosity formula shown above must be corrected for such effects.

Figure 20 shows the cumulative total integrated luminosity for the ATLAS experiment for each year of data taking between 2011 and 2017.² Typically, the LHC is operated from around March until early November with a series of minor technical and improvement stops in between. The winter months are used for more extensive maintenance. Throughout the year as well as the operating period, the performance of the machine typically improves as a result of minor upgrades and better fine-tuning of the machine.

In practice, the amount of collisions recorded by the experiments is lower than what is delivered by the machine due to a variety of technical reasons. Furthermore,

¹ Which is $f_{\text{Rev}} = \frac{c}{2\pi R_{\text{LHC}}} \approx \frac{c}{26\,659 \text{ m}} \approx 11.2 \text{ kHz}$.

² All examples of LHC performance presented in this section use ATLAS data.

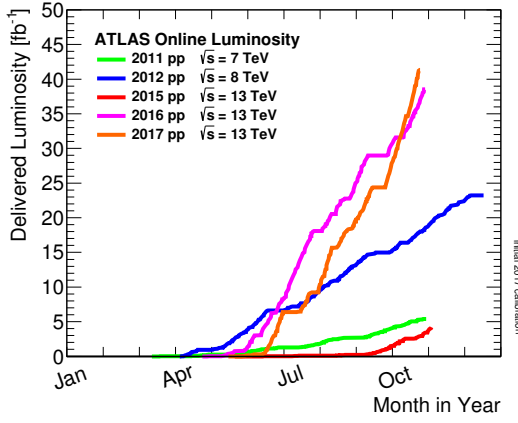


Figure 20: Cumulative luminosity delivered to ATLAS for both Run 1 and 2 shown individually for each year [94].

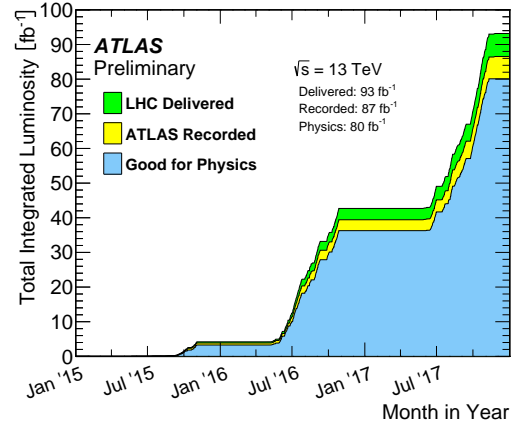


Figure 21: Cumulative integrated delivered and recorded luminosity and data quality during Run 2 [94].

some of the collision data recorded by the experiments may not be acceptable for physics analyses. For example, data taken during periods where some detector components were not fully operational is rejected. Data quality assessments are used after data-taking to evaluate whether a given period of recorded data should be rejected. Figure 21 shows a detailed breakdown of the data taken between 2015 and 2017 into the three resulting categories labelled *delivered*, *recorded*, and *all good for physics*.

Due to the large number of protons in each of the colliding bunches and the relatively high collision rate of about 40 MHz, multiple interactions occur during each of the bunch crossings at ATLAS. This induces a kind of noise into the measurement which must be understood and modelled in simulation. The mean number of interactions per bunch-crossing $\langle\mu\rangle$ quantifies the strength of this effect and is crucial for proper modelling in simulation. Figure 22 shows the distribution of $\langle\mu\rangle$ as observed by the ATLAS experiment during Run 2 operation.

Using the top-quark production cross-section predictions presented in Section 2.2 and the luminosity measurements performed by ATLAS, one can calculate the expected number of top quarks produced in the collisions at ATLAS: during the operational period of 2015 and 2016 more than 22.8 million top-quark pairs are expected to have been produced alongside with an additional 10 million single top-quarks.³ Furthermore, at peak

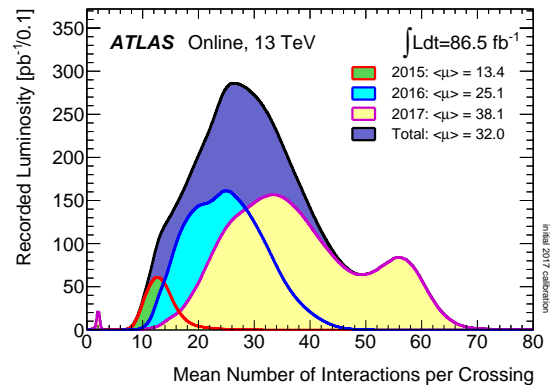


Figure 22: Luminosity-weighted distribution of the mean number of interactions per crossing [94].

³ This uses an integrated luminosity of $\mathcal{L}_{\text{Int}} = 36.1 \text{ fb}^{-1}$ which corresponds to the data classified as *all good for physics* for that period.

luminosity slightly more than ten top-quark pairs have been produced per second.⁴ However, not all of these top-quark events fall within the detector acceptance and are properly reconstructed and selected by analysis requirements. Consequently, the expected number of top-quark pair events observed by a measurement is considerably smaller.

⁴ The ATLAS experiment reports a peak luminosity of $\mathcal{L} = 13.8 \cdot 10^{33} \text{ cm}^{-2} \text{ s}^{-1}$ for operation during 2016 [94].

5 The ATLAS Experiment

CONTENTS		
5.1	Design Concepts and Requirements	47
5.2	The Detector Coordinate System	49
5.3	Detector Subsystems	50
5.3.1	The Inner Tracking System	51
5.3.2	The Calorimetry System	54
5.3.3	The Muon Spectrometer	56
5.3.4	The Magnet System	57
5.3.5	The Trigger System	58

In this section, the ATLAS experiment and its detector are presented. Section 5.1 outlines some design concepts and requirements motivated by physics analyses. The detector coordinate system is briefly introduced in Section 5.2 and the various detector components are discussed in Section 5.3.

The ATLAS experiment is a general-purpose particle-physics experiment. With a forward–backward symmetric cylindrical geometry, the ATLAS detector achieves a solid-angle coverage of almost 4π [88].

The detector is the physically largest of the LHC experiments, measuring roughly $44\text{ m} \times 25\text{ m}$ (length \times height / depth). It weighs around 7000 t which is about half of the mass of the CMS detector. The experiment is located at “*Point 1*” in a large underground cavern which shields the detector from background signals such as cosmic rays.

5.1 Design Concepts and Requirements

The ATLAS detector is composed of an inner tracking system, a solenoid magnet, a calorimeter system, a set of outer magnets, and a muon spectrometer. A schematic drawing can be found in Figure 23. Information from various detector components is interfaced with a trigger system which, in a simple analogy, operates like the shutter on a photo camera hence controlling data recording.

While the hunt for the HIGGS boson was an expressed goal when the detector was designed, the detector was constructed to allow a rich programme of particle-physics analyses beyond HIGGS. This design enables to study known Standard Model processes and provides high precision measurements of the model’s parameters and properties as well as searches for new particles — such as the HIGGS boson. Its general design resembles an onion in the sense that it is composed of many layers that enclose each other in a shell-like manner.

The detector encloses the collision point of the LHC beams almost fully, resulting in an almost complete coverage in solid angle. Two entry points for the beam pipes cut through the detector and are notable exceptions of the enclosure. The near-complete coverage allows very precise measurement of the total deposited energy and thus

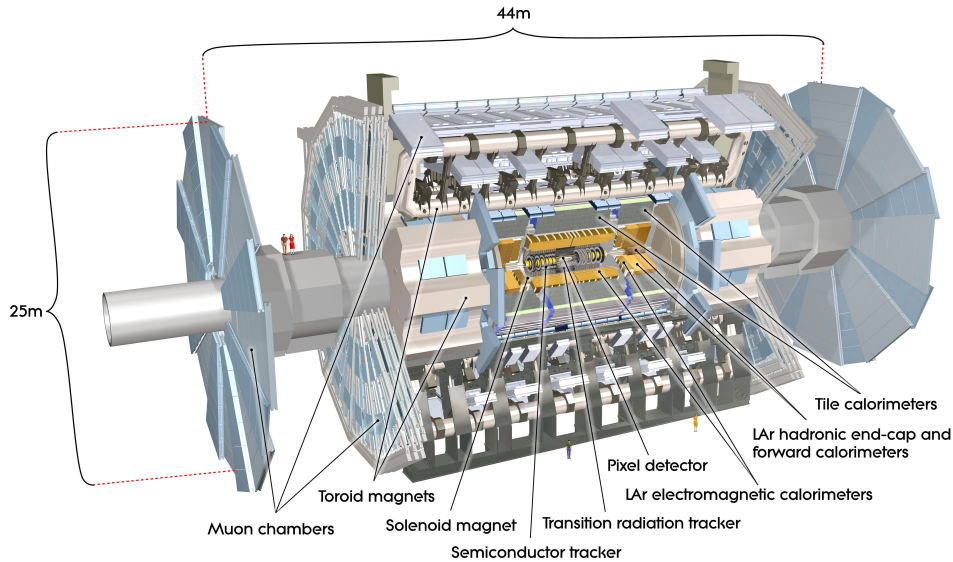


Figure 23: Schematic drawing of the ATLAS detector [88, 95].

an accurate estimate of the invisible energy, also-called missing energy. This is the contribution of energy from the primary collision that escapes the detector through non- or weakly interacting particles, i.e. neutrinos. This approach can be expanded to the total momentum sum of the invisible particles, however, at the LHC only the transverse component of the invisible momentum sum is available experimentally. This follows from the fact that the colliding particles are composite, hence the collision energies of the actual scattering process need not be symmetrical and therefore the centre-of-mass system of the collision can have a nonzero momentum along the beam axis.

One of the main engineering challenges when designing a multipurpose detector is to achieve an almost hermetic enclosure that fully contains the entirety of every event with the exception of neutrinos. To maximise the acceptance region, detector components have to be placed in regions with extreme radiation. However, additional material inserted into the detector may distort measurements further downstream. This is further complicated by the need to place services and other support structure throughout the detector which introduces blind spots. In the end, the technical and experimental necessities must be balanced along with financial considerations. As a result, detectors typically use the most precise components in regions of high importance and rely on less expensive and complex solutions for segments of the detector wherever possible.

The total dataset size is limited by the time spent taking data and the luminosity. In order to allow or improve measurements of rare processes, the luminosity must be increased. However, this also makes multiple simultaneous interactions more likely which in turn makes reconstruction of events more difficult. An ambiguity associated with each of the measured inputs is introduced: they can be either signal or *pile-up*.

In order to reduce this ambiguity, it is pivotal to measure the point of origin of the measured particle tracks with high precision. This allows to discriminate the pile-up tracks in many cases.

Many of the interesting physics processes involve \mathbf{b} -quarks, hence it is important to be able to tag jets originating from \mathbf{b} -quarks. Because these quarks and the hadrons they form are unstable but also more long-lived than their lighter relatives, the most straightforward approach is to tag jets which contain a secondary vertex with a large displacement relative to the production origin of the event. This displaced secondary vertex is a result of the distance travelled by the long-lived \mathbf{b} -hadron which subsequently decays and gives rise to new tracks. In order to achieve good tagging performance, a highly efficient and precise track and vertex measurement is required.

The complete detector but especially the inner detector are exposed to a harsh radiation environment. It is of utmost importance that the individual detector components are designed in a way that guarantees steady operation, high availability, and excellent precision throughout the complete lifetime. Due to the limited financial budget and time constraints — the detector is opened only for a short time every year — it is not feasible to rely on exchanging defective components: each subsystem must perform reliably.

5.2 The Detector Coordinate System

The ATLAS collaboration follows standard conventions for defining its detector coordinate system: a positive right-handed Cartesian coordinate system (x, y, z) with its origin at the nominal interaction point (IP) in the centre of the detector is used, see Figure 24 for a sketch. In practice, the true IP is not a fixed point due to the non-zero dimensions of the two colliding beams as well as shifts in the position of the collision region. The positive x -axis points towards the centre of the accelerator ring, the positive y -axis points straight upwards and the z -axis points along the beam and its direction is fixed by the other axes.

It is often convenient to use a spherical, right-handed coordinate system (ϕ, θ, p) when working with the momenta and tracks of particles which originate from the interaction vertex: the azimuth angle $\phi \in [-\pi, \pi]$ specifies the component in the x - y plane, the polar angle $\theta \in [-\pi/2, \pi/2]$ specifies the component in the y - z plane, and p is the scalar momentum.

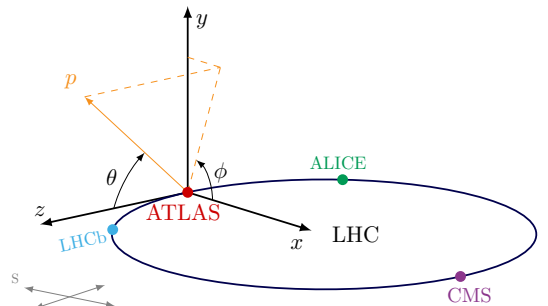


Figure 24: Illustration of ATLAS coordinate system.

Usually the polar component is expressed in terms of the *rapidity* y ¹ or the *pseudorapidity* η which are defined by Equation (8)

¹ Not to be confused with the cartesian coordinate using the same symbol.

using a particle's energy E and it's cartesian three-momentum $\vec{p} = (p_x, p_y, p_z)$.

$$y := \frac{1}{2} \cdot \ln \left[\frac{E + p_z}{E - p_z} \right] \quad \text{and} \quad \eta := -\ln \left[\tan \left(\frac{\theta}{2} \right) \right] \equiv \frac{1}{2} \cdot \ln \left[\frac{p + p_z}{p - p_z} \right] \quad (8)$$

The quantity η , which is experimentally more easily accessible, is an approximation of the rapidity y which improves in accuracy when the mass of the particle is small compared to its momentum. A useful property of the rapidity is that differences Δy are invariant under **LORENTZ**-transformations which is approximately true for η as well.

Transverse quantities are frequently used. They refer to the contributions that lie in the x - y plane of the coordinate system, i.e. perpendicular to the beam axis. The two most important quantities are the *transverse momentum* p_T and the *transverse energy* E_T which are given by Equation (9).

$$p_T := \sqrt{p_x^2 + p_y^2} = |p| \sin \theta \quad \text{and} \quad E_T := E \sin \theta \quad (9)$$

The radial separation of two objects a and b , or distance between them, is defined as

$$\Delta R := \sqrt{\Delta \phi^2 + \Delta \eta^2} = \sqrt{(\phi_b - \phi_a)^2 + (\eta_b - \eta_a)^2}, \quad (10)$$

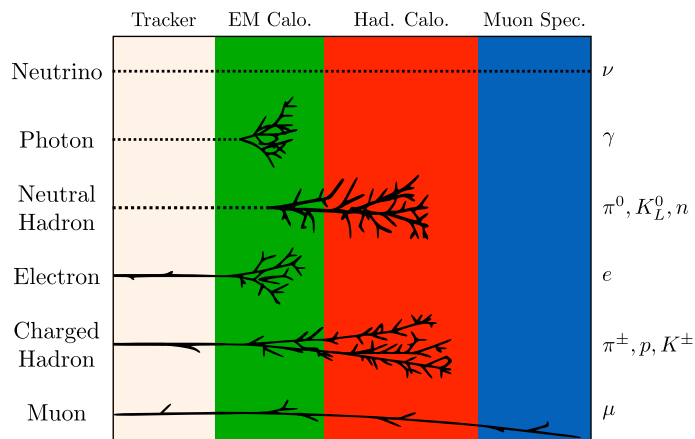
where $\Delta \phi$ must be corrected for coordinate wrap-around.

5.3 Detector Subsystems

The different subsystems of the detector each fulfil specialised needs of the experiment. They are designed to perform well given the collision rates and radiation doses expected at their specific position. In the following each major subsystem will be discussed.

By using different layers of differently functioning detector subsystems a crude method of particle identification can be performed. This is illustrated by Figure 25 which shows that different classes of particles penetrate the detector at different depths, interact with specific types of detectors — which includes that they do not interact — and produce different patterns within a detector subsystem. Combination of the information from all subsystems allows to exclude certain particle hypotheses.

Figure 25: Illustration of the penetration of different classes of particles in an idealised high-energy particle physics detector. Particles are produced at the left and traverse the detector towards the right. Differently coloured areas denote different detector components. Black solid lines denote measurement points while dotted lines denote the flight path of a particle without any measurement.



5.3.1 The Inner Tracking System

The Inner Tracking System [88, 96, 97] — or simply Inner Detector (ID) — consists of a pixel detector, a semiconductor tracker (SCT), and a transition radiation tracker (TRT). Figure 26 shows a cutaway sketch of the barrel section of the ID, Figure 27 of one end-cap section. The ID covers a cylindrical volume of 6.2 m in length and 1.15 m in the radial direction. This corresponds to an angular coverage of $|\eta| < 2.5$.

The inner detector components provide spatially resolved measurements of charged particles produced in the initial collision or as part of a decay chain. They rely on the fact that the charged particles interact with the detector matter, thus ionising it, without losing much of their energy. Hence, given that this interaction can be measured, this design allows for a minimally invasive measurement of the track over several sampling points (hits). Naturally this concept only works for charged particles as neutral particles do not ionise the detector material. In addition to the displaced vertex tagging discussed previously, the inner detector provides electron identification up to $|\eta| < 2$ using the TRT. The operational threshold of the ID is specified as low as 500 MeV in p_T for charged particles. An active cooling system is used to facilitate optimal operation of the ID components and is particularly important for silicon-based innermost sensors.

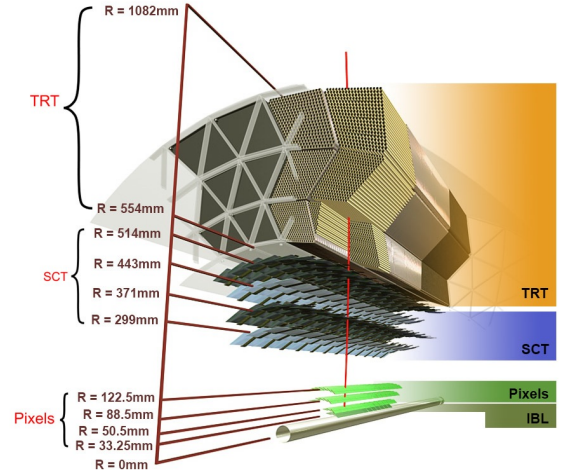


Figure 26: Cutaway sketch of the ATLAS inner detector and its components during Run 2 [97].

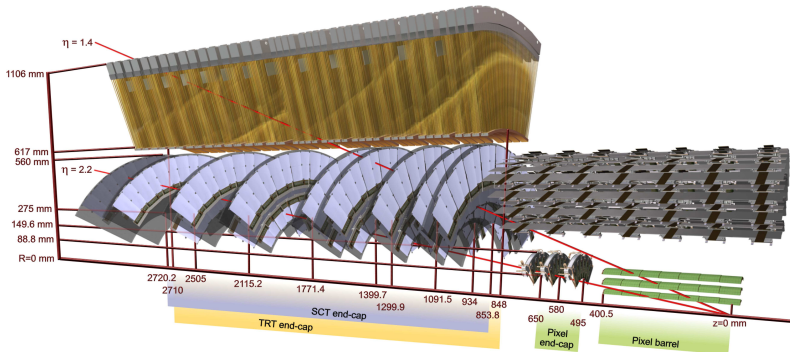


Figure 27: Schematic drawing of the sensors and structural elements in the end-cap inner detector [88]. Note that the IBL, which does not extend into the end-cap, is not present in this drawing. Also shown are two hypothetical tracks (in red) at $\eta = 1.4$ and $\eta = 2.2$, respectively.

§1. The Pixel Detector [98–101] is the innermost detector system and was originally designed and constructed with three layers of pixel sensors. In the intermediate time between the LHC’s first and second operating period, a new innermost layer was installed. This *Insertable B-Layer* (IBL) was inserted between the existing pixel detector modules and a new thinner beam pipe that was installed beforehand.

The pixel detector system was designed for precise tracking in proximity to the interaction point which ensures a long lever arm in the vertex calculation and optimal detection of displaced vertices. This precision is achieved by using a highly granular pixel matrix. As a result it accounts for about 80 % of the total readout channels of the whole experiment although it covers the smallest surface of all components. The four pixel layers are arranged in parallel to the beam pipe in the barrel region and perpendicular on three disks in each of the end-caps. The outermost plane is at a radius of about 12 cm and the total axial length of the pixel detector is about 1.3 m. With this arrangement, the pixel detector has an angular coverage of about $|\eta| < 2.5$.

The individual pixels of the three outer layers have a thickness of 250 μm and are either $50 \times 400 \mu\text{m}^2$ or $50 \times 600 \mu\text{m}^2$ large.² Individual pixel cells are part of a sensor which is bound to a frontend chip. These sensors are then combined in groups of 16 sensors to form a module which shares the same readout chain and power supply.

Due to its proximity to the interaction point, the IBL must cope with a higher particle flux resulting in increased pixel occupancy and a higher expected radiation dose compared to other pixel detector layers. Consequently, the sensors and electronics used for the IBL were designed specifically for the new task. The IBL pixels measure $50 \times 250 \mu\text{m}^2$ where the reduction in pitch length improves the z resolution. Two different pixel technologies are combined in the IBL: in the central region traditional planar pixel sensors with a thickness of 200 μm are used while in the outer region 3D pixels [102] with a thickness of 230 μm are used. In this design, an improved radiation hardness of the pixel sensor is achieved by placing the pixel electrode perpendicular to, and therefore protruding into, the sensor surface [103].

During Run 1, the pixel detector performed extremely well: 97.5 % of its pixels were operational and the hit efficiency exceeded the design expectations at about 99.9 % efficiency [104]. Similar performance has been found for Run 2 [105–107].

§2. The Semiconductor Tracker [88, 108] encloses the pixel detector and is similar in concept to the pixel detector. However, in order to reduce costs and increase feasibility, silicon strips are used instead of pixels. Each strip is about 13 cm long. They are arranged in parallel to the beam pipe in the barrel region and perpendicular in the end-cap regions. The sensor thickness is about 285 μm and the strip pitch is 80 μm . The SCT is composed of four layers in the barrel region and nine in the forward region, i.e. for $1.3 < |\eta| < 2.5$. Each layer is fitted with two modules which are tilted with respect to one another under a stereo angle to add position information along the strip.

The SCT has been designed to achieve a transverse momentum resolution of $\sigma_{p_T}/p_T = 0.05 \% \times p_T[\text{GeV}] \oplus 1 \%$ and a transverse impact parameter resolution of 10 μm for

² The pixel pitch depends on the pixel position relative to the frontend chips of a module, most (about 90 %) have the smaller pitch.

particles of high momenta in the central rapidity region [88]. During Run 1 more than 99% of the SCT strips were operational and the average hit efficiency was measured to be 99.7% [108].

§3. The Transition Radiation Tracker [88, 109] consists of about 300 000 cylindrical straws arranged in one single cylindrical volume in the barrel and two volumes for each end-cap. Each of the straws has a radius of 2 mm and measures either 144 cm (barrel) or 37 cm (end-cap) in length. The straws are arranged in parallel to the beam axis in the barrel section and perpendicular for the end-caps. The complete TRT covers a radial section $r \in [56.3, 106.6]$ cm at an axial length of 5.42 m. Each straw is filled with a gas mixture of Xenon, Oxygen, and CO₂. The TRT combines two detection methods:

- i) through primary ionisation and
- ii) through transition radiation.

Charged particles that traverse the TRT create ionisation charges inside the straw tubes. An anode wire at the centre of the straw forms a potential difference with the outer shell which acts as a cathode. The ionisation charge creates a charge avalanche that can be detected using a readout system connected to the anode wire.

The straws of the TRT are entangled with materials of varying dielectric constants. This allows detection through *transition radiation* (TR): when a highly relativistic, charged particle traverses a change in the dielectric constant of the medium it emits electromagnetic radiation called transition radiation. For an ultrarelativistic particle, the wavelength of the radiation is typically in the range of X-rays. The intensity of the emitted radiation is proportional to the LORENTZ factor $\gamma \equiv E/m$. Therefore, a measurement of the TR allows to perform particle identification by measuring the TR intensity and energy of the impinging particle separately and solving for the mass m . In practice, this allows to distinguish the light electrons from their heavier relatives and hadrons in general. The TR photons deposit additional signal which is read out using the same system as the primary ionisation signal. As a result there are two overlaid signals within the straws. However, the TR signal has a significantly larger amplitude which enables distinction of the two signals. This requires that the readout system of the TRT operates using two separate thresholds: one low threshold for detection through ionisation and another higher threshold for detection of transition radiation photons.

The TRT spatial resolution is approximately a factor of 10 worse than that of the SCT. However, the TRT provides typically between 22 and 36 additional hits to a track and extends the lever arm of the track measurement considerably further out in r . The efficiency of the TRT during Run 1 was estimated to exceed 94% [109, 110].

5.3.2 The Calorimetry System

The Calorimetry System [88, 111, 112] is designed to measure the energies of charged and neutral particles. Its working principle is to collect the full energy of electrons, photons, and generic hadrons by placing a massive absorber within their path. An impinging particle loses energy by scattering within the absorber material: it creates a so-called shower. Measuring the sum of the deposited energy allows to infer the incident particle's energy. By using a fine grained detection system, composed of many *calorimeter cells*, the energy information is combined with a spatial measurement. Furthermore, this allows to match calorimeter deposition to an incoming track. In order to capture all particles, it must be ensured that the depth of the calorimetry system is sufficiently large. It is designed such that — under normal operating conditions — only muons (and neutrinos) escape its absorbers and can traverse into the muon system.

The calorimetry system is composed of two subdetectors: there is the inner *electromagnetic calorimeter* (ECAL) and the outer *hadronic calorimeter* (HCAL), see Figure 28. Both calorimeters are located just outside the solenoid that provides the magnetic field to the inner detector. The two calorimeters are so-called *sampling calorimeters* which means that the absorber material is distinct from the detection material: layers of a dense absorber material, which are insensitive detector components, are interleaved with a detection system forming a sandwich-like structure.

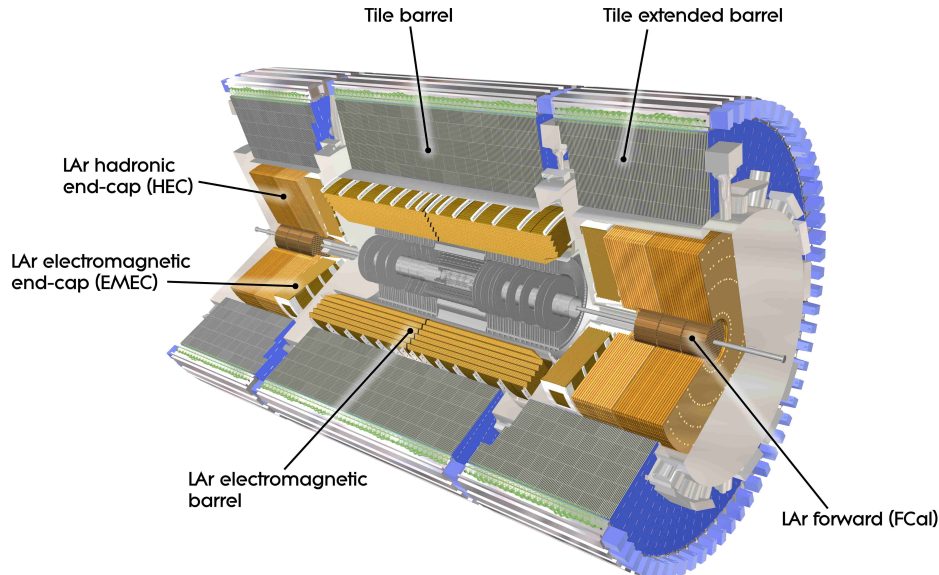


Figure 28: Cutaway schematic drawing of the ATLAS calorimetry system [88, 113].

§1. The Electromagnetic Calorimeter [111] is designed primarily for measuring the energy of electrons and photons. It is divided into a barrel section for $|\eta| < 1.475$ and two end-cap pieces for $1.375 < |\eta| < 3.2$. For $|\eta| < 1.8$ a presampler detector is included which corrects for the energy lost by electrons and photons upstream of the calorimeter. The dimensions and material of the ECAL are designed to prevent electrons and photons from traversing completely through. Consequently,

the ECAL acts as an electron and photon filter for the HCAL allowing identification based on the principles illustrated by Figure 25.

The ECAL uses liquid argon (LAr) as active material and lead plates as passive (absorber) material. In order to maintain liquidity of the argon, the ECAL is housed in a cryostat. For the barrel section it shares a common vacuum vessel with the solenoid in order to reduce the material budget impact of the system. The plate thickness of the absorber material varies with η which improves energy resolution performance. Electrodes are placed in the active detector material in order to detect the showers produced by impinging particles. These electrodes are arranged in an accordion-shaped geometry which ensures complete ϕ coverage without any cracks.

The cell pitch of the innermost layer is very fine — at $\Delta\eta = 0.0031$ compared to $\Delta\eta = 0.025$ for the subsequent layer — in order to allow accurate matching of calorimeter clusters and inner detector trajectories. Another advantage of this design is that it allows a relatively precise measurement of the direction of photons for which this component is the first non-transparent detection system.

§2. The Hadronic Calorimeter [112] actually consists of two subcomponents: the *hadronic tile calorimeter* and the *hadronic LAr calorimeters*, as shown in Figure 28. Its purpose is to fully contain all hadronic matter, such as energetic jets, and prevent any punch-through into the muon system. The central detector region up to $|\eta| < 1.7$, is fitted with a calorimeter using scintillating tiles and steel plates, whereas the forward region up to $|\eta| < 4.9$, is equipped with a LAr calorimeter which is similar to the ECAL.

In the tile calorimeter, layers made of scintillating tiles are alternated with iron plate layers. The former serve as active detector material and are equipped with wavelength shifters and photomultipliers for readout at each side, the latter form the passive absorber material. The whole tile calorimeter is segmented radially into three layers and consists of a central barrel and two extended barrel sections in the end-caps.

The hadronic LAr calorimeter is installed in the end-caps and is radially enclosed by the extended barrel tile calorimeter, see Figure 28. It consists of a coarse forward component in the high radiation very forward section of the detector (the Forward Calorimeter, FCal) and a more fine-grained hadronic LAr end-cap component (the Hadronic End-Cap Calorimeter, HEC). Both components are placed in the same cryostat as the ECAL end-cap. They use copper (and tungsten for the outer layers of the FCal) as passive material while they use the same active material and technology as the ECAL. The specific choice of absorber material guarantees optimal measurements of electromagnetic and hadronic showers in these subsystems.

5.3.3 The Muon Spectrometer

The Muon Spectrometer [88, 114] (MS) is an extremely large tracking system which is dedicated to measuring muons. For normal operation, muons are the only particle type expected to punch through the calorimeters. The MS uses a total of four different types of muon detection systems which are identified in the schematic drawing shown in Figure 29. The tracking acceptance of the MS is $|\eta| < 2.7$ for momenta up to 3 TeV. Furthermore, triggering capabilities are provided for events with at least one muon with $p_T \sim 4$ GeV over a range up to $|\eta| < 2.4$.

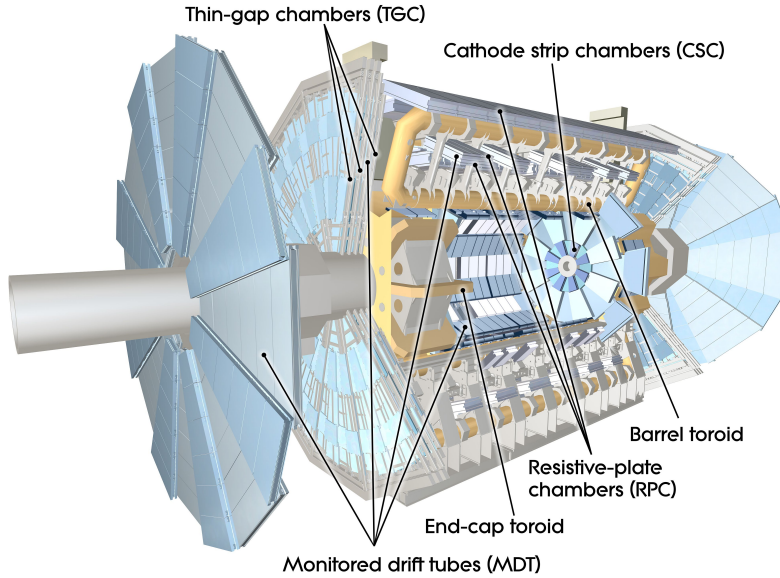


Figure 29: Schematic drawing of the ATLAS muon spectrometer components [115].

Tracking is provided by Monitored Drift-Tubes (MDTs) and Cathode Strip Chambers (CSCs). These detector components are arranged in a way that a muon track typically traverses at least three such detectors.

Trigger information is provided by Resistive Plate Chambers (RPCs) and Thin Gap Chambers (TGCs). The former are used in the barrel region, $|\eta| < 1.05$, while the latter are used in the end-caps, $1.05 < |\eta| < 2.7$. A fast readout time of the order of a nanosecond facilitates the use as input to the hardware-based triggering system. The RPC and TGC systems are arranged such that they can provide coordinate information complementary to the measurement of MDTs and CSCs.

In the barrel region, the detectors are arranged as three cylindrical layers at radii of $r \sim 5, 7.5, 10$ m. For the end-cap they are placed as wheels with four of them placed on each end of the detector at $z \sim 7.4, 10.8, 14.0, 21.5$ m. At $\eta \approx 0$ there is an uncovered gap in the muon system as a result of support routing. In addition, there are several regions of reduced acceptance in the lower half of the detector due to the overall support structure.

Information from the muon spectrometer is combined with data from the other detector subsystems to improve reconstruction and identification of muons. For

example, independent measurements of the muon charge from the ID and the MS can be used to reject candidates with inconsistent charge hypothesis.

5.3.4 The Magnet System

The Magnet System [88] provides a means to determine the momentum of the measured particles. Due to the magnetic field, charged particles traverse the detector on a curled trajectory. Measuring the curvature of this trajectory allows to infer the particle's momentum. In order to make use of this feature, all tracking detectors must be placed within the magnetic field of the magnet system.

The ATLAS magnet system is composed of two components: *a*) a solenoid magnet which immerses the inner detector in a magnetic field and *b*) a toroid magnet arrangement which induces a magnetic field into the muon system.

Figure 30 shows a rendering of the ATLAS magnet system; note that the solenoid is partially hidden within the tile calorimeter's steel tube. Both components are built using superconducting magnets which must be kept at a temperature of 4.5 K to remain operational.

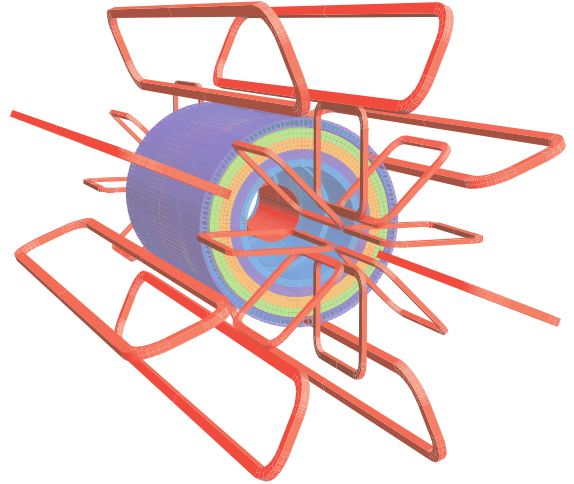


Figure 30: Rendering of the ATLAS magnet system (red) and the tile calorimeter steel (blue). Depicted are both the solenoid and the toroid coils [88].

§1. The Solenoid is placed between the inner detector and the calorimeters. It occupies a cylindrical space for radii between $1.22\text{ m} < r < 1.32\text{ m}$; along the beam axis the solenoid stretches for a distance of 5.8 m. The magnetic field induced by this component amounts to 2 T in the central region of the inner detector.

The main design constraint for the solenoid was its material budget: in order to reduce the impact of the traversed material (i.e. energy loss and deviation from incident path due to multiple scattering) on the measurements provided by the calorimeters, the radiation length of the solenoid must be reduced to a minimum.

Being a solenoid magnet, the field lines inside the solenoid volume are aligned parallel to the beam line. This implies that charged particles are deflected by the solenoid within the r - ϕ plane.

§2. The Toroid consists of eight air-core coil-loops along the barrel and two end-cap pieces (each composed of eight air-core coils), see Figures 23, 29 and 30. All components are placed outside of the calorimeters and are geometrically part of the muon system. Each of the barrel coils has an axial length of 25.3 m and extends through the radial section of $9.4\text{ m} < r < 20.1\text{ m}$. For the end-cap pieces each coil

has an axial length of 5 m and extends through the range $1.65 \text{ m} < r < 10.7 \text{ m}$. The magnetic field that is produced by this system amounts to 3.9 T in the central part and 4.1 T in the forward region measured on the superconductor. Each of the barrel components has its own cryostat while there is only one cryostat for each end-cap.

The field lines of the toroid magnetic field run roughly circular around the beam line. Therefore, charged particles traversing the toroid's magnetic field are deflected in the r - z plane.

5.3.5 The Trigger System

During normal LHC operation, the expected bunch collision rate is around 40 MHz with $\mathcal{O}(10)$ inelastic proton-proton collisions per bunch collision at ATLAS' interaction point. This rate is by far higher than what can be read-out, reconstructed, and stored. Therefore, one must devise a data reduction strategy. The implementation of this strategy is precisely the purpose of the Trigger System [116–118]. The desired event rate after reduction is about 1 kHz which is imposed by computing and data storage constraints.

Fortunately, the vast majority of all events produced at the interaction points are well-known, high-statistics scattering processes that occur at low energies. These are of little use or interest to most physics analyses, and by removing them the event rate can be reduced to an acceptable level. The trigger system makes use of the overall event signature to provide a keep-or-discard decision. However, one must be very careful at this event rejection because careless selection might throw away interesting physics processes or introduce some (unintended) selection bias and thus impede a discovery. Dedicated triggers, which typically use a random decision component, allow to retain some of the events which do not have a specific signature. These events are called *minimum bias event* since the triggering is intended to apply only minimal bias on their topology. They are crucial to a range of applications from calibration to performance studies and enable model and signature independent searches.

ATLAS uses a two-stage triggering system,³ where a very fast hardware-based trigger — the L1 trigger — reduces the incoming data rate and feeds its knowledge into a more complex, software-based trigger — the HLT trigger — which produces a final trigger decision. This approach leverages the power of a fast but relatively inflexible hardware trigger with that of a much more flexible but also less performant software implementation.

³ During Run 1, the HLT used two separate computing farms operating as two successive levels of software triggers, the L2 and Event Filter triggers. As part of the Run 2 upgrade of the trigger system, these two components have been merged. This merge, in combination with other factors, has enabled to increase the output rate of the trigger from about 400 Hz (Run 1) to 1 kHz (Run 2). A summary of changes to the trigger system for Run 2 can be found in Ref. [118].

§1. The L1 Trigger [116] is designed to reduce the data rate to about 70 kHz which was increased to 100 kHz for Run 2 [119, 120]. This improvement was made possible by upgrades to the L1 hardware and improvements to the ATLAS readout system. The required decision time for the L1 is rated at about $2\ \mu\text{s}$ with an additional contingency of 500 ns. This is achieved by using fast hardware components with low latency and a simple selection logic that just applies a chain of vetoes or coincidence conditions. These high rates can only be facilitated by using a subset of the ATLAS components, namely the RPCs and TGCs of the muon system and the calorimeter read-out at a reduced granularity. This allows to define two main trigger recipes: a muon trigger (L1Muon) and a calorimeter (L1Calo) trigger. The L1 muon trigger aims to identify events with a high- p_T muon, while the calorimeter trigger tries to identify events with highly energetic electrons, photons, jets, or τ -leptons. Furthermore, the calorimeter trigger allows to select based on the total deposited or total missing transverse energy and has the option to apply isolation cuts. As part of the upgrades leading to Run 2, a new topological trigger recipe (L1Topo) was added to the L1 which uses the information from both L1Muon and L1Calo trigger objects to provide a topology-based decision. For example, this allows trigger requirements on variables such as di-object invariant mass or transverse mass.

There are several different trigger lines for each of the objects defined in the L1 trigger; these lines are different in terms of the cuts applied on the object kinematics and the multiplicity of the objects. Typically, different L1 trigger lines pass the accepted events on to different HLT trigger lines, hereby establishing a logical selection line. Furthermore, each trigger line can be configured using a so-called prescaler. Essentially, a prescaler is a factor n_p that reduces the incoming number of events such that only every n_p -th of the triggered events is passed on to the next trigger system.

§2. The High Level Trigger (HLT) has access to the full detector signal including all subcomponents at their nominal granularity and precision. Its algorithms are seeded using the η , ϕ , and p_T values that caused selection by the respective L1 trigger line. These seeds are then used to define a so-called region-of-interest (RoI) for the HLT trigger routine and the actual detector readout is restricted to the RoI in order to allow for a reasonably low trigger latency. The reconstruction algorithms used by the HLT are designed to be as similar as possible to the algorithms used by the full event reconstruction that is applied later.

The upgrades leading up to Run 2 have added a new **F**ast **T**rac**K**er (FTK) [121] which provides hardware-based tracking information to the HLT using the silicon tracking detector information. This allows to efficiently implement triggers which rely on large-scale tracking information such as **b**-jet triggers. The average output rate of the HLT system for Run 2 is 1 kHz with a processing time of about 200–250 ms.

Trigger Naming Shorthand identifiers are used as trigger names. These typically use the following scheme

`<LEVEL>_<OBJECT><pT><EXTRA_INFO>`

where `<LEVEL>` identifies the trigger level (L1 or HLT), `<OBJECT>` is the target physics object (e.g. `e` for electrons), `<pT>` is a minimum p_T cut specified in GeV, and `<EXTRA_INFO>` are labels for additional information or selection requirements which may be omitted if there are none. Using this scheme, the trigger `L1_MU20` is a L1 muon trigger which requires a minimum muon candidate p_T of 20 GeV; similarly, the `HLT_e60_lhmedium` trigger is an HLT trigger for electrons with at least 60 GeV transverse momentum which pass a likelihood-based identification classifier at a “*medium*” quality working point.

6 Future and Upgrades

CONTENTS	
6.1	Overview of Upgrade Plans 61
6.1.1	Accelerator Upgrades 61
6.1.2	Upgrades to the ATLAS Experiment 62
6.2	Personal Contributions to Upgrade Work 64
6.2.1	Implementation of Baseline Geometries 64
6.2.2	Setup of Simulation and Performance Analysis 66
6.2.3	Performance Analysis of Baseline Geometries 68
6.2.4	Designing an Extended Ring Geometry 70
6.2.5	Simulating the Extended Ring Geometry 72
6.2.6	Conclusion 74

Modern high-energy particle-physics experiments are among the most complex and large-scale scientific endeavours ever conceived. For a collider experiment such as the LHC, typically many years pass between the conception or initial proposal of an experiment and its commissioning. The lifetime of an experiment can be extended by inserting periods of upgrades between periods of operation. Scientific analysis of data obtained during early periods is performed in parallel to work towards ongoing or future upgrades. This allows to benefit from operational experience gained during early periods as well as improvements in accelerator and detector design and construction.

This section consists of two parts: in Section 6.1 a brief overview of LHC and ATLAS upgrade plans is presented. The work carried out by the author as part of this thesis is the topic of Section 6.2.¹

6.1 Overview of Upgrade Plans

Both the accelerator and the various experiments have a rich upgrade programme scheduled over the course of the coming years. The focus in this section will be on upgrades planned for the LHC and ATLAS. A general overview including activities planned by other LHC experiments can be found in Ref. [122].

6.1.1 Accelerator Upgrades

The LHC has pushed back the collider energy boundary again and again, first with Run 1 and more recently with Run 2. Following LS1, the beam energy was almost doubled. However, to further sustain and possibly extend the discovery potential of the LHC experiments a significant increase in the production rate of yet rare processes is needed. This effective increase in dataset size cannot be achieved alone by raising the beam energy within the LHC's capabilities.

¹ Note: the overview presented in Section 6.1 is based on recent developments and the latest upgrade proposal while the work carried out by the author as qualification task terminated at the end of 2015.

Figure 31 shows the planned roadmap for LHC operations and upgrades.² First, the upgrade plans for Run 3 will take the LHC beam energies up by a half GeV to a centre-of-mass energy of $\sqrt{s} = 14$ TeV, the nominal design energy of the LHC for pp collisions. The High-Luminosity LHC (HL-LHC) [123], which will be part of the Run 4 package, is a proposed upgrade configuration which plans to increase the integrated luminosity by a factor of ten over the original design value. This should increase the pp collision dataset from expected $\mathcal{L}_{\text{Int}} \sim 300 \text{ fb}^{-1}$ at the end of Run 3 to $\sim 3000 \text{ fb}^{-1}$.

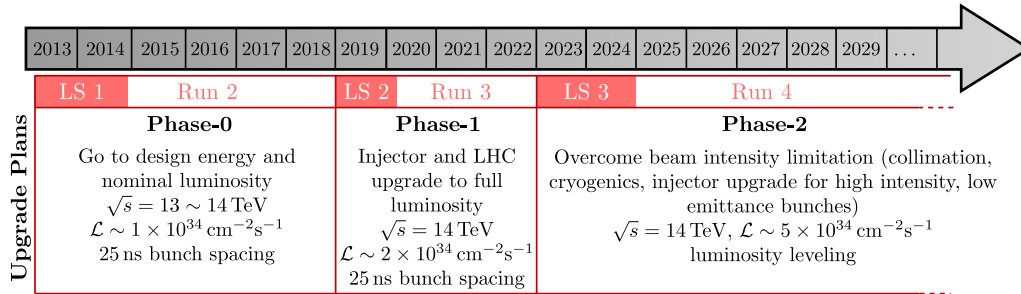


Figure 31: Planned roadmap for LHC operation and upgrades, illustration based on Ref. [122].

The LHC accelerator upgrades are only made possible by advances in the fields of accelerator design and construction. In addition, increased performance is achieved by replacing aged and worn-down components, thus rejuvenating the accelerator.

6.1.2 Upgrades to the ATLAS Experiment

Current operation has shown that the ATLAS detector is capable of handling an instantaneous luminosity that exceeds the original design specification. Regardless, an upgrade programme to the detector is required to cope with the conditions expected from the HL-LHC, for more details see Ref. [124]. The two main effects at play are the increased occupancy due to the higher luminosity and the reduced detector effectiveness due to its ageing and wear-down from radiation damage during the first three run-periods.

The Phase-2 upgrade [125] is planned to be a major overhaul which does not leave any of the major detector components untouched. The largest part of this upgrade is the replacement of the current inner detector with a fully silicon-based tracker (**Inner Tracker**, ITk) [125, 126].

The current inner detector was designed for ten years of operation with a peak instantaneous luminosity of $1 \times 10^{34} \text{ cm}^{-2} \text{ s}^{-1}$ at a centre-of-mass energy of $\sqrt{s} = 14$ TeV and a bunch spacing of 25 ns. With this configuration, each crossing is expected to result in ~ 23 pp interactions which are captured using a triggering system operating at 100 kHz [88]. The HL-LHC upgrade on the other hand is expected to deliver pp collisions at a rate that results in a five-fold increase in

² The specific dates of the roadmap are subject to changes, e.g. the start date of LS2 was already pushed back by one year.

peak instantaneous luminosity with ~ 130 pp interactions taking place during each crossing [127]. Clearly, a detector upgrade is required to exploit this enhanced collision profile.

The expected radiation dose at the end of Run 3 necessitates a replacement of the inner detector. Although the radiation hardness of the ID is expected to be able to cope with the predicted exposure for Run 3 while maintaining high efficiency detection, operation beyond LS3 is not feasible. At the expected HL-LHC conditions, the readout bandwidth of the ID systems is expected to be beyond full saturation. As a result, loss of data would be a common theme, which would negatively impact physics operation. Similarly, the increased occupancy resulting from up to ~ 140 pp interactions per bunch crossing at the current detector granularity would compromise hit detection and therefore tracking efficiency.

Requirements on the ITk are plentiful, see Ref. [125] for a review. In summary, higher granularity and increased readout rates are needed to achieve physics goals set out by the ATLAS collaboration while improved radiation hardness is imposed to enable the planned ten-year operating period. In addition, fully efficient tracking coverage up to $|\eta| < 4$ is planned to gain access to an increased range of phase space.

Figure 32 shows the latest proposal for the layout to be used for the ITk, the so-called *Inclined Duals* layout. The ITk comprises two subsystems: a strip detector (marked in blue), providing a coverage of up to $|\eta| < 2.7$, surrounds a pixel detector (marked in dark red) which extends coverage up to $|\eta| < 4$. The strip detector uses double modules at a small stereo angle in each layer to facilitate a fully three-dimensional measurement. A support tube separates the strip and pixel-detector subsystems.

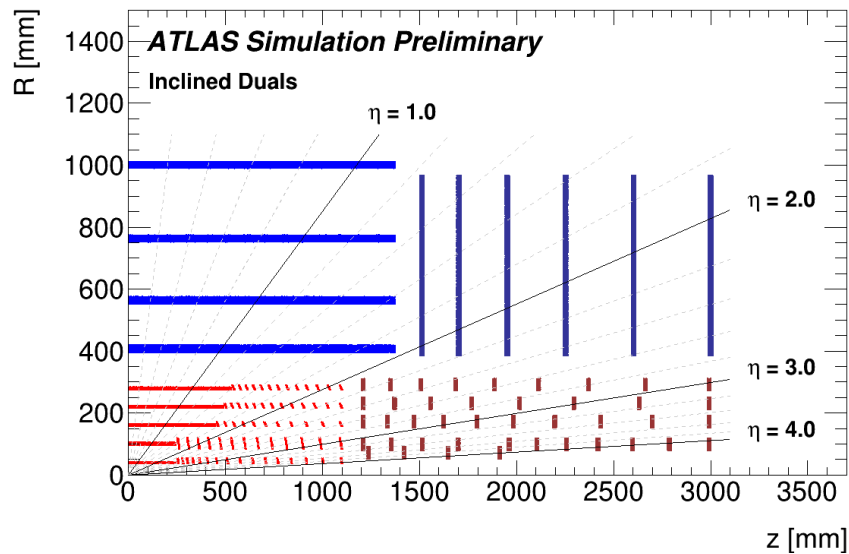


Figure 32: Schematic layout proposal *Inclined Duals* of ITk for HL-LHC upgrade. Figure represents only one quadrant of the detector and only active detector elements are shown. The coordinate origin represents the (nominal) interaction point, the horizontal axis runs along the beam line, the vertical axis corresponds to the radius measured from the (nominal) interaction point. Figure taken from Ref. [126].

The innermost two pixel-detector layers, which are separated from the outer layers by a support tube, can be separated from the rest of the ITk and are designed to be replaceable. This allows to swap out the most heavily irradiated sensors and rejuvenate the ITk. In the barrel, the combination of strip and pixel sensors provides an expected number of 13 hits per track up to $|\eta| < 2.6$ which is reduced to 11 in the strip detector transition region between barrel and end-cap. The pixel end-cap is designed to provide at least 9 hits per track up to $|\eta| < 4$.

Two novel design concepts are used in the pixel detector: the pixel sensors in the outer part of each barrel layer are inclined w.r.t. the barrel layer plane. This is clearly visible in Figure 32 where the barrel pixel-sensors are tilted w.r.t. the horizontal axis starting from around $\sim 1/3$ to $\sim 1/2$, depending on the layer, of the distance along the horizontal axis. This provides a number of advantages, most importantly an improved angular coverage as the tilted sensors are more perpendicular to incident tracks. Overall, the material budget is reduced, which improves general performance. Furthermore, some of the performance degradation from the barrel to end-cap transition is recovered. The second novel concept is the use of rings of pixel sensors in the end-cap of the pixel subsystem instead of disk modules. Rings can be placed individually in locations optimised for each layer separately given the overall geometry. Furthermore, individual rings can be added in regions of low hit count without imposing added material to all layers. Additional details regarding the specifics of the geometry of pixels, modules, and the combination of all those can be found in Ref. [126].

6.2 Personal Contributions to Upgrade Work

The contributions of the author to the upgrade simulation studies for the HL-LHC upgrade of the ATLAS detector consist of two main parts: implementation of an “*open rings*” style ITk pixel end-cap in the ATLAS simulation framework, and analysis of the performance of the end-cap layout — in particular the tracking quality.

6.2.1 Implementation of Baseline Geometries

The ATLAS simulation infrastructure [128] makes use of the `Geant4` [129] detector simulation framework to model interactions of simulated particles with the ATLAS detector accurately. A model must be constructed which describes the physical detector as a collection of volumes and surfaces that `Geant4` can interpret. Each volume represents a specific material as a part of the physical detector. A trade-off between accuracy and simplicity of the detector model must be balanced.

A simple detector module with a silicon pixel element and some readout electronics can be modelled with high accuracy, by using many volumes which describe the silicon pixel bulk and individually the various components of the supporting structure and electronics. In this approach, each physical component is described by a volume

configured to have the appropriate radiation characteristics. Going to the other extreme, a very simplified detector description might model the entire module using just two volumes: one for the silicon pixel bulk and a second for the entire support system. In this case, the radiation characteristics of the second volume must be chosen such that they represent the average (or equivalent) effect of the real, full-scale module. While simulation using the simplified geometry is no longer sensitive to small-scale detector components, the runtime performance of the simulation is greatly improved.

Detector volume prototypes, such as pixel sensor modules with their readout electronics, are implemented as C++ classes. These are then repeatedly instantiated by the geometry builder software and placed in their appropriate locations using steering information provided as single text files or xml files. Finally, the setup is interfaced with Geant4 to simulate particle interactions with the material. A second set of algorithms turns the interaction information into simulated detector readout data.

Initial testing consists of implementation and comparison of two pixel end-cap geometries: the so-called Letter-of-Intent (LoI) design and an initial “ring-style” geometry. The simulation software provides an event display functionality that can be used to create render images of the detector description. Figure 33 shows render images of the two geometries.

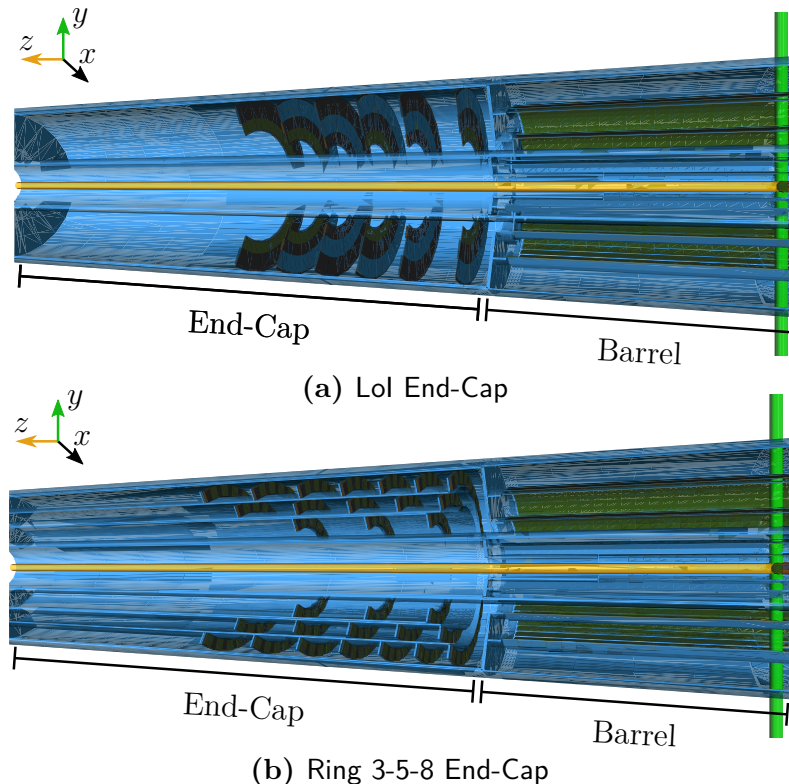


Figure 33: Render images of the innermost, positive half of the detector for two geometry setups. Shown are (a) the Letter-of-Intent (LoI) reference geometry and (b) the initial “ring-style” (Ring 3-5-8) geometry.

A disk-style geometry, such as the Lol geometry, uses disks which extend across the entire distance from the inner- to outermost radius of the end-caps. In contrast, ring-style geometries use structures which are placed only within individual layers. Key differences between the two geometry styles can be identified in Figure 33: the disk geometry is serviced and structurally supported by a single tube enclosing the entire end-cap while the ring-style geometry relies on two tubes interleaved into the geometry.

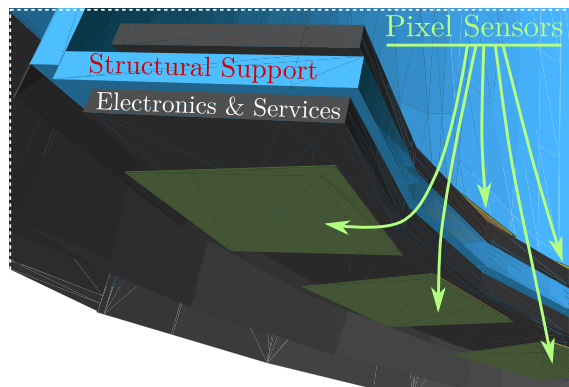
The Lol geometry is a simple geometry which uses six disks with pixel modules for each end-cap. It is not intended as a candidate for the HL-LHC upgrade but rather as a baseline comparison model. The initial ring-style geometry is an early design using three layers of pixel ring-modules with three, five, and eight rings per layer counting from the innermost to the outermost — the short-hand Ring 3-5-8 is derived from this arrangement of rings.

The base material budget introduced by a disk geometry is typically higher than that of a ring geometry since its elements are more massive and require stronger supports. This gets enhanced by the fact that service routing must traverse the entire radial distance of the disk. A ring-style geometry on the other hand can use individual service routing for each layer, thus reducing the material budget and structural load.

The two initial geometries are implemented using the existing software infrastructure which only provides simplified detector volume prototypes for the disks and rings. The silicon bulk of the pixel modules is modelled using explicit volumes. However, the support, servicing, and electronics are modelled using simple volumes with approximately equivalent radiation characteristics. For both disk and ring geometries, the pixel-sensor modules are placed on both sides of the volume in an alternating pattern. Figure 34 shows a render image of the resulting sandwich arrangement of a ring.

Figure 34: Render image showing the sandwich structure of a ring module. For illustrative purposes, the image shows a half-ring meaning that the upper half of the ring module, corresponding to positive values of the ϕ coordinate, has been removed.

The blue volumes are structural support, dark gray volumes represent electronics and services, and the green volumes are the pixel sensors.



6.2.2 Setup of Simulation and Performance Analysis

Simulated data are used to evaluate the performance of the detector geometries presented in this thesis. Single-particle events are generated by injecting a single lepton with transverse momentum $p_T = 25 \text{ GeV}$ and pseudorapidity $\eta \in [0.5, 3.5]$

into the simulation.³ The full interaction of the lepton with the detector material is then simulated using the test geometry. Simulation does not include the outer detector components, i.e. the calorimeters and muon spectrometer, as well as the trigger system. Afterwards, the digitisation and reconstruction stages of the detector simulation are applied.

The reconstruction procedure uses the same algorithms that are used for measured data. However, since the simulation only includes the inner detector, this simplifies to the reconstruction of tracks and vertices. Truth information, i.e. the kinematics of the original simulated lepton as well as all subsequently produced particles, is retained by the reconstruction. Following the three-stage simulation, the actual performance analysis is executed. Using the truth information of each event, a *fiducial phase-space volume* is constructed. An event passes the fiducial requirements if there is at least one lepton which passes the fiducial object requirements. This defines a set of events which an optimal detection and reconstruction scheme must be able to find. The fiducial requirements are:

- must be a lepton classified as physical by the simulation;
- must have a transverse momentum within 1% of the original generated value;
- must be within the intended end-cap pseudorapidity $1 < \eta < 2.7$;
- tracks formed from the truth trajectory must be close to the nominal detector centre, i.e. less than 1 mm (150 mm) in the transverse plane (along z axis).

Reconstructed tracks are selected using a set of quality cuts designed to reflect typical cuts applied by the full ATLAS reconstruction. However, full reconstruction requires additional cuts which are necessary for effective operation in realistic event topologies. The track quality requirements applied here are:

- a minimum reconstructed transverse momentum $p_T > 5$ GeV;
- must fall within the intended end-cap pseudorapidity $1 < \eta < 2.7$;
- tracks must be close to the reconstructed primary vertex of the event, i.e. less than 1 mm (150 mm) in the transverse plane (along z axis);
- the number of pixel detector holes, that is the number of missed hits not due to a known dead module, must not exceed two;
- the combined number of silicon hits N_{Hits} must exceed 10. This quantity combines the hits from the pixel detector with those from the silicon tracker (SCT).

An event passes the reconstruction selection cuts if it contains at least one track which satisfies the quality requirements.

³ Since the detector is symmetric w.r.t. the pseudorapidity η , in this chapter the simplification $\eta \geq 0$ is used and therefore $\eta \equiv |\eta|$.

Using these definitions, events that pass the reconstruction cuts are a subset of the events that pass the fiducial requirements. The latter are all events an optimal detector would be capable of measuring while the former are the subset that is actually measured and reconstructed properly. Only events which pass the fiducial cuts are used as reference in the calculation of efficiencies.

6.2.3 Performance Analysis of Baseline Geometries

The simulated events are generated as single-particle events. Hence, the highest- p_T track that satisfies the reconstruction requirements is highly likely to correspond to the initially generated truth particle. Contamination, which is small, will be investigated later.

Performance of the two geometries is compared through tracking residuals and the tracking efficiency. The residuals are the difference between a quantity measured for the reconstructed track and the value of the corresponding truth particle. Residuals on the p_T and η show similar performance for the two geometries. The resolutions, which are constructed as the standard deviation of the residual distributions across the full dataset, are consistent within the statistical precision. However, a key difference is observed in the tracking efficiency.

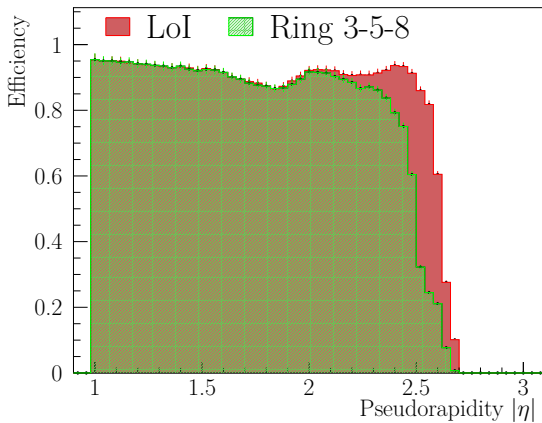


Figure 35: Comparison plot of tracking efficiency as function of track η calculated for the LoI and baseline ring detector geometry. Error bars indicate propagated statistical uncertainties.

Figure 35 shows the tracking efficiency for the LoI and Ring 3-5-8 geometries as a function of the reconstructed η . This efficiency is calculated as the fraction of events selected by the fiducial requirements that also pass the reconstruction selection cuts. The two distributions agree well for low η , up to about $\eta \sim 1.9$. This is unsurprising as this is the barrel–end-cap transition region. For larger η however, the reconstruction efficiency of the ring-design end-cap is considerably lower than that of the LoI-style end-cap. A degradation of the tracking efficiency below 90% is observed at $\eta \sim 2.2$ (2.5) for the Ring 3-5-8 (LoI) geometry. The efficiency drops to zero at $\eta = 2.7$ which coincides with the fiducial requirements.

By varying the track selection cuts and calculation of intermediate efficiencies after each cut has been applied, the performance difference between LoI and baseline ring design was further investigated. This shows that the difference originates from a cut that is applied on the N_{Hits} variable of the reconstructed tracks. Generally, tracks reconstructed from the LoI data have more associated hits for larger η than those from the ring data.

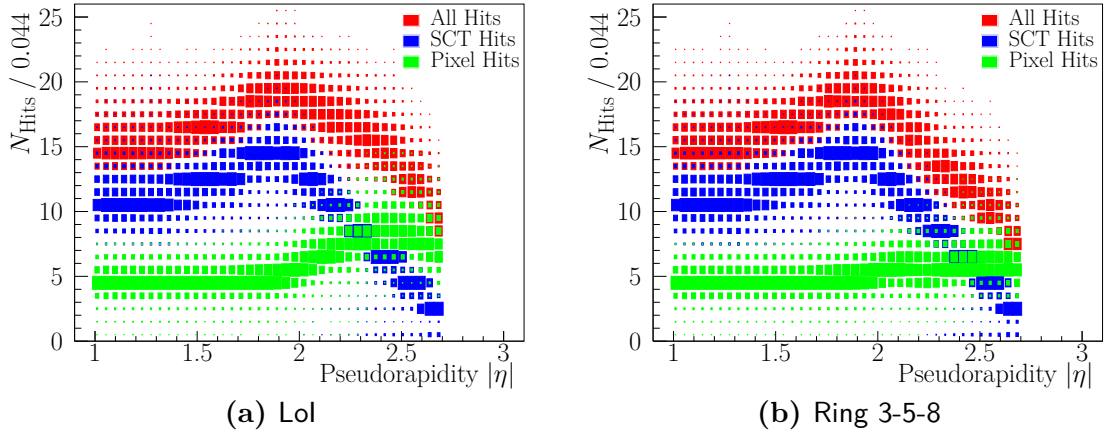


Figure 36: Distribution of the number of hits associated with a track as function of track η for the pixel and SCT hits as well as the combination. The partial distributions for each slice in η are normalised. The size of the boxes corresponds to the normalised number of entries.

This observation is supported by the per- η -slice hit multiplicity distributions shown in Figure 36 for the two detector geometries. Each subfigure shows the hit multiplicity distribution broken down by the subdetector component, that is pixel or SCT. Since the SCT does not change for the two geometries, the number of pixel hits (green distribution) is the most relevant. The distributions for all hits of both end-cap geometries exhibit a reduction of N_{Hits} at high $\eta \gtrsim 2$ resulting from the fact that the SCT does not provide coverage anymore. This loss is recovered to some extent by the pixel detector which, since it is closer to the beam axis, can provide larger η coverage at a smaller geometric size. However, this recovery is much more pronounced for the Lol design which is a direct result of the different geometric arrangements: while the Lol has fewer modules, they are considerably larger than those of the Ring 3-5-8, resulting in an increased module overlap. For the Lol design a mean N_{Hits} of around nine is observed at high η whereas for the ring layout the mean is around six. Application of a fixed N_{Hits} cut in the relevant region has a stronger impact on tracking efficiency for the Ring 3-5-8 design compared to the Lol design.

This leads to the question whether a strong cut on the total number of track hits is justified. In order to study the effect of varying the N_{Hits} cut, tracks which pass the reconstruction requirements are grouped into three categories:

Good Tracks are all those which correspond to an actual truth particle which itself matches the fiducial requirements.

Fake Tracks do not correspond to a generated truth initial particle. They can be mis-identified secondary tracks or mis-reconstructed tracks, e.g. from noise hits or by mismatching hits from different tracks.

Ghost Tracks have an associated truth particle, which does not meet the fiducial requirements. Ideally, they should have been rejected by the track reconstruction or track selection requirements.

An optimal selection results in zero fake and ghost tracks while preserving all good tracks, i.e. the selection efficiencies should follow $\varepsilon_{\text{Fake}} = \varepsilon_{\text{Ghost}} = 0$ and $\varepsilon_{\text{Good}} = 1$.

Using simulated data it is found that the Ring 3-5-8 layout performs better than the Lol layout in terms of the pollution by ghost and fake tracks. Using the standard track selection cuts, the fraction of good tracks is 97% for the Ring 3-5-8 layout and 95% for the Lol design. The fraction of fake tracks is negligible for both designs, however, the selected Lol dataset contains more ghost tracks.

By relaxing the N_{Hits} cut, the efficiency distributions for Lol and Ring 3-5-8 converge, however, at the same time the ghost fraction increases. By relaxing the N_{Hits} cut down to a value of 5, the good track fraction decreases down to 95.5% (93.3%) for the Ring 3-5-8 (Lol) geometry design. In conclusion, the Lol layout is generally more susceptible to pollution by ghost tracks and their relative contribution rises more quickly as the N_{Hits} cut is relaxed, compared to the Ring 3-5-8 layout.

Judging by the results of this study, a relaxation of the N_{Hits} cut down to a cut value of ≥ 9 is justified since this does not result in a significant reduction of the tracking quality. However, the results presented above are based on single-particle events and use a very basic approach for evaluation of the tracking performance. Rejection of fake and ghost tracks for events with multiple primary tracks relies on strict cuts on the number of hits and the deviation of the track hypothesis from the hit envelope. A premature relaxation of the N_{Hits} cut based on single-particle data is likely to result in trouble for realistic event topologies. In particular, this is a problem for any subsequent geometry optimisation that includes the relaxed cut value. Consequently, a relaxed number-of-hits requirement is rejected in favour of the existing, more conservative value.

6.2.4 Designing an Extended Ring Geometry

The previous studies have shown that the Ring 3-5-8 geometry is not competitive, in relation to the Lol design, since it fails to provide sufficient hits at $\eta > 2$. Unfortunately, this is a result of the number of ring modules that are available rather than their placement. Consequently, a new geometry with an increased number of rings is designed: this new geometry uses a total of 25 rings which is a significant step up from the 16 rings used by the baseline ring geometry. The pseudorapidity coverage of the new extended ring-geometry is not increased.

A simplified toy approach is used to find an optimised placement for the rings within each layer: this toy approach relies on a geometrical model that assumes incident tracks traverse the detector without magnetic field and scattering. This model can be used to evaluate the expected number of hits as a function of the incident track's pseudorapidity and the current geometry configuration — assuming a fully efficient hit reconstruction.

An optimal placement is found by selecting the configuration that achieves $N_{\text{Hits}} \geq 5$ over the whole pseudorapidity range, $\eta < 2.7$, and maximises the average number of

hits over the range $\eta \in [1.7, 2.7]$. The radial layer position as well as the minimal and maximal allowed ring position within each layer is fixed. Therefore, optimisation is allowed to shift the layer index as well as the bounded positions of the 25 rings along the z -axis.⁴ This yields an optimal ring placement with five, eight, and twelve rings in the innermost, middle, and outermost layer respectively. Consistent with the previous naming scheme, the extended ring-geometry is labelled as Ring 5-8-12. Figure 37 shows an illustration comparing the sensor positions and coverage of the initial and new ring geometries.

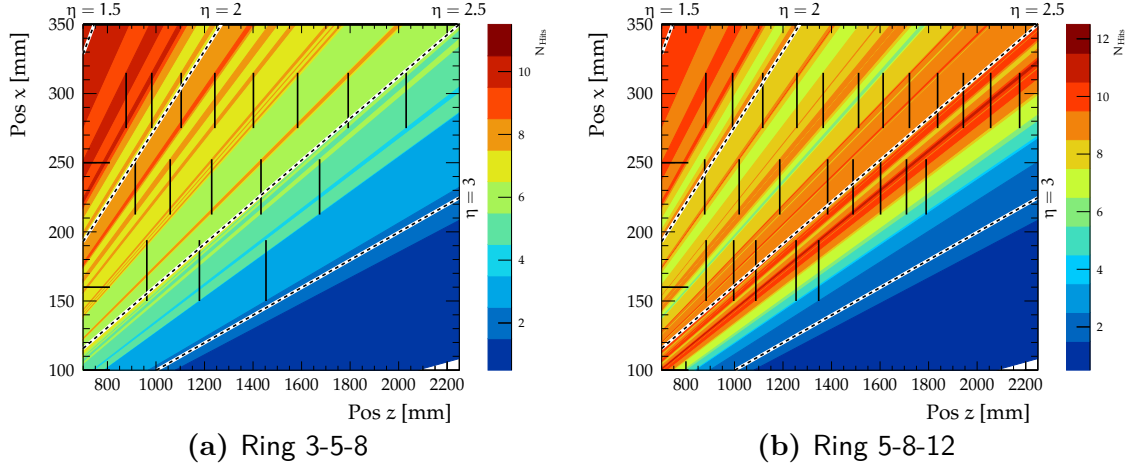


Figure 37: Visualisation of the positive η end-cap region for the baseline and extended ring-geometry. Note that the coordinate origin is offset from the detector centre. Shown in black are active detector planes; the colour-coded regions denote η -slices of a specific maximum number of plane hits; the black-dashed on white lines correspond to specific η values.

The illustrations in Figure 37 also show the expected hit multiplicity through colour-coded slices of η . While they are not shown, the barrel pixel-sensors are also considered for calculating the expected hit multiplicity. With the exception of small holes, the new ring geometry considerably extends the volume with an expected number of hits that exceeds nine to about $\eta \sim 2.7$.

Using the toy geometry-simulation, the Ring 5-8-12 is studied further and compared to the Lol and Ring 3-5-8 geometries. The expected number of hits is binned in slices of pseudorapidity $\Delta\eta = 0.15$. Each slice may contain contributions from several η -slices with different expected number of hits. For example, around $\eta \sim 2.6$ the slices of constant number of expected hits are very small and therefore multiple slices are expected to contribute to a single $\Delta\eta$ bin. The contributions are weighted by the size of the η -slice with that specific expected hit multiplicity. The bin content is thus

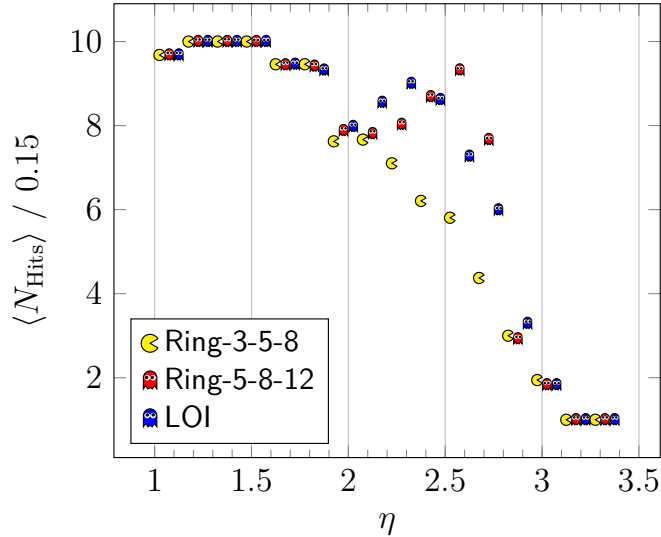
$$b_i = \frac{\sum_{s \in \mathcal{S}} N_s \cdot \Delta\eta(s, i)}{\sum_{s \in \mathcal{S}} \Delta\eta(s, i)},$$

where b_i is the content of the i -th bin, s is a summation index that runs over the set \mathcal{S} of all η -slices, N_s is the number of hits, and $\Delta\eta(s, i)$ is the part of the η -slice s that falls into the range of the bin i .

⁴ The optimisation procedure is performed using the `scipy` python package [130].

Figure 38 shows the resulting distributions for the three end-cap geometry designs. The distributions support the previous finding that the ring and Lol layouts perform similarly up to $\eta \sim 1.9$. While the Lol end-cap can recover the hit reduction up to about $\eta \sim 2.4$, the Ring 3-5-8 design achieves this to about $\eta \sim 2.2$ at an overall lower number of expected hits. This is consistent with the findings from studies using properly simulated single-particle events.

Figure 38: Figure showing the weighted, averaged expected number of hits $\langle N_{\text{Hits}} \rangle$ per unit η slice ($\Delta\eta = 0.15$) for the three geometries investigated in the study. The data points for Ring 3-5-8 and Lol have been shifted in η by $\eta = \pm 0.05$ respectively to prevent overlap of data points. The calculation of the average has weighted each contribution by the effective $\Delta\eta$ slice size for this contribution to that specific bin.



The toy geometry-simulation shows that the Ring 5-8-12 geometry achieves a higher expected number of hits than the two other designs at large η . An extended coverage, up to the desired $\eta \sim 2.7$, is predicted. At intermediate $\eta \sim 2.3$, a lower number of hits is predicted relative to the Lol design. However, this is not a problem as the toy geometry-simulation does not consider the SCT which provides additional hits through its end-cap. Full detector simulation is required to determine whether the fact that the Lol has a larger $\langle N_{\text{Hits}} \rangle$ in the range $\eta \in [2, 2.4]$ has a significant impact on the performance.

6.2.5 Simulating the Extended Ring Geometry

As was previously discussed, even the full detector simulation uses an approximate approach to model the radiation characteristics of service and support components. In particular, the support and routing components are not modelled as explicit volumes with a given radiation length but rather included in the ring structure.

An extended copy of the geometry builder for ITk “ring-style” geometries is created to facilitate a more detailed and thus realistic description of the ring modules. The extended builder allows for routing of services on both the inner and outer radii of the support cylinders. A new placement mode is introduced which enables placement of pixel modules on opposite sides of an inner support structure. Hence, the support cylinder can service two layers of ring modules, one on its inner side (closer to the beam axis) and one on its outer side (further from the beam axis). The servicing and routing structure is layered between the pixel modules on either side and the support.

Furthermore, the extended geometry builder allows for placement of servicing components on the physical rings in the space between pixel modules. This enables to explicitly include e.g. power supply and readout modules which are located in these gaps. Several different service module designs are included in the geometry builder as C++ classes and can be configured and placed using steering files. These modules differ in their shape and can be configured to include additional components placed on top of the base module in a flexible manner.

Figure 39 shows a mock-geometry constructed with the extended geometry builder. In this example, each layer has its own support tube. Different servicing components are placed on the rings. The rough dimensions and shape of these components are taken from preliminary designs for the power supply and readout modules.

The new Ring 5-8-12 geometry is implemented including a preliminary configuration of the support and servicing components. A render image of the final geometry is shown in Figure 40. Note that the two innermost layers share the same support cylinder. The render image shown in the figure does not include the service modules that are placed on the rings.

Single-particle events are generated, reconstructed, and selected according to the prescriptions discussed previously. Using this simulation, it is found that the Ring 5-8-12 design performs better than both reference designs: it reaches the desired coverage of $\eta = 2.7$ at a tracking efficiency that exceeds 90%.

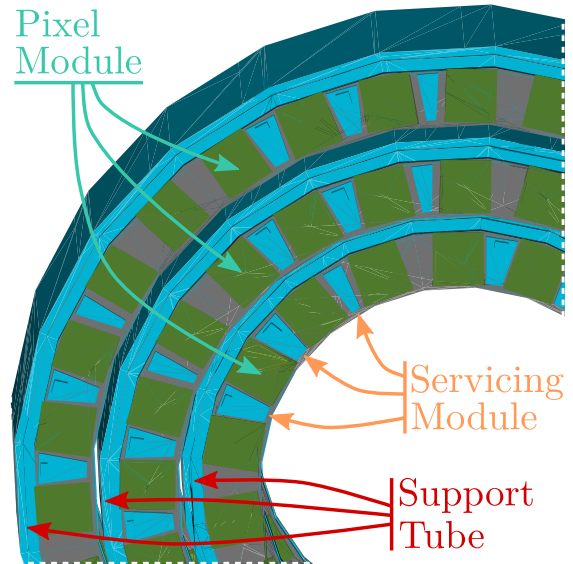


Figure 39: Render image of mock-geometry with improved support and servicing tubes and detailed servicing components.

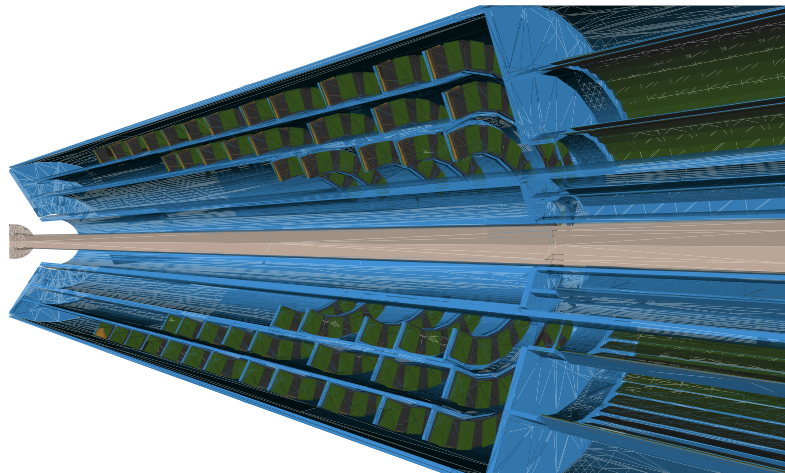


Figure 40: Render image of positive, inner end-cap of the new “ring-style” geometry Ring 5-8-12. Service modules placed on the rings are not shown.

Figure 41 shows the simulated tracking efficiency as function of absolute η of the simulated particle associated with the track. Additional simulation samples are generated for single-particle transverse momenta between $p_T = 10$ GeV and $p_T = 100$ GeV. Similar behaviour can be observed across all considered simulation configurations.

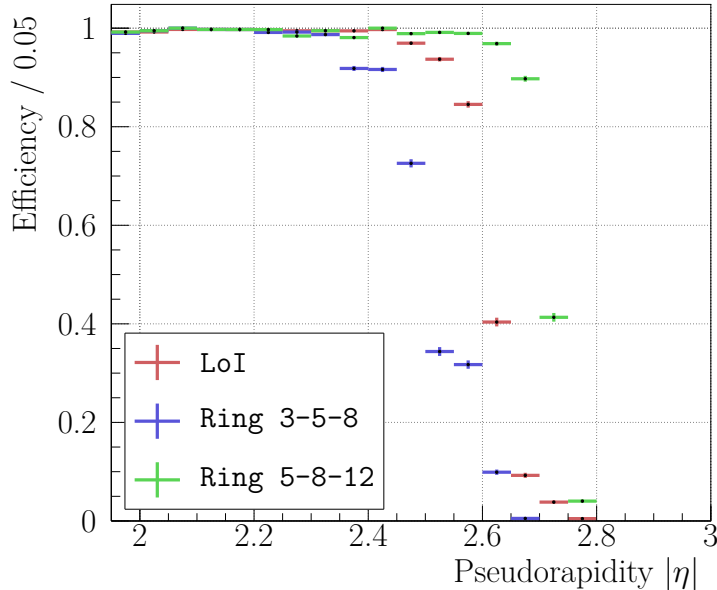


Figure 41: Tracking efficiency for the reference (LoI) geometry as well as the *baseline* (Ring 3-5-8) and improved (Ring 5-8-12) “ring-style” geometries.

The fake and ghost rates as well as track residuals of the improved layout are comparable to or better than the corresponding values for the reference geometry. Furthermore, the efficiency as function of η shows a more consistent behaviour for the improved layout. The cut-off at the end of the instrumented volume is more pronounced, which is expected to result in a more predictable tracking performance.

6.2.6 Conclusion

An initial ring-style geometry for the Phase-II upgrade of the ATLAS detector was implemented in the existing simulation infrastructure. Its performance was compared to a reference design and found to be insufficient. An extended ring-style geometry was constructed which improves upon the initial design and achieves the design goal. Furthermore, the geometry builder program was extended to facilitate different support structures and to more accurately model the servicing components.

In the time that followed the work presented in the previous sections, efforts towards the Phase-II upgrade have progressed significantly. A decision was made to extend coverage up to a pseudorapidity of $|\eta| \sim 4$. To achieve this coverage drastic changes to the design and layout of both barrel and end-cap of the pixel detector are needed — see Figure 32. Consequently, the Ring 5-8-12 geometry presented here is not considered for the final upgrade proposal. However, the work presented in the previous sections, along with the efforts of many other ATLAS collaborators, is a small part of the journey that led to the current Phase-II upgrade proposal.

IV

Analysis Definitions and Tools

In this chapter, various definitions and tools used to facilitate analyses and measurements at ATLAS are presented. First, Section 7 briefly introduces concepts of Monte Carlo event simulation which is used extensively by analyses and measurements at ATLAS. Afterwards, Section 8 describes the reconstruction procedures, definitions, and requirements that are used by the work presented in this thesis. Section 9 describes a method used to correct measured data for detector effects and introduces the concept of fiducial measurements at particle level. A method that is used to construct a simulation sample which has the general $t\bar{t}$ topology but also contains exotic colour flow is the topic of Section 10. This sample is uniquely useful for work presented in this thesis. Finally, in Section 11 an important type of background, the “fake lepton” background, is presented together with the Matrix Method, which is a technique used to estimate this type of background.

7 Simulation of Events

CONTENTS	
7.1	Matrix Element Calculation 77
7.2	The Parton Shower 77
7.3	Hadronisation and the Underlying Event 78
7.4	Detector Simulation 79

Meaningful interpretation of data measured by the ATLAS experiment often requires precise predictions of the actual physical processes and resulting detector response. Such predictions may adhere either to the SM or an alternative (exotic) model or extension. In addition, predictions of known processes may be used as a tool when analysing the recorded data. For example, reconstruction efficiencies can be studied using a combination of measured data and simulation to infer correction factors or assess systematic uncertainties.

In this section, the main stages of general-purpose event simulation for ATLAS are briefly introduced. While specifics of the simulation may differ between implementations, this section gives an overview of the most important steps. A more thorough and detailed review of the mechanics, tools, and challenges relevant for generating simulated events can be found in Refs. [131, 132].

The calculation of predictions depends on processes which cover a wide range of length scales: from 10^{-20} m for the initial collision, the “*hard-scatter*”, to $\mathcal{O}(10)$ m for the size of the detector. Figure 42 illustrates the complexity of an event generated for a pp collision as well as the multi-phase approach used to facilitate the simulation. It relies on the fact that the physical laws involved *factorise*: the whole process can be split into multiple phases where each successive phase takes place at a lower energy scale and only depends on the outcome of the previous scale. In other words, this description results in a sequence of decreasing energy or momentum transfers. The effect on the energy scale relates inversely to the distance scale, meaning that each successive phase considers larger distances.

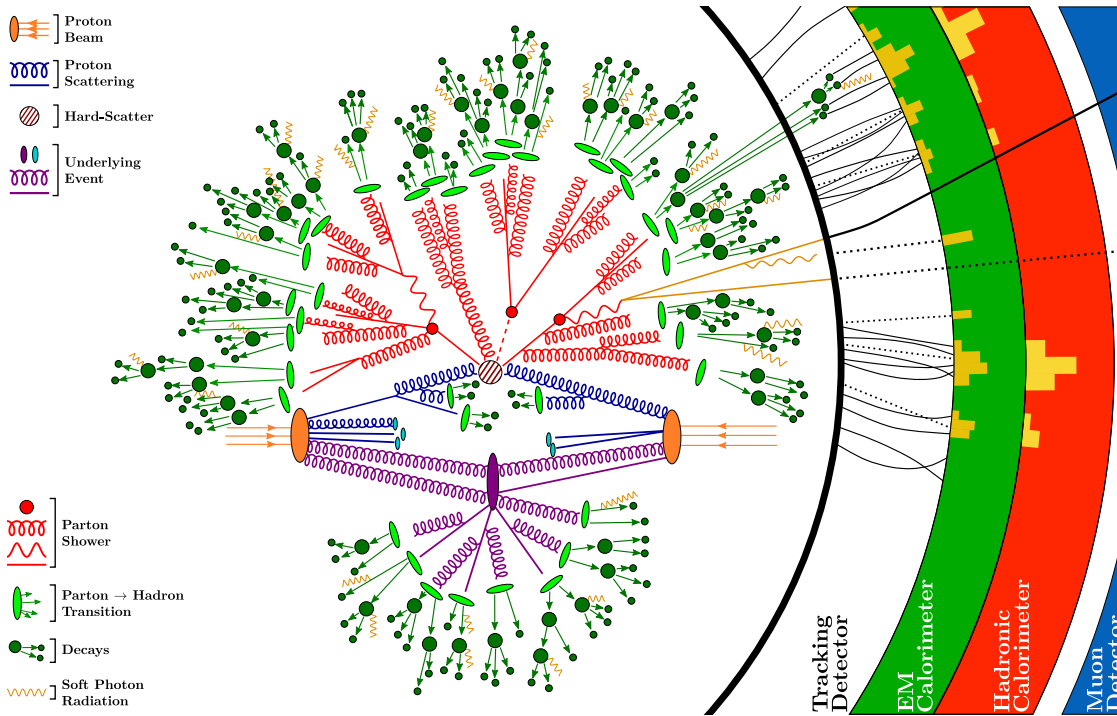


Figure 42: Sketch of a hadron-hadron collision event as it might be produced by a Monte Carlo generator for the LHC. The colliding proton beams enter from left and right resulting in the hard-scatter collision shown in the upper part of the sketch; a secondary hard-scatter event is shown in the lower part. Then the collision result undergoes parton showering. Thereafter follow parton-to-hadron transitions, hadron decays, and soft photon radiation. Finally, towards the right, the interaction of the event with an ATLAS-like detector is visualised. The distances of the different phases are not to scale. Illustration inspired by figure shown in Ref. [132].

Before turning to the specifics of the different stages of event simulation as used for particle-physics, the notion of the *event record* shall be introduced: computer programs utilised to create simulated data have complete knowledge over the state of each particle that is simulated and they can provide this data in form of the event record. This record lists the properties of each particle along with information about its relation to other particles. For example, parent and child references convey information about decays or radiation. Using the relations between particles, the *event record history* can be constructed which describes the successive nature of time-ordered decay and radiation. However, some parts of the event record or the relations and transformations of particles may be unphysical or purely a result of

practical requirements of the simulation program. Any work that relies on direct use of the event record must carefully consider the validity of the information that is extracted.

7.1 Matrix Element Calculation

The hard-scatter process is described by matrix element (ME) calculations which are performed at “*fixed order*”. This means that the perturbative expansion performed to calculate the process is cutoff at some fixed order of expansion in the coupling α of the fundamental interaction governing the process. As a result, the calculation considers only contributions up to a certain number of real or virtual emissions.

Plain ME events are of limited use since they represent a phase-space that is experimentally inaccessible. A second algorithm must simulate the parton shower (PS) which further evolves the hard-scatter final state from the high-energy realm of the ME calculation down to some lower energy scale. In doing so, the PS adds the higher order emissions and branchings which are not included in the ME calculation.

Generating events for the process $\text{pp} \rightarrow \text{X}$, for some final state X composed of n particles, is related to calculating the cross-section

$$\begin{aligned} \sigma(\text{pp} \rightarrow \text{X}) = & \sum_{a,b \in \{\text{g}, \text{q}\}} \int_0^1 dx_a dx_b \int d\Phi_{\text{X}} f_a(x_a) f_b(x_b) \\ & \times \frac{1}{2x_a x_b s} \times |\mathcal{M}_{ab \rightarrow \text{X}}(\Phi_{\text{X}})|^2, \end{aligned} \quad (11)$$

where $a, b \in \{\text{g}, \text{q}\}$ are the partons that interact in the actual collision and have the momentum fractions x_a and x_b according to the PDFs f_a and f_b , see Section 1.3. The matrix element $\mathcal{M}_{ab \rightarrow \text{X}}$ encodes the process-specific description of the hard-scatter event. All final-state properties are described by Φ_{X} which also includes the final state kinematics. The ability to separate the long- and short-distance physics in Equation (11) is a consequence of the factorisation theorem of QCD.

Calculation of the cross-section according to Equation (11) requires solving the integrals which is cumbersome if done analytically. Therefore Monte Carlo (MC) integration is used which replaces the continuous integration by a summation over N randomly generated phase-space points.

7.2 The Parton Shower

Generation of hard-scatter events using the ME calculations provides reasonable description of the momenta and distribution of jets. However, the fixed-order calculation fails at the description of the internal structure of jets or accompanying particles. Parton showers provide an approximation of real emissions of higher order to the hard-scatter ME calculation by simulating the branching of a single parton into two partons.

Given the outgoing partons from the ME calculation, which are typically at an energy scale of $t_{\text{ME}} \sim \mathcal{O}(10) - \mathcal{O}(100)$ GeV, the PS evolves these partons in cascades down to some fixed cutoff scale $t_{\text{C}} \sim 1$ GeV. This splitting uses perturbative calculations and consequently the cutoff scale must exceed the scale at which perturbative theory breaks down. Electromagnetic radiation is usually also included at this stage either using the main PS program or an external tool. Compared to QCD radiation it is suppressed by $\alpha_{\text{em}}/\alpha_{\text{s}} \sim 1/10$.

PS algorithms have a variety of tuneable parameters, such as for example emission and cutoff energy or momentum scales. Many of these parameters are not parameters of the theory, which would have a physical meaning, but rather of the PS model. They cannot be derived from theory, instead they are obtained by comparison of simulation and data.

7.3 Hadronisation and the Underlying Event

Hadronisation is the process that combines coloured partons into colour-neutral hadrons. Due to the low energy scale at which this happens, this cannot be calculated using perturbative QCD and there is no model of hadronisation derived from first principles. Instead, phenomenological models which are inspired by the physical laws are used. The two most common models are the *Lund string model* [133] and the *cluster model* [134], see also Refs. [1, 131] for more details.

In addition, during hadronisation unstable particles, such as τ leptons or b -hadrons, are decayed. Most PS programs are capable of doing this, however, specialised software may be interfaced with the main PS to achieve a better accuracy of the resulting simulation. For the purpose of MC simulation for ATLAS, a particle is typically considered unstable and therefore must be decayed if it has a mean lifetime $\tau_0 < 30$ ps.

The term *underlying event* (UE) typically refers to any additional activity not part of the basic process. This includes initial and final state radiation, beam–beam remnants, and multi-parton interactions. In hadron–hadron collisions the UE is dominated by additional exchanges of colour charge between the colliding (composite) hadrons [1]. Multiple simultaneous interactions — the so-called *pile-up* [135] — are modelled by simulating independent inelastic *minimum bias* events and overlaying them on top of the hard-scatter event. The number of such additional collisions is not fixed per event but rather stochastic with a mean value that depends on the operating conditions of the colliding beams. Simulated pile-up must therefore be tuned to match the pile-up conditions observed in data. This treatment accounts for so-called *in-time pile-up*: additional radiation that originates from collisions that occurred during the same bunch crossing as the primary hard-scatter event. A second type of pile-up, the *out-of-time pile-up* which originates from bunch crossings before

and after the primary hard-scatter event, is modelled using the same technique. In this case, the overlaid events are offset in time w.r.t. the hard-scatter event.

Like the PS, the models used for hadronisation and the underlying event have a variety of tuneable parameters which must be configured such that the disagreement of simulation and data is minimised without introducing bias.

7.4 Detector Simulation

Events generated according to the procedure discussed above are up to this point independent of experimental assumptions: they can be shared across experiments. After the hadronisation algorithms are finished, all unstable particles have been decayed, and the underlying event treatment has been added, the remaining simulated particles must interact with the detector matter just like real particles produced at the LHC would. Simulation of these interactions as well as the subsequent readout and data processing and the triggering system is provided by the ATLAS simulation infrastructure [128]. The GEANT4 simulation framework [129] is used to simulate the interactions of the particles with the detector materials. This requires an accurate model of the ATLAS detector geometry and composition which must contain both active — i.e. sensors — and passive components such as cabling, the cooling and support structure. The particles are propagated individually through the material of each subdetector and associated structure. A variety of approximate models, which are inspired by the underlying physical laws, are used in combination with stochastic modelling to simulate the resulting interactions and energy depositions.

The deposited energy is converted into analogue or digital signal using custom algorithms and further processed to model the readout procedure [128]. Detector effects such as limited resolution and sampling or various noise contributions are accounted for as part of this stage. To facilitate accurate modelling of the real detector, the algorithms use the various voltage settings and tuning parameters of the sensors and readout infrastructure.

Simulation of the detector for the events produced by the basic MC simulation has a significant computing resource consumption. In particular, the simulation of the particle shower evolution in the calorimeter subdetectors takes a lot of time. As an alternative to the standard ATLAS detector simulation, a fast detector simulation may be used. This detector simulation, called `Atlfast II` (AFII) [136] relies on an approximative description of the calorimeter response. A speedup by a factor of about 25 compared to the full simulation has been reported [137]. The fast simulation uses a simplified detector geometry model for the calorimeter subdetectors. Furthermore, rather than explicitly simulating the evolution of showers within the calorimeters, a parameterised approach is used to determine the shower response. The description considers only three types of particles: electrons, photons, and charged pions; the latter are used in place of all hadrons (both neutral and charged).

Like real measured data, after detector simulation the simulated events correspond to “*detector hits*”. These hits are treated using the same reconstruction algorithms as real data and are subject to the quality and definition requirements. The reconstruction procedure employed for both measured and simulated data will be discussed in the next section.

8 Event Reconstruction

CONTENTS		
8.1	Inner Detector Tracks	81
8.2	Primary Interaction Vertex	82
8.3	Electrons	83
8.4	Muons	85
8.5	Jets	86
8.6	Missing Transverse Momentum	88
8.7	Overlap Removal Procedure	89

The primary tool of a high-energy particle-physics measurement is to study outgoing particles produced in a primary collision. In complex topologies, these outgoing particles may include multiple chains of particle decays which may be recovered. With a measurement of such states at hand, one can then make comparisons to theoretical predictions or perform other types of measurement.

However, from a practical perspective, reliably retrieving the necessary information is more complicated. The **ATLAS** detector is composed of a variety of different detector subsystems which differ significantly in their detection techniques and provide vastly different measurements of the particles traversing the detector. Consequently, raw data recorded by the detector bears little resemblance of the final states which the measurement has set out to study. Information from different detection systems must be brought into a common scheme and calibrations must be applied where appropriate. This applies quite naturally to objects such as electrons, muons, and — to a lesser extent — also photons. Quarks and gluons cannot be measured directly as a result of QCD confinement and are instead reconstructed as jets which introduces additional complexity. Finally, neutrinos are not measured at all and must be reconstructed indirectly through momentum balance constraints.

The purpose of the reconstruction procedures is to take the detector data and transform it such that it resembles the final state particles needed to perform a particle-physics measurement. Consequently, the specifics are highly dependent on the experimental setup and also, to a lesser extent, the type of measurement to be performed. In this section, the definitions of the various analysis objects used by work presented in this thesis are discussed. Reconstruction procedures are only briefly summarised, however, references are provided in the appropriate places which discuss these in more detail.

8.1 Inner Detector Tracks

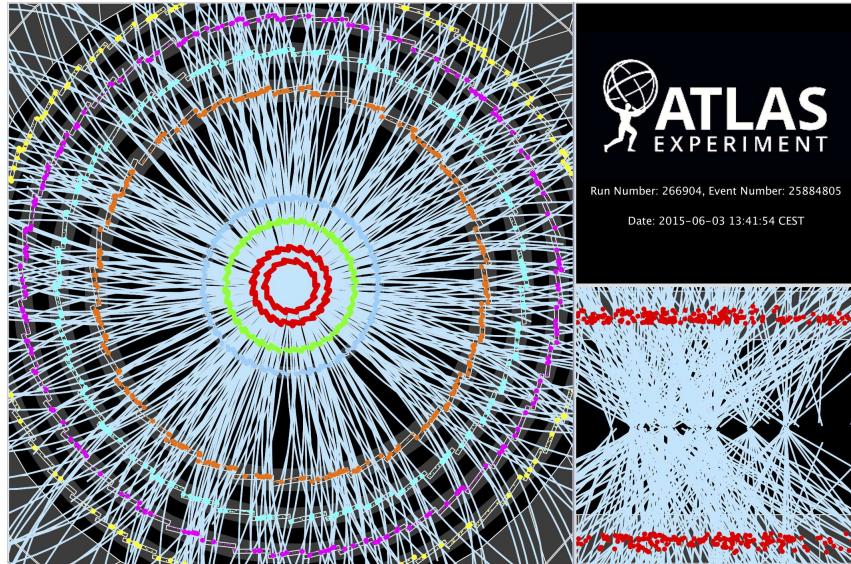
Inner-detector tracks are the precision-workhorse of **ATLAS** detector objects: they form the basis of electron and muon reconstruction and provide important contributions to the jet reconstruction and calibration. They also add an important constraint

for reconstructing the invisible momentum escaping the detector. Moreover, they are the basic ingredients used by the colour-flow measurement presented in this thesis.

The ID tracks are constructed from “*detector hits*” using a reconstruction algorithm [107] updated for Run 2 operation. It makes use of the newly introduced IBL [100] and a neural-network-based clustering algorithm [105, 138] to improve pixel cluster position resolution and the efficiency of reconstructing tracks in jets. Figure 43 shows an event display of tracks in the pixel and SCT detector components obtained during early Run 2 operation.

To ensure good quality, reconstructed tracks to be used for analysis purposes must satisfy $|\eta| < 2.5$ and $p_T > 0.5$ GeV. Further requirements may be applied on impact parameters w.r.t. a primary vertex to ensure that selected tracks originate from the primary hard-scatter collision.

Figure 43: Display of pp collision event recorded by ATLAS with the LHC’s first stable beams at $\sqrt{s} = 13$ TeV. Tracks are shown as light blue lines while hits are shown as coloured filled circles. Also shown are the pixel and SCT detector components. Figure taken from [139].



8.2 Primary Interaction Vertex

Due to the non-zero beamspot size and the composite nature of the colliding protons, the location of the primary interaction is in general not at the coordinate origin of the detector coordinate system. For each event the *primary interaction vertex* must be reconstructed. Due to the large number of simultaneous pp collisions, an ambiguity regarding which collision vertex is the primary vertex must be resolved. The event display shown in Figure 43, in particular visible in the right sub-panel, has a total of 17 reconstructed collision vertices.

A collection of collision vertices is constructed from all reconstructed tracks compatible with the interaction region given by the LHC beam-spot characteristics [140]. From this collection the hard-scatter primary interaction vertex is then selected as that vertex which has the largest $\sum p_T^2$, where tracks entering the summation must satisfy $p_T > 0.4$ GeV [104].

8.3 Electrons

Electrons and positrons, from here on collectively called electrons, which traverse the ATLAS detector give rise to tracks in the inner detector as well as energy deposits in the electromagnetic calorimeter (ECAL). Figure 44 shows an event display of a candidate event for $ZZ \rightarrow e\bar{e}\mu\bar{\mu}$. Electron tracks are symbolised by light-green lines with ECAL energy deposits shown as yellow bars.

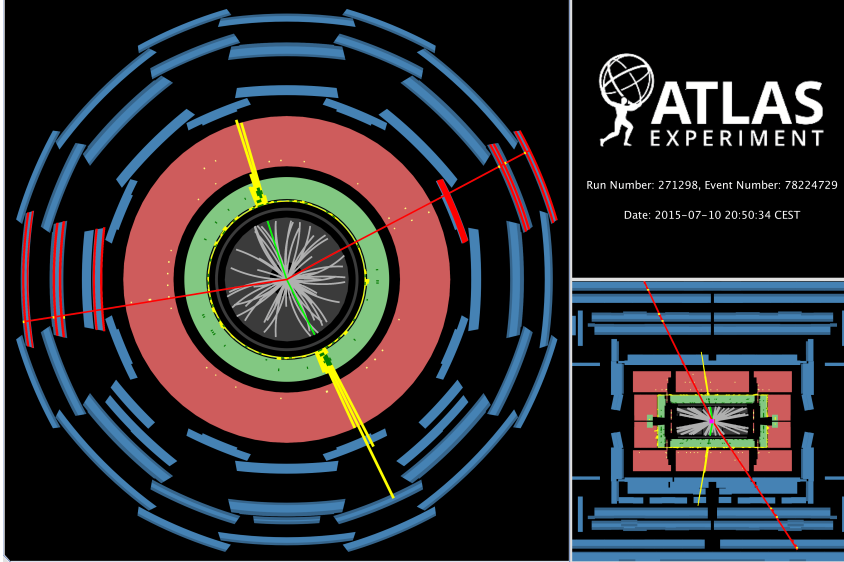


Figure 44: Display of a $ZZ \rightarrow e\bar{e}\mu\bar{\mu}$ candidate event from pp collisions recorded by ATLAS at $\sqrt{s} = 13$ TeV. Electron tracks are shown in light green with ECAL energy deposits in yellow, red lines symbolise muon tracks, gray helices denote additional ID tracks with $p_T > 1$ GeV. Figure taken from [141].

Electron candidates in the central detector region¹ — that is objects with $|\eta| < 2.47$ — are reconstructed by matching inner-detector tracks to seed clusters constructed from the energy deposits in the ECAL.² Candidates outside this pseudorapidity region are not considered. Any electrons that fall into the so-called “*crack region*”, $1.37 \leq |\eta| \leq 1.52$, are rejected. The energy resolution in this region is significantly degraded since it is the transition region between the barrel and end-cap ECAL and consequently the electron candidates are of poor quality. To be consistent with ATLAS-wide definitions and prescriptions, these pseudorapidity cuts use the position of the cluster in the second layer of the ECAL instead of the η component of the (calibrated) electron four-momentum. The resulting reconstruction efficiency exceeds 97% for electrons with low cluster E_T and rises to about 99% at $E_T \sim 60$ GeV.

To be considered as a signal electron, for the work presented in this thesis, electrons must satisfy $p_T > 25$ GeV. Furthermore, the electron’s primary track must satisfy $|d_0^{\text{sig}}| < 5$ and $|z_0 \sin \theta| < 0.5$ mm, where $|d_0^{\text{sig}}| = |d_0|/\sigma_{d_0}$ is the significance of the transverse impact parameter with respect to the beamline, and z_0 is the difference between the longitudinal impact parameter of the track and the primary vertex relative to the beamline.

¹ For this thesis only central electrons, muons, and jets are considered. This restriction is a standard procedure to ensure optimal performance.

² See Ref. [142] for a complete description of the electron reconstruction procedure.

§1. Identification Electron identification algorithms are used to separate signal-like candidates from those with background-like characteristics. The latter may be caused for example by hadronic jets with high ECAL activity or converted photons, i.e. $\gamma \rightarrow e^+e^-$. These background-like electron candidates are collectively called *non-prompt* or *fake electrons*. The identification relies on a likelihood classifier constructed from various detector inputs such as ECAL shower shape or track quality [142–145]. For the work presented in this thesis, the electron candidates must satisfy the so-called **TightLH** identification criterion as defined in [145]. Using simulated $Z \rightarrow ee$ and dijet events, for real or misidentified electrons respectively, the identification efficiency is found to exceed 80% at low p_T rising above 90% for $p_T > 60$ GeV with a misidentification efficiency that is below 0.25% everywhere [142].

§2. Isolation Electrons from the decays of the W , Z , and H_{IGGS} bosons are typically produced isolated from other particles. In contrast, those electrons originating from a semileptonic electroweak decay of a hadron are typically embedded in jets. Hence, isolation requirements play a key role for selecting true signal electron candidates. The electron isolation applies a cut using calorimeter and tracking requirements which reduces background from non-prompt and fake electrons [142, 146]. This cut is constructed such that the resulting efficiency increases linearly with the electron p_T starting at approximately 90% and reaches a plateau of 99% at approximately $p_T = 60$ GeV, the **GradientTight** working point.

§3. Corrections Since the MC simulation is only an approximate description of the real world and in particular the detector, small differences between the observed and predicted properties of electrons are expected. Additional corrections, mostly in the form of simple efficiency scale factors, are applied to reduce these deviations. These corrections are typically parameterised in kinematic variables such as the electron η and p_T or even more complex quantities like the amount of nearby radiation. For electrons, the following efficiencies are considered and correction factors are derived and applied accordingly:

reconstruction efficiency is the efficiency of the reconstruction procedure, i.e. it combines track and cluster reconstruction efficiency with that of matching an ID track to a cluster in the ECAL;

trigger efficiency accounts for electron candidates which did not fire a trigger and / or have not been matched to the (corresponding) trigger;

identification efficiency is the probability that an electron candidate passes the selected likelihood identification requirement;

isolation efficiency corresponds to the rate of electron candidates that satisfy the isolation criteria.

Each of these efficiencies gives rise to a correction factor which are assumed to be independent and therefore can simply be multiplied to produce a total correction

factor. If multiple electrons are present, the correction factors calculated for each electron are multiplied to form a total per-event correction factor. Efficiency correction factors are typically derived using the tag-and-probe method with (simulated or data) events obtained from a selection enriched in $Z \rightarrow e^+e^-$. This is a *standard candle* process because it is a clean signal that can be selected relatively easily to high purity and is well understood theoretically.

The correction factors account for differences between the description of efficiencies in data and simulation. However, the electron energy is affected by additional scaling effects [147]. These are accounted for by calibrating the energy measured from real data to a common scale. Conversely, in simulation, the electron energy is smeared. The magnitude of both scaling and smearing is also derived from $Z \rightarrow e^+e^-$ events by comparing the observed and predicted invariant mass distribution of the di-electron system. Using this distribution, the peak position gives rise to the scaling while the peak width governs additional smearing to be applied on simulation.

8.4 Muons

Muons traversing the detector give rise to tracks in the inner detector and uniquely the muon spectrometer (MS). Additional low-energy deposits may be found in the calorimeter. The event display shown in Figure 44 contains two muons which are symbolised by red lines. MS information is marked in red (trigger) and yellow (hits).

Muon reconstruction³ starts by separately reconstructing tracks in the inner detector (ID) and the muon spectrometer (MS) [106]. Candidate muons in the central detector region — that is objects with $|\eta| < 2.5$ — are reconstructed by matching the track segments from the ID to those from the MS. The resulting muon reconstruction efficiency is close to 99%. For the work presented in this thesis, muons must satisfy $p_T > 25$ GeV. Furthermore, the ID segment muon track must satisfy $|d_0^{\text{sig}}| < 3$ and $|z_0 \sin \theta| < 0.5$ mm which ensures that the muon originates from the primary interaction.

§1. Identification The muon identification algorithm applies cuts to suppress background contributions. These consist mainly of muons from in-flight decays of pions and kaons. Such in-flight decays frequently exhibit a “kink” in the topology of the reconstructed ID track due to the $1 \rightarrow 2$ particle split of the decay. This feature often results in a poor quality of the track fit or a mismatch of the kinematics of the ID and MS tracks. The muon identification applies cuts which exploit this feature. Additional requirements are applied on the number of hits as well as holes (missing hits) in the ID track for the pixel detector, SCT, and TRT [106]. An outlier criterion is applied to the TRT hits which requires that at least 90% of TRT hits for the track

³ See Ref. [106] for a complete description of the muon reconstruction procedure.

are not outliers. In combination, these cuts ensure that a robust muon momentum measurement is possible.

The muon candidates used for the work presented in this thesis make use of the so-called **Medium** muon identification criterion as defined in [106]. Using simulated $t\bar{t}$ events, the identification efficiency is determined to be above 96% for muons from (prompt) W boson decays and around 0.17% for misidentified muons from hadron decays [106].

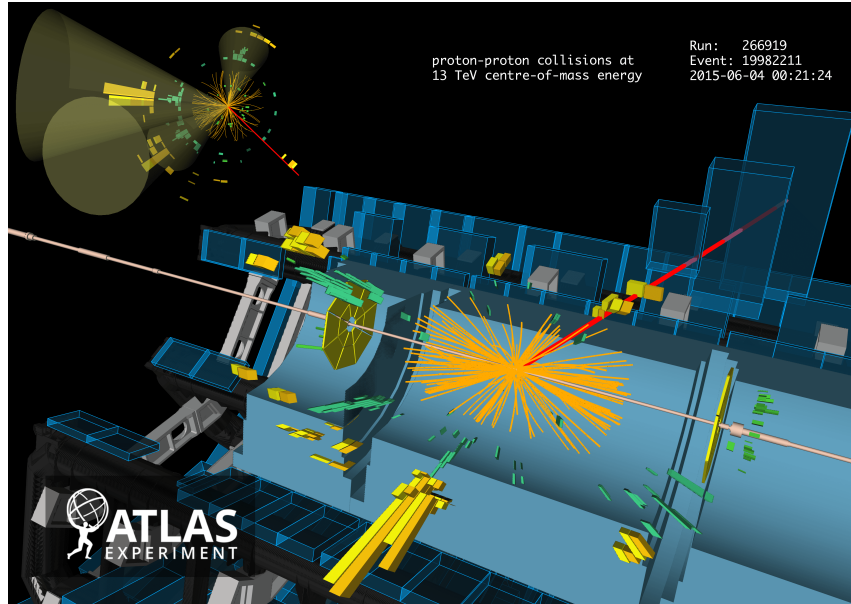
§2. Isolation Requirements on object isolation are applied on the muon candidates to ensure that the selected muons are well separated from other particles in the event. The procedure [106] is constructed to achieve similar efficiency characteristics as those quoted for electrons above.

§3. Corrections Efficiency correction factors and energy scale corrections and smearing are applied for muons in the same manner as is done for electrons [106]. The procedure for derivation and application of all of these is analogous to the techniques discussed in Section 8.3, except that the signature targets $Z \rightarrow \mu^+\mu^-$.

8.5 Jets

Jets are reconstructed through recombination of calorimeter energy deposits that likely originate from the same initial parton. Figure 45 shows an event display of a $t\bar{t}$ candidate event with four reconstructed jets. The green and yellow boxes denote the energy deposits in the calorimeter which are used to reconstruct the jets.

Figure 45: Display of a $t\bar{t} \rightarrow \mu + \text{jets}$ candidate event with four jets from pp collisions recorded by ATLAS at $\sqrt{s} = 13$ GeV. Green and yellow bars denote energy deposits in the ECAL and HCAL. The muon track is shown as red line, additional ID tracks are shown as orange arcs. Figure taken from [148].



There is no pre-determined recombination procedure used for jet *clustering* which follows from the theory. Instead, the specific algorithm and its configuration, the *jet definition*, are essentially part of the jet itself: study or use of a jet as a physics object only makes sense in the context of its jet definition [149]. For a single event, multiple different collections of jets may exist, each with a different algorithm or configuration.

However, in order to be safe to use from a theoretical perspective — and thus good for experimental use — a jet algorithm must be *IRC safe* which implies the following properties:

Infrared Safe (IR): the jet(s) must remain unchanged if a soft particle, $p_T \rightarrow 0$, is added. As a result, jets have reduced sensitivity to soft radiation in the event.

Collinear Safe (C): the jet(s) must remain unaffected if a particle with momentum p is replaced with two collinear particles, i.e. with small radial distance, that have momenta p_1 and p_2 such that $p = p_1 + p_2$.

The primary jet definition used by ATLAS measurements constructs jets with the anti- k_t algorithm [150] with radius parameter $R = 0.4$ as implemented by the FastJet [151, 152] package. The inputs to the jet algorithm are three-dimensional, massless, positive-energy topo(logical) clusters [153–155]. These topo clusters are constructed from neighbouring calorimeter cells that have a measured energy significantly above the noise threshold. The cell energy is measured at the electromagnetic scale, meaning it corresponds to the energy deposited by electromagnetically interacting particles [153, 155].

§1. Associated Tracks Inner-detector tracks are matched (*associated*) to the jets during the jet clustering procedure using a technique called *ghost association* [156]. This procedure treats the ID tracks as four-momentum vectors with infinitesimally small magnitude, i.e. $p \ll \mathcal{O}(\text{MeV})$, and includes the modified tracks in the jet clustering procedure. As a result, the tracks have no effect on the jet clustering result and yet they are clustered into the jet that most naturally encloses them according to the jet algorithm used.⁴ After the association procedure has finished, the original track momenta are restored.

§2. Calibration After the jet clustering has finished, the jet four-momentum is calibrated using an η - and energy-dependent scheme with *in situ* corrections based on data [155, 157]. Subsequently, the calibrated jets are required to satisfy $p_T > 25 \text{ GeV}$ and $|\eta| < 2.5$. To suppress jets originating from pile-up, an additional selection criterion based on the jet-vertex tagging (JVT) technique [158] is applied. This technique constructs a discriminant which quantifies the level of association of the jet with the primary vertex hypothesis using the ID tracks associated with the jet. Jets with $p_T < 60 \text{ GeV}$ and $|\eta| < 2.4$ are required to pass the so-called **Medium** JVT working point. This working point accepts 92 % of jets from the hard-scatter whilst rejecting 98 % of pile-up jets [155].

⁴ Strictly speaking this is only true for certain jet algorithms which weigh constituents and their influence on the resulting jet by their p_T .

§3. *b*-Tagging Being able to discriminate jets which originate from a **b**-quark from those which come from “*light*” quarks⁵ is an important tool for collider physics and crucial to most top-quark physics measurements.

Hadrons which contain a **b**-quark have comparably long mean lifetimes of typically $\tau_0 \sim 1.5 \text{ ps}$ ⁶ which in turn means that such a hadron travels a considerable distance, typically a few mm, before decaying. As a result, the decay vertex of the **b**-hadron, a so-called *secondary vertex*, is offset w.r.t. the primary interaction vertex. This can be measured using the high-precision vertex pixel sensors at the centre of the detector. The fact that the bottom quark has a considerably larger mass than its decay products also impacts the structure and kinematic of the subsequent decay chain. As a result, **b**-jets tend to be wider and have a larger number of constituents than those originating from light quarks. Modern **b**-tagging algorithms attempt to make use of multiple such features simultaneously.

The work presented in this thesis makes use of the MV2 multivariate **b**-tagging discriminant [159–161]. This discriminant combines information from jet kinematics, associated track impact parameters, secondary vertex reconstruction, and a multi-vertex decay-chain fit. It is used at a working point constructed to operate at an overall **b**-tagging efficiency of 70 % in simulated $t\bar{t}$ events for jets with $p_T > 20 \text{ GeV}$. Note that the precise **b**-tagging efficiency varies with the p_T of the jet. The corresponding *c*-, light-jet, and τ rejection factors are 12, 381, and 55 respectively, resulting in a purity of 97 %. Experimental data selected to be enriched in $t\bar{t} \rightarrow e\mu\nu\nu b\bar{b}$ are used to study the modelling of the **b**-tagging. Good agreement between the data and simulation is found.

8.6 Missing Transverse Momentum

Neutrinos are not accessible experimentally and due to the composite nature of the initial state, only the momentum transverse to the beamline is known exactly at the interaction vertex. Therefore, only the transverse momentum sum of all invisible particles, i.e. typically neutrinos, can be reconstructed from the momentum (im-)balance of the visible event.

Reconstruction of the missing transverse energy E_T^{miss} uses the transverse energy of selected hard objects to estimate the total transverse energy imbalance of the event, see Refs. [162, 163]. These objects include the electrons, muons, and jets reconstructed using similar requirements as discussed above. However, the specific object selection cuts, such as transverse momentum requirements, are different and typically lower. Detector information reconstructed as photons and τ -leptons is

⁵ Sometimes the charm quark is not included in the set of light quarks as it shares some experimental traits with the **b**-quark when it comes to jets. However, for most ATLAS measurements and also the work presented in this thesis, the charm quark is a light quark.

⁶ The “long” mean lifetime $\tau_0 \sim \mathcal{O}(1 \text{ ps} \equiv 10^{-12} \text{ s})$ should be compared to e.g. the lifetime of *W* or *Z* bosons which is $\mathcal{O}(10^{-25} \text{ s})$.

considered separately. An additional contribution which accounts for detector signals that are not associated with any of the reconstructed objects is included; this is the so-called soft term. The work presented in this thesis uses a soft term calculated from ID tracks.

The vectorial missing transverse momentum $\vec{E}_T^{\text{miss}} = (E_x^{\text{miss}}, E_y^{\text{miss}})$ is calculated as the negative vectorial sum of the contributions discussed before. More commonly used as part of an analysis is the scalar missing transverse energy E_T^{miss} which is the magnitude of this vector.

8.7 Overlap Removal Procedure

The detector information may correspond to objects which satisfy both the jet and lepton object definition criteria discussed above simultaneously. Furthermore, leptons may be produced in the decays of hadrons and such leptons may be reconstructed explicitly. While the latter case should be mostly prevented by the isolation selection discussed above, some contributions may remain. Both effects are undesirable and consequently an overlap removal procedure is used to remove overlaps and uniquely assign the detector information to a unique physics object hypothesis. The procedure works as follows:

- 1) Double-counting of electron energy deposits as jets is prevented by discarding the closest jet that falls within $\Delta R < 0.2$ to a reconstructed electron.
- 2) Subsequently, if an electron is within $\Delta R < 0.4$ to a jet, the electron is discarded in order to reduce the impact of non-prompt leptons.
- 3) Furthermore, if a jet has fewer than three associated tracks and is within $\Delta R < 0.4$ to a muon, the jet is discarded. Conversely, any muon that is within the same distance to a jet with at least three associated tracks is discarded.

9 Fiducial Measurements and Unfolding

CONTENTS		
9.1	Fiducial Phase Space	91
	9.1.1 Leptons	92
	9.1.2 Jets	92
	9.1.3 Missing Transverse Momentum	93
	9.1.4 Overlap Removal	93
9.2	Unfolding	93

When performing a precision measurement of some observable, directly reporting the observed result is often not desirable. The experimental apparatus which facilitates the measurement introduces *detector effects* — such as distortion, smearing, and other associated effects — onto the measured data. For many measurements using ATLAS data these effects have considerable impact. To allow comparison of measured data with theoretical predictions, a simulated detector must be applied to the latter. This introduces a dependence on the modelling of the experimental apparatus. Directly reporting the shape measured for some observable implies that the measurement retains a dependence on the specifics of the experimental apparatus. This lack of generality makes future use through direct comparison with theoretical predictions or measurements from other experiments difficult or outright impossible. Furthermore, certain types of derived work, such as parton density function fits or Monte Carlo tuning efforts, require inputs that are free from the effects of the detector response.

In combination, this motivates the use of a procedure that transforms the measured data from its original, detector-polluted and -dependent state to a new state designed to allow comparison. In Section 9.1, the notion of the *fiducial phase-space*, which corresponds to the desired state, is introduced. Thereafter, in Section 9.2, the transformation procedure, called *unfolding*, which converts the data from its original to the new state, is discussed.

9.1 Fiducial Phase Space

Due to practical reasons, an experimental apparatus at a particle-physics collider experiment usually has a finite coverage. For example, the beam pipe cuts a hole into the detector that cannot be instrumented. The concept of the *fiducial* region accounts for this by defining a volume which is properly instrumented by the detector. Anything outside of the fiducial region can be considered inaccessible. Further restrictions may be applied to constrain the region such that certain efficiency or resolution requirements are fulfilled within the fiducial region. This notion can be expanded from the simple geometrical perspective to the more general phase-space definition that could imply, for example, requirements on minimum momenta or energies of particles measured by the detector.

In the context of a measurement that uses an unfolding technique, a fiducial phase-space must be defined for both the pre-unfolding and the post-unfolding state.

The pre-unfolding phase-space, called *detector level*, is usually mostly defined by experimental constraints. Accordingly, for the work presented in this thesis, the pre-unfolding phase-space is wholly defined by the event and object reconstruction procedure discussed in Section 8 combined with the event selection applied by the respective measurement. The post-unfolding phase-space considered by the work presented here is the *particle level*.

The particle-level phase-space is constructed from the state of the MC event record prior to detector simulation. Consequently, particle-level quantities are unaffected by detector effects. Particle-level physics-objects are constructed using only stable¹ particles. To reduce dependence on specifics of MC simulation further, particle-level objects are defined in a manner that is similar to detector-level objects. Rather than relying on the unphysical omniscience of the MC event record, objects are reconstructed from the information in the event record through combination. Furthermore, object and event selection criteria are modelled after their detector-level counterparts. In the remainder of this section, the specifics of the particle-level event definition will be discussed.

9.1.1 Leptons

In line with the detector-level reconstruction procedure, only electrons and muons are explicitly reconstructed by the particle-level object definition, τ -leptons are not considered in their own right. Correspondingly, the term “*leptons*” when used for particle-level objects typically only refers to electrons and muons.

Stable electrons and muons are identified from the MC event record. Using the event record history, leptons are rejected if they originate from a hadron. This includes leptons from the decay chain $\text{hadron} \rightarrow \tau \rightarrow \ell$. For the simulation samples that are considered here, this requirement ensures that the leptons originate from the decay of a real W or Z boson, possibly through an intermediate τ -lepton.

Final-state photon radiation is considered to be part of the lepton through a procedure called “*lepton dressing*”. This is achieved by combining photons that are within a $\Delta R < 0.1$ cone around the lepton with the original lepton through four-momentum summation. Only photons which do not originate from a hadron, according to the above definition, are considered in the dressing procedure. In line with the detector-level object selection requirements, particle-level leptons are required to satisfy $p_T > 25 \text{ GeV}$ and $|\eta| < 2.5$.

9.1.2 Jets

Much of the relative safety and independence from simulation modelling that is achieved by using the particle-level comes from the fact that hadrons are not con-

¹ In terminology used by ATLAS, a particle is considered to be stable if the mean lifetime exceeds $\tau_0 \gtrsim 30 \text{ ps}$. A similar definition of $c\tau_0 > 10 \text{ mm}$ is used interchangeably.

sidered as individual particles. Furthermore, by relying on stable particles, direct access to quarks and gluons — which is in some sense unphysical as it has no equivalence in a real-world experiment — is impossible. Instead, much like the detector-level reconstruction, the particle-level definition relies on clustered jets.

Particle-level jets are constructed using all stable particles in the event record excluding leptons not from hadron decays as well as their radiated photons. The clustering algorithm and its configuration are selected to match the procedure used by the detector-level reconstruction. Hence, jets are clustered using the anti- k_t algorithm [150] — as implemented by the `FastJet` [151, 152] package — using radius parameter $R = 0.4$. In analogy to the detector-level object requirements, after reconstruction, particle-level jets must satisfy $p_T > 25 \text{ GeV}$ and $|\eta| < 2.5$.

b-Tagging Jets are classified as having originated from a b -hadron using the ghost-association procedure [156]. This procedure has been introduced previously for the association of inner-detector tracks to detector-level jets in Section 8.5. The method includes b -hadrons in the jet-clustering procedure after having scaled their four-momentum to have infinitesimally small magnitude. A jet is classified to be b -tagged if it contains at least one such ghost b -hadron. In order to be included in the classification procedure, a b -hadron must have $p_T > 5 \text{ GeV}$.

9.1.3 Missing Transverse Momentum

While the particle-level has access to the properties and kinematics of all neutrinos in an event, using such information directly is unphysical. The particle-level \vec{E}_T^{miss} is calculated as the transverse component of the total four-momentum sum of all neutrinos in the event. Neutrinos that originate from the decay of a hadron are excluded. Consistently with the particle-level lepton definition, this also excludes neutrinos from the decay of an intermediate τ -lepton that originates from a hadron.

9.1.4 Overlap Removal

For detector-level events, a complex overlap-removal procedure is needed due to experimental limitations. At particle level, these limitations are not present and thus an overlap-removal procedure is not needed. To improve equivalence between detector- and particle-level definitions, a simplified procedure is applied: any lepton which overlaps geometrically with a jet at $\Delta R < 0.4$ is removed from the event.

9.2 Unfolding

For the work presented in this thesis, the ultimate goal of the unfolding procedure is to take real measured data and revert the effects of the detector response to yield the particle-level equivalent of the measured data. The unfolding result has reduced dependence on the experimental apparatus and its modelling. Through careful definition of the particle level, dependence on simulation specifics and theory modelling is reduced as well.

In practice, detector-level and particle-level data are usually captured as histograms h_D and h_T , respectively. The unfolding procedure takes the measured histogram h_D and constructs an estimate of the underlying distribution h_T using information about the detector response for the considered observable. In order for this to work, a strong correlation between the true value and the corresponding value observed in measured data is advantageous. A stronger correlation intuitively implies that more information about the true value is encoded in the value observed from data.

As part of the unfolding procedure, a variety of effects must be accounted for and corrected. In many cases, the different effects are related and affect each other. A list defining key effects that must be considered is given below.

Acceptance and Efficiency Some fraction of the events produced within the experimental apparatus are lost due to the finite coverage of the detector. Moreover, even those events that are recorded properly may not pass the selections imposed by the measurement due to various requirements such as quality and identification criteria. Thus, in general the number of observed events is not equal to the number of events produced and the number of events predicted.

Background Contributions Typically the prediction is constructed for a specific signal process, such as $t\bar{t}$ production. The measured data on the other hand usually retains some contribution from non-signal processes after the event selection has been applied. The contribution resulting from such background processes must be removed as part of the unfolding.

Noise Contributions Even for events of the signal process, some of the recorded detector information may not originate from a particle that is part of the particle-level definition. For example, noise in the detector may appear like a genuine particle or track reconstruction might combine random hits to form a valid track by chance. In addition, the effects of pile-up may enter as a noise contribution. This effect enhances the number of observed events w.r.t. the number of produced events.

Observable Resolution Measurements provided by the experimental apparatus are smeared by some resolution w.r.t. the predicted value due to the finite resolution of the detector. This affects measured quantities directly and may then propagate to variables calculated from those.

Combinatorics in Observable Definition As a result of the various detector effects discussed previously, an object selected by some criterion from the detector level may not correspond to the object selected by the same criterion when applied at particle level. For example, the highest- p_T jet selected at detector level may not correspond to the highest- p_T jet found in the equivalent particle-level event. If multiple objects are combined to form an observable this may make the observable more susceptible to this effect.

The work presented in this thesis uses an unfolding method which was first introduced by D'AGOSTINI in Ref. [164] and further refined in Ref. [165]. To construct the formalism, the abstract unfolding operation is written as

$$\mathbf{h}_{T,i} = \sum_{j=1}^n \mathbf{P}(\mathbf{h}_{T,i}|\mathbf{h}_{D,j}) \cdot \mathbf{h}_{D,j}, \quad (12)$$

where $\mathbf{h}_{D,j}$ ($\mathbf{h}_{T,i}$) is the content of the j -th bin of the measured histogram (i -th bin of the predicted histogram), $\mathbf{P}(\mathbf{h}_{T,i}|\mathbf{h}_{D,j})$ is the probability that an event originates from bin i of \mathbf{h}_T and is measured and selected in bin j of \mathbf{h}_D .² For the sake of simplicity, the effects of acceptance / efficiency, background, or noise are not considered. Using BAYES Theorem, the conditional probability $\mathbf{P}(\mathbf{h}_{T,i}|\mathbf{h}_{D,j})$ can be rewritten to obtain

$$\mathbf{h}_{T,i} = \sum_{j=1}^n \frac{\mathbf{P}(\mathbf{h}_{D,j}|\mathbf{h}_{T,i}) \cdot \mathbf{P}(\mathbf{h}_{T,i})}{\sum_{i'} \mathbf{P}(\mathbf{h}_{D,j}|\mathbf{h}_{T,i'}) \cdot \mathbf{P}(\mathbf{h}_{T,i'})} \cdot \mathbf{h}_{D,j} \quad \Rightarrow \quad \mathbf{h}_T = \mathbf{U}^0 \mathbf{h}_D \quad (13)$$

where $\mathbf{P}(\mathbf{h}_{D,j}|\mathbf{h}_{T,i})$ is the probability to measure and select an event in bin j of \mathbf{h}_D given that it originates in bin i of \mathbf{h}_T and $\mathbf{P}(\mathbf{h}_{T,i}) \equiv \tilde{\mathbf{h}}_{T,i}^0$ is the bayesian *prior* for the distribution captured by \mathbf{h}_T . Since this prior is a probability density, it must satisfy $\sum_{i=1}^n \tilde{\mathbf{h}}_{T,i}^0 = 1$. The quantity $\mathbf{P}(\mathbf{h}_{D,j}|\mathbf{h}_{T,i})$ can be written as matrix \mathbf{R} which is called *response matrix*³ and forms a linear response model of the experiment. The matrix relates the probabilities for a true value to remain in the same bin following the measurement or to migrate to a different bin. Since it is not otherwise accessible, the matrix \mathbf{R} must be estimated using simulation. This separates the unfolding into a *training* stage, during which the response matrix and other quantities are derived, and an *application* stage in which the unfolding is applied to measured data.

The response matrix \mathbf{R} mixes contributions from different bins of the prior and the measured data to estimate the bin contents of the unfolding result. This dependence on the prior is not desired. An iterative approach can be used to dampen the impact of the prior:

$$\mathbf{U}^k = \sum_{j=1}^n \frac{\mathbf{R}_{ji} \tilde{\mathbf{h}}_{T,i}^{k-1}}{\mathbf{R}_{ji'} \tilde{\mathbf{h}}_{T,i'}^{k-1}} \quad \text{with} \quad \tilde{\mathbf{h}}_T^k = \mathbf{U}^{k-1} \mathbf{h}_D \quad \forall k > 0, \quad (14)$$

the initial case $k = 0$ for \mathbf{U}^k is given by Equation (13). The key element of the iteration procedure is that the result of each successive iteration is plugged into the equation in place of the prior. As a result, with each iteration, the dependence on the initial prior is reduced. With this iteration rule, the estimator function of the *Iterative Bayesian Unfolding Method* (IB) can be constructed as $\hat{\mathbf{h}}_T = \mathbf{U}^k \mathbf{h}_D$. This method has two free parameters: the number of iterations k and the (initial) prior distribution $\tilde{\mathbf{h}}_T^0$. Both cannot be derived from the unfolding method and must be chosen appropriately before the algorithm can be used.

² In the formalism used here, the detector-level (particle-level) histogram \mathbf{h}_D (\mathbf{h}_T) is indexed using j (i) and has n (m) bins, respectively.

³ Sometimes also called *migration matrix* as it encodes bin-to-bin migrations caused by the detector response.

The number of iterations is a so-called regularisation parameter and must be tuned, typically using simulated data. As k gets larger, the estimator $\hat{\mathbf{h}}_{\text{T}}$ converges towards \mathbf{h}_{T} and the regularisation decreases. However, at the same time statistical fluctuations are enhanced with increasing k . An appropriate choice balances the two effects. One approach to finding the optimal number of iterations is to increase the number of iterations, starting at $k = 1$, and observe the effect each successive increase has on the statistical and systematic uncertainties. Typically, after a few, $k \sim 3 \dots 4$, iterations the uncertainties pass through a minimum and start to increase. Selecting the number of iterations at or just below this threshold has proven effective in obtaining minimal systematic uncertainties — which implies the reconstructed distribution is least biased by the simulation encoded in prior and response matrix — without unreasonable statistical errors.

A common choice for the prior distribution is the true distribution that is constructed from the same sample as the response matrix \mathbf{R} . In general, the final result of the unfolding should not be strongly dependent on the choice of prior. However, using a prior that is similar in shape to the expected true distribution typically decreases the number of iterations required to achieve a convergent estimate.

The work presented in this thesis treats the effects of detector acceptance and efficiency, background, and noise contributions as part of the pre- and post-processing to the unfolding. This is achieved by replacing

$$\mathbf{h}_{\text{D}} \rightarrow \mathbf{h}'_{\text{D}} = \mathbf{h}_{\text{D}} - \mathbf{h}_{\text{B}} - \varepsilon_{\text{F}} \cdot \mathbf{h}_{\text{D}} \quad \text{and} \quad (15)$$

$$\mathbf{h}_{\text{T}} \rightarrow \mathbf{h}'_{\text{T}} = \varepsilon_{\text{E}} \cdot \mathbf{h}_{\text{T}}, \quad (16)$$

where \mathbf{h}_{B} corresponds to the background contributions and ε_{F} (ε_{E}) accounts for the events which are selected at detector (particle) level but not at particle (detector) level. Just like the response matrix \mathbf{R} these quantities are estimated from simulation which holds a copy of each event at both detector level and particle level. In summary, the practical methodology to unfolding that is used throughout this thesis uses the following recipe:

1. Estimate the response matrix \mathbf{R} , the correction factors ε_{F} and ε_{E} , and the predicted particle-level distribution, which will be used as initial prior, from simulation.
2. Subtract contributions that originate from background and noise from the measured data using \mathbf{h}_{B} and ε_{F} . This reduces the content of the histogram plugged into the actual IB method.
3. Apply the IB method to obtain an estimate for the particle-level distribution according to $\hat{\mathbf{h}}'_{\text{T}} = \mathbf{U}^k \mathbf{h}'_{\text{D}}$ using an appropriate number of iterations k .
4. Use the correction ε_{E} to reintroduce the contributions which fail due to detector acceptance or efficiency and thus obtain $\hat{\mathbf{h}}_{\text{T}}$.

10 Simulating Exotic Colour Flow

CONTENTS		
10.1	Motivation	98
10.2	Methodology	98
10.3	Validation	100
10.3.1	Analysis Description	100
10.3.2	General Kinematics	101
10.3.3	Colour Flow	103

As part of the work presented in this thesis, a simplified model with exotic colour flow is constructed. The basic idea behind the model is to construct normal $t\bar{t}$ events in the semileptonic decay channel and to replace the hadronically decaying W boson *ad hoc* by a colour octet. Figure 46 illustrates the concept by comparing the colour connections resulting from the two configurations.

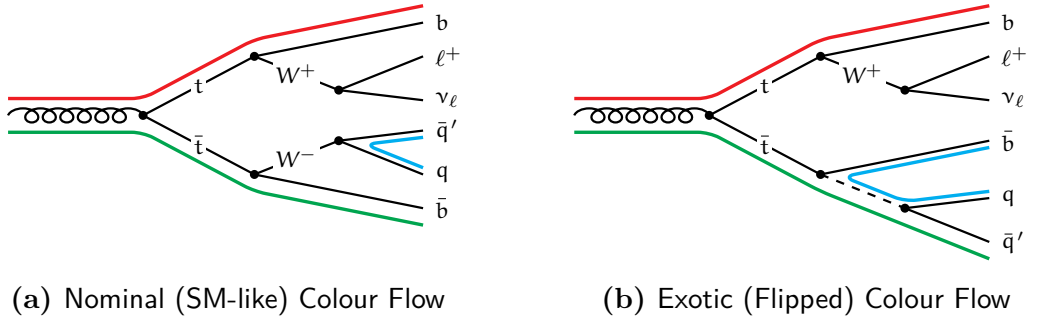


Figure 46: Illustration of a $t\bar{t}$ event which decays semileptonically. Thick coloured lines denote colour connections. Shown is (a) a diagram with colour flow according to the SM, and (b) a diagram with exotic colour flow. For the exotic colour flow, the hadronically decaying W boson has been replaced *ad hoc* by a colour octet which is shown as dashed line in the diagram.

It is important to understand that the simplified model introduced here is unphysical. The “exotic” model is obtained by modifying the hard-scatter event record rather than through official functionality of the Monte Carlo generator. By construction, it represents the most extreme alternative case to the SM colour-structure for the same topology under the assumption that other effects resulting from this extreme case can be neglected.

The model is intended to be a close copy of the desired $t\bar{t}$ signal in terms of event production and kinematics with the exception of the colour flow underlying to the decay of the hadronically decaying W boson. Indeed, as a result of the construction procedure, the hard-scatter kinematics of the exotic model are equal to those of regular SM $t\bar{t}$ events. While it is possible to construct a complete and theoretically rigorous model with a real colour octet, this is beyond what is needed for the studies and analysis presented in this thesis.

In the following, Section 10.1 briefly motivates the desire of an analysis for a simulation sample with exotic colour flow. Section 10.2 provides a detailed discussion of the method used to construct the model used by the work presented in this thesis. Afterwards, in Section 10.3 results from a validation study are presented.

10.1 Motivation

The purpose of the simulated sample with exotic colour flow in single-lepton $t\bar{t}$ events is threefold:

- To be able to investigate the sensitivity of an observable w.r.t. the actual colour structure by comparing distributions obtained from the Standard Model to those of the exotic model. This allows for example to optimise selection or variable definitions and study potential biasing effects.
- Related to the first point, the exotic colour model may be used for comparison. Given experimental data, the agreement with either SM-based or exotic prediction(s) can be quantified.
- When performing a measurement of colour flow which relies on inputs from simulation, the exotic model can be used to study how the colour flow of the simulation affects the measurement. In principle, this could be used to construct an uncertainty related to a potential bias originating from the colour-flow assumption of the simulation. However, due to the simplistic character of the exotic model and the fact that it is intentionally extreme, this is not generally needed.

10.2 Methodology

In Section 7, the different stages of Monte Carlo simulation have been introduced. Frequently, simulation of the hard-scatter event and the subsequent stages, such as parton shower and hadronisation, are performed using different computer programs. For example, one may generate $t\bar{t}$ hard-scatter events using an NLO ME generator such as **POWHEG-BOX v2** [166–168] which can be processed further by a parton shower simulation such as **PYTHIA 8** [169].

A standardised format for transferring the event information from the first to the second stage is the *Les Houches Event* (LHE) file format [170]. Figure 47 lists the content of a single $t\bar{t}$ event taken from an LHE file produced for regular SM $t\bar{t}$ Monte Carlo using **POWHEG-BOX v2**. At the level of the hard-scatter event, only particles up to the daughters of the W bosons, produced at the $t \rightarrow Wb$ vertex, are included. The tree structure of the event record is encoded into flat arrays through an indexing scheme and the mother or daughter references. Additional information such as kinematics, colour strings, and spin information of each particle or overall event metadata are stored as well.

Modern Monte Carlo generators generally use the large N_c limit, where N_c is the algorithmic number of colour charges, see Ref. [131]. This implies that whenever a new colour connection is created, a new *colour index* is produced. Therefore, each colour connection has a unique colour charge and can be treated independently. Furthermore, the colour index uniquely identifies colour connection of an event. For

no	id	name	status	mothers	daughters	colours	px	py	pz	E
1	21	g	-1	0	0	3 5 502 503	0.000	0.000	449.316	449.316
2	21	g	-1	0	0	3 5 504 505	0.000	0.000	-336.610	336.610
3	6	t	2	1	2	6 7 502 0	-19.518	56.243	378.283	419.636
4	-6	t_bar	2	1	2	8 9 0 505	53.012	-0.282	-219.844	286.635
5	21	g	1	1	2	-1 -1 504 503	-33.494	-55.961	-45.732	79.655
6	24	W+	2	3	3	10 11 0 0	50.092	34.258	153.765	183.497
7	5	b	1	3	3	-1 -1 502 0	-69.611	21.985	224.518	236.139
8	-24	W-	2	4	4	12 13 0 0	65.878	37.124	-224.195	246.533
9	-5	b_bar	1	4	4	-1 -1 0 505	-12.866	-37.406	4.351	40.102
10	-3	s_bar	1	6	6	-1 -1 0 506	-9.748	28.876	18.948	35.890
11	4	c	1	6	6	-1 -1 506 0	59.840	5.382	134.817	147.607
12	11	e-	1	8	8	-1 -1 0 0	72.000	24.032	-217.950	230.789
13	-12	nu_e_bar	1	8	8	-1 -1 0 0	-6.122	13.092	-6.245	15.744

Figure 47: Example printout of a single event of LHE file produced for nominal $t\bar{t}$ Monte Carlo.

any given particle, a colour and an anti-colour index exist which identify the two parts of the colour connection this particle participates in. In the example shown in Figure 47 the two indices are listed in the column labelled *colours*, indexing starts at 502 and continues through to 506. A value of zero denotes absence of the connection. As colour charge can neither be destroyed nor created, the total sum of colour minus anti-colour at the start of the event ($\text{status} = -1$) must be equal to the total sum at the end of the event ($\text{status} = 1$).

The procedure used to construct the model with exotic colour flow relies on the ability to modify the LHE event files in between execution of the hard-scatter generator and the parton shower:

- 1) Hard-scatter events are generated for the $t\bar{t}$ process at the LHC according to the SM using **POWHEG-Box v2**. The work presented in this thesis studies colour flow in the single-lepton final-state of $t\bar{t}$ production, consequently events are filtered such that at least one lepton is present in the final state. The events are stored as LHE files.
- 2) The LHE files are modified in order to create exotic colour flow. This is done by changing (“*flipping*”) the (anti-)colour indices of the daughters of the hadronically decaying W boson such that, effectively, the W boson becomes an *ad hoc* colour octet. No modifications are required for events with two leptons in the final state. The modified events are stored as LHE file.
- 3) The **PYTHIA 8** MC program reads the modified LHE file and the parton shower and subsequent simulation algorithms are applied.

The colour-flipping procedure is applied to the example shown in Figure 47 and a printout of the LHE record for the resulting hard-scatter event with exotic colour flow is shown in Figure 48.

In the specific example event considered here, inversion of the colour structure is achieved by exchanging the colour indices of the b and c quarks. Generally, the procedure must locate the b/\bar{b} quark originating from the same vertex as the

no	id	name	status	mothers	daughters	colours	px	py	pz	E
1	21	g	-1	0	0	3 5 502 503	0.000	0.000	449.316	449.316
2	21	g	-1	0	0	3 5 504 505	0.000	0.000	-336.610	336.610
3	6	t	2	1	2	6 7 502 0	-19.518	56.243	378.283	419.636
4	-6	t_bar	2	1	2	8 9 0 505	53.012	-0.282	-219.844	286.635
5	21	g	1	1	2	-1 -1 504 503	-33.494	-55.961	-45.732	79.655
6	24	W+	2	3	3	10 11 0 0	50.092	34.258	153.765	183.497
7	5	b	1	3	3	-1 -1 506 0	-69.611	21.985	224.518	236.139
8	-24	W-	2	4	4	12 13 0 0	65.878	37.124	-224.195	246.533
9	-5	b_bar	1	4	4	-1 -1 0 505	-12.866	-37.406	4.351	40.102
10	-3	s_bar	1	6	6	-1 -1 0 506	-9.748	28.876	18.948	35.890
11	4	c	1	6	6	-1 -1 502 0	59.840	5.382	134.817	147.607
12	11	e-	1	8	8	-1 -1 0 0	72.000	24.032	-217.950	230.789
13	-12	nu_e_bar	1	8	8	-1 -1 0 0	-6.122	13.092	-6.245	15.744

Figure 48: Example printout of a single event of LHE file produced for colour-flipped $t\bar{t}$ Monte Carlo.

hadronically decaying W boson.¹ Afterwards, the colour index of the b/\bar{b} quark is swapped with that of the appropriate daughter of the hadronically decaying W boson, i.e. $b \leftrightarrow q$ respectively $\bar{b} \leftrightarrow \bar{q}'$. Note that the c (b) quark after application of the procedure, see Figure 48, has colour index 502 (506).

Unfortunately, the PYTHIA algorithms produce a crash when reading the naively colour-flipped LHE files. A safe-guarding mechanism detects unphysical colour structure in the input data: the SM W boson is not a colour octet. As a work-around, after performing the colour-flipping, the W bosons and top quarks are removed from the LHE file. Due to further safeguards this must be done for both the semileptonic and dileptonic events. Events of allhadronic type are removed completely as part of the event filtering procedure. All internal references, such as mother–daughter indices, are recomputed. Otherwise further self-consistency checks of the MC applications will terminate with error. The need for the removal of the top quarks and W bosons is a downside of the simple colour-flipping procedure used for the exotic model as it is a departure from a realistic $t\bar{t}$ topology.

10.3 Validation

Considering that the simulation model with exotic colour flow presented in this section is not validated by the MC program authors, some validation must be performed. However, due to the simplicity of the model, leniency regarding the faults of the model should be employed. In a sense, the model validation should be more about discovering and understanding the faults rather than ensuring that there are none.

10.3.1 Analysis Description

The validation studies are performed using two MC samples that have been generated with POWHEG-Box v2 using the exact same configuration. Afterwards, the resulting LHE files are either left untouched, to produce regular $t\bar{t}$ events simulated according to the SM, or modified to produce exotic colour flow. Regardless, the events stored in

¹ This is particularly crucial when the chosen generator and configuration allows b quarks in the PDF or generally production of b quarks other than those from the top-quark decay.

the LHE files are showered using `PYTHIA 8`. For the purpose of the validation studies, no detector simulation is applied. The `Rivet` analysis framework [171] is used to construct an object and event reconstruction procedure² according to the fiducial phase-space definitions presented in Section 9.1. An event selection is applied which requires exactly one lepton and at least four jets. Two of the jets must be tagged to likely originate from a b -hadron.

10.3.2 General Kinematics

Comparison of general kinematic variables of the lepton and the jets shows good agreement between the normal SM simulation and the exotic model. In particular angular variables, such as the pseudorapidity, appear to be completely unaffected. Small deviations can be observed in the missing transverse energy which are, however, at the level of the statistical precision. Kinematics of the two leading b -tagged jets remain essentially unchanged. More pronounced deviations can be found when comparing variables which are more directly related to the hadronically decaying W boson and its decay.

Figure 49 compares kinematics of the four-momentum sum of the leading untagged jet pair, which is a good estimator for the hadronically decaying W boson, taken from the nominal SM $t\bar{t}$ MC sample to those taken from the colour-flipped exotic model.

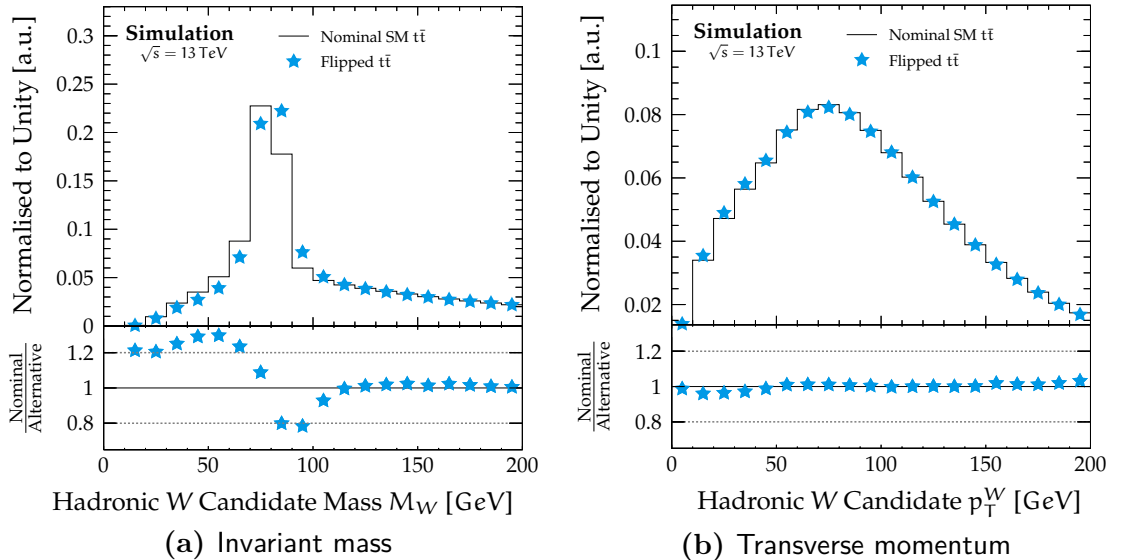


Figure 49: Kinematics of leading untagged jet pair for $t\bar{t}$ events generated using the nominal SM prediction as well as the colour-flipped exotic model. Shown are (a) the invariant mass distribution and (b) the transverse momentum.

The invariant dijet mass is of particular relevance as it is sensitive to soft large-angle emissions. It is therefore, in principle, an observable sensitive to the colour flow in an event. Indeed, a difference can be found which separates the two samples: the

² Specifically, a custom validation analysis routine implemented in version v2.5.4 of the `Rivet` framework is used.

exotic model favours larger dijet masses than the SM. This is consistent with the expectation since one expects more large-angle radiation from the colour-flipped model where the colour connection must trace to the (on average) more large-angle \mathbf{b} quark. Much smaller deviations can be observed in the distributions of the p_T of the dijet system or the individual two jets it is composed of.

To understand the deviations observed between the nominal SM and the exotic model better, a variation of the colour-flipping procedure discussed in the previous section is created. Instead of flipping the colour-strings and removing top quarks and W bosons, this *no-flip* procedure only performs the removal of top quarks and W bosons from the LHE file. This allows, to some extent, to disentangle the two effects and hence paints a clearer picture of the observed deviations. Figure 50 compares distributions from the additional validation sample, labelled as “*without t/W*”, to those taken from the SM $t\bar{t}$ simulation and the colour-flipped sample.

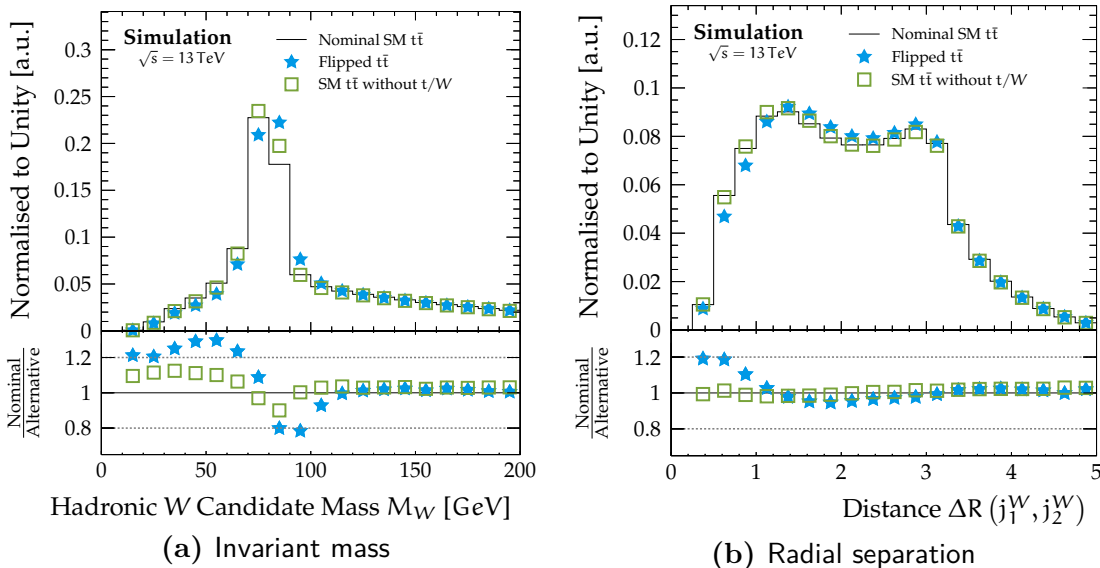


Figure 50: Comparison of SM $t\bar{t}$ MC to colour-flipped exotic model and *no-flip* validation t/W model (labelled as “*without t/W*”). Shown are (a) the invariant mass of the leading untagged jet pair and (b) the radial separation of the two leading untagged jets.

Figure 50a compares the invariant mass distribution of the hadronically decaying W candidate and shows that the no-flip sample, like the exotic model, fails to reproduce the nominal configuration. However, the observed deviation is considerably smaller than that observed from the exotic model. This effect is likely a result of the procedure the `PYTHIA` MC program uses the produce radiation, which accounts for the presence of top quarks in $t\bar{t}$ pair production.³

³ Without the top quark in the hard-scatter event, additional radiation that may be produced by the dipole formed by the outgoing \mathbf{b} quark and its colour-connection partner in the initial state has access to rather larger energy (up to $\mathcal{O}(\text{TeV})$). If instead a top quark is present, `PYTHIA` preserves the virtuality of the top quark which limits the potential energy radiated by the hard-scatter final state. Thanks to Ben Nachman for explaining this subtle and generator-specific effect.

The radial separation of the two subjects that form from the hadronically decaying W boson is another variable which is intuitively sensitive to the radiation pattern and thus colour-structure of the dijet system. Indeed, small deviations between the SM and the exotic model can be observed, see Figure 50b. In the exotic model, the two leading untagged jets tend to be farther apart than those from the SM simulation. As a result of the absence of the colour-connection between the two daughters of the hadronically decaying W boson, additional radiation from one daughter is no longer pulled towards the other daughter. This impacts the location of the jet-centre and thus also the estimated radial distance. Note that the no-flip sample agrees reasonably well with the regular SM simulation.

In addition to the deviations observed for some of the control variables, a small change in the selection efficiency is observed for the exotic model: the fraction of events which pass the selection criteria is about 3.5% larger relative to the SM comparison sample. However, the same deviation is also observed from the no-flip sample and therefore likely caused by the removal of the top quarks and W bosons.

While the deviations observed so far are not ideal, as they make comparison of the SM and exotic case more difficult, they are no cause for alarm and essentially follow trends which can be expected. The changes imply that any measurement that wishes to make comparisons to the exotic model should not rely (too strongly) on the kinematics of the dijet system expected to come from the hadronically decaying W boson. In particular, constraints on the invariant dijet mass and the radial separation of the two subject should be avoided in order to not introduce bias. For the measurement presented in this thesis, the impact of this effect is studied using a reweighting test which will be presented as part of the next section.

10.3.3 Colour Flow

Finally, to assess the efficacy of the colour-flipping procedure used to construct the exotic model, the distributions of an observable constructed for its sensitivity to the colour flow are compared for the three models. This observable is the jet-pull angle, which will be introduced in more detail in Section 13.

For the moment, the jet-pull angle $\theta_{\mathcal{P}}$ will be used for validation of the colour-flipping procedure without proper introduction. Nevertheless, two remarks are important: the observable can be calculated for a pair of jets using their constituents and it is expected to follow a sloped distribution when the two jets have a colour-connection and to be distributed (approximately) flat otherwise. Figure 51 shows the jet-pull angle distributions for the three models in two different configurations: once calculated using all jet constituents and once using only those which have a non-zero electric charge.

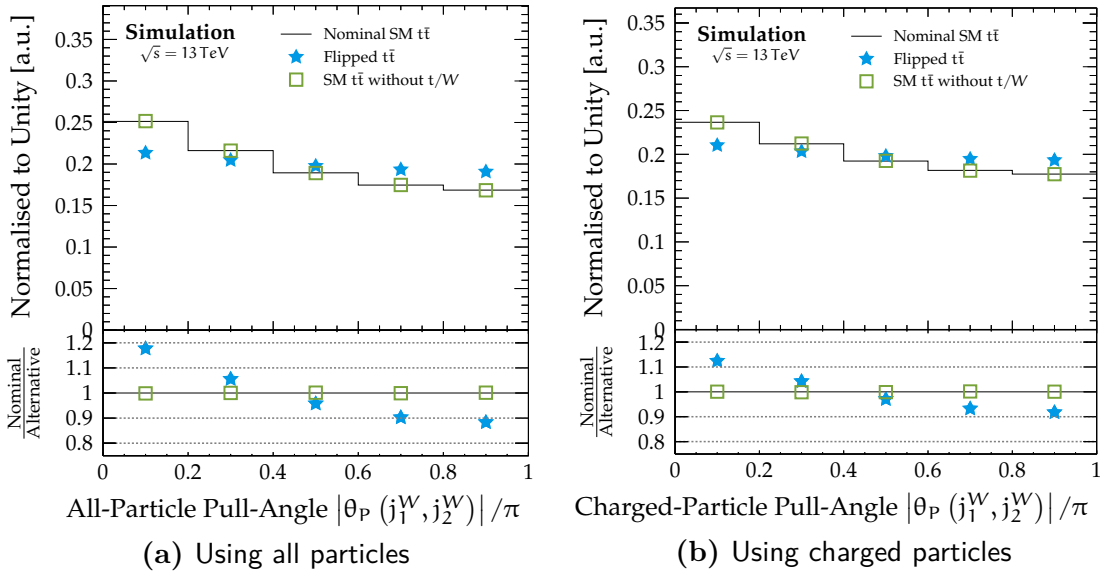


Figure 51: Comparison of pull-angle distributions for validation of the model with exotic colour flow. Three samples are shown: the (nominal) SM prediction, the exotic model, as well as the *no-flip* validation model (labelled as “*without t/W*”). Shown are (a) the pull-angle calculated from all valid particles and (b) the same observable calculated only from the charged particles.

The distributions from the regular SM and exotic model are notably different and exhibit the expected shape: a slightly more sloped distribution observed for the SM relative to the exotic model indicates presence of a colour connection in the former sample and absence in the latter sample. Furthermore, the distribution obtained for the no-flip validation sample closely follows that of the nominal configuration, hence, the observable is truly sensitive to the change in colour-structure rather than just the removal of top quarks and W bosons.

As a final check, a reweighting test is performed to check that a change in the invariant mass distribution does not meaningfully distort the colour flow observable. The colour-flipped sample is reweighted such that the invariant mass distribution of the hadronically decaying W boson is equivalent to that observed in the nominal $t\bar{t}$ sample. For calculation of the weights 100 bins of M_W are used whose width is determined dynamically using evenly spaced quantiles on the data.⁴ The procedure yields per-event weights which can be applied to any variable and in particular to the colour-encoding observables. Application to the exotic model produces the “reweighted exotic model”. The resulting invariant mass distribution is shown in Figure 52a while Figure 52b shows the effect of applying the same weights when constructing the distribution of the radial separation of the two subjects to the dijet system.

By construction, the invariant mass distribution of the reweighted exotic model recovers the shape predicted by the nominal SM quite well. The deviations observed

⁴ In practice this is done using the `BinsReweighter` tool provided by the `hep_ml` python package [172].

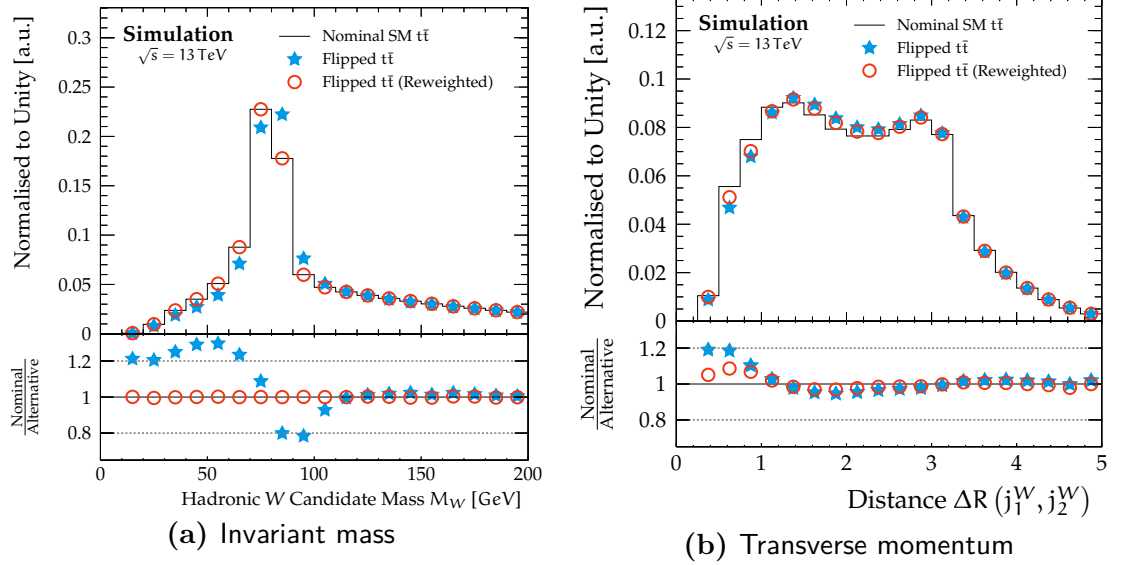


Figure 52: Results of reweighting test. Compared are distributions from the nominal SM configuration to those from the exotic model as well as the reweighted exotic model. Shown are (a) the invariant mass distribution of the dijet system constructed from the two leading untagged jets and (b) the radial separation of the same jets.

for the radial separation ΔR are smaller for the reweighted sample, however, they do not vanish fully.

The correction weights, which have been obtained from the reweighting procedure, can also be applied when constructing the distributions of the jet-pull angle. Figure 53 compares the regular distributions to those obtained when including the correction weights. Both subfigures show that the sensitivity of the jet-pull angle to the colour flow remains essentially unchanged by the reweighting procedure.

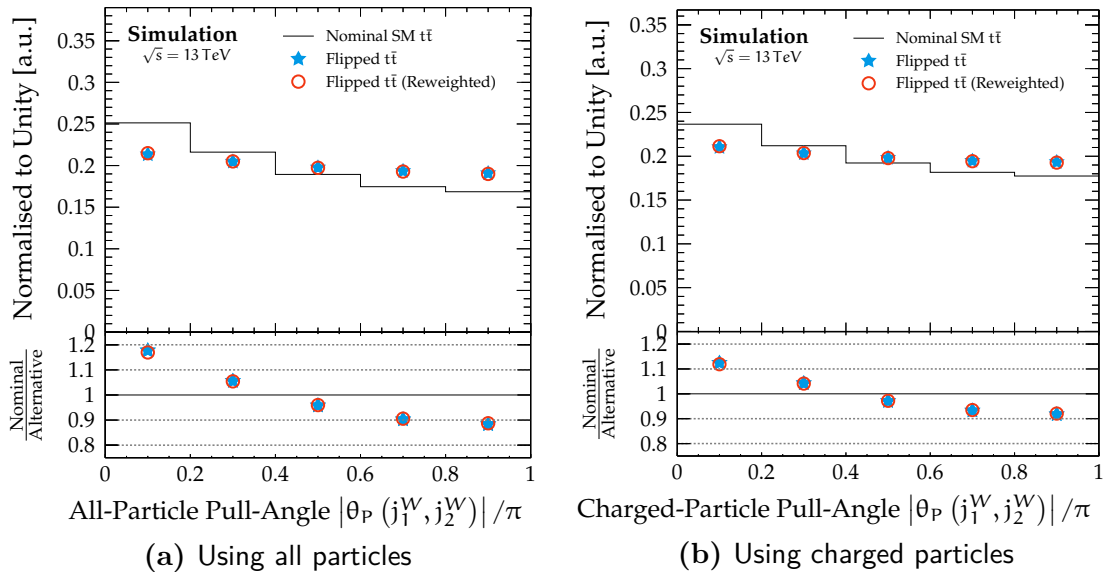


Figure 53: Results of the reweighting test; see Figure 51 for description of observables shown in the figure. Three configurations are compared: the nominal SM prediction, the exotic model and the reweighted exotic model.

11 Modelling of Fake Lepton Background

CONTENTS	
11.1 Sources of Fake and Non-Prompt Leptons	107
11.2 The Matrix Method	108
11.2.1 Operating Principle	109
11.2.2 Determination of Efficiencies	111

The use of final state signatures that contain at least one lepton is motivated by a variety of factors. Among various experimental and theoretical considerations, the relatively high background rejection rate that can be achieved is a motivation of considerable importance. At the ATLAS experiment, the use of highly efficient lepton identification criteria allows to reject the vast majority of events produced without a lepton.

The objects defined by the reconstruction procedure introduced before represent *real* physical particles that originate from the primary hard-scatter reaction. For example, lepton objects represent electrons or muons from the immediate hard-scatter production and decay. In opposition, *fake* objects are those which imitate the real signal without actually representing a real physical particle. Potential sources of fake objects for electrons and muons are discussed below.

Due to the large production cross-sections of background processes which imitate real signal leptons, contamination is non-negligible irrespective of the high efficacy of the lepton identification. Production of QCD multijet events is an example of a process that has a high production rate but does not have any isolated high- p_T leptons in its final state. A considerable number of events may appear signal-like and therefore pass the lepton identification criteria. This contribution remains in the signal selection and must be properly accounted for. On account of the fact that the events somehow imitate the lepton signal signature, this type of background is collectively called *non-prompt* and *fake lepton* background.¹

11.1 Sources of Fake and Non-Prompt Leptons

There is not one singular process which is the origin of the fake leptons background. Rather, all types of production which occur in the pp collisions that imitate the real lepton signal contribute. Consequently, the fake lepton signal may be caused by a variety of effects:

Fake Electrons typically arise from photon bremsstrahlung from muons, charged hadrons, semi-leptonic heavy-flavour decays, or photon conversion.

In the first case, the ID track of a high- p_T muon can be confused with that from an electron and the radiated photons produce a signature in the ECAL which is difficult to distinguish from the signature of an electron.

¹ For simplicity also abbreviated as “Fakes”, “Fake Leptons”, or “NP/Fake Leptons”.

Similarly, jets with charged hadrons and considerable EM activity can imitate an electron signature where the charged hadron produces an electron-like ID track. Additional photons, e.g. from the decay of neutral pions inside the jet, or simply large EM activity of the jet may add electron-like deposits in the ECAL.

Semi-leptonic heavy-flavour decays and photon conversion produce actual electrons. However, these are *non-prompt* meaning that they do not originate from the original and immediate signal process of the pp collision.

Fake Muons are typically caused either by in-flight decays of mesons or semi-leptonic heavy-flavour decays. This is a direct result of the fact that muons are mostly reconstructed with the help of the muon spectrometers which are very resilient against fakes that are not caused by an actual muon. Additional, much smaller contributions may arise from very long-lived charged hadrons and simple combinatoric misreconstruction and matching of ID and muon spectrometer tracks.

The background arising from lepton misidentification is not expected to be modelled properly by MC simulation. In a simplified way this can be explained by the fact that such a simulation-based prediction would require not only to simulate the particles which are misidentified but also to then combine this with an accurate model of how the misidentification applies to those particles. Furthermore, many of the fake lepton sources would require generation of an immense amount of statistics of which the majority gets rejected by analysis cuts. While this high rejection is excellent news for the analysis itself, it means that accurate simulation is not feasible from an economic perspective.

Instead of using a simulation-based modelling, data-driven techniques are preferred. These make use of measured experimental data to infer the contribution of the fake lepton background to the signal selection. One such method, which is used by the work presented in this thesis, is the *Matrix Method*.

11.2 The Matrix Method

The Matrix Method [173, 174] is a generic approach to estimate contributions of different processes to a dataset. It has been used by the ATLAS collaboration in top-quark physics analyses of both Run 1 [175, 176] and Run 2 [177] data. Fundamentally, it works by splitting a global enclosing dataset according to some selection criterion into subsets. The relative contributions of the different (potentially overlapping) subsets are then used to infer the content of one subset from the contents of all others. This requires that the relative composition of the global dataset into these subsets is estimated beforehand. The matrix method is a data-driven approach meaning that the estimate is dominantly inferred using experimental data rather than simulation. Additional components of the procedure, such as efficiencies used

in the calculation of the estimate, may be derived either from data using control regions or from simulation.

11.2.1 Operating Principle

The following discussion applies the Matrix Method to the problem of estimating the contribution of the fake lepton background to an event selection in the $t\bar{t} \rightarrow \ell + \text{jets}$ channel. In addition to the lepton type — which was defined above and which may be either *fake* or *real* — a lepton identification scheme, with the labels *loose* and *tight*, is defined. The tight lepton identification corresponds to that identification which is used to perform the actual analysis, see Section 8. In contrast, the loose lepton identification uses more relaxed requirements. The regions overlap such that all tight leptons are included within the loose subset. In addition, many lepton candidates of lesser quality are included as well.

Figure 54 illustrates how the global dataset is split into subsets using the two definitions introduced above. The vertical direction in the illustration separates the global dataset into events which have a “*real*” lepton and those with a “*fake*” lepton according to the definition laid out above; the horizontal direction splits the same dataset according to the lepton identification criteria.

For an analysis, the real lepton subset, marked in green, is relevant and ideally the analysis selects exclusively real leptons. In practice, the purity is not unity but to increase it, the *tight* lepton identification criterion is applied. Therefore, the task of the fake lepton estimate comes down to determining the fake leptons which pass the tight lepton identification, marked in dark red.

After selecting the inclusive dataset \mathbb{S} , which is symbolised by the enclosing rectangle in Figure 54, this sample can be subclassed into two disjoint sets: events may either pass the tight selection (class \mathbb{T}) or pass exclusively the loose selection (class \mathbb{L}). Furthermore, the sample \mathbb{S} can be divided into the subset of events which contain a real lepton (class \mathbb{R}) or a fake lepton (class \mathbb{F}). Overall, this means that the following set equation holds:

$$\mathbb{S} = \mathbb{L} + \mathbb{T} = \mathbb{F} + \mathbb{R}. \quad (17)$$

In this notation, the fake lepton background events that contribute to the analysis are located in the intersection of \mathbb{T} and \mathbb{F} . The matrix method is based on utilising

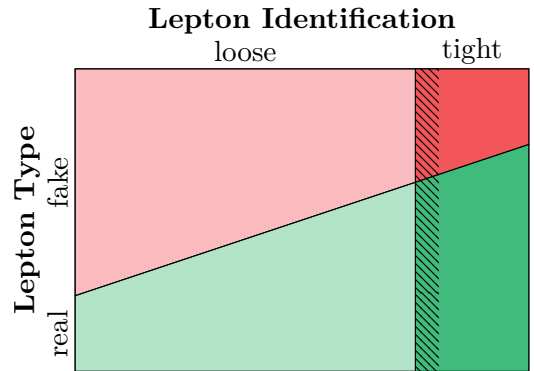


Figure 54: Schematic drawing of the dataset splits used for applying the Matrix Method to the problem of estimating the fake lepton contribution to an analysis selection. The shading on the vertical cut line illustrates that the subset passing the *tight* lepton identification is included in that passing the corresponding *loose* lepton identification.

this split to relate the contents of the four sets according to the formula

$$\begin{pmatrix} \langle n_{\mathbb{T}} \rangle \\ \langle n_{\mathbb{L}} \rangle \end{pmatrix} = \begin{pmatrix} \varepsilon_r & \varepsilon_f \\ \bar{\varepsilon}_r & \bar{\varepsilon}_f \end{pmatrix} \cdot \begin{pmatrix} n_{\mathbb{R}} \\ n_{\mathbb{F}} \end{pmatrix} \quad (18)$$

which relates the expected number of events passing the tight or loose selection respectively, $\langle n_{\mathbb{T}} \rangle$ and $\langle n_{\mathbb{L}} \rangle$, to the unknown and desired number of events featuring a real or fake lepton respectively, $n_{\mathbb{R}}$ and $n_{\mathbb{F}}$, using two coefficients related to selection efficiencies. These coefficients, ε_r and ε_f , describe the probability of a real or fake lepton to pass the tight selection criteria. Consequently the two quantities are called the *real* and *fake* efficiencies. The coefficients $\bar{\varepsilon}_i$ are defined as $\bar{\varepsilon}_i := 1 - \varepsilon_i$ and relate the probability for the opposite outcome.

To account for dependencies of the efficiencies on event and object properties, such as kinematics, they are parameterised in terms of event and object quantities such as the lepton $p_{\mathbb{T}}$, the jet multiplicity, or derived quantities such as the transverse W boson mass $m_{\mathbb{T}}^W$. Multiple parameterisations can be combined using a multiplicative approach where every efficiency after the first is scaled by the average efficiency $\tilde{\varepsilon}$. For a combination n of different efficiency parameterisations this translates to:

$$\varepsilon_{\text{Combined}} = \frac{1}{\tilde{\varepsilon}^{n-1}} \cdot \prod_{k=1}^n \varepsilon_k. \quad (19)$$

The fake and real efficiency must be extracted before the matrix method can be used to estimate the contribution of the fake lepton background. Parameterised efficiencies are usually derived using a combination of control regions in data and simulation. The procedure used for constructing the parameterisations used by the work presented in this thesis are discussed in the next section.

Having derived fake and real efficiency parameterisations, the matrix method is applied on the complete set of measured data to infer the contribution of the fake lepton background to the signal selection. This requires that the tight lepton identification requirements are disabled, the analysis selection, however, remains active. Using the efficiency parameterisations, the fake and real efficiencies are calculated on an event-by-event basis. With these efficiencies at hand, a per-event weight is assigned:

$$w_{\mathbf{e}} := \frac{\varepsilon_f}{\varepsilon_r - \varepsilon_f} (\varepsilon_r - \delta_{\mathbf{e} \in \mathbb{T}}), \quad (20)$$

where $\delta_{\mathbf{e} \in \mathbb{T}} = 1$ if the event \mathbf{e} satisfies the tight lepton requirements and zero otherwise. This event weight quantifies how fake-like a specific data event is. The total estimated contribution of the fake lepton background can be calculated by summation of $w_{\mathbf{e}}$ over all events. These event weights may also be used to calculate the fake background contribution to some bin of a given distribution. The bin content for the fake lepton

contribution is given as the sum of w_{ϵ} over all data events ϵ that enter this bin for the given variable.

11.2.2 Determination of Efficiencies

A crucial ingredient for the matrix method are the fake and real lepton efficiencies which must be extracted from data or simulation first. The work presented in this thesis uses efficiency parameterisations which have been derived from control regions constructed in data which are enriched in real or fake leptons.

The event and object reconstruction procedure has been described in Section 8. However, the matrix method relies on a set of *loose* lepton identification requirements which are essentially a relaxed variant of the *tight* lepton identification requirements. Table 3 compares the two sets of lepton identification requirements.

	Loose Lepton	Tight Lepton
Electron Identification	MediumLH	TightLH
Muon Identification	Medium	Medium
Lepton Isolation	None	GradientTight
Electron Track-To-Vertex Association	Disabled	$ d_0^{\text{sig}} < 5$ and $ z_0 \cdot \sin \theta < 0.5$
Muon Track-To-Vertex Association	Disabled	$ d_0^{\text{sig}} < 3$ and $ z_0 \cdot \sin \theta < 0.5$

Table 3: Summary of selection requirements for *loose* and *tight* lepton definitions. Refer to Section 8 for specifics on the terminology used in the table.

Figures shown in the remainder of this section are representative of the data used to construct the NP and fake lepton estimate. They have been created and supplied by the authors of the centrally provided efficiency parameterisation data. However, these figures only contain the 2015 subset of the measured data. The actual estimates of the NP and fake lepton contaminations to the measurements performed as part of this thesis will be shown as part of the discussion of these measurements.

§1. Measurement of Real Efficiencies The real efficiencies ε_r are measured from data in control regions enriched in $Z \rightarrow ee$ and $Z \rightarrow \mu\mu$ events using the tag-and-probe method. An unbiased sample of real loose leptons (the probe) is selected by requiring that the other lepton (the tag) from the Z boson decay satisfies the tight lepton requirements. By applying the tight selection requirement on the probe, the real efficiency ε_r can be determined, see Equation (21). In order to avoid bias of the selected probe sample, for each event, both leptons of the $Z \rightarrow \ell\ell$ pair may serve as tag and probe.

$$\varepsilon_r = \frac{\# \text{ of probe leptons that pass tight requirement}}{\# \text{ number of all probe leptons}} \quad (21)$$

The control region is defined by selecting events with an opposite-sign same-flavour lepton pair which are expected to originate from a Z boson. Events must have been selected by a single-lepton trigger and one of the two leptons must be matched to the

trigger object using a geometric matching definition. The trigger signature used for the measurement of the efficiencies should closely resemble those used later by the subsequent analysis. However, triggers must be selected such that they do not use any isolation or strict lepton identification requirements as this would interfere with the loose lepton definition. Furthermore, they must not require a higher p_T cut than is used for the actual analysis. In summary, the triggers used for the estimation of the efficiencies must not be more restrictive than those used by the analysis. Additional event-level quality requirements such as the presence of a primary vertex, good operating conditions of the LHC beams, and availability of all detector components are applied. In addition to the lepton requirement, events must have at least one jet. An invariant mass cut is applied on the dilepton invariant mass to select events which have $61 \text{ GeV} < M_{\ell\ell} < 121 \text{ GeV}$. A tighter cut of $81 \text{ GeV} < M_{\ell\ell} < 101 \text{ GeV}$ defines the signal region while the other events fall into the sideband region.

Figure 55 shows the invariant mass distributions with the Z boson mass peak clearly visible around $M_{\ell\ell} \sim 90 \text{ GeV}$. The signal and sideband regions are highlighted. In addition to the signal, the contribution from same-sign same-flavour lepton pairs is shown. Prior to calculating the real lepton efficiency from the tag-and-probe yields in the signal region according to Equation (21), the remaining background contributions must be subtracted. This is achieved by subtracting the averages taken from the two sidebands from the yield measured in the signal region.

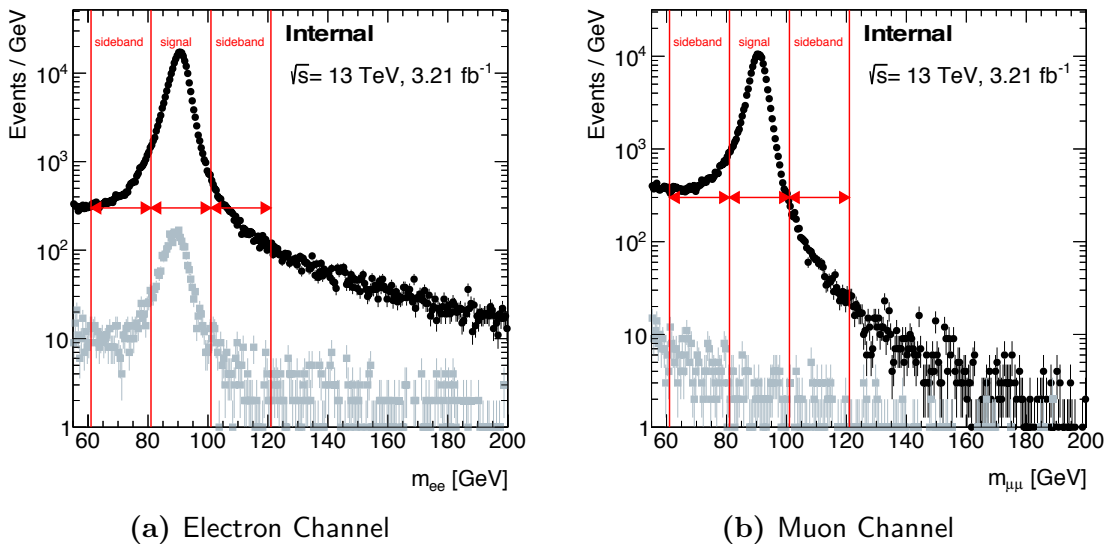


Figure 55: Invariant mass distribution of the dilepton pair for (a) the electron and (b) muon channel. Both figures show the opposite-sign contributions in black while the same-sign contributions (which are not part of the signal) are shown in gray. The data correspond to the dataset collected during 2015.

§2. Measurement of Fake Efficiencies The fake efficiencies ε_f are measured from control regions enriched in fake leptons which at the same time have a composition that is comparable to that expected from the signal region of the final analysis. This fake lepton control-region requires presence of a single loose lepton. Application

of the tight requirement on the lepton is used to determine the fake lepton efficiency as the ratio between the count of tight and loose leptons in the control region, see Equation (22).

$$\varepsilon_f = \frac{\# \text{ of events in fake lepton control-region with tight lepton}}{\# \text{ of events in fake lepton control-region}} \quad (22)$$

The fake lepton control region requires the same event-level quality requirements as used to define the real lepton control region. Furthermore a single-lepton trigger must have fired, with the same considerations towards the trigger signature as discussed previously for the real lepton control region. The event selection requires the presence of exactly one lepton which must be matched to the trigger object using a geometric matching definition. In addition, at least one jet must be present. Figure 56 shows the distribution of the missing transverse energy observed after application of this event selection.

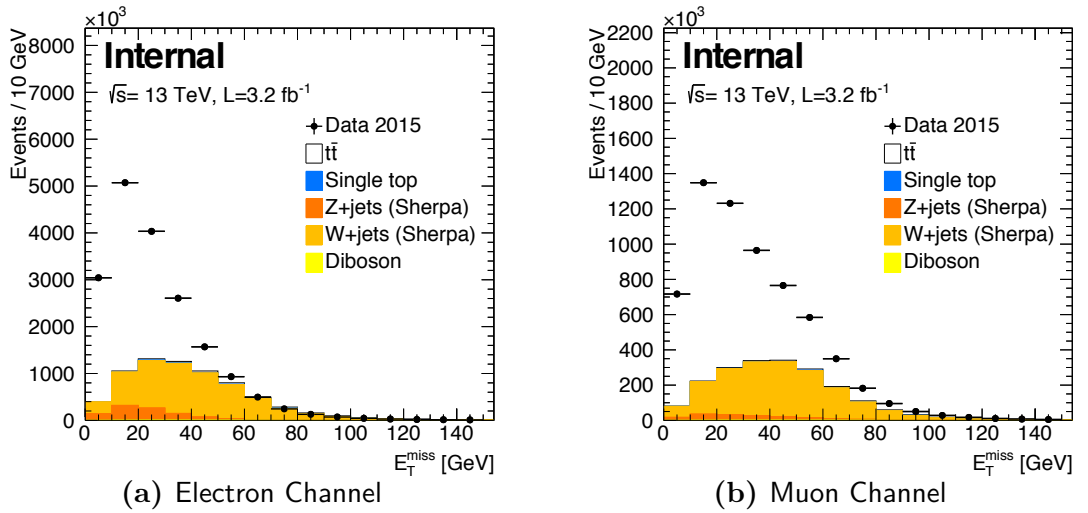


Figure 56: Missing transverse energy distribution of events with exactly one loose lepton and at least one jet for (a) the electron and (b) muon channel. The data correspond to the dataset collected during 2015.

Contribution of non-prompt and fake leptons is enhanced by requiring small missing transverse energy or a large transverse impact parameter. This greatly reduces contributions from W +jets, which contains a high-momentum muon, and semileptonic b -hadron decays. As the remaining contribution of real leptons to the control region is not negligible, it must be subtracted from both counts beforehand. Consequently, both numerator and denominator of Equation (22) are reduced by the count of real leptons that satisfy the respective requirements. The contamination of real leptons to the fakes control region is estimated using Monte Carlo simulation.



Measurements and Studies

In Section 12, a measurement of the top-quark pair production cross-section at 13 TeV using early Run 2 data is presented. Section 13 presents a measurement of colour flow in $t\bar{t}$ events at 13 TeV. Finally, in Section 14, the prospects for studying and measuring colour flow in boosted $t\bar{t}$ topologies are investigated.

12 A Measurement of Top-Quark Pair Production

CONTENTS	
12.1 Analysis Strategy	116
12.2 Data and Simulation Samples	117
12.2.1 Measured Data	117
12.2.2 Simulation	117
12.3 Reconstruction and Event Selection	120
12.4 Estimation of Background Contributions	121
12.5 Evaluation of Uncertainties	123
12.5.1 Experimental Uncertainties	123
12.5.2 Signal Modelling Uncertainties	125
12.5.3 Background Modelling Uncertainties	127
12.5.4 Uncertainty Breakdown	128
12.6 Results	129

During the first year of Run 2 operation, 2015, the LHC experiments have performed many so-called *early-data measurements*. These measurements were often developed shortly before the start-up phase or over the course of the summer of 2015. In many cases, the primary purpose of these measurements is not to provide a final high-precision measurement of the physics goals under investigation. Instead, the aim is to measure a relatively well-known or well-predicted quantity in order to get familiar with the operating conditions at the unprecedented high centre-of-mass energy. A measurement of the top-quark pair production cross-section, performed by the ATLAS experiment, is among these early-data measurements and shall be discussed in this section.¹

¹ The work discussed in this section was executed as part of a larger analysis team and is documented in a conference note [178]. While the work presented in the conference note includes measurements in both dilepton and $\ell + \text{jets}$ channels, this section will concentrate on the measurement in the $\ell + \text{jets}$ channel, to which the author of this thesis contributed.

At the operating conditions of the LHC, top quarks are predominantly produced as $t\bar{t}$ pairs originating from the gluon fusion process, see Section 2.2. The total production rate is determined by the inclusive cross-section $\sigma_{t\bar{t}}$ which depends on the centre-of-mass energy. Calculations of $\sigma_{t\bar{t}}$ at different LHC energies predict an increase of the production rate by about 3.3 moving from a centre-of-mass energy of $\sqrt{s} = 8$ TeV to 13 TeV. Prediction of $\sigma_{t\bar{t}}$ using a fully theoretical approach is a formidable challenge for QCD calculation tools. Primarily, precision measurements of $\sigma_{t\bar{t}}$ have sensitivity to the parton distribution functions (PDFs) of the proton, the strong coupling constant α_s , and the top-quark mass m_t . However, an enhanced $\sigma_{t\bar{t}}$ may also be a result of physics beyond the Standard Model. Assuming a top-quark mass of 172.5 GeV, the production cross-section is predicted to be 832^{+46}_{-51} pb — refer to Section 2.2 for more details.

The rest of this section is organised as follows: in Section 12.1 the overall analysis strategy is introduced. Section 12.2 describes the experimental data used for the measurement as well as simulation samples that are needed. Thereafter, in Section 12.3 the event selection is presented and the selected data are shown. Section 12.4 reviews the modelling of background contributions, followed by a discussion of the treatment of uncertainties in Section 12.5. Finally, in Section 12.6 the measurement results are presented.

12.1 Analysis Strategy

In essence, a cross-section measurement is simply a counting experiment. Given precise knowledge of the number of proton–proton collisions that have occurred, through the integrated luminosity \mathcal{L}_{Int} , a direct measurement of the count of signal events N_{Sig} allows to calculate the production cross-section for the signal process as $N_{\text{Sig}}/\mathcal{L}_{\text{Int}}$. However, in practice the situation is more complicated due to the finite acceptance, efficiency, and resolution of the experimental apparatus. For example, instrumentation of the ATLAS detector limits most measurements to the pseudorapidity range $|\eta| < 2.5$ which implies that some signal events produced in the primary collision escape detection thereby reducing the observed count. Furthermore, backgrounds, especially those irreducible, may imitate the signal, hence, the simple event-count is polluted by backgrounds and must be corrected accordingly.

Instead of the simple direct counting-experiment procedure, the measurement presented here employs a slightly more complicated strategy to extract $\sigma_{t\bar{t}}$. The event selection, which will be discussed further in Section 12.3, is a crucial tool for establishing a set of events rich in the signal contribution. Given an appropriate signal-event selection, the following procedure is applied:

- 1.) Count the number of observed events N_{Obs} that pass the event selection.
- 2.) Subtract the estimated background contribution N_{Bkg} from the observed event count which produces the estimated signal yield.

- 3.) Correct the estimated signal yield by the efficiency ε . This accounts for signal events that have not been observed due to detector effects or are otherwise lost by the reconstruction procedure. It also includes the efficiency of the signal selection procedure.
- 4.) Divide by the integrated luminosity \mathcal{L}_{Int} of the data to retrieve the total inclusive cross-section.

In summary, the procedure is therefore given by the following equation:

$$\sigma_{\text{tt}} = \frac{N_{\text{Obs}} - N_{\text{Bkg}}}{\mathcal{L}_{\text{Int}} \cdot \varepsilon}. \quad (23)$$

The correction factor ε is extracted from MC simulation, the integrated luminosity is measured alongside normal data taking, and the background contributions are estimated using a combination of data-driven methods and simulation. If the correction factor ε is extracted from pre-filtered MC simulation, e.g. filtered to contain a specific final state, an additional correction factor must be applied to account for the filter efficiency.

12.2 Data and Simulation Samples

In this section, properties of the measured data as well as the configurations used to generate simulation samples are discussed.

12.2.1 Measured Data

The early-data cross-section measurement is performed using data collected by the ATLAS detector between 13th June and 16th July of 2015. During this early pp collision phase at $\sqrt{s} = 13 \text{ TeV}$, a bunch spacing of 50 ns was used which is twice that of subsequent data taking periods. In total the data correspond to an integrated luminosity of $\mathcal{L}_{\text{Int}} = 85 \text{ pb}^{-1}$ after applying a requirement to ensure that all detector subsystems are fully operational. Single-electron or single-muon triggers are used to preselect the data. These triggers are designed to be almost fully efficient at a lepton transverse momentum of $p_{\text{T}} > 25 \text{ GeV}$. Under these operating conditions, each triggered event includes additional detector-signals from on average 19 extra inelastic pp collisions.

12.2.2 Simulation

Samples of events simulated using MC methods are used by the cross-section measurement for several purposes: foremost, the measured data are compared to the prediction. This allows to assess the validity of the MC simulations and cross-check the analysis procedure using simulation. Furthermore, the extraction of the production cross-section σ_{tt} requires correction factors and estimates for the background contamination which are obtained from the MC simulations. Finally, a variety of systematic uncertainties are estimated using simulated samples. Table 4 summarises the different MC samples used by the cross-section measurement.

Process	Generator	Type	Version	PDF	Tune ³
$t\bar{t}$	POWHEG-Box v2 [166–168]	NLO ME	r3026	CT10 [25]	–
	+PYTHIA 6 [180]	+LO PS	v6.428	CTEQ6L [181]	PERUGIA 2012 [182]
	+EVTGEN [183]	+HF decays	v1.2.0	–	–
$t\bar{t}^\dagger$	POWHEG-Box v2	NLO ME	r3026	CT10	–
	+HERWIG++ [184]	+LO PS	v2.7.1	CTEQ6L1	UEEE5
	+EVTGEN	+HF decays	v1.2.0	–	–
$t\bar{t}^\dagger$	MG5_aMC [185]	NLO ME	v2.2.2	CT10	–
	+HERWIG++	+LO PS	v2.7.1	CTEQ6L1	UEEE5
	+EVTGEN	+HF decays	v1.2.0	–	–
Single top	POWHEG-Box v1	NLO ME	r2819	CT10	–
	+PYTHIA 6	+LO PS	v6.425	CTEQ6L1	PERUGIA 2012
	+EVTGEN	+HF decays	v1.2.0	–	–
WW, WZ, ZZ	SHERPA [186–188]	LO/NLO multileg ME+PS	v2.1.1	CT10	Default
W/Z + jets	SHERPA	LO/NLO multileg ME+PS	v2.1.1	CT10	Default

Table 4: Monte Carlo samples used for the top-quark pair production cross-section measurement. The first part of the table shows samples generated for the signal process $t\bar{t}$, the second those for processes considered to be a background. Samples marked with \dagger refer to alternative signal MC samples used to evaluate signal modelling uncertainties. The following abbreviations are used: *ME* – matrix element; *PS* – parton shower; *LO* – leading-order calculation in QCD; *NLO* – next-to-leading order calculation in QCD; *PDF* – parton distribution function; *HF* – heavy flavour; *Tune* – refers to a specific setting of configurable parameters of the MC generator.

§1. Signal Samples All $t\bar{t}$ simulation samples are filtered to final states where at least one lepton is produced in the hard-scatter interaction. The top-quark mass m_t is set to 172.5 GeV for all simulation samples. Where applicable, the POWHEG modelling parameter h_{damp} , which controls the p_T of the first emission beyond the LO configuration in POWHEG, is set to the top-quark mass.²

The baseline signal sample, also called “*nominal*” sample, is generated using POWHEG-Box v2 as NLO ME generator which is then interfaced with PYTHIA 6 for simulation of the PS, hadronisation, and underlying event. This sample is used to evaluate the agreement of data and simulation, estimate the signal yield, and extract the correction factors required by Equation (23).

Additional $t\bar{t}$ samples, marked with a \dagger in Table 4, are generated in order to study the effects of the modelling of the signal process on the measurement. One sample is generated using an alternative PS, HERWIG++, while another is generated using an alternative ME generator, MADGRAPH5_aMC@NLO (MG5_aMC). In addition, two variations of the nominal sample are generated to assess the effects of initial- and final-state radiation (ISR/FSR) [179]:

² The main effect of h_{damp} is that by regulating the high- p_T emission against which the $t\bar{t}$ system recoils, it also affects the p_T of the $t\bar{t}$ system, for more details see Ref. [179].

for enhanced radiation $h_{\text{damp}} = 2 \cdot m_t$, renormalisation and factorisation scales are set to half their nominal values, and the **PERUGIA 2012 radHi** tune³ is used;
for reduced radiation $h_{\text{damp}} = m_t$, renormalisation and factorisation scales are set to twice their nominal values, and the **PERUGIA 2012 radLo** tune is used.

All other simulation parameters are either set to values determined by the tune indicated for the sample, the SM expectation, or the default configuration of the MC program. For comparison with data, the signal simulation is normalised to the theoretical $t\bar{t}$ cross-section of 832 pb.

§2. Background Samples Contributions from various sources of background contamination are estimated using dedicated simulation samples. Specifics of the MC generators used for this purpose and their configuration can be found in the second part of Table 4. Background contaminations must be subtracted from data as part of the cross-section measurement. Hence, the predictions obtained from simulation must be normalised according to the theoretical or expected cross-section for each process. The specific procedure used to determine the normalisation factor varies by process and is discussed further in Section 12.4.

§3. Simulation of Pile-Up and Heavy-Flavour Decays Multiple overlaid proton–proton collisions are simulated with the soft QCD processes of **Pythia** 8.186 [169] using the **A2** [189] tune and the **MSTW2008L0** PDF set [190]. These dedicated simulation samples are overlaid on top of the basic simulation samples that have been generated for a specific process. By doing so, the effects of in- and out-of-time pile-up are modelled in a natural way. With the exception of the MC samples produced by **SHERPA**, all MC samples use the **EVTGEN v1.2.0** program [183] to model the decays of heavy-flavour hadrons — the charm and bottom hadrons.

§4. Detector Simulation Most simulation samples are processed using the full **ATLAS** detector and trigger simulation [128] which is based on the **Geant4** [129] detector simulation framework. The alternative $t\bar{t}$ samples are processed using a faster simulation called **AtIfast II** [136], see Section 7.4 for more details.

After the detector simulation, all simulation samples are processed using the same reconstruction algorithms and analysis chain as the real data. Small corrections are applied as part of the object and event reconstruction to achieve better modelling of the data by simulation. Such corrections are extracted globally and hence are not specific to the analysis or the applied event selection — see Section 8 for more details.

³ The term *tune* refers to a specific setting of configurable parameters of the MC generator. A tune variation can be used to assess the effects of MC modelling on an analysis as configured by the tuning parameters.

12.3 Reconstruction and Event Selection

The reconstruction procedures and physics-object definitions that are used by the measurement have been introduced and discussed in Section 8. Using these objects, an event selection is applied to select a data sample enriched in $t\bar{t}$ signal. The desired $\ell + \text{jets}$ topology has been introduced and visualised in Section 2.3.

Basic event quality requirements such as stable beams, a fully operational detector, and presence of a primary vertex are required for all events. Furthermore, events are required to pass at least one of the following single-lepton triggers:

e+jets	HLT_e24_lhmedium_L1EM20VH	μ+jets	HLT_mu20_iloose_L1MU15
	HLT_e60_lhmedium		HLT_mu50
	HLT_e120_lhloose		

Triggered and subsequently reconstructed events are required to have exactly one lepton. This lepton must be matched, using a geometrical definition, to the trigger object of one of the triggers that has fired for the event. Events are furthermore required to have at least four jets and at least one of the jets must be **b**-tagged. This requirement is well-motivated by the $t\bar{t}$ topology, see Section 2.3, and greatly reduces contamination by the non-prompt (NP) and fake lepton background as well as from the production of a W boson in association with jets. The NP and fake lepton background is further suppressed by applying requirements on the missing transverse energy E_T^{miss} and the transverse mass m_T^W .⁴ Specifically, events in the electron channel are required to satisfy $E_T^{\text{miss}} > 40$ GeV or $m_T^W > 50$ GeV while those in the muon channel are required to have $E_T^{\text{miss}} + m_T^W > 60$ GeV.

The observed number of events is listed in Table 5 for the two analysis channels separately. In addition, the estimated composition of the selected data sample separated by the production process type is shown. A combination of simulation-based and data-driven methods is used to estimate the composition of the selected data. This will be discussed in more detail in the next section. The expected signal purity is about 80% and the remaining background is dominated by the $W + \text{jets}$ process with smaller contributions from single-top production and events produced without a real, prompt lepton.

Figure 57 shows the observed distributions of the lepton p_T and η , the transverse W boson mass m_T^W , and the jet p_T for the events passing the event selection. A coloured stack of histograms shows the expected composition of the selected data separated by the production process. The distributions observed from data agree reasonably well with the predictions.

⁴ The transverse mass m_T^W is defined as $m_T^W := \sqrt{2p_T^\ell E_T^{\text{miss}}(1 - \cos \Delta\phi)}$, where p_T^ℓ is the p_T of the lepton and $\Delta\phi$ is the difference in the azimuthal angle between the lepton and the missing transverse momentum vector.

Sample	$e + \text{jets}$	$\mu + \text{jets}$
$t\bar{t}$	2800 ± 400	2620 ± 340
$W + \text{jets}$	340 ± 100	230 ± 60
Single top	192 ± 34	180 ± 30
$Z + \text{jets}$	71 ± 35	45 ± 22
Diboson	10 ± 5	10 ± 5
NP/Fake Lepton	200 ± 70	130 ± 60
Total background	820 ± 130	600 ± 100
Total expected	3600 ± 500	3320 ± 350
Observed	3439	3314

Table 5: Observed event yields in the $e + \text{jets}$ and $\mu + \text{jets}$ channels individually. In addition, the expected background contributions as well as the expected $t\bar{t}$ event yield are listed. The uncertainties shown on the expected sample composition are due to experimental uncertainties only.

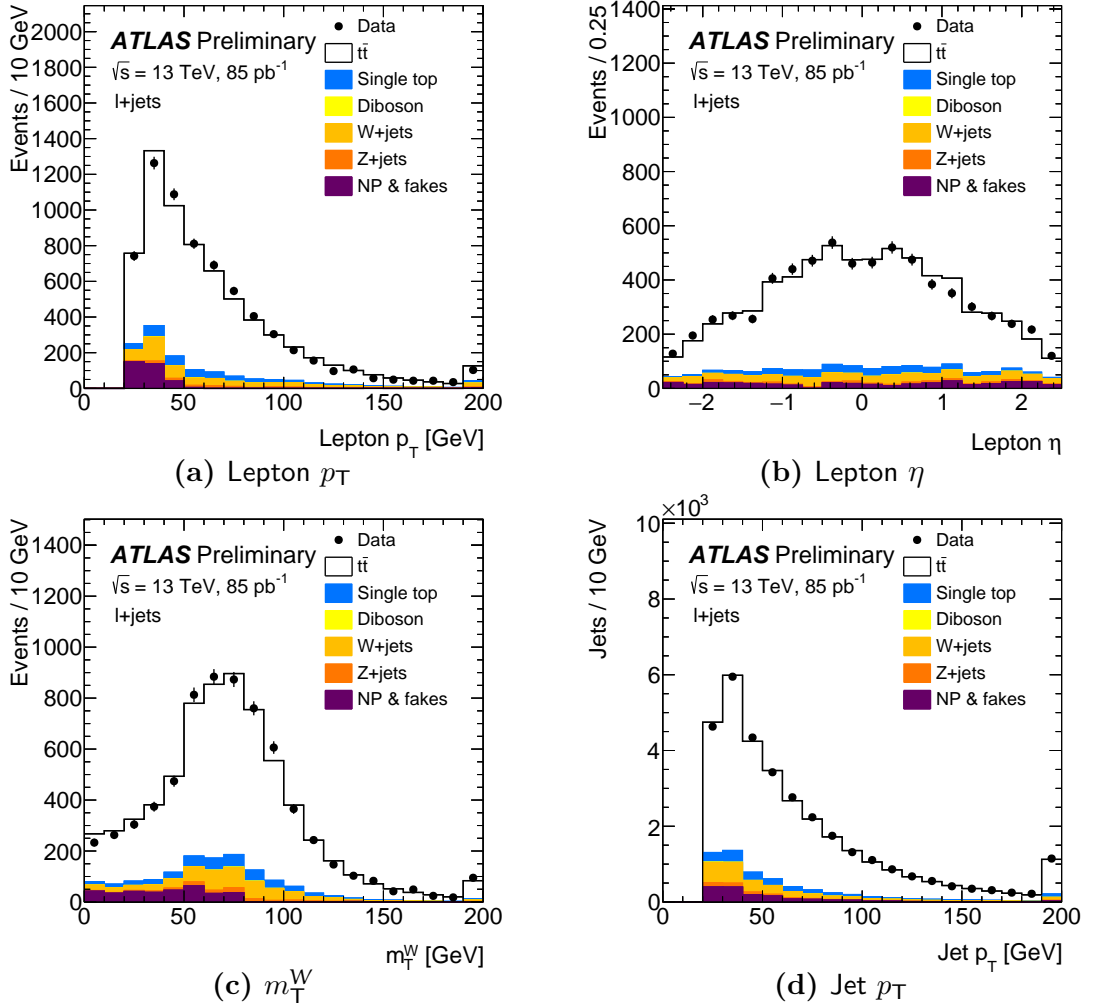


Figure 57: Distributions of selected kinematic control-variables. Shown are (a) the p_T and (b) pseudorapidity η of the lepton, (c) the transverse mass of the leptonically decaying W boson, and (d) the jet p_T . Contributions from the electron and muon channels are combined in this figure.

12.4 Estimation of Background Contributions

For the majority of background sources, the contributions to the selected data are estimated using simulation. Specifically, contributions originating from single top-quark, $Z + \text{jets}$, or diboson production are estimated by applying the event selection procedure on simulated samples generated for the process. The yields obtained

from this procedure are then scaled to cross-section predictions obtained to at least next-to-leading order (NLO) precision in QCD.

Contamination from $W + \text{jets}$ is expected to be the most dominant background contribution. While the distributions of observables for this background type are obtained from dedicated MC samples, the normalisation is estimated using the so-called charge asymmetry method. This technique exploits the fact that the production rate of positively charged W bosons is expected to be about $1/3$ larger than that of negatively charged W bosons at the LHC, see Ref. [191]. Consequently, the fraction of positively charged leptons originating from the $W + \text{jets}$ background is expected to be similarly enhanced. This asymmetry can be quantified using the charge asymmetry observable \mathcal{A}_Q which is defined as

$$\mathcal{A}_Q = \frac{N^+ - N^-}{N^+ + N^-}, \quad (24)$$

where N^+ and N^- are the number of events with a positively or negatively charged W boson, respectively.

The charge asymmetry method for the normalisation of the $W + \text{jets}$ background is based on the assumption that \mathcal{A}_Q is better predicted and modelled by simulation than the overall normalisation in the signal region. A control region which requires exactly zero \mathbf{b} -tagged jets is constructed for the $W + \text{jets}$ background. The ratio of the observed yield $N_{0\mathbf{b}}^{W,DD}$ to the predicted yield $N_{0\mathbf{b}}^{W,MC}$ in the control region is a data-driven data–MC scale-factor. This scale-factor is applied to the predicted yield in the signal region according to

$$N_{\geq 1\mathbf{b}}^{W,DD} = N_{\geq 1\mathbf{b}}^{W,MC} \cdot \frac{N_{0\mathbf{b}}^{W,DD}}{N_{0\mathbf{b}}^{W,MC}}, \quad (25)$$

where $N_{\geq 1\mathbf{b}}^{W,MC}$ is the yield in the signal region predicted from simulation and $N_{\geq 1\mathbf{b}}^{W,DD}$ is the final data-driven $W + \text{jets}$ estimate. With the charge asymmetry method, the data-driven estimate in the control region is calculated using

$$N_{0\mathbf{b}}^{W,DD} = \frac{\left(N_{\text{Data}}^+ - N_{\text{Bgr}}^+\right) - \left(N_{\text{Data}}^- - N_{\text{Bgr}}^-\right)}{\mathcal{A}_Q}, \quad (26)$$

where N_{Data}^\pm are the number of selected data events with a positively or negatively charged W boson respectively, N_{Bgr}^\pm are the number of events expected from non-charge-symmetric background contributions, and \mathcal{A}_Q is the charge asymmetry predicted for the $W + \text{jets}$ processes from simulation. The single-top process is the only other background source expected to have a meaningful contribution to the signal selection that is non-charge-symmetric. Hence, this is the only source considered for N_{Bgr}^\pm . The quantity is extracted from simulation for production in the t - and Wt -channels; production in the s -channel is neglected since it is expected to be very small.

Background contamination originating from non-prompt or fake leptons is estimated using the data-driven matrix method which has already been introduced in Section 11. In the electron channel, the fake and real efficiencies required to extract the fake lepton background are parameterised in terms of the difference in azimuthal angle between the electron and the missing momentum as well as the number of \mathbf{b} -tagged jets. For the muon channel, a parameterisation in terms of the missing transverse energy E_T^{miss} as well as the azimuthal angle between the muon and the missing momentum is chosen.

12.5 Evaluation of Uncertainties

A variety of sources of uncertainty affect the data used to construct the cross-section measurement and the impact of each source must be propagated onto the final measurement result. This is achieved by estimating the effect of each individual source of uncertainty onto the components that enter the cross-section formula, Equation (23), and then recalculating the cross-section using these varied inputs. By doing so, systematic correlations across different components are taken into account. For each source of uncertainty, a new cross-section value is extracted. The deviation of each varied $\sigma_{\bar{t}t}$ w.r.t. the nominal value is calculated. By adding the deviations arising from all effects in quadrature, the total uncertainty on $\sigma_{\bar{t}t}$ is calculated, assuming that the sources of uncertainty are independent. In the remainder of this section, the different sources of uncertainty that are considered will be discussed.

12.5.1 Experimental Uncertainties

Experimental uncertainties are estimated individually for each source from the same simulation samples that are also used to perform the nominal cross-section measurement. However, objects and events are varied according to the effect of each uncertainty. Varied events are processed using the regular analysis procedure and thus reproduce the components of Equation (23) for the (systematically) varied configuration in a natural way.

An uncertainty may affect event scale-factors and therefore just influence the relative importance of each of the selected events. Other sources of uncertainty affect object calibration and thus may modify the four-momentum of objects such as leptons or jets. Hence, the varied event might contain a significantly different object or contain (or miss) objects that are (are not) part of the nominal event. This has cascading effects: a varied, new, or missing object may influence the overlap removal procedure, see Section 8.7, which in turn might further change which objects are reconstructed for an event.

The following sources of experimental uncertainty are considered:

Integrated Luminosity The integrated luminosity \mathcal{L}_{Int} is a direct ingredient of the cross-section extraction procedure. Precise knowledge of \mathcal{L}_{Int} is key to

a precision measurement. For the early data-taking period, however, the uncertainty is quite large at 9%. It is derived following a methodology similar to that detailed in Ref. [192], from a calibration of the luminosity scale using x - y beam-separation scans performed in June 2015. In addition to Equation (23), \mathcal{L}_{Int} is also used to normalise the single top, $Z + \text{jets}$, and diboson predictions which enhances the impact of this source of uncertainty on the total uncertainty of $\sigma_{t\bar{t}}$.

Lepton Uncertainties The modelling of leptons in simulation directly affects the cross-section measurement as it impacts the event selection efficiency for both signal and background.

A variety of lepton modelling properties, such as trigger and identification efficiencies, energy scales and resolutions are studied using data and simulation samples selected for $Z \rightarrow e\bar{e}$ and $Z \rightarrow \mu\bar{\mu}$ decays [145, 193]. Comparisons between data and MC are also used to extract correction factors, to improve modelling of the data by simulation, and calibrations. The associated uncertainties obtained from their measurements are propagated onto the parameters that enter Equation (23).

Similarly, the modelling of the lepton isolation requirements is studied and efficiencies and their uncertainties are extracted in a scheme parameterised in the lepton p_T , η , and the amount of nearby hadronic activity.

Jet Uncertainties Similar to leptons, modelling of jets in simulation affects the measurement through the event selection for signal and background. Since this is an early-data measurement, no studies of the uncertainties on the jet energy scale (JES) and jet energy resolution (JER) using 13 TeV data were available for use. Instead, JES and JER are based on those measured at 8 TeV and extrapolated to 13 TeV [194].

b-Tagging Uncertainties The modelling of b-tagging directly affects the selection efficiency and thus the value extracted for $\sigma_{t\bar{t}}$. The b-tagging properties, notably the efficiency, are taken from simulation. Uncertainties on the b-tagging modelling are determined using prescriptions evaluated using 8 TeV data. Additional uncertainties are added to account for the newly introduced IBL, which improves b-tagging, and the extrapolation to 13 TeV [160].

E_T^{miss} **Uncertainties** The missing transverse energy E_T^{miss} is used by the analysis to discriminate signal events from background contamination. Whenever a detector modelling uncertainty modifies an object — such as a lepton or jet — the momentum balance sum is changed and consequently the E_T^{miss} measurement is adjusted accordingly, see Section 8.6. Therefore, this type of effect is accounted for directly by other detector modelling uncertainties. Additional uncertainty effects related to the modelling of the E_T^{miss} soft-term scale and resolution are applied to signal and background contributions [163].

12.5.2 Signal Modelling Uncertainties

Uncertainties related to the modelling of the signal process are evaluated from signal events generated with variations of the nominal configuration or MC simulation program. The following sources of signal modelling uncertainty are considered:

Modelling of the $t\bar{t}$ Process Uncertainties that arise from the choice of the signal Monte Carlo program are assessed using alternative signal MC samples, see Section 12.2. The correction factor ε is extracted for each sample and the uncertainty is determined from the difference between the cross-section value calculated when using ε from the nominal or the alternative simulation sample, respectively.

While the different signal MC samples used to evaluate the signal modelling uncertainties broadly agree across a wide range of observables, some deviations can be observed. As an example, Figure 58 compares the leading jet p_T distribution obtained from each of the samples. At larger transverse momentum, agreement between the different samples is reasonable. However, there are clear deviations towards smaller jet p_T .

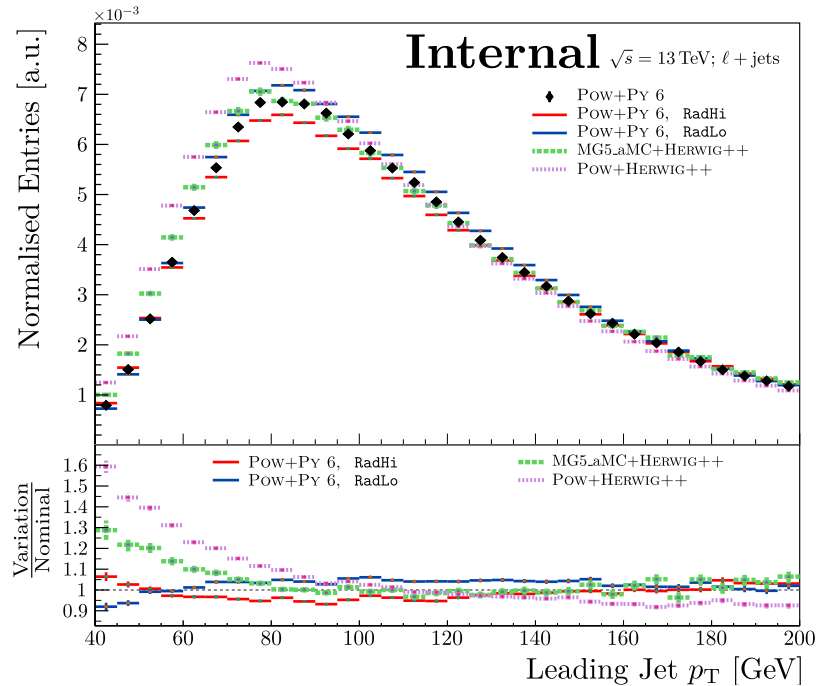


Figure 58: Normalised leading-jet p_T distribution obtained from the $t\bar{t}$ simulation samples used by the measurement. The electron and muon channels are combined. The following abbreviations are used: POW – POWHEG, PY – PYTHIA, RadHi / RadLo – the sample variation with enhanced / reduced radiation activity.

Deviations such as these affect the efficiency correction ε as they modify the object reconstruction efficiencies and therefore the event selection efficiency. They give rise to systematic shifts of ε which are then propagated to the cross-section measurement in a natural way.

Three separate uncertainties are considered:

- The NLO generator uncertainty is estimated as the relative difference between two samples generated with different NLO generators, `MADGRAPH5_aMC@NLO` or `POWHEG`, but processed using the same parton shower and hadronisation, `HERWIG++`.
- An uncertainty related to the modelling of initial- and final-state radiation is evaluated by comparing samples that have increased or reduced radiation activity relative to the nominal sample. The uncertainty is taken as half of the relative difference between the `POWHEG+PYTHIA 6` samples with increased or reduced radiation.
- The shower and hadronisation uncertainty is taken as the relative difference between two samples produced with the same NLO generator, `POWHEG`, but processed with a different parton shower and hadronisation program, `PYTHIA 6` and `HERWIG++`.

Parton Distribution Functions An uncertainty resulting from the limited knowledge of the proton PDFs is evaluated using three different PDF sets, `CT14` [195], `MMHT 2014` [196], and `NNPDF 3.0` [197]. The $t\bar{t}$ signal sample generated with `MG5_aMC + HERWIG++` is used to evaluate the effect of different PDFs and associated uncertainties. An event reweighting scheme is applied using the `LHAPDF` library [198] to construct replicas of the `MG5_aMC + HERWIG++` data which are varied according to uncertainties of the different PDFs — this produces so-called PDF error sets. These replicas are then used to construct systematically varied estimate value for $\sigma_{t\bar{t}}$. Following the `PDF4LHC` prescription [199], the total PDF uncertainty is calculated from these values as half of the envelope which encompasses all three PDF error sets with their uncertainty bands.

The three PDFs listed above were derived using measurements from a variety of experiments, including data from LHC Run 1. Since the measurement presented here is one of the first `ATLAS` measurements of Run 2, the PDF uncertainty is also evaluated using PDFs used for Run 1 measurements. These “old” PDF sets are the `CT10` [25], `MSTW 2008` [190], and `NNPDF 2.3` [200] PDFs. Each of these PDFs is essentially a predecessor to one of the “new” PDFs, for example `CT10` is predecessor to `CT14`. All of the new PDF sets use data from LHC measurements, some including measurements of top-quark physics. This is not the case for the old PDF sets. Comparison of the results obtained using either old or new PDF sets allows to study how the LHC data of Run 1 starts to affect ongoing and new analyses. Figure 59 compares the relative variation of the estimated cross-section $\sigma_{t\bar{t}}$ for the various PDF sets.

Comparing the values obtained from the old PDFs, Figure 59a, to those calculated using the new PDFs, Figure 59b, shows that the overall spread

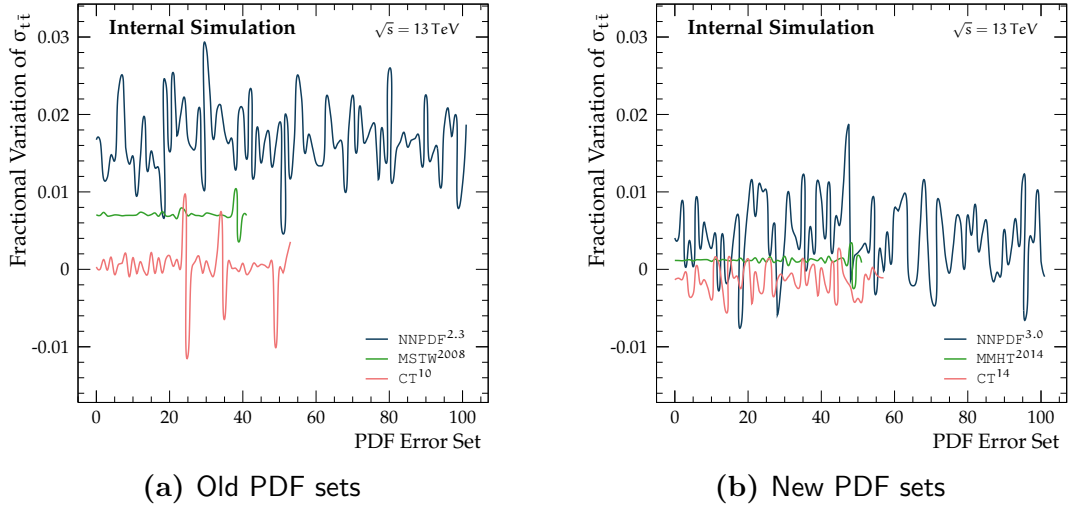


Figure 59: Fractional variation of cross-section value $\sigma_{t\bar{t}}$ using the weights from the PDF error sets as function of PDF error set index. Compared are (a) the values obtained using the old Run 1 PDFs and (b) the new PDF sets for Run 2.

between different PDF families has decreased. Furthermore, the total spread of the different error sets for the CT PDF family, i.e. CT10 and C14, has decreased considerably. The constraints provided by Run 1 LHC measurements have resulted in a reduced uncertainty of PDF modelling. The effect observed when comparing the different parts of Figure 59 can also be quantified through the final PDF uncertainty of $\sigma_{t\bar{t}}$: the PDF uncertainty based on the new PDF sets is about half of the value calculated using the Run 1 default PDFs. In conclusion, precision measurements from Run 1 enable improved precision for Run 2 measurements.

12.5.3 Background Modelling Uncertainties

The subtraction of remnant background contributions is a critical part of the cross-section measurement. Uncertainties on the background estimate directly enter the cross-section calculation and linearly affect the measurement result. The following uncertainties on the background modelling are considered:

Modelling of Single-Top Background Alternative simulation samples are used to estimate the impact of the modelling of the single-top processes. The effect of increased or reduced radiation is evaluated in the same way as is done for the $t\bar{t}$ modelling with alternative samples produced using a similar prescription. Events generated in the Wt -channel at NLO in α_s can have the same final state as $t\bar{t}$ events which results in interference between the two processes. This irreducible higher-order overlap must be accounted for when generating events. The nominal Wt MC sample uses the “*diagram removal*” (DR) scheme which completely removes diagrams with two intermediate top quarks, so-called doubly resonant diagrams, from the NLO Wt calculation [201]. Alternatively, the NLO Wt cross-section can be modified to include a subtraction term which

cancels the $t\bar{t}$ contribution to Wt , this is the so-called “*diagram subtraction*” (DS) scheme. An uncertainty related to the modelling of this interference effect is evaluated by comparing the nominal result to that obtained when using the Wt background prediction from a sample generated with the diagram subtraction scheme.

Furthermore, a normalisation uncertainty is applied to account for the uncertainty on the single-top cross-section calculation. The normalisation uncertainty ranges from 3.6 to 5.3% [44, 46, 47] depending on the specific single-top process.

Modelling of $W + \text{jets}$ Background The charge asymmetry method used to calculate the normalisation of the $W + \text{jets}$ prediction relies on correct modelling of the charge asymmetry \mathcal{A}_Q and the ratio $N_{\geq 1b}^{W,MC}/N_{0b}^{W,MC}$ in simulation. An alternative $W + \text{jets}$ sample generated using POWHEG+PYTHIA 8 is used to evaluate this effect. The parameters are extracted from the alternative sample and the charge asymmetry method is applied using the varied parameters. By taking the difference between the measurement result with the alternative normalisation predictions, the impact of this uncertainty is assessed. Experimental uncertainties affect the $W + \text{jets}$ estimate through the single-top background subtraction and the charge asymmetry value taken from simulation. However, since they are expected to affect events with positive and negative leptons in a similar way, the impact on the $W + \text{jets}$ estimate is expected to be reduced.

Modelling of NP and Fake Lepton Background The NP and fake lepton background is estimated using the data-driven matrix method which requires a choice of efficiency parameterisation. A modelling uncertainty related to this choice is evaluated by varying the parameterisations used by the fake lepton estimate. This is done by dropping one of the variables used for the efficiency parameterisation and recalculating the NP and fake-lepton estimate for each resulting alternative parameterisation. The uncertainty is chosen to be the maximum difference between the different varied background estimates and the nominal estimate.

Modelling of Other Backgrounds An uncertainty of 48% is used for the normalisation of the diboson and $Z + \text{jets}$ backgrounds. This uncertainty combines the base uncertainty on the inclusive cross-section with an additional contribution for each jet required by the signal selection [202, 203]. The base uncertainty is 4% and the additional uncertainty is 24% per required jet of which there are four; the contributions are added in quadrature.

12.5.4 Uncertainty Breakdown

Table 6 lists a summary of all sources of uncertainty considered by the measurement for the combined $\ell + \text{jets}$ channel. In the table, the total analysis uncertainty, the luminosity uncertainty as well as the total resulting uncertainty are listed as well. The

uncertainty on the integrated luminosity is the most dominant single contribution to the total uncertainty followed by the jet energy scale.

Uncertainty	$\Delta\sigma_{t\bar{t}}/\sigma_{t\bar{t}}$ [%]
Data statistics	1.5
$t\bar{t}$ NLO modelling	0.6
$t\bar{t}$ hadronisation	4.1
Initial / final state radiation	1.9
Parton density function	0.7
Single-top cross-section	0.3
Diboson cross-section	0.2
Z + jets cross-section	1.0
W + jets method statistics	1.7
W + jets modelling	1.0
Electron energy scale / resolution	0.1
Electron identification	2.1
Electron isolation	0.4
Electron trigger	2.8
Muon momentum scale / resolution	0.1
Muon identification	0.2
Muon isolation	0.3
Muon trigger	1.2
E_T^{miss} scale / resolution	0.4
Jet energy scale	+10 -8
Jet energy resolution	0.6
b-tagging	4.1
Non-prompt & fake lepton background	1.8
Analysis systematics	+13 -11
Integrated luminosity	+11 -9
Total uncertainty	+17 -14

Table 6: Summary of relative statistical, systematic, and total uncertainties on the measurement of the top-quark pair production cross-section $\sigma_{t\bar{t}}$ performed in the $\ell + \text{jets}$ channel.

12.6 Results

The cross-section measurement is performed in two channels, $e + \text{jets}$ and $\mu + \text{jets}$, separately and in the combined channel. The combined measurement is performed by merging the two datasets prior to the extraction of the variables that enter Equation (23). Table 7 lists the measured cross-sections for each sub-channel as well as the combination. All three cross-section measurements are consistent with each other within their uncertainties. Furthermore, they are consistent with the theoretical cross-section of 832 pb from NNLO+NNLL QCD calculations.

Channel	Measurement Result [pb]	Total Unc. [%]
$e + \text{jets}$	775 ± 17 (stat) ± 123 (syst) ± 85 (lumi)	19
$\mu + \text{jets}$	862 ± 18 (stat) ± 93 (syst) ± 94 (lumi)	15
$\ell + \text{jets}$	817 ± 13 (stat) ± 103 (syst) ± 88 (lumi)	17

Table 7: Summary of the 13 TeV early-data measurements of the $t\bar{t}$ production cross-section $\sigma_{t\bar{t}}$ using the $\ell + \text{jets}$ final state. The listing shows the measurements for each sub-channel separately as well as the combined measurement. The last column lists the total relative uncertainty.

Although the measurement is performed using a small subset of the expected full Run 2 dataset, it can be noted that the statistical uncertainty is already not a limiting factor. Subsequent Run 2 measurements using the same approach can expect an improved precision due to a more accurate luminosity measurement as well as reduced systematic uncertainties as a result of improved calibrations.

The ratio of the production cross-sections extracted from the two different channels can be calculated, taking into account correlated systematic shifts. This results in cancellation of uncertainties and therefore an overall reduction in uncertainty. The ratio is measured to be

$$\frac{\sigma_{tt}^{e+jets}}{\sigma_{tt}^{\mu+jets}} = 0.90 \pm 0.03 \text{ (stat)} \pm 0.10 \text{ (syst)} \pm 0.00 \text{ (lumi)}. \quad (27)$$

The measurement presented here confirms the theoretical predictions. However, it is clearly not a precision measurement and might be regarded instead as an exploratory introduction into 13 TeV top-quark precision measurements. In line with this sentiment, Figure 60 shows a comparison of Run 1 and early-data Run 2 ATLAS measurements of the top-quark pair production cross-section at different centre-of-mass energies. The measurements performed at $\sqrt{s} = 13$ TeV are consistent with the theory prediction and have similar uncertainties.

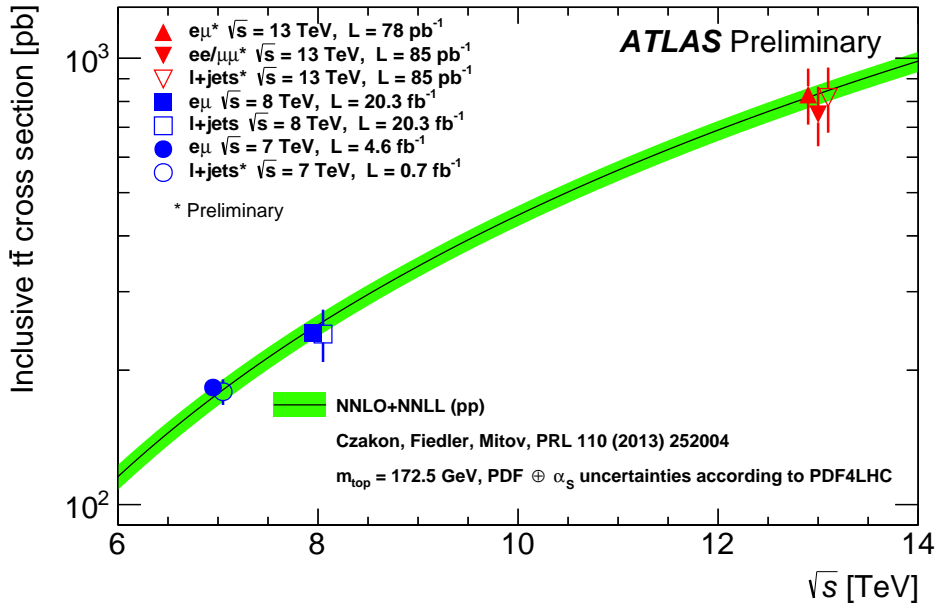


Figure 60: Cross-section for top-quark pair production in proton-proton collisions as function of the centre-of-mass energy \sqrt{s} for LHC energies. Selected results from the ATLAS experiment at $\sqrt{s} = 7, 8, \text{ and } 13$ TeV are shown and compared to the theory prediction with its uncertainty band.

Over the course of Run 2 new measurements are expected to extend this picture and improve upon the precision achieved by the early-data measurements. Indeed, Figure 9 shown in Section 2 depicts a recent comparison, created in late 2017, which includes measurements with larger datasets and improved precision. Yet the measurement presented in this thesis is still part of the figure and has not been superseded.

13 Measuring Colour Flow at 13 TeV

CONTENTS	
13.1	Analysis Strategy 132
13.2	Data and Simulation Samples 133
13.2.1	Measured Data 133
13.2.2	Simulation 133
13.3	Prospects for Measuring Colour Flow 136
13.3.1	Simplified Toy Monte Carlo 137
13.3.2	The Jet Pull 140
13.3.3	Studies at Particle Level 143
13.4	Reconstruction 147
13.4.1	Event Reconstruction and Selection 147
13.4.2	Background Determination 148
13.4.3	Observable Definition and Reconstruction 151
13.4.4	Particle-Level Definition 156
13.5	Unfolding 157
13.6	Treatment of Uncertainties 161
13.6.1	Experimental Uncertainties 162
13.6.2	Signal Modelling Uncertainties 165
13.6.3	Background Modelling Uncertainties 166
13.6.4	Unfolding Procedure Systematic 168
13.6.5	Statistical Uncertainty 168
13.7	Results 169
13.7.1	Comparison with Standard Model Predictions 172
13.7.2	Comparison with Exotic Colour Flow 176
13.7.3	Statistical Correlations 177
13.7.4	Goodness of Fit Tests 178

Colour flow, which has been introduced in Section 3, is a feature of QCD that is predicted to have subtle but measurable effects. Measurements of colour flow probe the fundamental structure of QCD and therefore provide important validation of the theory and phenomenology. Like other features of the theory, modelling of colour-flow effects in simulation must be studied and its accuracy verified. Measured data may also be used to improve modelling of these effects by tuning the simulation to data. The potential use of colour flow as an event-by-event topology-discriminant further motivates the need to understand colour-flow-sensitive variables and their modelling in simulation. Such a discriminant classifies jets based on the colour connections between the partons that seed them, i.e. whether there is a connection or not, and is in principle independent to kinematic quantities which amplifies its potential.

Previous measurements, e.g. in Ref. [85], have found that the accuracy of the modelling of colour flow in simulation varies considerably between MC generators. While predictions broadly agree with data, the deviations are large enough to question how the simulation-dependence of a colour-flow-sensitive discriminant might negatively impact its use. Further measurements of variables sensitive to the colour flow are needed to expand this picture to 13 TeV and motivate tuning efforts. In this section, a measurement of colour flow in $t\bar{t}$ events using quantities derived from the jet-pull vector is presented [204, 205]. The measured quantities are unfolded to particle level,

in order to remove detector effects, and reported as normalised distributions. The unfolded distributions are compared to a selection of simulation-based predictions as part of the measurement. Unfolded distributions can be compared to theoretical predictions in a straightforward manner. The removal of detector effects is crucial for simulation tuning efforts which further motivates the use of unfolding.

The remainder of this section is organised as follows: first, in Section 13.1 the general analysis strategy is presented. Section 13.2 describes the measured and simulated data that are used to perform this measurement. In Section 13.3 a pedagogical introduction to measuring colour flow will be presented and the *jet pull* observable is introduced. The event, object, and observable reconstruction as well as details on the background estimation procedure are the topic of Section 13.4. Section 13.5 presents the unfolding procedure and detector response model used by this measurement and the treatment of uncertainties is discussed in Section 13.6. The measurement results are presented in Section 13.7.

13.1 Analysis Strategy

The goal of the analysis presented here is to measure normalised unfolded distributions of variables that are sensitive to the colour flow of jet pairs in $t\bar{t}$ events. A subset of events in the single-lepton final state is used, as the corresponding topology contains two jets that originate from a colour singlet, the hadronically decaying W boson, and two jets which are not expected to be colour-connected. This will be discussed in detail in the next section. Distributions measured from data are corrected for detector effects through unfolding to particle level, see Section 9. The unfolded distributions are the measurement result. Using these results, comparisons of the data to various theoretical predictions taken from simulation are performed.

Roughly, the analysis strategy operates according to the following recipe:

- 1) An event selection is applied to measured data in order to obtain a dataset enriched in $t\bar{t}$ events in the single-lepton final state.
- 2) Observables that are sensitive to the colour flow in the $t\bar{t}$ topology are constructed from the selected data.
- 3) Background contributions are estimated using a combination of simulation and data-driven estimates. The contributions of background sources to the distributions of the observables measured in data are subtracted. This yields the estimated signal distributions for each observable.
- 4) The effects of the finite acceptance and efficiency as well as the response of the detector on the analysis observables are estimated using simulation. This builds a detector-response model for each of the observables.
- 5) The signal distributions estimated from data are unfolded to particle level using the detector-response model. These unfolded distributions are normalised

and the impact of various sources of uncertainty from the measurement is estimated.

- 6) The unfolded data is reported as the measurement result along with the covariance matrix obtained from evaluation of the uncertainties. In addition, the unfolded distributions are compared to predictions obtained from simulation at particle level and the agreement is quantified.

13.2 Data and Simulation Samples

Properties of the measured data as well as the configurations used to create samples of simulated data are the topic of this section.

13.2.1 Measured Data

The measurement presented in this section is performed with data collected by ATLAS in 2015 and 2016 during pp collision runs provided by the LHC at a centre-of-mass energy of $\sqrt{s} = 13$ TeV. The data were collected in pp collisions at a bunch spacing of 25 ns. Requirements imposing stable beams and a fully operational detector are applied. The data correspond to an integrated luminosity of $\mathcal{L}_{\text{Int}} = 36.1 \text{ fb}^{-1}$ after applying data-quality requirements. Single-electron or single-muon triggers are used to preselect the data. At these operating conditions, each triggered event contains combined detector signal from on average 14 (25) additional inelastic pp collisions for the 2015 (2016) dataset.

13.2.2 Simulation

Simulation samples are used by the measurement for a variety of purposes: simulation is used to estimate the contributions of background processes to the signal event-selection, to perform comparisons with the measured data, and to obtain a description of how the detector response affects the observables that are measured. Additional simulation studies are used to investigate potential analysis observables and their efficacy. The simulation follows the procedures discussed in Section 7 and the different samples used by the measurement are summarised in Table 8. In all simulation samples the top-quark mass m_t is set to 172.5 GeV. Heavy-flavour decays are simulated using the EVTGEN v1.2.0 program [183] in all samples except those generated with SHERPA.

§1. Nominal Signal Sample Among the MC simulation samples that are generated for the $t\bar{t}$ signal process one sample is selected to be the “nominal” sample. This sample is used to predict the number of signal events that pass the event selection, to evaluate the agreement of data with simulation, and to obtain the nominal detector-response description. Furthermore, it is used for the treatment of various sources of uncertainty, in particular those relating to experimental effects.

Consistent with other ATLAS top-quark physics measurements, the nominal $t\bar{t}$ simulation sample is generated using the POWHEG-BOX v2 [166–168] event generator.

Process	Generator	Type	Version	PDF	Tune
$t\bar{t}$	POWHEG-BOX v2 [166–168] +PYTHIA 8 [169] +EvtGEN [183]	NLO ME +LO PS +HF decays	r3026 v8.186 v1.2.0	NNPDF 3.0 [197] NNPDF 2.3 [200] –	– A14/A14.v1 [†] /A14.v3c [†] [206] –
$t\bar{t}^\dagger$	POWHEG-BOX v2 +HERWIG 7 [207] +EvtGEN	NLO ME +LO PS +HF decays	r3026 v7.0.1.a v1.2.0	NNPDF 3.0 MMHT 2014 [196] –	– H7UE –
$t\bar{t}^\dagger$	MG5_aMC [185] +PYTHIA 8 +EvtGEN	NLO ME +LO PS +HF decays	v2.3.3.p1 v8.112 v1.2.0	NNPDF 3.0 NNPDF 2.3 –	– A14 –
$t\bar{t}^*$	POWHEG-BOX v2 +PYTHIA 6 [180] +EvtGEN	NLO ME +LO PS +HF decays	r2819 v6.428 v1.2.0	CT10 [25] CTEQ6L1 [181] –	– PERUGIA 2012 [182] –
$t\bar{t}^*$	SHERPA [186–188]	LO/NLO multileg ME+PS	v2.2.1	NNPDF 3.0	Default
Single top	POWHEG-BOX v1 +PYTHIA 6 +EvtGEN	NLO ME +LO PS +HF decays	r2819 v6.425 v1.2.0	CT10 CTEQ6L1 –	– PERUGIA 2012C –
WW, WZ, ZZ	SHERPA	LO/NLO multileg ME+PS	v2.1.1	CT10	Default
W/Z + jets	SHERPA	LO/NLO multileg ME+PS	v2.2.1	NNPDF 3.0	Default
$t\bar{t}W/Z$	MG5_aMC +PYTHIA 8 [208] +EvtGEN	NLO ME +LO PS +HF decays	v2.3.3 v8.210 v1.2.0	NNPDF 3.0 NNPDF 2.3 –	– A14 –
$t\bar{t}H$	MG5_aMC +PYTHIA 8 +EvtGEN	NLO ME +LO PS +HF decays	v2.2.3.p4 v8.210 v1.2.0	NNPDF 3.0 NNPDF 2.3 –	– A14 –

Table 8: Monte Carlo samples used for the colour-flow measurement presented in this thesis. The first part of the table shows samples generated for the signal process, the second those for processes considered to be a background. Samples / tunes marked with \dagger refer to alternative signal MC samples used to evaluate signal modelling uncertainties, those marked with \star are used for comparison to the measurement result. The following abbreviations are used: *ME* – matrix element; *PS* – parton shower; *LO* – leading-order calculation in QCD; *NLO* – next-to-leading order calculation in QCD; *PDF* – parton distribution function; *HF* – heavy flavour; *Tune* – refers to a specific setting of configurable parameters of the MC generator.

The value of the h_{damp} parameter — which controls the p_T of the first emission beyond the LO configuration in POWHEG — is set to $1.5 m_t$. Hard-scatter events generated with POWHEG are further processed with PYTHIA 8 [169] to simulate the parton shower (PS), hadronisation, and underlying event. The nominal sample is listed in the first row of Table 8.

§2. Alternative Signal Samples Additional $t\bar{t}$ samples are generated to evaluate the impact of systematic uncertainties that are related to modelling of the signal process. These alternative samples and tunes are marked with the \dagger symbol in Table 8. The impact of the choice of the hard-scatter generator or the PS / hadronisation algorithm is estimated using two samples generated with alternative MC programs: for each sample, one of the components, ME generator or PS / hadronisation algorithm, is replaced by a different choice. For the hard-scatter generator the

substitute is `MADGRAPH5_aMC@NLO` (`MG5_aMC`) [185] while `HERWIG 7` [207] is used as second PS / hadronisation algorithm.

To assess the impact of increased or reduced radiation, variations of the configuration used for the nominal $t\bar{t}$ sample are used [209]:

for enhanced radiation $h_{\text{damp}} = 3 \cdot m_t$, renormalisation and factorisation scales are set to half their nominal values, and the `A14.v3c` up tune variation is used;

for reduced radiation $h_{\text{damp}} = 3/2 \cdot m_t$, renormalisation and factorisation scales are set to twice their nominal values, and the `A14.v3c` down tune variation is used.

Similarly, two samples generated with the `A14.v1` tune variations are used to assess the impact of colour reconnection. These variations modify `PYTHIA` simulation parameters which configure the strength of the colour-reconnection mechanism as well as the strength of the strong coupling constant α_s in multi-parton interactions. The nominal values for h_{damp} and the renormalisation and factorisation scales are used by `A14.v1`.

To facilitate comparison with a more diverse range of simulation-based predictions, two additional simulation configurations are used to generate $t\bar{t}$ signal. These samples are marked with the \star symbol in Table 8. One sample is generated using `POWHEG-Box v2` — with h_{damp} set to the top-quark mass — interfaced to `PYTHIA 6` to simulate the PS, hadronisation, and underlying event. The second sample is generated using `SHERPA` [186–188] which combines ME and PS calculations in a single MC program.

Signal MC simulation samples are normalised to a cross-section of 832^{+46}_{-51} pb. This theoretical cross-section is calculated to NNLO order in perturbative QCD including resummation of NNLL soft-gluon terms. More details are given in Section 2.2. Normalised signal MC simulation is used to estimate the signal contribution to the event selection and for comparison of the observed data to the prediction.

§3. Background Samples Contaminations originating from processes that are not considered to be signal by this measurement are in most cases modelled using simulation. The second part of Table 8 gives a detailed listing of the various background simulation samples categorised by their production process. As part of the measurement, background contributions are subtracted from data in order to obtain only the contribution considered as signal. This requires that the background samples are properly normalised to the cross-sections corresponding to their production process. All background MC simulation samples are normalised to theoretical cross-sections that are obtained to at least NLO precision in QCD [44, 46, 47, 210–215].

§4. Pile-Up Simulation The effect of multiple overlaid pp collisions, so-called pile-up, is considered by combining the events generated according to the desired production process with events generated for the pile-up. Events for the pile-up contributions are generated using the soft QCD processes of `PYTHIA 8.186` [169]

using the A2 [189] tune and the MSTW2008LO PDF set [190]. This procedure fixes the average number of interactions for the simulation sample at the time it is generated. However, in measured data this quantity follows a stochastic process whose properties are determined by the operating conditions of the colliding beams. A reweighting procedure is applied to the simulation samples on an event-by-event basis such that the distribution of the average number of pp interactions reflects the conditions observed in data.

§5. Detector Simulation The generated events are processed further using the ATLAS detector and trigger simulation [128] in order to simulate the interactions between particles and detector material, simulate the detector readout, and to provide simulated triggering information — see Section 7.4 for more details. Samples used to construct the nominal prediction, i.e. all background samples as well as the nominal $t\bar{t}$ sample, are generated using the full detector simulation. The alternative $t\bar{t}$ simulation samples are instead processed using the fast detector simulation.

§6. Signal Sample with Exotic Colour Flow A $t\bar{t}$ sample with exotic colour flow is generated according to the prescription discussed in Section 10. In this measurement, the sample with exotic colour flow is also labelled (*colour-*)*flipped*.

For this sample $t\bar{t}$ events are generated in final states with at least one lepton and the hadronically decaying W boson (if it exists) is *ad hoc* replaced by a colour octet. Events are generated with POWHEG and use PYTHIA 8 for the PS, hadronisation, and underlying event — just like the nominal $t\bar{t}$ sample. Likewise, the configurations of POWHEG as well as PYTHIA 8 are taken to be exactly the same as for the nominal $t\bar{t}$ sample. This minimises differences w.r.t. the regular SM prediction. The sample with exotic colour flow is processed using the fast detector simulation, just like the alternative $t\bar{t}$ samples used for the treatment of systematic uncertainties. The colour-flipped sample is primarily used for two purposes:

- i) to study the sensitivity of the measured observables to the colour flow, and
- ii) to compare measured unfolded distributions to predictions taken from $t\bar{t}$ simulation with exotic, i.e. non-SM, colour flow.

Furthermore, when comparing the measured data to the prediction obtained from the sample with exotic colour flow, the colour model itself is considered as a source of modelling uncertainty. This uncertainty is evaluated using the sample with exotic colour flow, the procedure will be discussed further in Section 13.6.

13.3 Prospects for Measuring Colour Flow

For an introduction to the prospects of studying and measuring colour flow in $t\bar{t}$ events, a simpler event topology is considered first. Specifically, this topology corresponds to proton–proton collisions which produce di-jet events where the intermediary may be either a colour singlet or a colour octet — symbolically: $pp \rightarrow X \rightarrow q\bar{q}$ (\rightarrow jet jet).

The resulting event (colour) structure is shown in Figure 61. In the Standard Model, a potential colour-singlet intermediary would be a Z or Higgs boson while the gluon is a colour-octet intermediary.

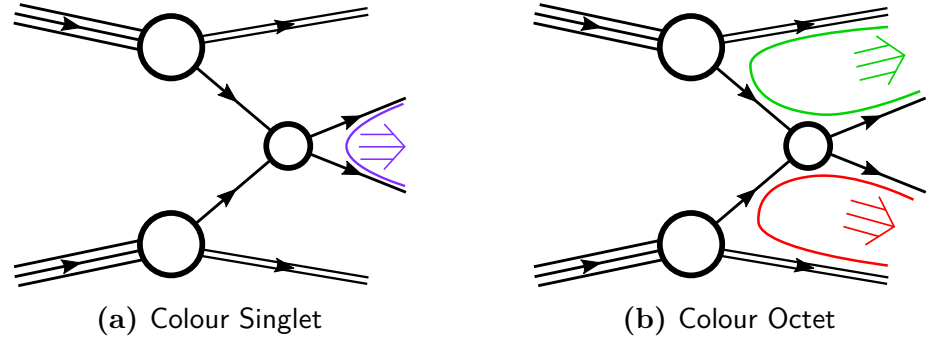


Figure 61: Pictographic representations for possible colour connections in $pp \rightarrow X \rightarrow q\bar{q}$ events where X may either be (a) a colour singlet (“signal”) or (b) an octet (“background”). Coloured lines denote colour connections, coloured arrows the area with expected enhanced radiation. Illustration inspired by material in Ref. [80].

Furthermore, a simplified toy Monte Carlo simulation will be used. Specifics of the toy MC simulation will be explained in Section 13.3.1.

13.3.1 Simplified Toy Monte Carlo

For a simplified toy MC simulation, the hard-scatter event with its kinematics and colour connections is set explicitly for every event rather than being simulated through ME calculations. Furthermore, the intermediate particle X is ignored and instead colour connections are traced explicitly. Hence, the hard-scatter final state consists of four particles: the two quarks $q\bar{q}$ and the two beam-remnant particles. The two quarks from the hard-scatter final state are either colour-connected to one another (effectively X is a colour singlet) or to the beam remnants (effectively X is a colour octet).

The PYTHIA 8 program is used to apply its parton showering and hadronisation algorithms to the fixed parton configuration. Furthermore, the outgoing quarks of the hard-scatter event are defined to be b quarks. They are placed at $(y, \phi) = (0, \pm 1)$ in rapidity–azimuth space, each with $p_T = 200$ GeV. The beam remnants are at $y \sim -\pm \infty$. A detector simulation is not considered. The overall procedure is inspired by, and similar to, the procedure used in Ref. [80].

The toy simulation cannot be used as ingredient of a measurement since the partonic initial state of the hard-scatter event is unphysical.¹ However, the parton shower and hadronisation are simulated properly using PYTHIA. The toy simulation can be used to understand how the PS and hadronisation react to different kinds of colour flow. Furthermore, it may be used to understand potential observables that encode colour structure better.

¹ In addition, several sanity checks performed by PYTHIA must be disabled in order for the procedure to work.

Figure 62 shows radiation density maps obtained when the radiation from many repeated applications of PYTHIA to the same fixed hard-scatter event is combined. Figure 62a depicts the scenario where the two b quarks are colour connected to one another, while Figure 62b shows the scenario where they are connected to the corresponding beam particle.

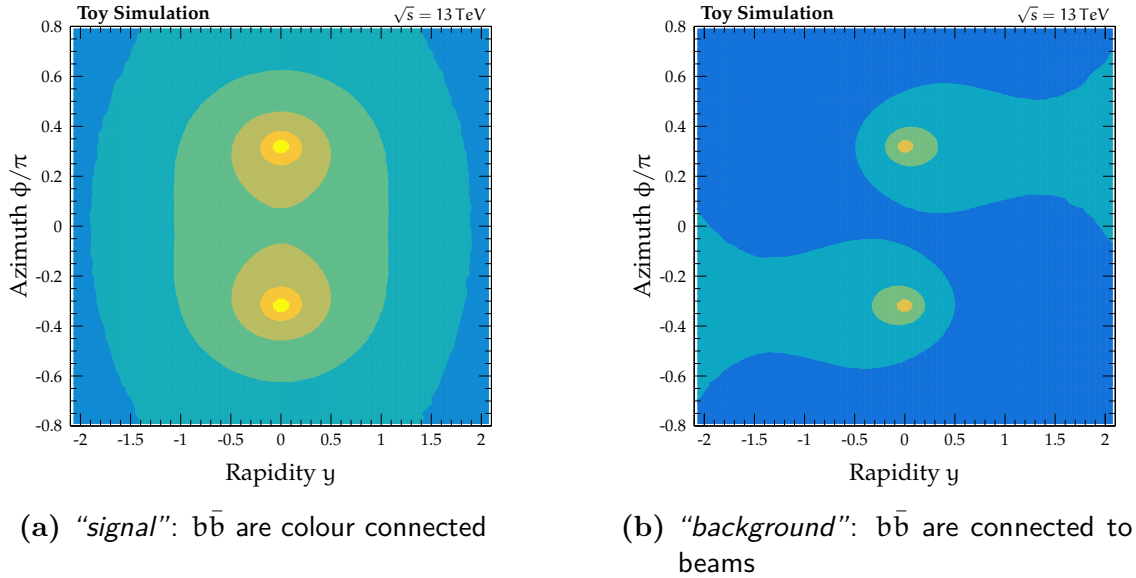


Figure 62: Radiation density map, i.e. accumulated p_T , after repeated showering of a fixed initial parton phase-space point 20 million times. Shown are a partonic initial state where (a) two b quarks are colour connected and (b) two b quarks are colour connected to the beam particles. Different contours denote a change in the radiation density by a factor of ten.

A clear structure encoding the colour connections can be identified: the radiation around each of the two b -jets is enhanced in the direction of its colour-connection partner. When the two b quarks are colour connected, each resulting jet tends to shower towards the other b quark. Conversely, the radiation tends to be skewed towards the closest (and colour connected) beam particle otherwise. Radiation that emanates from one end of the colour dipole is pulled towards the other end of the colour dipole defined by the colour connection.

Ideally, an observable that encodes colour flow is constructed such that it condenses the information from the global event shape difference that is apparent in Figure 62 into a single variable. Given such a variable, further studies and measurements can be performed. In addition, the observable may be used to distinguish whether the radiation pattern of the process $X \rightarrow q\bar{q}$ originates from a state X that is a colour singlet or colour octet. Typically, the singlet case would be considered “signal-like” while the octet case would be considered a “background-like” configuration — as in Figure 62a and Figure 62b, respectively.

However, constructing a local observable which uses only information obtained from either one or two jets has a number of advantages over a global event shape variable. Foremost, since it can be constructed for a sub-region of an event, it is a more generic

tool that can be used with a multitude of event topologies. Additionally, jets are relatively commonplace objects and are generally better understood than event-shape variables. This also implies that calibrations are expected to be of high quality. The work presented here concentrates on constructing a colour-flow observable using the event sub- and superstructure defined by at most two jets.

The toy-approach with a fixed position of the $b\bar{b}$ partons is very convenient for better understanding of how the colour connections shape subsequent radiation. However, the fixed placement is problematic for subsequent studies. Since all four participating partons — i.e. the two b quarks and the two beam particles — are always at the same location, the coordinates of event superstructure (global coordinate system) and local substructure (coordinate system of one jet w.r.t. to the other) are equivalent. In other words, even when the two jets do not originate from partons which are colour connected, an enhancement in radiation will always be at the same location w.r.t. the di-jet coordinate system. This can be mitigated by placing the two b quarks randomly on an event-by-event basis. A copy of the above “*signal*” and “*background*” toy-event definitions is defined: the two b quarks are placed at a random orientation on opposing sides of a circle with radius $r = 1$ that is centred on the coordinate origin in y - ϕ space. The resulting radiation density maps are shown in Figure 63.

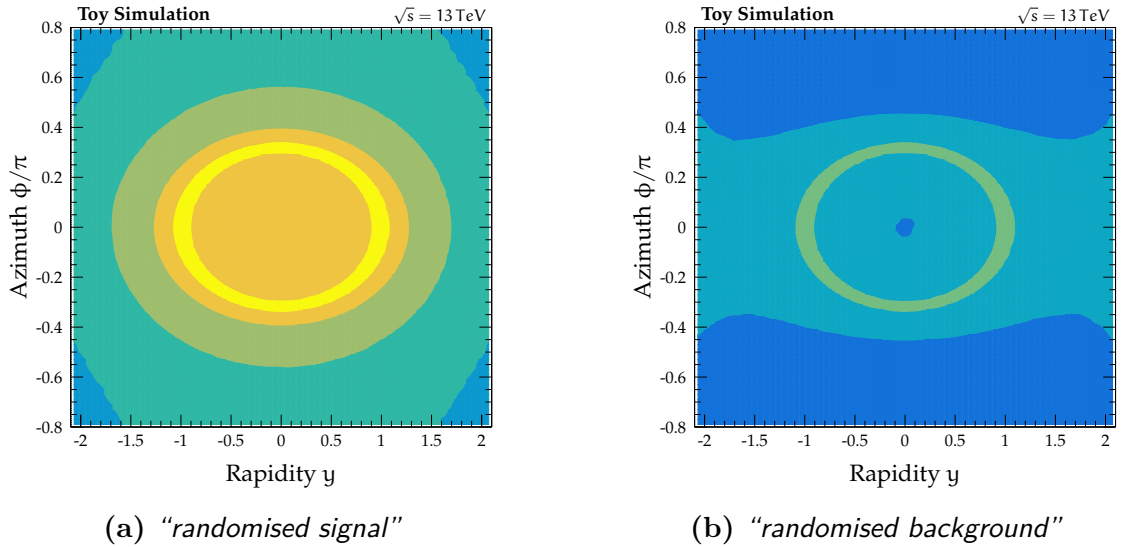


Figure 63: Radiation density map, i.e. accumulated p_T , after repeated showering of a fixed-configuration, randomised-location initial parton phase-space point 20 million times. Shown are a partonic initial state where (a) two b quarks are colour connected and (b) two b quarks are colour connected to the beam particles. Different contours denote a change in the radiation density by a factor of ten.

As a result of the random orientation of the $b\bar{b}$ system, the two b quarks can no longer be identified as “poles” in the radiation density maps. In comparison to the initial configuration, the colour connections are less apparent in Figure 63.

13.3.2 The Jet Pull

An observable predicted to encode colour information about a jet is the jet-pull vector $\vec{\mathcal{P}}$ [80], a p_T -weighted radial moment of the jet. For a given jet j with transverse momentum p_T^j , the observable is defined as

$$\vec{\mathcal{P}}(j) \equiv \sum_{c \in j} \frac{|\vec{r}_c| \cdot p_T^c}{p_T^j} \cdot \vec{r}_c. \quad (28)$$

The summation in Equation (28) runs over the constituents c of the jet j which have transverse momentum p_T^c and are located at $\vec{r}_c = (\Delta y_c, \Delta \phi_c) = \vec{c} - \vec{j}$, i.e. the offset of the constituent from the jet axis $\vec{j} = (y_j, \phi_j)$ in y - ϕ space. Using the rapidity y instead of the pseudorapidity η makes the vector \vec{r}_c invariant under boost and is expected to improve discriminant power of the pull-vector observable [80].

The jet-pull vector $\vec{\mathcal{P}}$ is an IRC safe quantity which is an important property for an observable, see Section 8.5. If a very soft particle is added to j , and thus the summation in Equation (28), its impact on $\vec{\mathcal{P}}$ is weighted by its p_T . Since the constituent's p_T is negligible compared to p_T^j , the soft particle has a negligible contribution to $\vec{\mathcal{P}}$. If a particle splits into two collinear particles at the same \vec{r}_c , the pull vector remains unchanged as it itself is linear in p_T^c and \vec{r}_c . In addition to making the observable more stable and well-behaved from a theoretical perspective, these properties also ensure that the jet-pull vector is fairly insensitive to specifics of the detection system, such as granularity or energy resolution, and the jet clustering.

The constituents considered by the summation in Equation (28) do not necessarily have to be the actual constituents used to cluster the jet. Naturally, the reconstructed objects must have sensitivity to the radiation emitted in the decay, shower, and hadronisation of the hard object. Furthermore, they must be associated to the jet using an appropriate association scheme. This allows use of calorimeter clusters or tracks from the detector or (appropriately chosen) truth particles for simulation.

Given two jets j_1 and j_2 , the jet-pull vector $\vec{\mathcal{P}}(j_1)$ can be used to construct another observable: the jet-pull angle $\theta_{\mathcal{P}}(j_1, j_2)$. Both quantities are illustrated in Figure 64 for an idealised di-jet system. The jet-pull angle $\theta_{\mathcal{P}}(j_1, j_2)$ is defined by Equation (29). It is defined as the angle between the jet-pull vector $\vec{\mathcal{P}}(j_1)$ and the vector connecting j_1 to another jet j_2 in y - ϕ space, $(y_{j_2} - y_{j_1}, \phi_{j_2} - \phi_{j_1}) = \vec{j}_2 - \vec{j}_1$, the so-called jet-connection vector.

$$\theta_{\mathcal{P}}(j_1, j_2) \equiv \angle(\vec{\mathcal{P}}(j_1), \vec{j}_2 - \vec{j}_1) \quad (29)$$

The jet-pull angle relates the local colour-structure information of j_1 — which is encoded in the jet-pull vector $\vec{\mathcal{P}}(j_1)$ — to the global superstructure of the two jets. It is expected to be symmetric around zero and takes values ranging from $-\pi$ to π .

It is therefore convenient to consider the normalised absolute jet-pull angle $|\theta_{\mathcal{P}}|/\pi$ instead. The jet-pull angle is not commutative w.r.t. exchange of j_1 and j_2 , i.e. in general $\theta_{\mathcal{P}}(j_1, j_2) \neq \theta_{\mathcal{P}}(j_2, j_1)$. This is a result of the fact that the two pull angles are calculated using different jet-pull vectors, which *a priori* are independent.

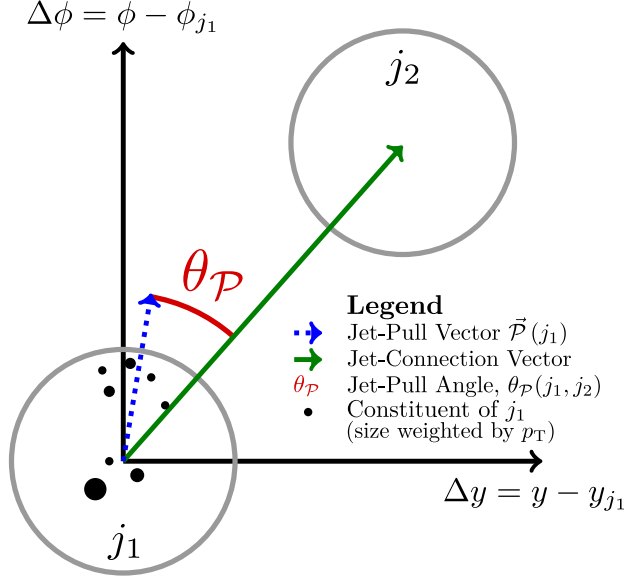


Figure 64: Illustration of jet-pull observables for an idealised di-jet system. For a jet j_1 the jet-pull vector (blue dashed) is calculated using an appropriate set of constituents (for example tracks, calorimeter clusters, or truth particles). The variable of particular sensitivity to the colour structure of j_1 with respect to j_2 is the jet-pull angle (red), which is the angle between the pull vector for j_1 and the vector connecting j_1 to another jet j_2 in localised y - ϕ space (green).

The jet-pull angle is particularly suited for studying the colour structure of an object decaying or splitting into a di-jet system — such as a W , Z , or H IGGS boson, or a gluon. In this situation, the inputs into the calculation are well-defined through the desired topology and the observable is expected to be sensitive to the presence or absence of a colour connection.

For a system of two colour-connected jets, it is expected that $\vec{\mathcal{P}}$ is aligned with the jet-connection vector and therefore $\theta_{\mathcal{P}} \sim 0$. If $\theta_{\mathcal{P}}$ is calculated for two jets without any particular colour connection, the jet-pull vector and the connection vector are not expected to have any prior alignment and thus $\theta_{\mathcal{P}}$ is expected to be distributed uniformly.

The jet-pull vector is constructed for each event from the toy simulation data and averaged across all events. Figure 65 shows the radiation density maps with the averaged jet-connection vector and jet-pull vector overlaid. Shown are the non-randomised “*signal*” and “*background*” scenarios of the toy simulation. As expected, the jet-pull vectors are aligned with the jet-connection vector or the beam-axis depending on the colour-connection scenario.

Using the jet-pull vectors and jet-connection vector, the jet-pull angle is constructed for all events from the different scenarios of the toy simulation. Figure 66 compares the pull angle distributions for three cases: the non-randomised *colour connected* and *connected to beam* scenarios as well as the randomised variant of the *connected to beam* scenario.

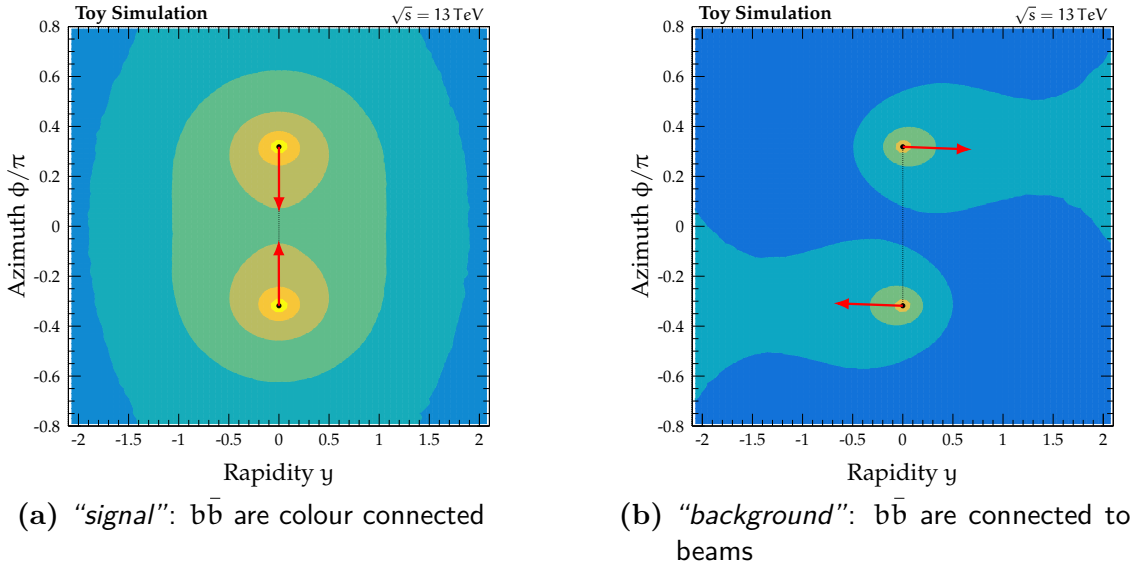
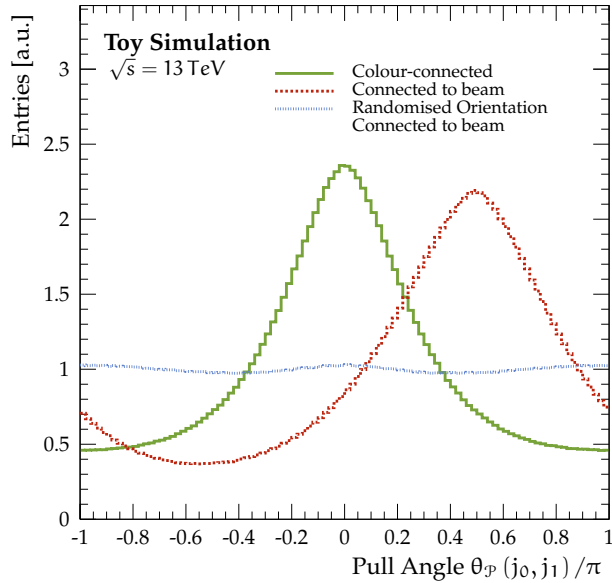


Figure 65: Radiation density map constructed in the same way as Figure 62. Shown are a partonic initial state where (a) two b quarks are colour connected and (b) two b quarks are colour connected to the beam particles. Overlaid are the averaged jet-centres (black dot), jet-connection vector (dotted line), and jet-pull angles (red arrows).

Figure 66: Distributions of jet-pull angle $\theta_{\mathcal{P}}(j_0, j_1)$ obtained for three different configurations of the toy Monte Carlo. The jet j_0 (j_1) is built from stable particles in a cone of $\Delta R = 0.5$ around the b (\bar{b}) quark of the partonic hard-scatter event. Two configurations with fixed placement and orientation of the b quarks are used (green solid and red dashed) and one configuration with a randomised orientation of the di- b -system is used (blue dotted).



The predicted behavior can be observed: for the *colour connected* scenario, the distribution peaks at $\theta_{\mathcal{P}} \sim 0$ and has minima at ± 1 . A similar shape is found for the non-randomised *connected to beam* scenario, albeit the peak is shifted to $\sim 1/2$. The shape is a result of the fact that jet-pull vectors are still aligned with one another through the fixed placement of the initial state.

This is precisely the reason for constructing the randomised scenarios. Indeed, the flat distribution expected from a case where the two initial quarks are not colour connected can be found for the randomised *connected to beam* scenario. This illustrates that other effects that align the jet-pull vector with the jet-connection vector can in principle imitate presence of a colour connection. However, for realistic topologies no such effects are expected.

13.3.3 Studies at Particle Level

The toy MC simulation is useful for getting a general feeling of the colour connections and how they affect radiation patterns. However, meaningful studies to be used for designing a measurement should be evaluated using a more realistic simulation. The sensitivity achieved with the toy simulation is no real indication of real-world sensitivity. A particle-level analysis is implemented using the `Rivet` analysis framework [171].² This analysis is used to study the $t\bar{t}$ simulation samples previously discussed in Section 13.2.2.

The analysis applies a simple event selection requiring exactly one lepton and at least four jets. At least two jets must be tagged to have likely originated from a b -hadron. Furthermore, the missing transverse energy E_T^{miss} must exceed 20 GeV. This selection transfers well to a subsequent detector-level event selection that, when applied on data, selects a dataset rich in $t\bar{t}$ events in the single-lepton final state.

The topology of the single-lepton $t\bar{t}$ final state contains four jets. Using b -tagging information, these jets can be identified to originate either from the $t \rightarrow Wb$ decay or from the decay of a W boson. In the former case, the jet's colour flow originates from a colour-charged object, the top quark, while in the latter case, it originates from a colour singlet.

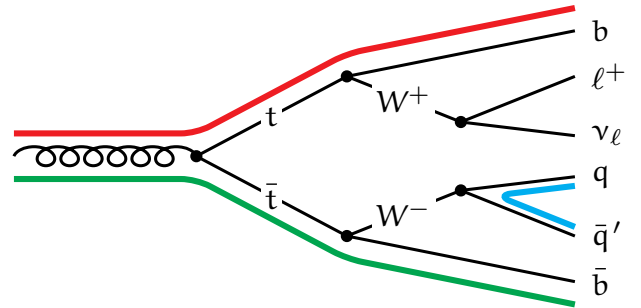


Figure 67: Illustration of $t\bar{t}$ event in the single-lepton final state with typical colour connections (symbolised by thick coloured lines).

Jets from these categories are expected to be sensitive to colour flow that is significantly different for the two categories. Figure 67 illustrates the colour connections typically present in the $t\bar{t}$ topology for the single-lepton final state.

The two jets from the $W \rightarrow q\bar{q}'$ decay are sensitive to well-defined colour flow: they have a direct connection. Based on the fact that this category resembles a signal process which could be selected using colour-flow information, it is labelled “*signal colour flow*”. This category is expected to probe colour flow of two jets originating from colour-connected quarks. Through the top-quark decay, the two jets from the b quarks are sensitive to the colour flow of the gluon initial-state. However, this connection is more large-scale and less well-defined. In this spirit, it is labelled “*spurious colour flow*”. The colour flow that these jets are sensitive to is similar to two non-colour-connected jets. Table 9 summarises these definitions and illustrates the colour flow for the two categories.

² Refer to Section 9.1 for a discussion of the particle level.

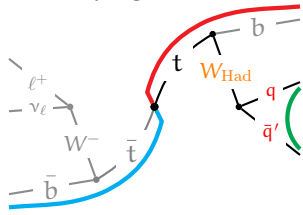
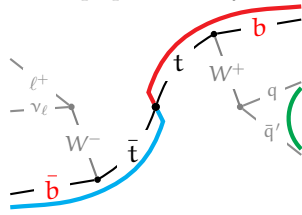
Target colour flow	Signal colour flow (j_1 and j_2 are colour connected)	Spurious colour flow (j_1 and j_2 are not colour connected)
Hard-scatter target	Daughters of hadronically decaying W boson 	b-quarks from top-quark decay 
	Jet assignment	
	j_1^W : leading- p_T non- b -tagged jet j_2^W : 2 nd leading- p_T non- b -tagged jet	j_1^b : leading- p_T b -tagged jet j_2^b : 2 nd leading- p_T b -tagged jet

Table 9: Summary of the jet-pairing definitions.

The most straightforward algorithm for assigning jets to the latter category associates the two highest- p_T b -tagged jets with the $t \rightarrow Wb$ decay. For simplicity, the two highest- p_T non- b -tagged jets are associated with the $W \rightarrow q\bar{q}'$ decay. Figure 68 compares the jet-pull angles for both categories extracted from SM $t\bar{t}$ simulation to those obtained from the simulation with exotic colour flow.

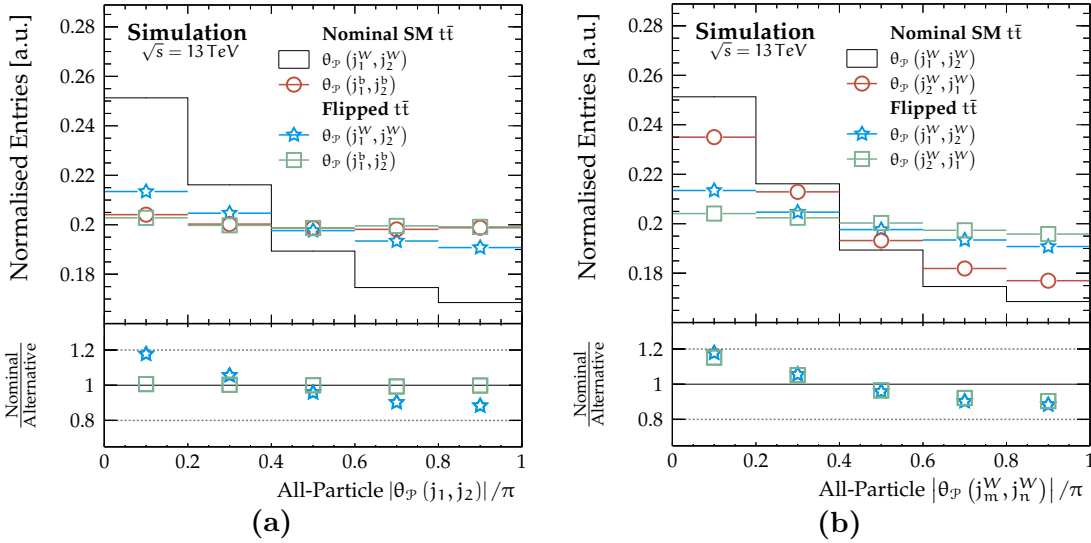


Figure 68: Comparison of jet-pull angle distributions taken from regular SM $t\bar{t}$ simulation and $t\bar{t}$ simulation with exotic colour flow. Compared are (a) the pull angle sensitive to “signal colour flow” with the pull angle sensitive to “spurious colour flow” and (b) the pull angles from the W boson daughters.

In particular, Figure 68a shows that distributions for “signal colour flow” are subtly sloped while those for “spurious colour flow” are flat by comparison. Furthermore, the variables constructed from the W jets can discriminate between the SM colour flow and the exotic colour-flow scenarios. Distributions obtained using the b -tagged jets are essentially flat for both scenarios, i.e. they are insensitive to the difference between the SM and exotic colour flow. Figure 68b shows that the jet-pull vector from either the leading- or sub-leading- p_T jet may be used to construct a colour-flow discriminating jet-pull angle observable. However, the pull angles constructed from

the jet-pull vector of the sub-leading jet are slightly less capable of discrimination than those from the leading jet.

The magnitude of the jet-pull vector $|\vec{\mathcal{P}}(j)|$ is another derived scalar quantity one may consider. Figure 69 compares distributions obtained for the magnitude of the jet-pull vector from simulations with SM or exotic colour flow. Generally, the magnitude of the jet-pull vector exhibits a distribution that peaks close to zero and drops off rapidly. The SM scenario favours slightly larger values for $|\vec{\mathcal{P}}(j_1^W)|$. This follows the naive expectation as the component-offset vectors \vec{r}_c , see Equation (28), are more likely to be aligned with each other for a jet whose radiation is pulled towards another jet. However, a strong discriminatory power is not observed.

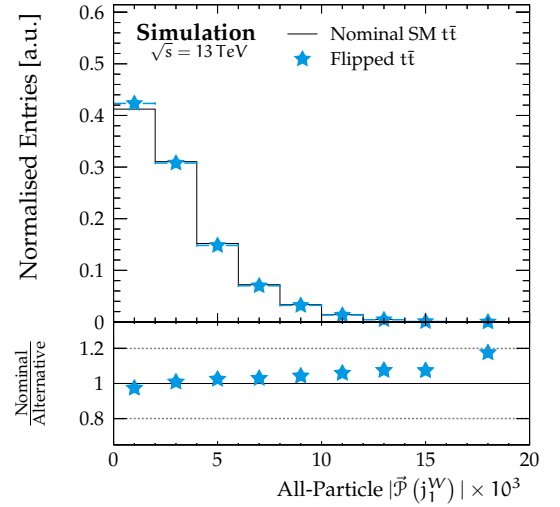


Figure 69: Comparison of magnitude of jet-pull vector taken from regular SM $t\bar{t}$ simulation and $t\bar{t}$ simulation with exotic colour flow.

The jet-pull angle $\theta_{\mathcal{P}}(j_1, j_2)$ is sensitive to the jet substructure of only one of the two jets whose colour connection it encodes. Ideally an observable should have sensitivity to the substructure of both objects. Various combination schemes have been investigated. Two examples are presented here: the jet-pull-angle asymmetry

$$\mathcal{A}_{\mathcal{P}}(j_1, j_2) \equiv \frac{|\theta(j_1, j_2)| - |\theta(j_2, j_1)|}{|\theta(j_1, j_2)| + |\theta(j_2, j_1)|} \quad (30)$$

and the combined jet-pull angle

$$\Theta_{\mathcal{P}}(j_1, j_2) \equiv \angle(\vec{\mathcal{P}}(j_1), \vec{\mathcal{P}}(j_2)). \quad (31)$$

Figure 70 shows the distributions for both variables using the jets for the “*signal colour flow*” category. Both variables exhibit power to discriminate between the SM and exotic colour-flow scenarios.

Figure 70a shows that the asymmetry $\mathcal{A}_{\mathcal{P}}$ favours larger absolute values for two connected jets. Separation between the two colour models is at the level of about 10% in the most extreme cases. The combined jet-pull angle $\Theta_{\mathcal{P}}$ which is shown in Figure 70b exhibits a sloped distribution for two connected jets and a roughly uniform shape otherwise. However, the level of separation between the two models is rather small.

None of the schemes used to combine information from the jet-pull vectors of the leading and sub-leading jet have shown real promise of improving sensitivity to the underlying colour flow. Figure 71 shows the linear correlation coefficients for a variety

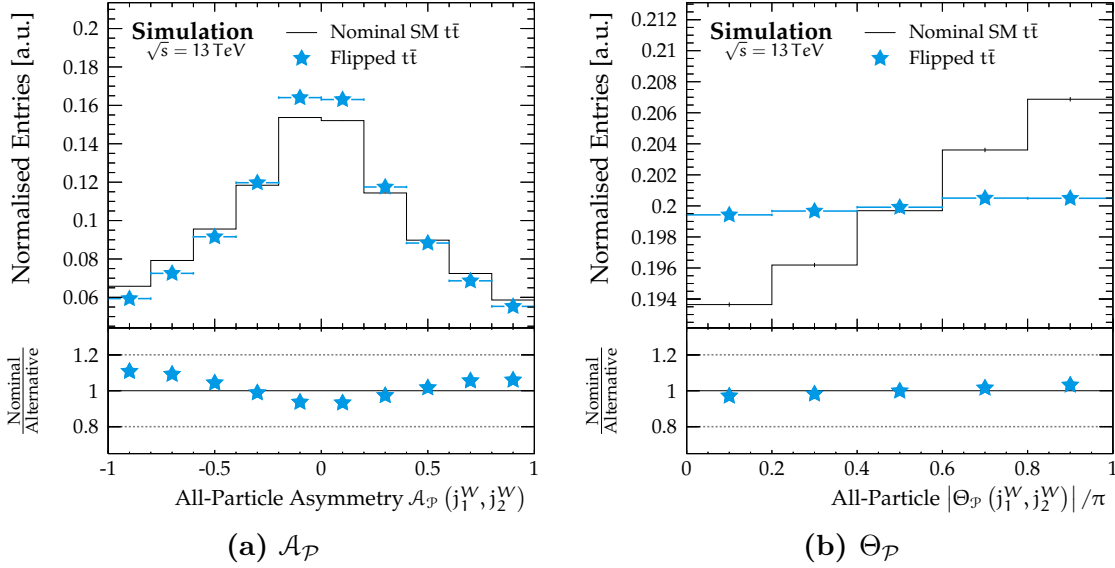


Figure 70: Comparison of jet-pull observables that combine information from the jet-pull vectors of both daughters of the hadronically decaying W boson. Shown are (a) the jet-pull-angle asymmetry $\mathcal{A}_{\mathcal{P}}$ and (b) the combined jet-pull angle $\Theta_{\mathcal{P}}$.

of variables derived from the jet-pull vectors of the jets sensitive to the signal and spurious colour flow scenarios.

$ \vec{p}(j_2^W) $	1																		
$ \vec{p}(j_1^W) $	2	1																	
$ \vec{p}(j_1^W) $	1	2	1																
$\theta_{\mathcal{P}}(j_2^W, j_1^W)$	0	0	-0	0															
$\theta_{\mathcal{P}}(j_2^W, j_1^W)$	-0	-3	1	-0	-0														
$\theta_{\mathcal{P}}(j_1^W, j_2^W)$	-1	0	-1	0	0	-0													
$\theta_{\mathcal{P}}(j_1^W, j_2^W)$	-0	-1	1	-3	-0	3	-0												
$\mathcal{A}_{\mathcal{P}}(j_1^W, j_2^W)$	-1	0	-1	0	-66	0	66	0											
$\mathcal{A}_{\mathcal{P}}(j_1^W, j_2^W)$	0	2	0	-2	0	-64	-0	65	-0										
$\Theta_{\mathcal{P}}(j_1^W, j_2^W)$	-0	0	-0	0	-1	-0	1	0	1	0									
$\Theta_{\mathcal{P}}(j_1^W, j_2^W)$	0	1	-0	0	0	-11	0	-7	-0	2	0								
$ \vec{p}(j_2^W) $																			
$ \vec{p}(j_2^W) $																			
$ \vec{p}(j_1^W) $																			
$ \vec{p}(j_1^W) $																			
$\theta_{\mathcal{P}}(j_2^W, j_1^W)$																			
$\theta_{\mathcal{P}}(j_2^W, j_1^W)$																			
$\theta_{\mathcal{P}}(j_1^W, j_2^W)$																			
$\theta_{\mathcal{P}}(j_1^W, j_2^W)$																			
$\mathcal{A}_{\mathcal{P}}(j_1^W, j_2^W)$																			
$\mathcal{A}_{\mathcal{P}}(j_1^W, j_2^W)$																			
$\Theta_{\mathcal{P}}(j_1^W, j_2^W)$																			

Figure 71: Linear correlation coefficients in percent of various observables derived from the jet-pull vector.

across a statistical ensemble they are practically uncorrelated.

In conclusion, two categories of colour flow are identified within $t\bar{t}$ events in the single-lepton final state: “*signal colour flow*” and “*spurious colour flow*”. The jet-pull-angle observables are found to be sensitive to discriminating between the two categories. For the former category, they are also found to be sensitive to discriminating between the SM and the simulation with exotic colour flow. The magnitude of the jet-pull vector is also found to have sensitivity, albeit to a lesser

The observed correlations are rather small except for the jet-pull-angle asymmetry $\mathcal{A}_{\mathcal{P}}$ which is (anti-)correlated with the jet-pull angles it is derived from. Note that the correlations between two jet-pull observables for the same pair of jets are rather small. For example, the linear correlation between $\theta_{\mathcal{P}}(j_1^W, j_2^W)$ and $\theta_{\mathcal{P}}(j_2^W, j_1^W)$ is at the level of 3%. Each observable is independently sensitive to the underlying colour flow. However, at the same time the sensitivity is rather low, hence,

extent. Independent treatment of observables related to the two jets for each category appears to be favourable over an attempt to combine the information.

13.4 Reconstruction

In this section, the analysis reconstruction, event selection, and background estimation will be discussed. In addition, the observables which are measured and unfolded by the work presented here, are introduced.

13.4.1 Event Reconstruction and Selection

The general event reconstruction procedure has already been introduced and discussed in Section 8. With these definitions at hand basic event level quality criteria, such as the presence of a primary vertex and the requirement of stable detector conditions, are applied. Events are selected by requiring that a single-electron or single-muon trigger has fired. The triggers are designed to select well-identified charged leptons with high p_T . They require a p_T of at least 20 (26) GeV for muons and 24 (26) GeV for electrons for the 2015 (2016) dataset and also include requirements on the lepton quality and isolation. These triggers are complemented by triggers with higher p_T requirements but loosened isolation and identification requirements to ensure maximum efficiencies at higher lepton p_T . The full list of triggers considered by the analysis is:

	2015	2016
e + jets	HLT_e24_lhmedium_L1EM20VH	HLT_e26_lhtight_nod0_ivarloose★
		HLT_e24_lhmedium_nod0_L1EM18VH †
	HLT_e60_lhmedium	HLT_e60_lhmedium_nod0
	HLT_e120_lhloose	HLT_e140_lhloose_nod0
μ + jets	HLT_mu20_iloose_L1MU15	HLT_mu26_ivarmedium★
		HLT_mu24 †
	HLT_mu50	HLT_mu50

For the data measured in 2016 two sets of triggers are used. They differ only in the lowest- p_T trigger used for each lepton. The lowest- p_T regular triggers used by the analysis for data collected in 2016 are not suitable for the procedure used to estimate the fake lepton background contribution. They either apply a strict lepton identification requirement or an isolation requirement. Hence, alternative low- p_T triggers are used for the fake lepton estimate. The regular triggers are marked with a ★ while the alternative triggers are marked with a †, all other triggers are shared between the two configurations.

The reconstructed lepton must satisfy $p_T > 27$ GeV and must match the trigger object that fired using a geometric matching. No additional lepton may be present. Furthermore, selected events must contain at least four jets. At least two of the jets in the event must be **b**-tagged. Finally, E_T^{miss} must exceed 20 GeV.

Table 10 lists the “*cutflow*”, i.e. successive event yields, found when applying this event selection on the measured data.

Selection	Yield	Selection	Yield
Initial	3 050 531 010	Initial	3 050 531 010
Primary Vertex	3 050 521 520	Primary Vertex	3 050 521 520
Trigger	434 214 072	Trigger	497 443 364
$N_e(p_T > 27 \text{ GeV}) \geq 1$	260 845 087	$N_\mu(p_T > 27 \text{ GeV}) \geq 1$	277 741 487
$N_e(p_T > 25 \text{ GeV}) = 1$	248 474 657	$N_\mu(p_T > 25 \text{ GeV}) = 1$	257 922 926
$N_\mu(p_T > 25 \text{ GeV}) = 0$	248 194 849	$N_e(p_T > 25 \text{ GeV}) = 0$	257 686 594
Trigger Matching	247 745 640	Trigger Matching	256 819 128
$N_{\text{Jet}}(p_T > 25 \text{ GeV}) \geq 1$	102 226 195	$N_{\text{Jet}}(p_T > 25 \text{ GeV}) \geq 1$	79 772 128
$N_{\text{Jet}}(p_T > 25 \text{ GeV}) \geq 2$	31 924 741	$N_{\text{Jet}}(p_T > 25 \text{ GeV}) \geq 2$	24 049 030
$N_{\text{Jet}}(p_T > 25 \text{ GeV}) \geq 3$	10 353 870	$N_{\text{Jet}}(p_T > 25 \text{ GeV}) \geq 3$	7 933 344
$N_{\text{Jet}}(p_T > 25 \text{ GeV}) \geq 4$	3 663 208	$N_{\text{Jet}}(p_T > 25 \text{ GeV}) \geq 4$	2 950 421
$N_{b\text{-Jet}}(70\%) \geq 1$	821 034	$N_{b\text{-Jet}}(70\%) \geq 1$	771 880
$N_{b\text{-Jet}}(70\%) \geq 2$	653 840	$N_{b\text{-Jet}}(70\%) \geq 2$	617 266
$E_T^{\text{Miss}} > 20 \text{ GeV}$	590 767	$E_T^{\text{Miss}} > 20 \text{ GeV}$	562 236

(a) Electron Channel
(b) Muon Channel

Table 10: Cutflow tables obtained from applying the event selection on the measured data. Note that the cut labelled *Initial* does not refer to the full dataset measured by the ATLAS experiment but rather to a pre-skimmed selection requiring at least one lepton and jet each with $p_T > 15 \text{ GeV}$.

13.4.2 Background Determination

After filtering the events using the selection discussed before, a variety of background sources remain. The event yields listed in Table 10 include a mixture of signal events and background contamination. To understand the selected data better and assess the data–prediction agreement, an estimate of the signal and background contributions is constructed. This is also used at a later stage to subtract the background contributions from data.

Several contributions to the data contain real top-quarks and yet are not considered to be part of the signal. Events which contain a single top-quark are the dominant contribution to this type of background. Smaller contributions originate from associated $t\bar{t}$ production, i.e. $t\bar{t} + X$ with X being either a W , Z , or H IGGS boson. These contributions are expected to be small and practically negligible.

Production of events with either one or two electroweak bosons in association with jets can be misidentified as signal. In particular, the W +jets contribution is expected to contaminate the signal selection as it is relatively similar to the $t\bar{t} \rightarrow \ell + \text{jets}$ signal. Contributions from Z +jets and diboson (also labelled as VV symbolising two electroweak bosons V) are expected to be small. Finally, processes which produce several jets and contain a non-prompt (NP) or fake lepton — as discussed in Section 11 — are a contribution that is expected to be sizeable.

With the exception of the NP and fake lepton background, all background sources are modelled using MC simulation. In Section 13.2 a detailed listing of the simulation

samples that are used is given. The NP and fake lepton background is modelled using the data-driven matrix method which has been discussed in Section 11.

Estimates for the signal contribution and background contamination to the selected data are constructed using the event selection defined before. Table 11 lists the number of selected events for data alongside with the estimated composition of the signal selection. Background contaminations from the single top-quark and NP or fake lepton categories are the most dominant contributions. The signal yield is estimated to be approximately 88 % pure in $t\bar{t}$ events.

Sample	Yield		
$t\bar{t}$	1 026 000	\pm	95 000
$t\bar{t}V$	3270	\pm	250
$t\bar{t}H$	1700	\pm	100
Single top	48 400	\pm	5500
Diboson	1440	\pm	220
W + jets	27 700	\pm	4700
Z + jets	8300	\pm	1400
NP/Fake leptons	53 000	\pm	30 000
Total Expected	1 170 000	\pm	100 000
Observed	1 153 003		

Table 11: Event yields after selection. The uncertainties are the sum in quadrature of the detector modelling uncertainties and the uncertainties on the data-driven non-prompt and fake lepton background estimate. Refer to Section 13.6 for a detailed description of the uncertainties that are considered.

In the measurement presented here, the signal is defined to be the $t\bar{t}$ contribution. However, while the event selection aims to select $t\bar{t}$ events from the single-lepton final state, $t\bar{t}$ events in the dilepton channel may contaminate the signal. This contamination is not considered to be a source of background. Hence, it is included in the yield labeled as “ $t\bar{t}$ ” and is not subtracted from data. The dilepton pollution to the $t\bar{t}$ signal is estimated using the nominal $t\bar{t}$ MC to be approximately 9.8 %.

In Figure 72 the distributions observed for several kinematic variables and event properties, reconstructed from the events that pass the signal selection, are shown. The data are compared to the prediction constructed from the nominal $t\bar{t}$ simulation and the background estimates. The different contributions are merged into four groups: the $t\bar{t}$ signal, backgrounds which include top quarks (single top and $t\bar{t} + X$), backgrounds which include electroweak bosons (V + jets and diboson), and the NP and fake lepton background.

The total prediction generally agrees well with the data. In the ratio of data over the prediction, very few data points diverge significantly from unity. A small mismodelling effect is observed for a b -jet multiplicity that is greater than or exceeds four. This is an effect known from other measurements and likely related to heavy-flavour modelling in simulation. A cross-check found that the effect does not negatively impact this measurement. The contribution of events with at least four b -jets is less than half a percent to the total selected data.

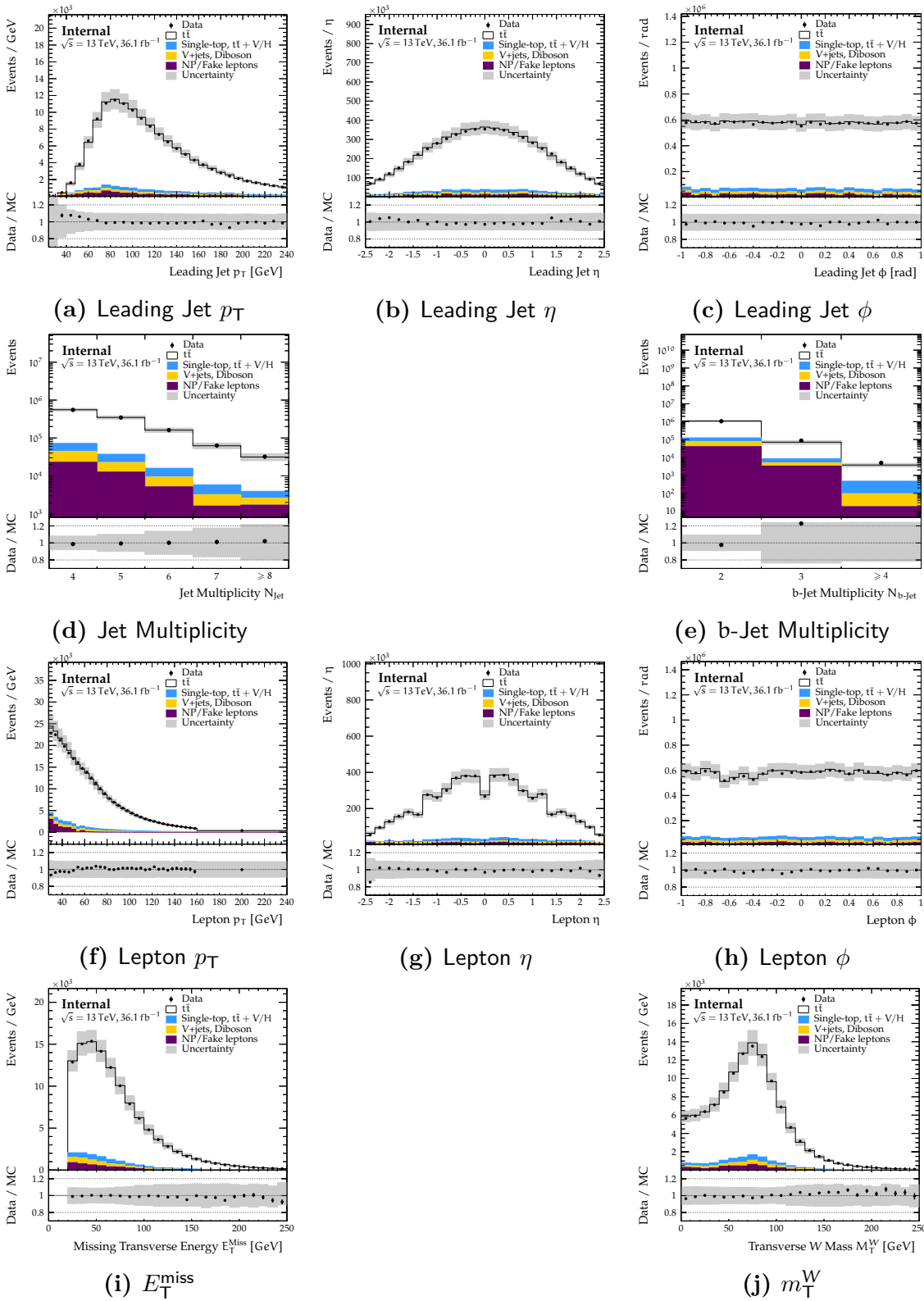


Figure 72: Distributions of a variety of variables used to study data–prediction agreement in the signal region. Data from electron and muon channels are combined. The uncertainty bands shown in the SM prediction include only detector modelling uncertainties.

13.4.3 Observable Definition and Reconstruction

The $t\bar{t}$ topology in the single-lepton final state and the colour flow therein was already discussed in detail in Section 13.3. Using the definitions introduced before, the measurement presented here constructs four observables from the jet-pull vector. These observables and their definitions are summarised in Table 12.

Target colour flow	Signal colour flow (j_1 and j_2 are colour connected)	Spurious colour flow (j_1 and j_2 are not colour connected)
Hard-scatter target	Daughters of hadronically decaying W boson	b -quarks from top-quark decay
Jet assignment	j_1^W : leading- p_T non- b -tagged jet j_2^W : 2 nd leading- p_T non- b -tagged jet	j_1^b : leading- p_T b -tagged jet j_2^b : 2 nd leading- p_T b -tagged jet
Observables	$\theta_{\mathcal{P}}(j_1^W, j_2^W)$: “forward pull-angle” $\theta_{\mathcal{P}}(j_2^W, j_1^W)$: “backward pull-angle” $ \vec{\mathcal{P}}(j_1^W) $: “pull-vector magnitude”	$\theta_{\mathcal{P}}(j_1^b, j_2^b)$: “forward di- b -jet-pull angle”

Table 12: Summary of the observable definitions.

Three observables are constructed to be sensitive to “*signal colour flow*”. These observables are: the magnitude jet-pull vector of the leading daughter of the hadronically decaying W boson $|\vec{\mathcal{P}}(j_1^W)|$ and the two jet-pull angles constructed using the daughters of the hadronically decaying W boson $\theta_{\mathcal{P}}(j_1^W, j_2^W)$ and $\theta_{\mathcal{P}}(j_2^W, j_1^W)$. The last observable is the jet-pull angle of the leading b -jet $\theta_{\mathcal{P}}(j_1^b, j_2^b)$ which is sensitive to the “*spurious colour flow*”.

The jet-pull vectors used for the calculation of the observables are constructed using inner-detector tracks that have been associated with the selected jet. Section 8.5 discusses the association technique in detail. To account for the fact that the inner-detector coverage extends only up to $|\eta| \sim 2.5$, jets selected for the calculation must be within $|\eta| < 2.1$. This ensures that the entire area of the selected jet, which was clustered using a radius parameter of $R = 0.4$, is within the coverage of the inner detector. Inner-detector tracks must satisfy $p_T > 500$ MeV as well as requirements on the minimum number of hits and holes within the pixel and SCT detectors. Furthermore, to mitigate pile-up effects and suppress tracks of poor quality, track-to-vertex-association cuts are applied: $|d_0| < 2$ mm and $|z_0 \cdot \sin \theta| < 3$ mm.³ Finally, the jet-pull vector for a jet is only considered to be valid if at least two tracks have passed the selection requirements and are available for calculation.

In addition to the set of jet constituents, the jet-pull-vector calculation requires the coordinates of the jet axis in y - ϕ space. However, the natural jet-axis is calculated from the (calibrated) calorimeter clusters rather than the inner-detector tracks which are used for the jet-pull vector calculation. To ensure consistency between these two inputs to the calculation, the jet axis is recalculated for each jet from the set of

³ Refer to Section 8 for variable definitions.

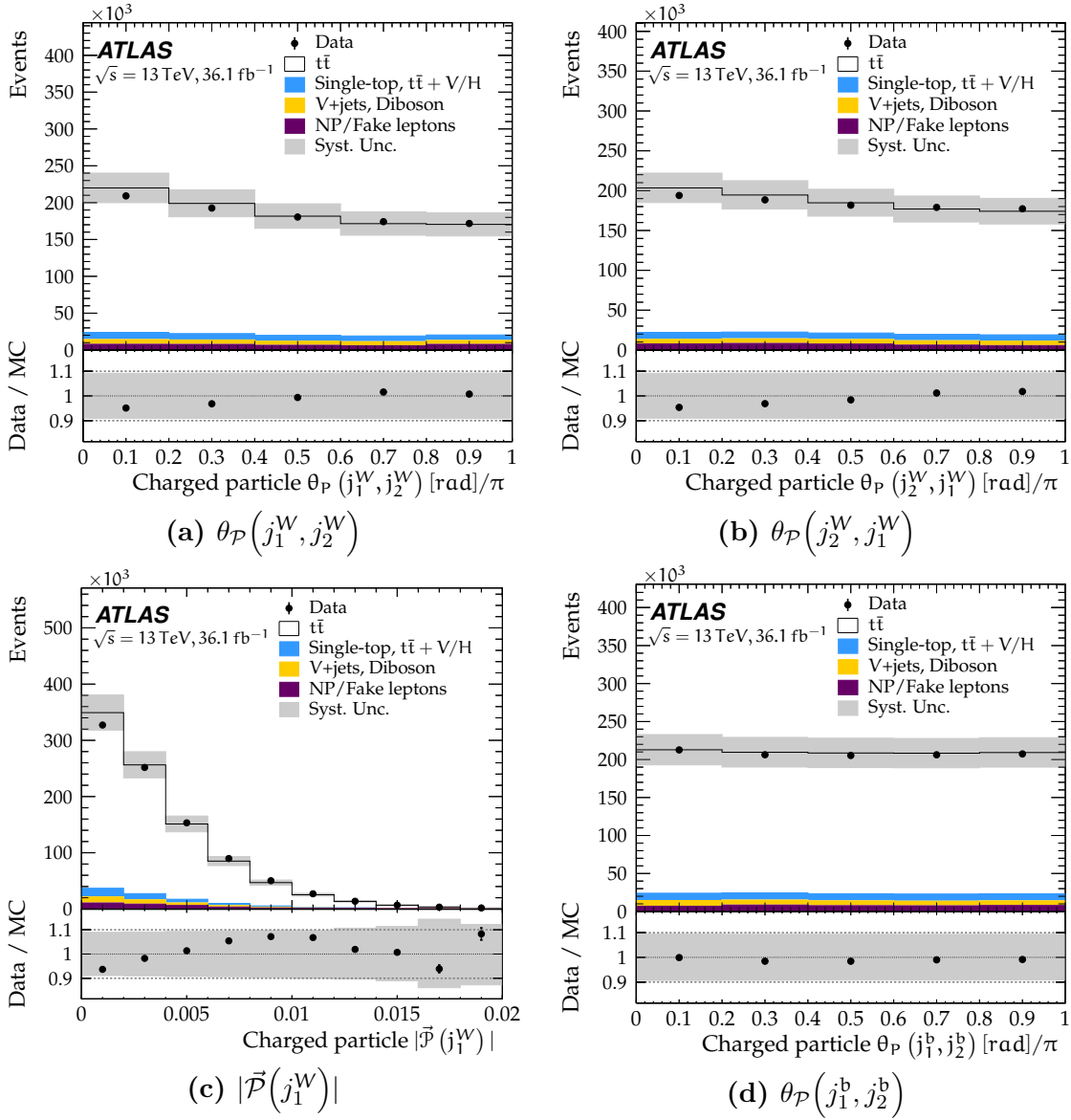


Figure 73: Detector-level distributions for the four considered observables: the (a) forward and (b) backward pull angle for the hadronically decaying W boson daughters, the (c) magnitude of the jet-pull vector from the leading W daughter, and the (d) forward di-b-jet-pull angle. Uncertainty bands shown include the experimental uncertainties to the event selection and observable calculation as well as uncertainties related to the modelling of the fake lepton background.

selected inner-detector tracks. This recalculated axis is then used by the jet-pull-vector calculation according to Equation (28). In line with the same consistency argument, the jet transverse momentum p_T^j used in the denominator of the jet-pull vector formula, Equation (28), is replaced by the p_T of the recalculated jet-axis as well.

Figure 73 shows the distributions measured for each of the observables in data. The distributions exhibit shapes similar to those found by the studies performed at particle-level using simulated data. In particular, the distributions of the jet-pull angles from the daughters of the hadronically decaying W boson are subtly sloped. By comparison, the distribution of the di-b-jet-pull angle is essentially flat.

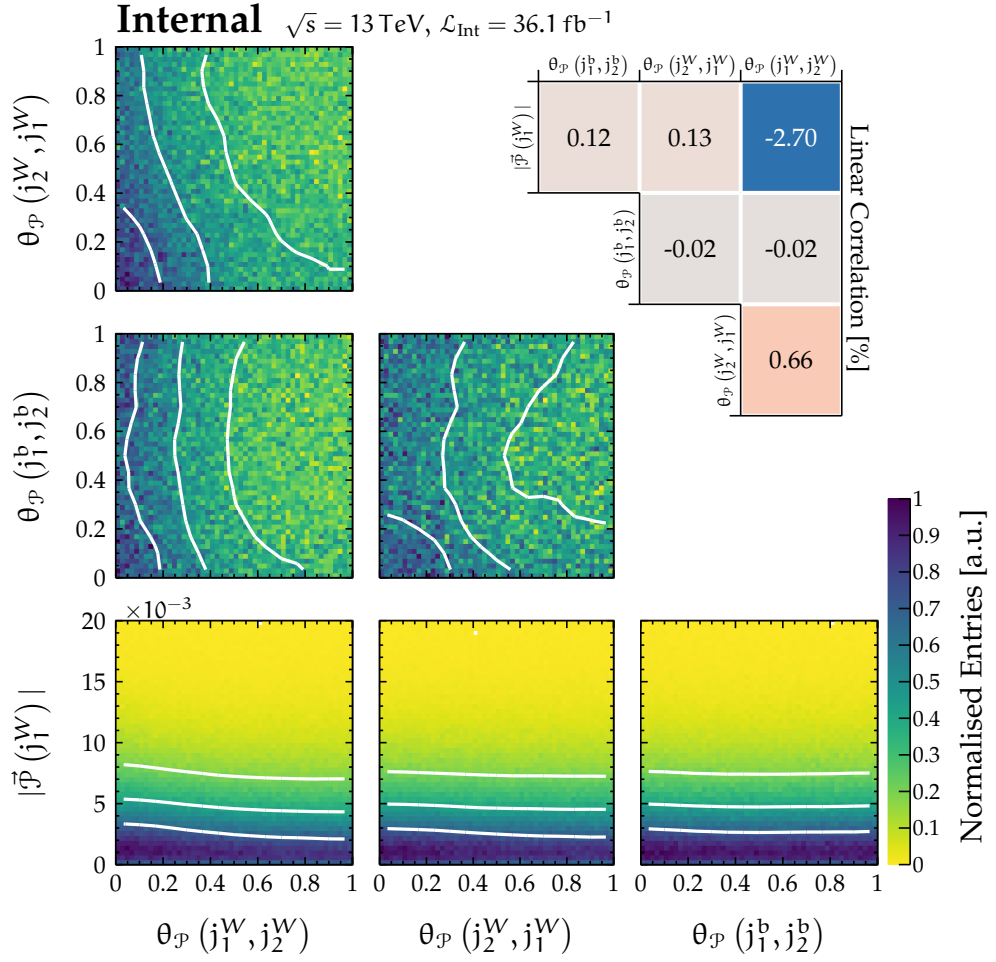


Figure 74: Scatter-plots of the distributions observed in measured data for the four analysis observables. White lines within each sub-panel denote contour levels at 25, 50, and 75% of the (normalised) value range. The panel in the top-right corner lists the linear correlation coefficients calculated between the observables.

The measured distributions are compared with predictions constructed using the signal and background estimates. These predictions agree with the data within the considered uncertainties. The selected data are highly enriched in $t\bar{t}$ events. Sloped deviations between prediction and observed data can be found for the two pull angles from the W boson decay. Data favours a less strongly sloped shape for the two pull angles. For the magnitude of the leading W boson daughter $|\vec{\mathcal{P}}(j_1^W)|$ data favours a more gradual descent from the peak value at zero than the prediction. For the di- b -jet-pull angle, the prediction agrees extremely well with the observed distribution.

Figure 74 depicts scatter-plots for all combinations of the four observables as obtained from the measured data. The different sub-panels show how pairs of observables correlate with one another. A listing of the linear correlation coefficients between the four observables is shown in the top-right corner of the figure.

In general correlations between the different observables are small. Notably, there is a small anti-correlation between the different observables. Notably, there is a small anti-correlation between the magnitude of the jet-pull vector $|\vec{\mathcal{P}}(j_1^W)|$ and the

jet-pull angle $\theta_{\mathcal{P}}(j_1^W, j_2^W)$. The small positive correlation between the two jet-pull angles constructed using the same jets, $\theta_{\mathcal{P}}(j_1^W, j_2^W)$ and $\theta_{\mathcal{P}}(j_2^W, j_1^W)$, which was found at particle-level, has been reduced to essentially zero.

§1. Choice of Jet Constituents As discussed before, the jet-pull-vector calculation used by the measurement presented here relies on inner-detector tracks as jet constituents. However, in general there are two different types of detector objects that might be considered as constituents to the calculation: calorimeter clusters and tracks.

For a measurement using the ATLAS experiment, the former class is extremely straightforward in its use: the calculation simply uses the constituents that make up a target jet. Using tracks is slightly less straightforward as one must either define a matching criterion for associating tracks to the target jet or switch to jets that are clustered from inner-detector tracks. The two classes perform quite differently and can draw benefit from different properties. For example, a track-based calculation benefits from the high spatial resolution of the tracking system while a calorimeter-cluster based calculation benefits from a more complete energy measurement and sensitivity to electrically neutral hadrons.

In recent years a new type of jet class has been introduced within ATLAS, the *particle-flow jets* [216], which attempts to improve jet quality by combining information from the inner detector and the calorimeter. The particle-flow jet-algorithm considers both tracks and calorimeter clusters during jet building. However, simply combining the two object types would lead to double counting as a charged object may create a track and also deposit energy in the calorimeter cells. To remedy this, the initial stage of the particle-flow jet-algorithm removes calorimeter deposits which have been classified as originating from a charged hadron — the most obvious classification would simply attempt to perform a geometric match to any of the measured tracks. The tracks that belong to the cluster are retained and thus — for charged particles — the more precise inner-detector information is utilised. Neutral particles on the other hand still contribute through the calorimeter information. Unlike ATLAS, the CMS experiment has been using this kind of procedure for its jets since the start of LHC operations [217]. Naturally one may also utilise these particle-flow jets and their constituents for the calculation of colour-flow observables.

As part of the analysis presented here, the performance of the three different constituent inputs to the calculation of the jet-pull observables was studied. At the time this was done, the use of particle-flow jets within ATLAS was purely experimental and calibrations were preliminary. Consequently, the results presented here for the performance of particle-flow jets for studying quantities derived from the jet-pull vector are not expected to be final.

Figure 75 shows the residual distributions obtained for the jet-pull angle utilising the three constituent classes discussed above. For each event, the residual is constructed relative to the particle-level equivalent jet-pull angle value. The definitions used to calculate the jet-pull angle at particle-level will be discussed in Section 13.4.4.

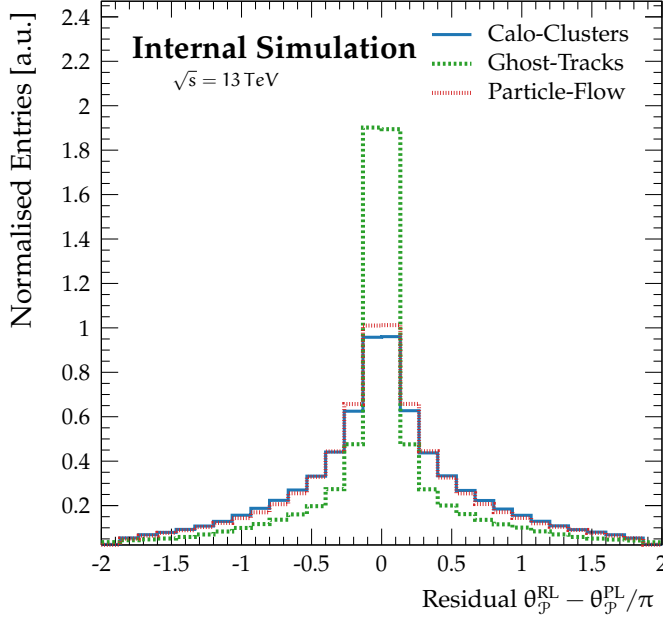


Figure 75: Residual distributions obtained for the pull angle observable when calculated for the leading jet originating from the hadronically decaying W boson in $t\bar{t}$ events using different types of constituent definitions. The distributions labelled *Calo-Cluster* and *Ghost-Tracks* use calorimeter clusters respectively ghost-associated tracks taken from the same jet. While the calorimeter clusters are the constituents of the original jet, the ghost-associated tracks are not used for construction of the jet. The distribution labelled as *Particle-Flow* uses an experimental, alternative jet definition which combines calorimeter and track information in the jet clustering.

In each case, the jet axis is recalculated from the list of constituents used for calculation and all valid quality cuts have been applied. It is immediately obvious that the track-based calculation performs vastly better than the other classes. Even though the data used for this comparison uses only preliminary calibrations and an experimental particle-flow jet reconstruction, the calculation based on particle-flow jets improves upon the calculation based on calorimeter clusters.

The residual distribution shown in Figure 75 demonstrates that the high spatial resolution provided by the inner-detector tracks is extremely beneficial to a colour-flow measurement based on the jet-pull vector. Hence, to achieve optimal precision, the measurement presented here relies on a track-based calculation of the jet-pull vector. A measurement based on calorimeter information is not considered.

§2. Jet Axis Recalculation and Track Quality Cuts As was mentioned before, the jet-axis used by the calculation of the jet-pull vector is recalculated from the selected constituents prior to calculation of the jet-pull vector.

Figure 76 shows the residual of the difference between the regular and recalculated jet-axis position in y - ϕ space. Using the jet-axis recalculation was found to be beneficial for the resolution of the jet-pull angle. Figure 77 compares the residual distributions obtained with and without application of the recalculation procedure.

The impact that other selection requirements have on the magnitude of the jet-pull vector and the jet-pull angle as well as their residuals was studied as well. It

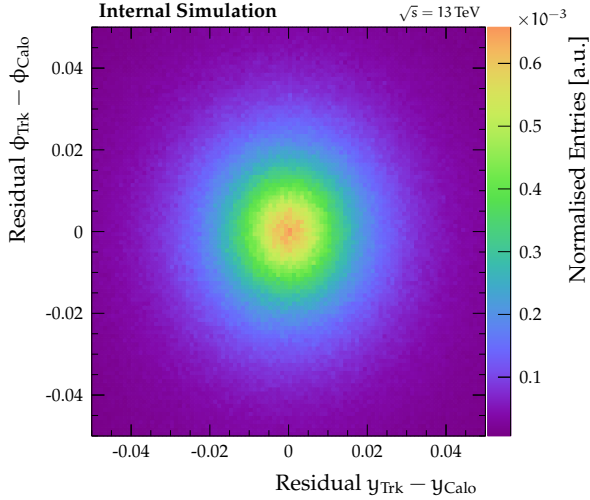


Figure 76: Residual of the jet-axis position in y - ϕ space. The two scenarios which are considered are: *a*) the jet-axis is recalculated from the tracks considered for calculating the analysis observables ($y_{\text{Trk}}, \phi_{\text{Trk}}$), *b*) the jet-axis is taken directly from the calibrated jet four-momentum ($y_{\text{Calo}}, \phi_{\text{Calo}}$).

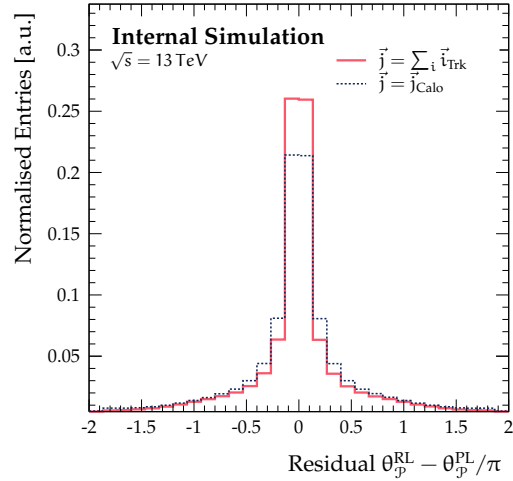


Figure 77: Comparison of residuals for jet-pull angle calculated using inner-detector tracks either with axis-recalculation (solid line) or without (dashed line).

was found that the track quality requirements, in particular the track-to-vertex-association cuts listed above, considerably improve the expected resolution. The use of a stricter cut on the number of tracks required to enter the calculation of the jet-pull vector was considered. Indeed, the resolution is found to improve when applying a higher cut value, e.g. $N_{\text{Trk}} \geq 5$. However, in order to remain general and to reduce dependence on accurate modelling of the number of charged hadrons, the cut value is left unchanged at $N_{\text{Trk}} \geq 2$.

13.4.4 Particle-Level Definition

The concept of the fiducial particle-level phase-space has already been introduced in Section 9.1 alongside with definitions of the physics-objects used at particle level. Table 13 lists a summary that compares the physics-object definitions at detector- and particle-level.

The event selection at particle level is constructed to closely match the event selection that is applied at detector level which was already discussed. Thus, events are selected by requiring:

- exactly one lepton that satisfies $p_T > 27$ GeV,
- no additional lepton at the regular p_T cut of 25 GeV,
- at least four jets, with at least two **b**-tagged jets, and
- a missing transverse energy E_T^{miss} that exceeds 20 GeV.

At detector level, the jet-pull vector is calculated using inner-detector tracks that have been associated with the jet. Inner-detector tracks originate from charged particles, consequently, the particle-level equivalent uses only particle-level jet-constituents that have a non-zero electric charge. Furthermore, the jets used by the detector-

Object	Detector Level	Particle Level
Leptons	<ul style="list-style-type: none"> • Lepton ID @ <code>TightLH</code> (e), <code>Medium</code> (μ) • $d_0 /\sigma_{d_0} < 5$ (e), 3 (μ) • $z_0 \cdot \sin \theta < 0.5$ mm • Track & Calorimeter Isolation @ <code>GradientTight</code> WP • $\eta < 1.37$ or $1.52 < \eta < 2.47$ (e), $\eta < 2.5$ (μ) • $p_T > 25$ GeV • Not overlapping with any jet • Matched to active selected single-lepton trigger 	<ul style="list-style-type: none"> • Truth particle must not originate from hadron • $\eta < 2.5$ • $p_T > 25$ GeV • Not overlapping with any jet
Jets	<ul style="list-style-type: none"> • $\eta < 2.5$ • $p_T > 25$ GeV • JVT cut (if $p_T < 60$ GeV and $\eta < 2.4$) 	<ul style="list-style-type: none"> • $\eta < 2.5$ • $p_T > 25$ GeV
b-Tag	<ul style="list-style-type: none"> • MV2c10 score exceeds 70 % WP cut 	<ul style="list-style-type: none"> • At least one ghost-associated B-hadron at $p_T > 5$ GeV
E_T^{miss}	<ul style="list-style-type: none"> • Transverse component of negative of vector sum of all objects in the event 	<ul style="list-style-type: none"> • Transverse component of vector sum of neutrino truth particles not from hadron

Table 13: Summary of the requirements for detector- and particle-level object definitions.

level calculation must satisfy $|\eta| < 2.1$ and each inner-detector track must have $p_T > 500$ MeV. Both requirements are motivated by detector limitations. In principle, these requirements are not needed at particle level, however, to reduce extrapolation during the unfolding, the same requirements are applied to the particle-level jets and jet constituents. With this selection, the jet-pull-vector calculation directly follows Equation (28).

13.5 Unfolding

The measured distributions are unfolded to particle level using the iterative Bayesian (IB) method [165] using its implementation in the `RooUnfold` framework [218]. Section 9.2 has already introduced both the concept of unfolding as well as the IB method.

The procedure employed by this measurement to transform the measured data into its particle-level equivalent actually consists of multiple stages: first, the background contributions are subtracted bin-by-bin from the observed data to obtain an estimated signal distribution from the data. Afterwards, the detector response model is used to remove the detector effects from the estimated signal distribution. The IB unfolding uses the response matrix to correct the signal distribution back to particle-level. Two correction factors are applied, one before and the other after the IB unfolding. These account for non-overlap in the fiducial phase-space at detector- and particle-level, i.e. they correct for events which are part of the fiducial phase-space at one level but not the other.

The complete procedure used by the measurement presented here can be symbolically summarised by the equation

$$\frac{d\sigma_{\text{Fid}}^t}{dX^t} = \frac{1}{\mathcal{L}_{\text{Int}} \cdot \Delta X^t} \cdot \frac{1}{\epsilon^t} \sum_r \mathcal{M}_{r,t}^{-1} \cdot \epsilon_{\text{Fid}}^r \cdot (N_{\text{Obs}}^r - N_{\text{Bkg}}^r), \quad (32)$$

where t indicates the bin index at particle level, r the detector-level bin index, \mathcal{L}_{Int} is the integrated luminosity of the data, \mathcal{M} is the response matrix and the inversion symbolises unfolding using the IB method, N_{Obs} is the number of observed events, N_{Bkg} the number of expected background events, and ϵ and ϵ_{Fid} are the phase-space correction factors. The two correction factors are defined as

$$\epsilon^t = \frac{N_{\text{Tru}\wedge\text{Rec}}^t}{N_{\text{Tru}}^t} \quad \text{and} \quad \epsilon_{\text{Fid}}^r = \frac{N_{\text{Tru}\wedge\text{Rec}}^r}{N_{\text{Rec}}^r}. \quad (33)$$

The variable N_{Tru} (N_{Rec}) denotes the number of events that fulfill the fiducial requirements at particle level (selection requirements at detector level) while $N_{\text{Tru}\wedge\text{Rec}}$ is the number of events that pass both sets of requirements applied at their respective level. The detector response model and the two correction factors are obtained from $t\bar{t}$ simulation. Figures 78 to 81 show the response matrices (top panel of each figure) and correction factors (middle panel of each figure) for each of the four analysis observables.

The migration matrices are normalised row-wise and presented in percent. Therefore, the value shown for a bin in row i and column j describes the percentage of events that originate from bin i in the particle-level distribution and migrate to bin j at detector level. Due to the comparatively poor resolution of the jet-pull observables, the fraction in the on-diagonal bin — that is $i = j$ — does not exceed sixty percent for most bins. The content of the on-diagonal bin describes the percentage of events which do not migrate due to detector effects.

Each of Figures 78 to 81 also includes a diagram of the migration flow for the observable in the bottom panel. Like the migration matrix, the migration-flow diagram illustrates how the bin contents at particle level (left) migrate into bins at detector level (right). The bar height on each side represents the migration-matrix content as percentage of the total events. Unlike the migration-matrix representation shown in the top panels of the figures, the migration-flow diagram shows migrations bidirectionally. Hence, it is straightforward to identify the contributions of different particle-level bins to a given detector-level bin.

The bin edges were chosen by optimisation studies using simulated $t\bar{t}$ data. Each on-diagonal bin must contain at least fifty percent of the row-wise content. Furthermore, a numerical optimisation of the bin-edge position was used to maximise the fraction of events within the on-diagonal bin. Additional constraints imposed on the minimisation force the on-diagonal fraction for different bins to be of similar value. A

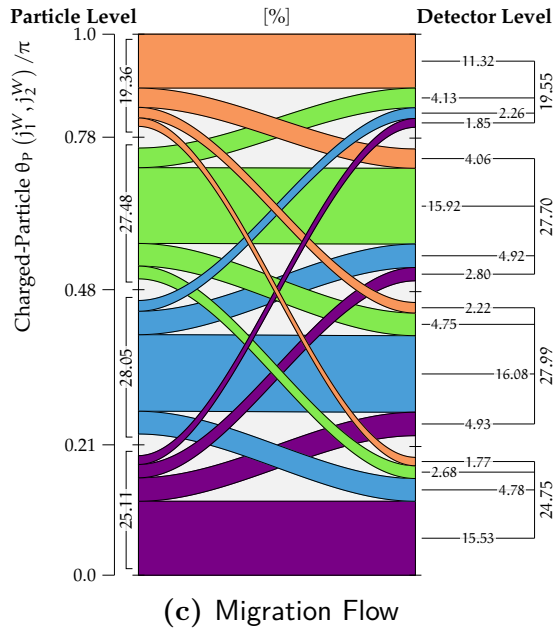
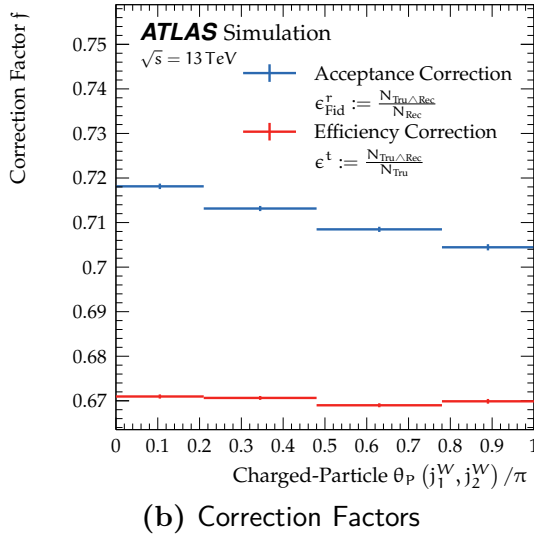
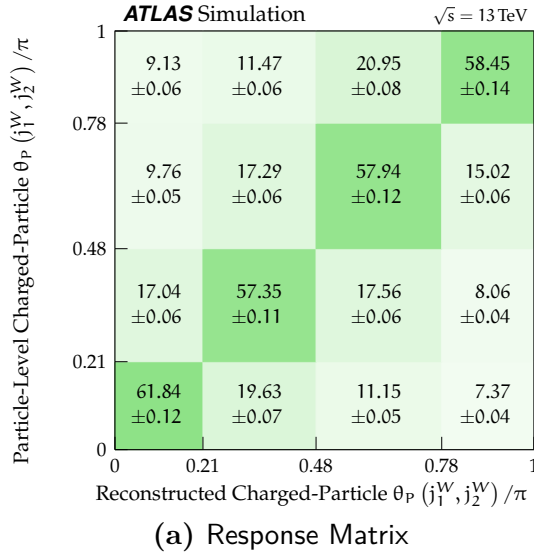


Figure 78: Detector model parameterisations for the forward signal-jet-pull angle $\theta_P(j_1^W, j_2^W)$. Shown are (a) the response matrix, (b) the correction factors, and (c) a flow diagram illustrating the migratory flow of bin contents going from particle level to detector level.

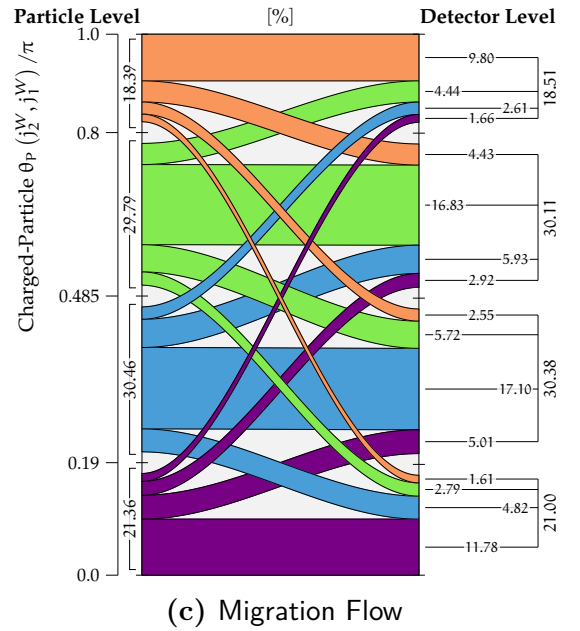
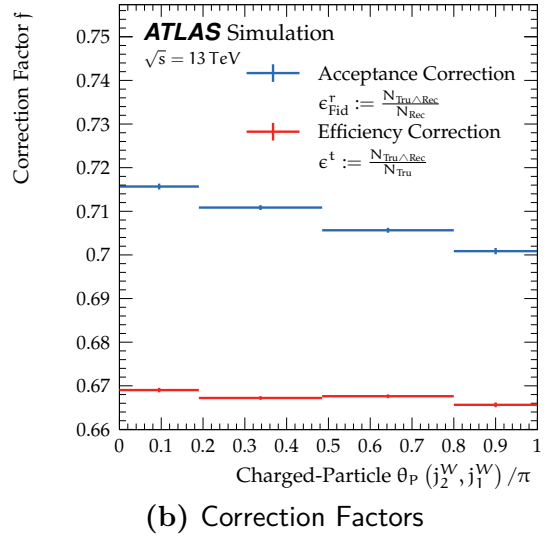
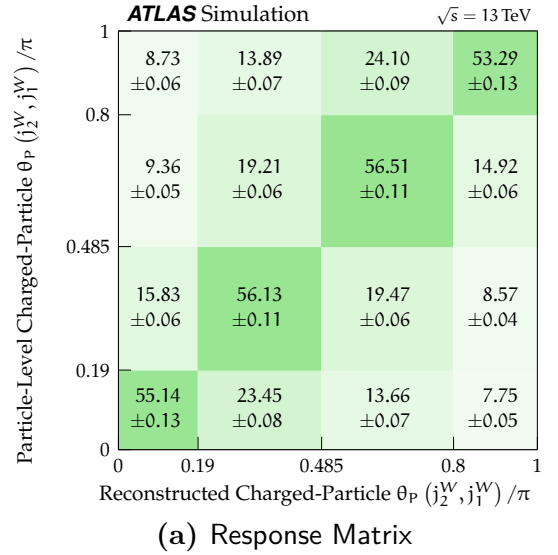


Figure 79: Detector model parameterisations for the backward signal-jet-pull angle $\theta_P(j_2^W, j_1^W)$. Shown are (a) the response matrix, (b) the correction factors, and (c) a flow diagram illustrating the migratory flow of bin contents going from particle level to detector level.

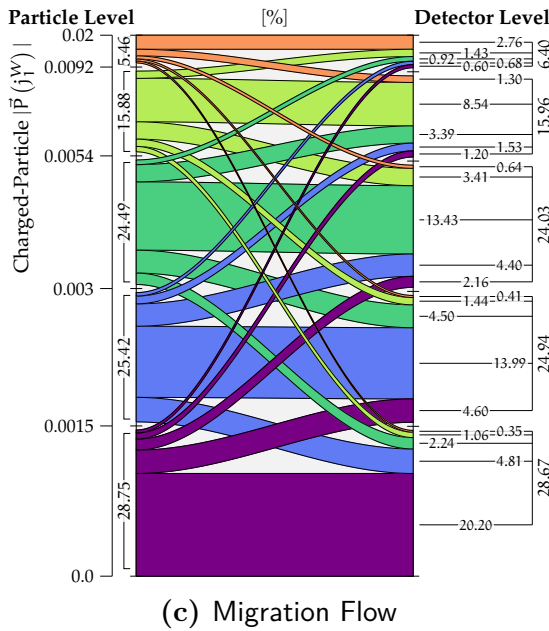
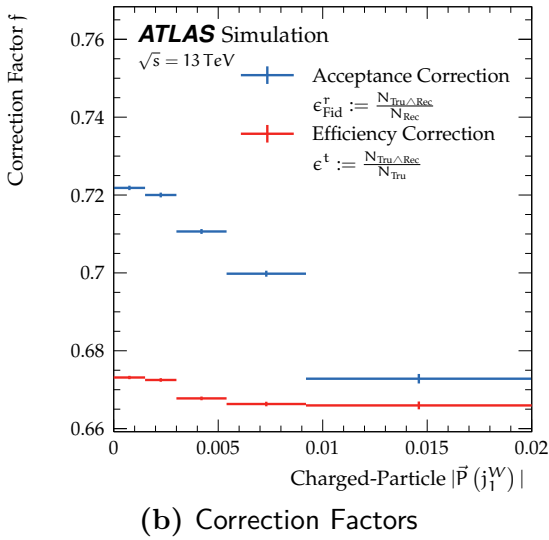
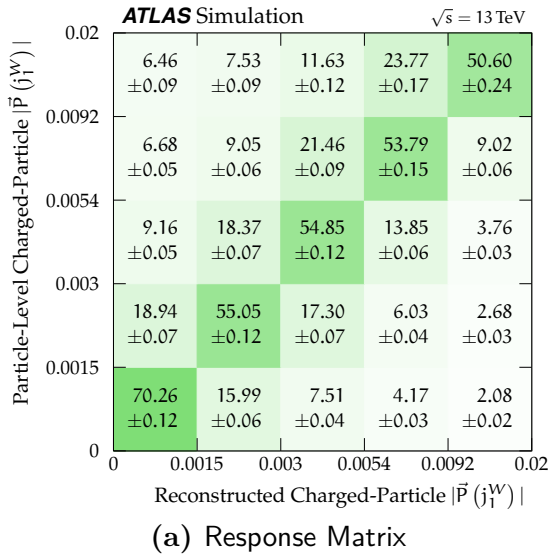


Figure 80: Detector model parameterisations for the magnitude of the leading W daughter's jet-pull vector. Shown are (a) the response matrix, (b) the correction factors, and (c) a flow diagram illustrating the migratory flow of bin contents going from particle level to detector level.

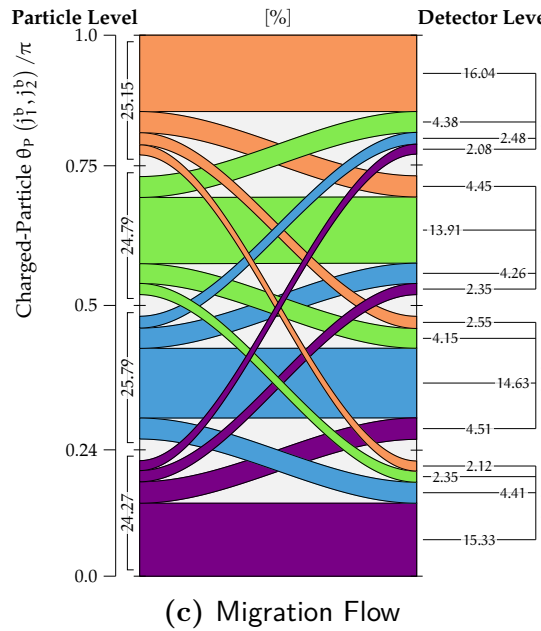
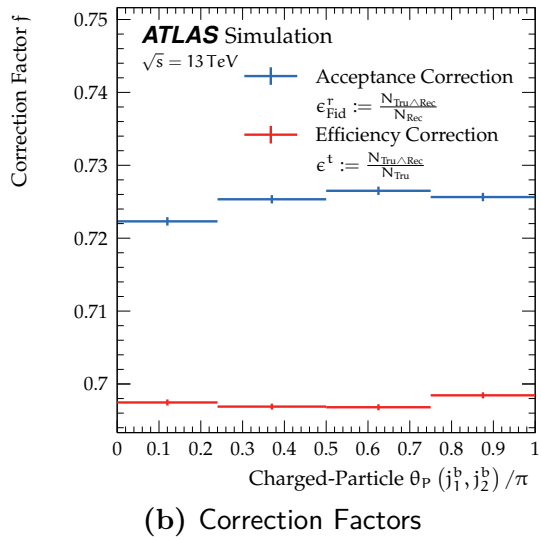
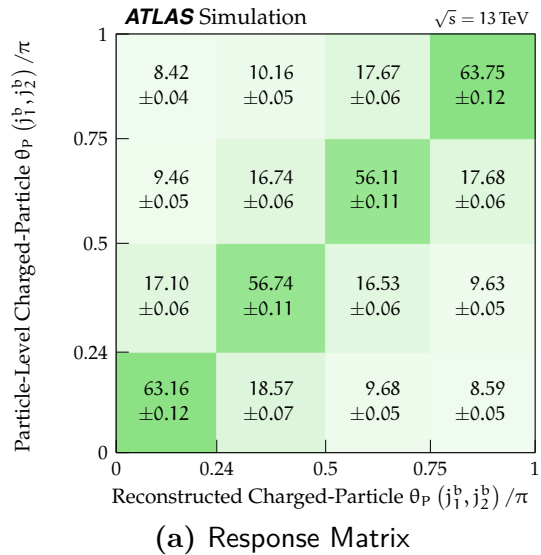


Figure 81: Detector model parameterisations for the forward di-b-jet-pull angle $\theta_P(j_1^b, j_2^b)$. Shown are (a) the response matrix, (b) the correction factors, and (c) a flow diagram illustrating the migratory flow of bin contents going from particle level to detector level.

more fine-meshed binning is not advisable since it implies that the unfolding has to cope with a further degraded detector resolution. For example, using a scheme of five bins for $\theta_{\mathcal{P}}(j_1^W, j_2^W)$ implies that the bin width of at least some bins is considerably smaller than the resolution determined for the observable from simulation.

The number of iterations used by the IB method is a regularisation parameter of the unfolding and must be determined for the measurement. A standard approach to finding this parameter is to study how the relative uncertainties on the unfolding result change as the number of iterations is increased. Figure 82 shows the relative uncertainty for each bin of the four observables parameterised in the number-of-iterations parameter.

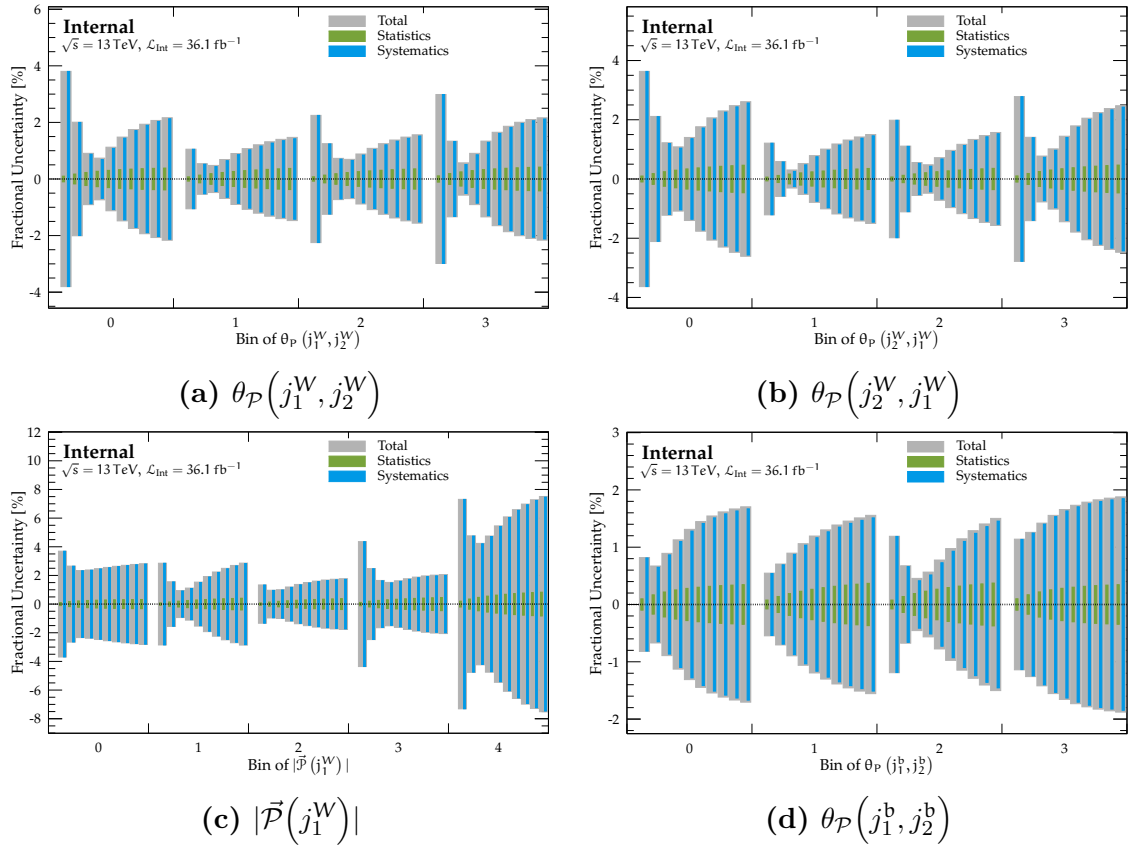


Figure 82: Illustration of relative per-bin uncertainty as function of number-of-iterations parameter of unfolding. Shown are the (a) forward and (b) backward pull angle for the hadronically decaying W boson, (c) the magnitude of the jet-pull vector for the leading W daughter, and the (d) forward di-b-jet-pull angle. Within each bin, the number of iterations used by the unfolding increases from unity to ten from left to right.

13.6 Treatment of Uncertainties

The measured quantities are affected by a variety of uncertainties. Sources of systematic uncertainty are grouped into four categories:

- experimental uncertainties,
- uncertainties related to the modelling of the background contribution(s),
- uncertainties related to the modelling of the signal process, and
- an uncertainty related to the unfolding procedure.

In addition, the statistical uncertainty of the measured data must be considered. In the remainder of this section, the various sources of uncertainty as well as the techniques used to estimate their respective impact are discussed in detail.

Each source of uncertainty is treated individually. For each source the treatment procedure yields a covariance matrix which describes the effect of this uncertainty for all bins of all measured observables simultaneously. Hence, the covariance matrix contains information about cross-correlations. Given a set of multiple covariance matrices, each corresponding to a different source of uncertainty, the combined uncertainty is obtained by summation of the covariance matrices. By combining the covariance matrices from all considered sources of uncertainty, the total uncertainty is determined which retains the cross-correlations. Therefore, the total covariance matrix includes information regarding how the combined uncertainty simultaneously affects different bins and also different observables.

13.6.1 Experimental Uncertainties

Sources of experimental uncertainty affect the measurement in a variety of ways. These sources are mostly related to uncertainties of the modelling of the general detector response. In the unfolding formalism symbolised by Equation (32), experimental uncertainties can affect the luminosity \mathcal{L}_{Int} , the phase-space correction factors ϵ and ϵ_{Fid} , the detector response matrix \mathcal{M} , and the background estimate N_{Bkg} . Each source of experimental uncertainty is treated individually by repeating the full unfolding procedure using inputs that have been varied according to the effect of the source of uncertainty. This is illustrated in Figure 83.

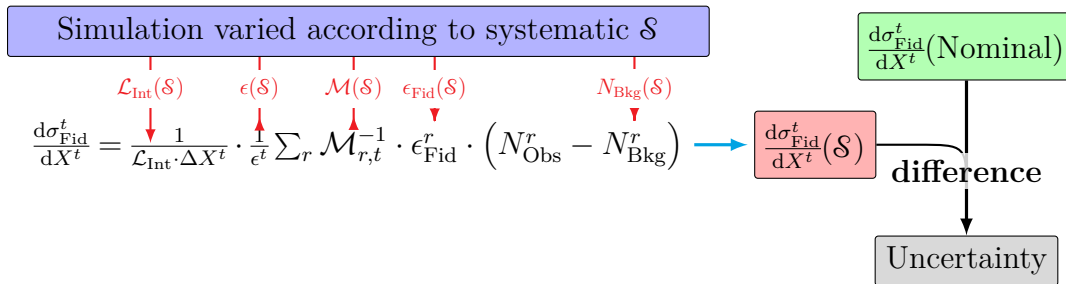


Figure 83: Illustration of procedure used to evaluate detector modelling uncertainties.

The varied inputs are constructed following a procedure similar to that discussed in Section 12.5.1: events with systematically varied physics-objects, such as electrons or jets, are constructed from the nominal simulation samples. Varied unfolding inputs are constructed from these events using the regular analysis procedure. The unfolding result obtained from the varied inputs is compared to the nominal result and the difference is taken as systematic uncertainty. For each bin, the sign of the difference is relevant for the off-diagonal terms of the covariance matrix as it encodes the direction of bin-by-bin correlations. In this approach, the measured data remain unchanged and enter the calculation for each source of experimental uncertainty.

Integrated Luminosity The integrated luminosity is used to scale the simulation-based background predictions which are subtracted from data before unfolding. This uncertainty does not require to create systematically varied copies of the simulated data. Rather, the luminosity scale-factor used by the background predictions is modified according to the pre-determined uncertainty on the luminosity to construct varied inputs for the unfolding. The uncertainty on the combined 2015 and 2016 integrated luminosity is 2.1% which is derived following a methodology similar to that detailed in Ref. [192], from a calibration of the luminosity scale using x - y beam-separation scans performed in August 2015 and May 2016.

Pile-Up Reweighting As was discussed in Section 7.3, pile-up is modelled in simulation using an overlaid minimum bias simulation. A reweighting procedure is employed to ensure that the conditions in simulation, which are fixed at the time the MC samples are generated, reflect the conditions in data. An uncertainty related to the reweighting is evaluated by varying the weight factors according to uncertainties constructed to cover differences between the observed and expected inelastic pp cross-sections [219].

Lepton Uncertainties As was discussed in Section 8, the lepton identification, isolation, reconstruction, and trigger requirements give rise to efficiency corrections and kinematic calibrations. Uncertainties due to the modelling of these items are evaluated by scaling efficiencies and calibrations according to uncertainties derived from data in control regions enriched in $Z \rightarrow \ell\ell$, $W \rightarrow \ell\nu$, or J/Ψ events [106, 142, 147, 220]. A variety of individual effects is considered separately, each giving rise to one component of the total lepton uncertainty.

Jet Uncertainties Modelling of the jet energy scale (JES) and resolution (JER) affects the measurement in several ways. In addition to the event selection, the assignment of jets to different parts of the topology may be affected by a change in the jet four-momenta. This affects the p_T -order of the jets and thus influences which jet is selected for the calculation of each measured observable. Uncertainties on JES and JER are derived using a combination of simulation, test-beam data, and *in situ* measurements [157, 194, 221–223]. Additionally, contributions from η -intercalibration, single-particle response, pile-up, jet flavour composition, punch-through, and variations in the calorimeter response to different jet flavours are considered. For the JES, this results in a scheme composed of 20 systematic variations.

b-Tagging Uncertainties Modelling of the b -tagging has effects similar to those of the modelling of JES and JER. In simulation, corrections are applied to efficiencies related to the performance of the b -tagging procedure in order to account for differences between data and simulation. These correction factors are extracted through comparison of simulation and data separately for b -,

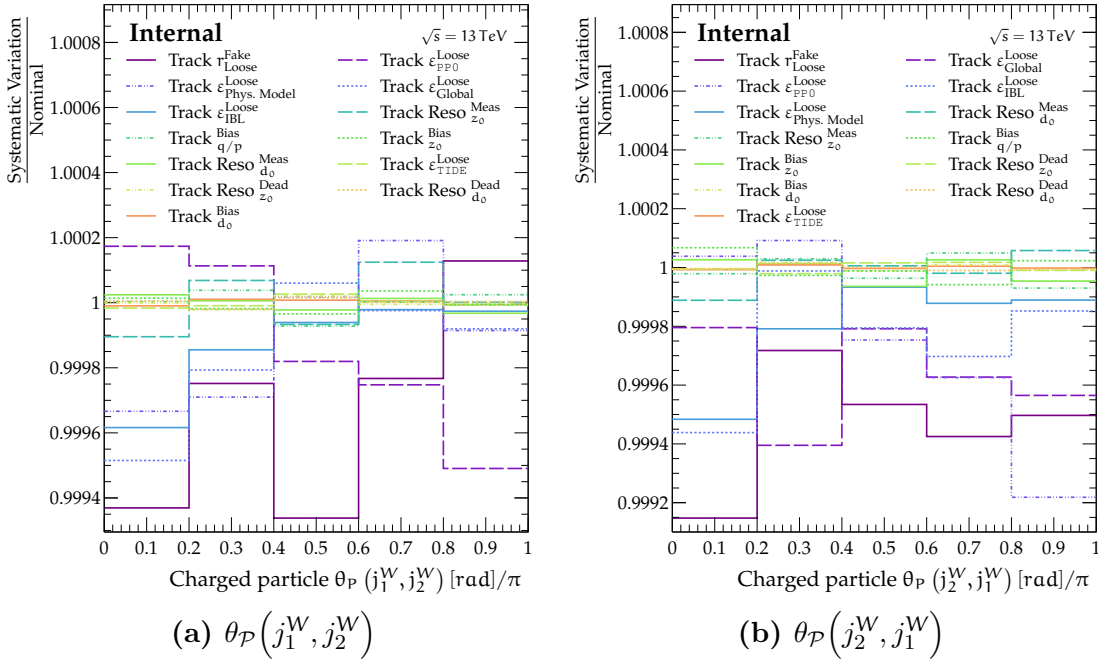


Figure 84 (1/2): Effect of track object systematics on the shape of the analysis observables. Each subfigure shows the ratio of the systematic variation over the nominal configuration. The systematic sources are ordered by their total absolute deviation from nominal. Shown are the (a) forward and (b) backward pull angle for the hadronically decaying W boson daughters, (c) the magnitude of the leading W daughter’s jet-pull vector, and (d) the forward di-b-jet-pull angle.

c -, and light jets, which also accounts for mis-tags. Uncertainties related to this procedure are propagated by modifying the correction factors within their uncertainties [159, 224, 225].

$E_{\text{T}}^{\text{miss}}$ Uncertainties Calculation of $E_{\text{T}}^{\text{miss}}$ depends on the calibrated four-momenta of leptons and jets. Uncertainties on $E_{\text{T}}^{\text{miss}}$ due to systematic shifts in the corrections and calibrations applied for those objects are treated in a fully correlated way as part of the specific lepton and jet systematics. Additional uncertainties on $E_{\text{T}}^{\text{miss}}$ arise due to the modelling of the soft-term scale and resolution. They are treated separately using uncertainties derived from data [163, 226].

Track Object Systematics Inner-detector tracks are used as jet constituents that directly enter the calculation of the jet-pull vector, see Equation (28). Consequently, uncertainties due to the modelling of the reconstructed ID tracks directly influence the measured jet-pull vector. The track object systematics are expressed as change in the tracking efficiency or as smearing of the track momentum [105, 107]. A combination of simulation and measured data — from minimum-bias, dijet, and $Z \rightarrow \mu\mu$ selections — is used to extract corrections and scale factors as well as their uncertainties. In most cases, the systematic shifts that account for the uncertainties are parameterised in the track p_{T} and η to account for variations in the modelling, see Ref. [107].

Figure 84 shows the ratio of the distributions obtained from the systematically varied and nominal $t\bar{t}$ configuration for each of the measured jet-pull observables and track object systematics.

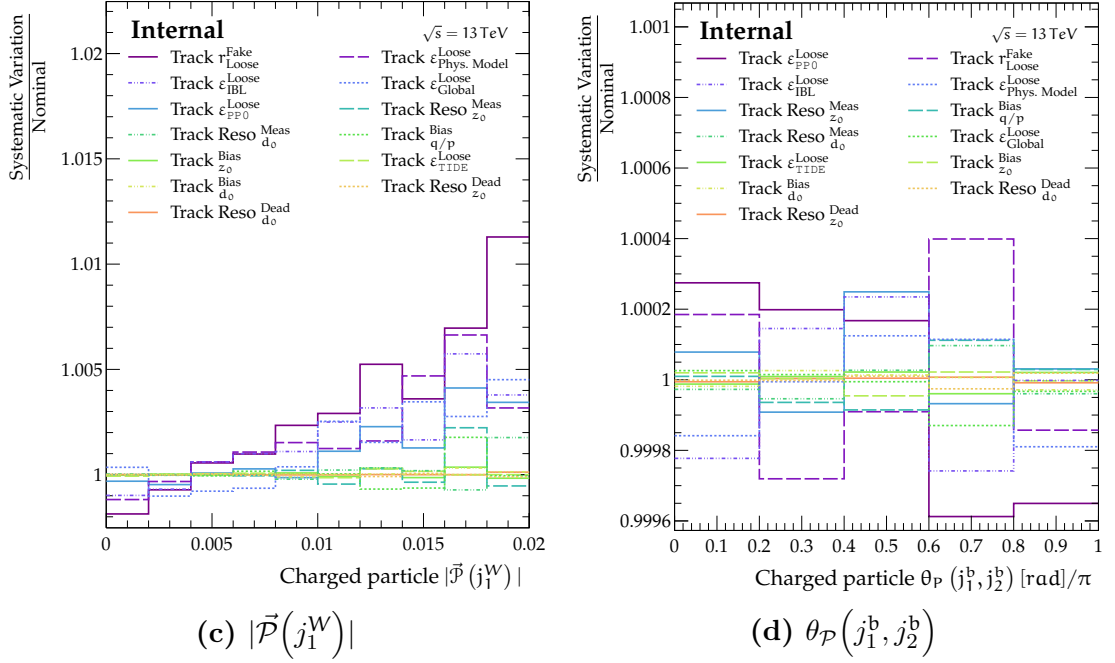


Figure 84 (2/2): continued

In general, the fake rate and efficiency components are dominant across all four observables. In comparison with other modelling effects, such as in particular the signal modelling effects related to the overall simulation modelling of the $t\bar{t}$ process, the impact of the track object systematics on the shape of the observed distributions is small.

13.6.2 Signal Modelling Uncertainties

The method used to evaluate the signal modelling uncertainties differs from the general procedure used to estimate the other sources of uncertainty. Signal modelling uncertainties are evaluated using only $t\bar{t}$ simulation samples. Each type of signal modelling uncertainty is estimated using a different *alternative* $t\bar{t}$ simulation sample. Roughly the evaluation procedure follows the diagram shown in Figure 85, which translates to:

- 1.) For a given observable, the detector-level and particle-level distributions are constructed from the alternative $t\bar{t}$ sample.
- 2.) The detector-level distribution from the alternative $t\bar{t}$ sample is directly unfolded. In the unfolding formalism given by Equation (32), this corresponds to replacing the difference $N_{\text{Obs}} - N_{\text{Bkg}}$ by $N_{\text{Sig}}^{\text{MC}}$, where $N_{\text{Sig}}^{\text{MC}}$ is the detector-level distribution from the alternative $t\bar{t}$ simulation. Unfolding uses the regular response matrix and correction factors taken from the nominal $t\bar{t}$ simulation sample.
- 3.) The bin-by-bin deviations between the unfolding result and the particle-level distribution taken from the alternative $t\bar{t}$ sample are assigned as uncertainty.

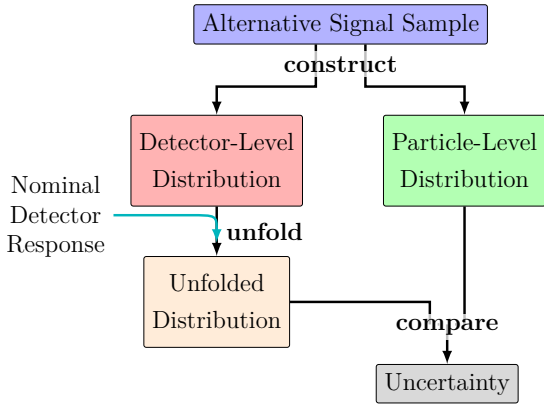


Figure 85: Illustration of signal modelling uncertainty estimation procedure.

Modelling uncertainties related to the amount of initial- and final-state radiation (ISR/FSR) and the amount and strength of the colour-reconnection (CR) mechanism are evaluated using samples generated with variations of the setup used for the nominal $t\bar{t}$ sample. In Section 13.2.2 more details on these simulation samples are given.

Uncertainties related to the choice of PDF are evaluated using weight variations available in the nominal $t\bar{t}$ simulation. The weight variations are calculated as part of generating the hard-scatter event according to the PDF4LHC prescription [199]. This measurement uses a scheme of 30 different weight variations. Detector- and particle-level distributions are constructed for each weight variation. The detector-level distributions are unfolded using the procedure discussed above and for each variation the deviation between the unfolding result and the corresponding particle-level distribution is calculated. A single per-bin PDF uncertainty is constructed from all deviations using the PDF4LHC procedure.

13.6.3 Background Modelling Uncertainties

The estimated background contributions are subtracted from the measured data prior to unfolding. Consequently, systematic uncertainties related to the modelling of the background estimate affect the signal distributions that enter the unfolding.

Uncertainties on NP and Fake Lepton Estimate The contribution of the NP and fake lepton background is estimated from data. A normalisation uncertainty of 50% is assigned to the estimated background contribution. This normalisation uncertainty is considerably larger than the magnitude of any observed data–MC disagreement, see Section 13.4.2.

In addition, a modelling uncertainty that is related to the choice of parameterisation used by the matrix method is assigned. The regular efficiency parameterisation is replaced by an alternative choice and the fake-lepton estimate is re-evaluated. The unfolding is repeated with the alternative fake-lepton estimate and the deviation w.r.t. the nominal unfolding result is assigned as uncertainty. The alternative parameterisation was chosen such that the resulting uncertainty adequately covers any disagreement observed for kinematic

control variables between data and prediction in various background-dominated control regions.

Uncertainties on Cross-Section Predictions Each of the backgrounds that are estimated directly from simulation must be scaled to the size of the measured dataset using a theoretical cross-section prediction. A normalisation uncertainty is assigned to account for the uncertainty of the cross-section prediction. Table 14 lists the size of the normalisation uncertainty for each type of background. For the $W/Z + \text{jets}$ backgrounds, the uncertainties are parameterised in the number of jets to include a contribution from the overall cross-section normalisation (4 %) as well as an additional 24 % uncertainty added in quadrature for each jet [202, 203].

Sample	Uncertainty [%]	
Single top (s -channel, t)	3.6	[46]
Single top (s -channel, \bar{t})	4.8	[46]
Single top (t -channel, t)	4.0	[44]
Single top (t -channel, \bar{t})	5.0	[44]
Single top (Wt)	5.3	[47]
$W + \text{jets}$	$\sqrt{4^2 + N_{\text{Jets}} \times 24^2}$	[202, 203]
$Z + \text{jets}$	$\sqrt{4^2 + N_{\text{Jets}} \times 24^2}$	[202, 203]
Diboson	6	[227]
$t\bar{t}W$	13	[213, 228]
$t\bar{t}Z$	12	[213, 228]
$t\bar{t}H$	100	

Table 14: Breakdown of the relative uncertainties on the cross-section predictions used to scale the background Monte Carlo samples.

Single-Top Background Modelling Alternative simulation samples are used to estimate the impact of increased or reduced radiation in single-top events. These samples are generated using a procedure similar to that used to create $t\bar{t}$ signal samples with increased or reduced radiation, see Section 13.2. For both settings, an alternative single-top prediction is calculated and used as part of the unfolding instead of the nominal prediction.

Single-top events produced at NLO in the Wt channel have an irreducible overlap with events generated for the $t\bar{t}$ signal, as discussed previously in Section 12.5.3. The nominal configuration uses the DR scheme to treat this overlap. A systematic uncertainty is assigned to the modelling of the overlap by replacing the nominal Wt single-top prediction with that obtained from a sample that uses the DS scheme instead. The systematic uncertainty is evaluated as the difference between the unfolding results obtained when using the DR and the DS scheme.

Due to the higher-order overlap of the $t\bar{t}$ signal and the Wt single-top background, the colour flow in Wt events is of the same type as the colour flow in the $t\bar{t}$ signal topology. However, since Wt is considered to be a background,

this contribution is simply estimated from simulation and subtracted from data. As a result, a mismodelling of the colour flow in Wt could affect and potentially bias the result. For each of the measured observables, a Wt colour-model uncertainty is constructed using the following procedure:

- 1.) The sum of $t\bar{t}$ and Wt , as obtained from simulation, is reweighted such that it matches the distribution observed in data.
- 2.) The nominal Wt single-top distribution of each observable is replaced by the Wt single-top component of the reweighted distribution.
- 3.) The unfolding proceeds as normally but uses the reweighted Wt single-top distributions as part of the background subtraction.
- 4.) The difference of the unfolding result w.r.t. the nominal unfolding result is assigned as uncertainty.

13.6.4 Unfolding Procedure Systematic

A data-driven approach is used to assess the uncertainty that arises from the unfolding procedure, also called non-closure uncertainty. For each of the measured observables, simulated $t\bar{t}$ events are reweighted at particle level such that the corresponding detector-level distribution is in better agreement with the data. A linear-weight function is used and the particle-level weights are propagated to the corresponding detector-level events. The distributions constructed at detector level using these weights are unfolded using the nominal detector-response model. Deviations of the unfolding result from the reweighted particle-level distributions are assigned as non-closure uncertainty.

13.6.5 Statistical Uncertainty

The statistical uncertainty of the data is evaluated using the bootstrap method [229]. The method is as follows: a replica of the measured distribution for each observable is created by sampling from the data. Events from the data may enter the resampling multiple times. Each individual event is considered with a frequency given by a **POISSON** distribution with $\lambda = 1$. In the end, the replica is constructed using $n' = \text{POISSON}(\lambda = n)$ events from the data, where n is the number of events of the original dataset. The process is repeated many times, yielding a new independently sampled replica each time. These replicas differ by an amount that is related to the statistical precision of the data. Each replica is unfolded individually using the regular response matrix. The variance of the unfolding results across the ensemble of bootstrap replicas is then used to assess the statistical uncertainty. Similarly, the statistical component of the covariance matrix of the measurement result is obtained directly from the unfolded bootstrap replicas.

In addition to estimating the statistical uncertainty, the bootstrap replicas can also be used to evaluate statistical bin-to-bin correlations of pre- or post-unfolding distributions.

$\Delta\theta_{\mathcal{P}}(j_1^W, j_2^W)$ [%]	$\theta_{\mathcal{P}}(j_1^W, j_2^W)$			
	0.0 – 0.21	0.21 – 0.48	0.48 – 0.78	0.78 – 1.0
Hadronisation	0.55	0.13	0.24	0.14
Generator	0.32	0.25	0.50	0.01
<i>b</i> -tagging	0.35	0.13	0.20	0.31
Background Model	0.30	0.16	0.16	0.27
Colour Reconnection	0.22	0.16	0.16	0.18
JER	0.11	0.12	0.23	0.02
Pile-up	0.19	0.16	0.00	0.01
Non-closure	0.14	0.07	0.07	0.18
JES	0.12	0.06	0.14	0.06
ISR / FSR	0.15	0.02	0.12	0.02
Tracks	0.05	0.04	0.03	0.06
Other	0.02	0.01	0.01	0.02
Syst.	0.88	0.44	0.71	0.51
Stat.	0.23	0.19	0.19	0.25
Total	0.91	0.48	0.73	0.57

(a) $\theta_{\mathcal{P}}(j_1^W, j_2^W)$

$\Delta\theta_{\mathcal{P}}(j_2^W, j_1^W)$ [%]	$\theta_{\mathcal{P}}(j_2^W, j_1^W)$			
	0.0 – 0.19	0.19 – 0.485	0.485 – 0.8	0.8 – 1.0
Non-closure	0.54	0.00	0.02	0.53
Hadronisation	0.31	0.36	0.20	0.57
<i>b</i> -tagging	0.37	0.06	0.16	0.24
ISR / FSR	0.34	0.15	0.08	0.25
Colour Reconnection	0.34	0.22	0.09	0.16
Generator	0.27	0.06	0.23	0.18
Pile-up	0.32	0.04	0.14	0.06
JES	0.24	0.09	0.08	0.25
Background Model	0.25	0.11	0.13	0.19
JER	0.09	0.02	0.07	0.19
Tracks	0.13	0.05	0.07	0.08
Other	0.02	0.02	0.02	0.02
Syst.	1.04	0.48	0.43	0.97
Stat.	0.30	0.21	0.21	0.30
Total	1.08	0.52	0.48	1.02

(b) $\theta_{\mathcal{P}}(j_2^W, j_1^W)$

Table 16 (1/2): Summarised uncertainty breakdown for the four measured observables. Listed are the uncertainties for the (a) forward and (b) backward pull angle for the hadronically decaying *W* boson daughters, (c) the magnitude of the leading *W* daughter’s jet-pull vector, and (d) the forward di-*b*-jet-pull angle. Uncertainties are expressed in percent of the measured value and are ordered by the mean value across all bins. The contributions of the uncertainties due to jet energy scale, jet energy resolution, and initial / final state radiation are abbreviated as “JES”, “JER”, and “ISR / FSR”, respectively; the category “Other” summarises various smaller uncertainty components.

$\Delta \vec{\mathcal{P}}(j_1^W) $ [%]	$ \vec{\mathcal{P}}(j_1^W) \times 10^3$				
	0.0 – 1.5	1.5 – 3.0	3.0 – 5.4	5.4 – 9.2	9.2 – 20.0
Colour Reconnection	1.19	0.34	0.47	0.47	0.47
ISR / FSR	1.08	0.23	0.47	0.47	0.47
Generator	0.93	0.30	0.09	0.49	1.72
Pile-up	0.72	0.23	0.28	0.56	1.21
Background Model	0.68	0.31	0.30	0.42	1.00
JES	0.65	0.35	0.05	0.76	1.84
Hadronisation	0.53	0.31	0.41	0.67	0.10
Tracks	0.35	0.25	0.14	0.39	0.79
b -tagging	0.36	0.08	0.11	0.31	0.55
Non-closure	0.03	0.26	0.38	0.09	2.65
JER	0.14	0.29	0.06	0.45	0.74
Other	0.05	0.03	0.02	0.04	0.06
Syst.	2.33	0.92	0.99	1.63	4.21
Stat.	0.22	0.21	0.19	0.26	0.47
Total	2.34	0.94	1.00	1.65	4.24

(c) $|\vec{\mathcal{P}}(j_1^W)|$

$\Delta\theta_P(j_1^b, j_2^b)$ [%]	$\theta_P(j_1^b, j_2^b)$			
	0.0 – 0.24	0.24 – 0.5	0.5 – 0.75	0.75 – 1.0
Hadronisation	0.71	0.37	1.18	0.87
ISR / FSR	0.23	0.23	0.07	0.52
Colour Reconnection	0.21	0.21	0.05	0.37
Generator	0.00	0.23	0.04	0.27
Non-closure	0.17	0.00	0.01	0.17
JER	0.12	0.02	0.02	0.12
Background Model	0.10	0.02	0.05	0.07
b -tagging	0.08	0.03	0.04	0.07
Pile-up	0.07	0.04	0.02	0.01
JES	0.06	0.02	0.03	0.04
Tracks	0.03	0.02	0.02	0.01
Other	0.02	0.01	0.02	0.01
Syst.	0.81	0.54	1.19	1.14
Stat.	0.10	0.08	0.08	0.10
Total	0.82	0.55	1.19	1.14

(d) $\theta_P(j_1^b, j_2^b)$ Table 16 (2/2): *continued*

The magnitude of the jet-pull vector is sensitive to the number of objects that enter the jet-pull-vector calculation. Modelling of the colour reconnection mechanism is known to affect average hadron multiplicities within jets, see Refs. [52, 53]. This is reflected in the fact that the CR modelling uncertainty is the dominant source of uncertainty on the measurement of the magnitude of the jet-pull vector $|\vec{\mathcal{P}}(j_1^W)|$.

The uncertainty that is related to the modelling of the background prediction is sub-dominant. The largest contribution to this uncertainty category comes from the modelling of the single-top background, in particular the uncertainty related to the Wt colour-model.

Uncertainties on the track objects have comparatively small uncertainties, especially for the pull angles. Their effect is somewhat larger for the magnitude of the jet-pull vector $|\vec{\mathcal{P}}(j_1^W)|$, which is possibly related to its sensitivity to the number of particles that enter the jet-pull-vector calculation. Uncertainties related to the modelling of leptons, the missing transverse energy E_T^{miss} , and the JVT as well as the uncertainty on the luminosity have practically negligible impact on the total uncertainty, as does the uncertainty due to the modelling of the PDFs in the $t\bar{t}$ signal sample.

13.7.1 Comparison with Standard Model Predictions

Figure 86 shows the measured and unfolded distributions graphically and compares them to a variety of Standard Model predictions. The same measured distributions are compared to an extended set of predictions in Figure 87. All predictions are obtained directly at particle level from simulated $t\bar{t}$ events using the samples discussed in Section 13.2.2.

The majority of SM predictions are generated using POWHEG as the NLO generator. The PS and hadronisation is then either performed with PYTHIA, in version 6 or 8, or using HERWIG 7. One SM prediction is generated using MG5_aMC instead but also uses PYTHIA 8 for the PS and hadronisation. Lastly, one SM prediction is taken from SHERPA which is an MC generator that combines ME and PS simulation in a single program. The extended comparison shown in Figure 87 adds panels that compare the unfolded data to samples generated as variations of the nominal signal MC. These are the variations used to assess the effects of ISR / FSR and CR.

For the observables sensitive to the “*signal colour flow*”, predictions obtained from POWHEG + HERWIG 7 agree best with the measured data. Generally, agreement of the nominal SM $t\bar{t}$ prediction with the observed distribution is poor for these observables. The predictions obtained from MG5_aMC combined with PYTHIA 8 are in considerably better agreement with the data than those obtained from POWHEG combined with PYTHIA 8. None of the predictions model the magnitude of the jet-pull vector of the leading W boson daughter $|\vec{\mathcal{P}}(j_1^W)|$ well. While POWHEG + HERWIG 7

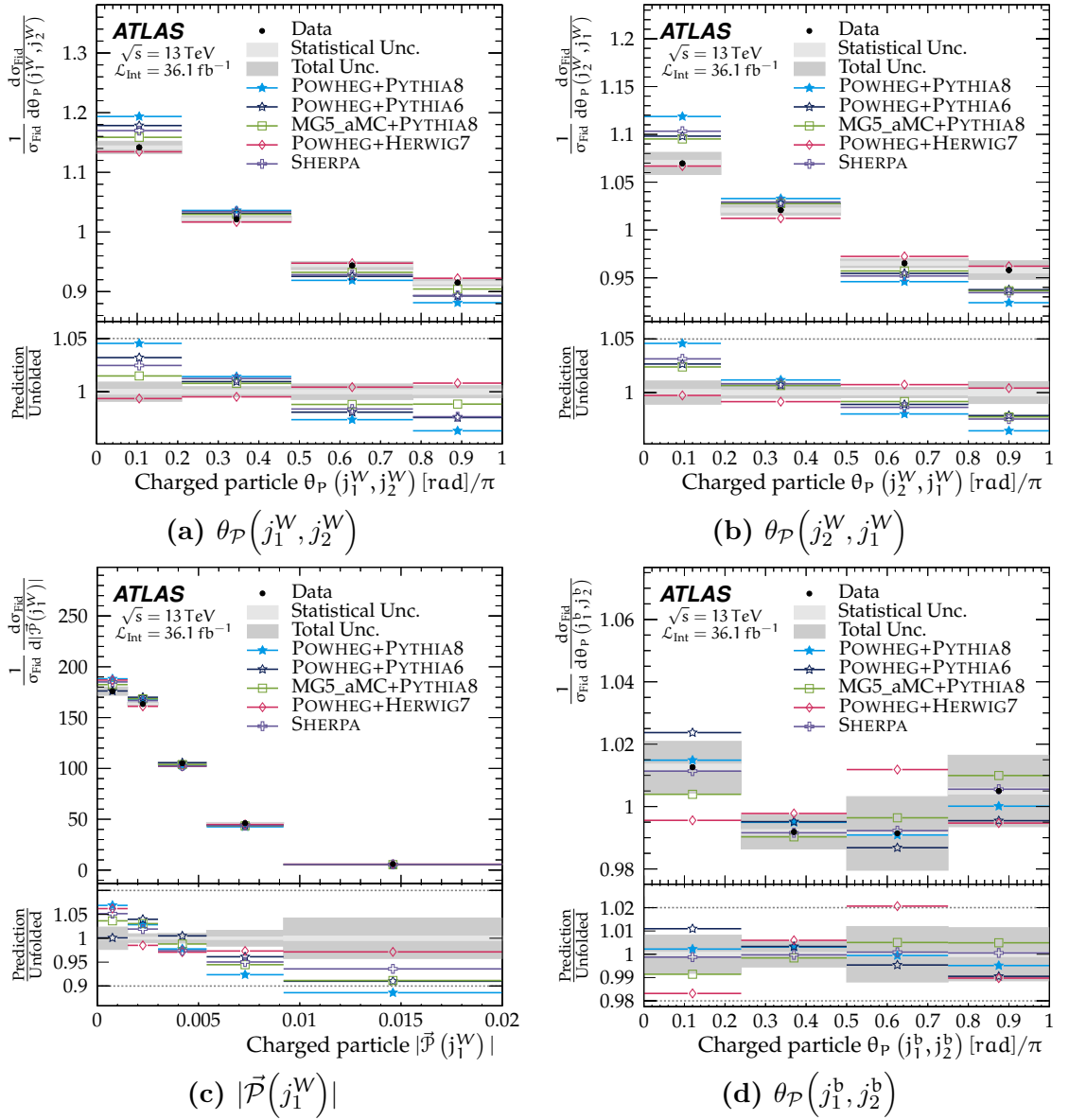


Figure 86: Normalised fiducial differential cross-sections as a function of the (a) forward and (b) backward pull angle for the hadronically decaying W boson daughters, (c) the magnitude of the leading W daughter’s jet-pull vector, and (d) the forward di- b -jet-pull angle. The data are compared to various SM predictions. The statistical uncertainties in the predictions are smaller than the marker size.

describes the four highest-valued bins quite well, it predicts considerably more events with small $|\vec{\mathcal{P}}(j_1^W)|$.

For the forward di- b -jet-pull angle $\theta_{\mathcal{P}}(j_1^b, j_2^b)$, all predictions broadly agree with the observed distribution. The prediction from **POWHEG + HERWIG 7** exhibits the strongest deviations w.r.t. the data. **SHERPA**, which otherwise has similar deviations as **POWHEG + PYTHIA 6**, agrees extremely well with the measured data.

Predictions from **POWHEG** combined with the older **PYTHIA 6** are in better agreement with the data than **POWHEG** combined with the more recent **PYTHIA 8**.⁴ However, this trend is not found for the di- b -jet-pull angle although both predictions agree reasonably well for this observable.

⁴ Note that the sample generated with **PYTHIA 6** uses a different configuration than the sample generated with **PYTHIA 8**, see Section 13.2.2.

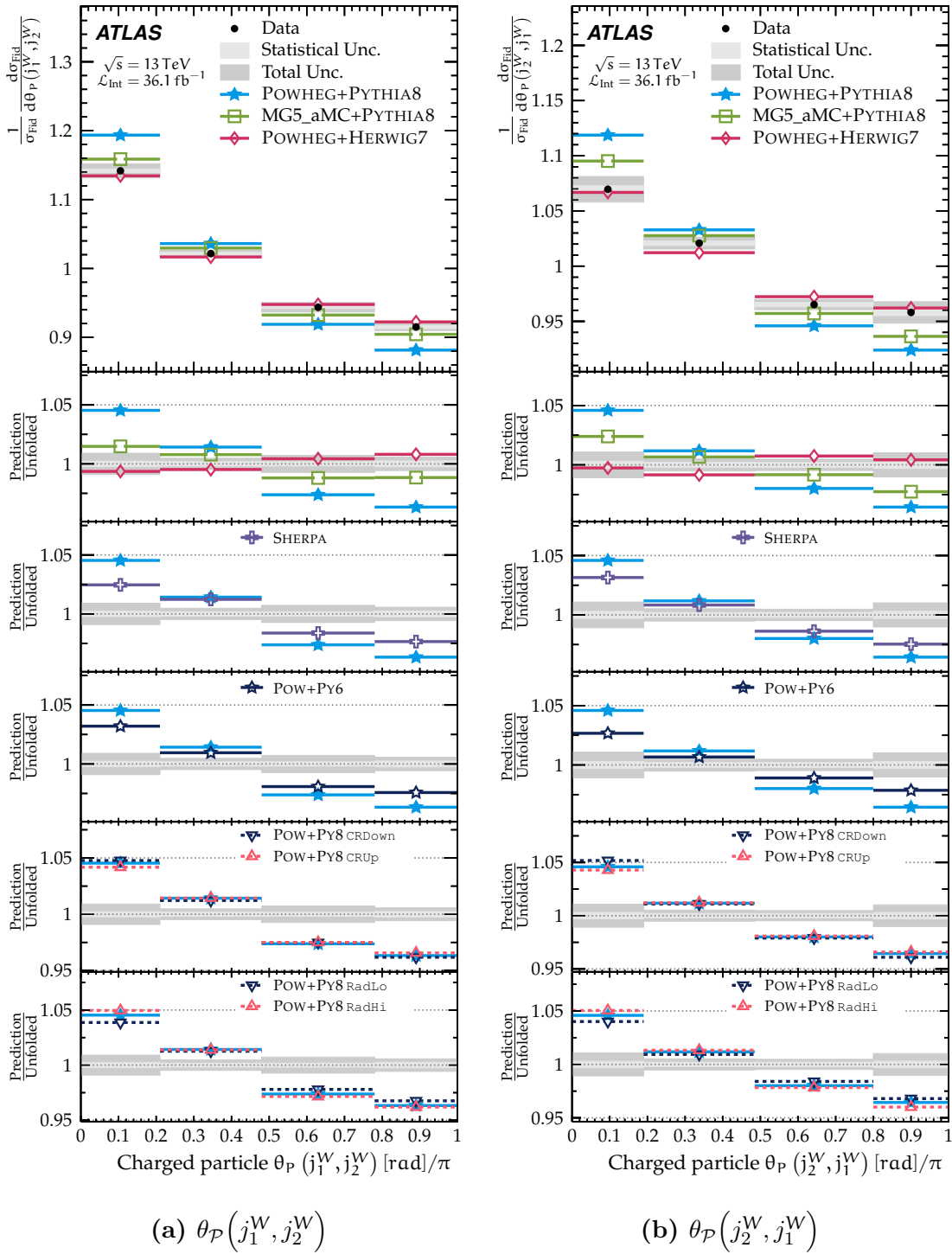
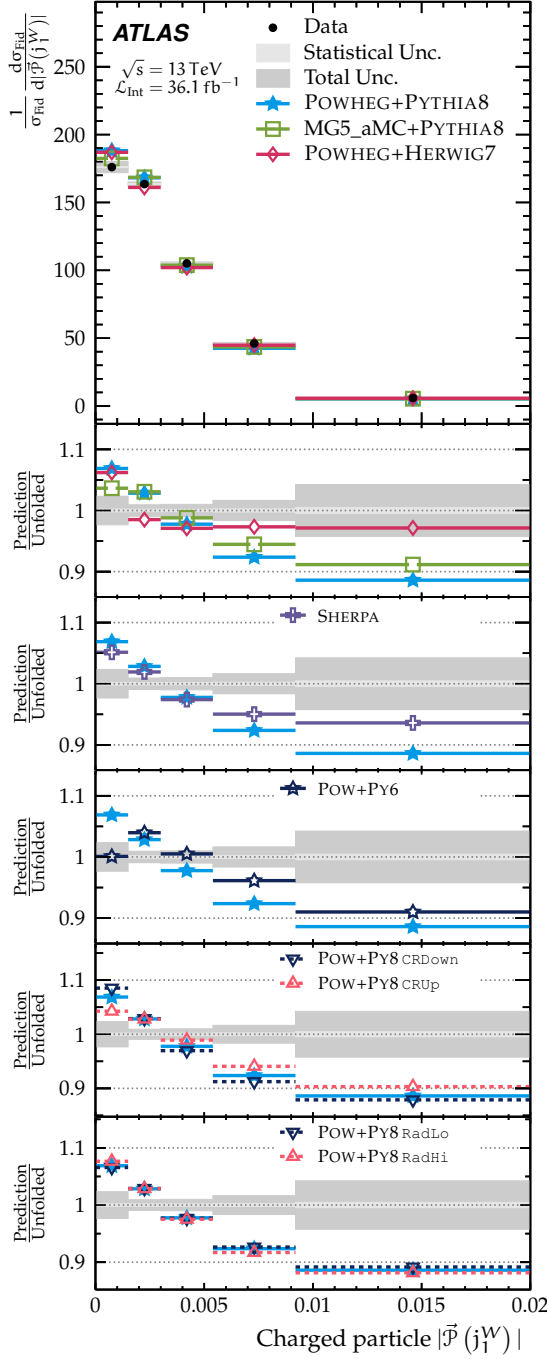
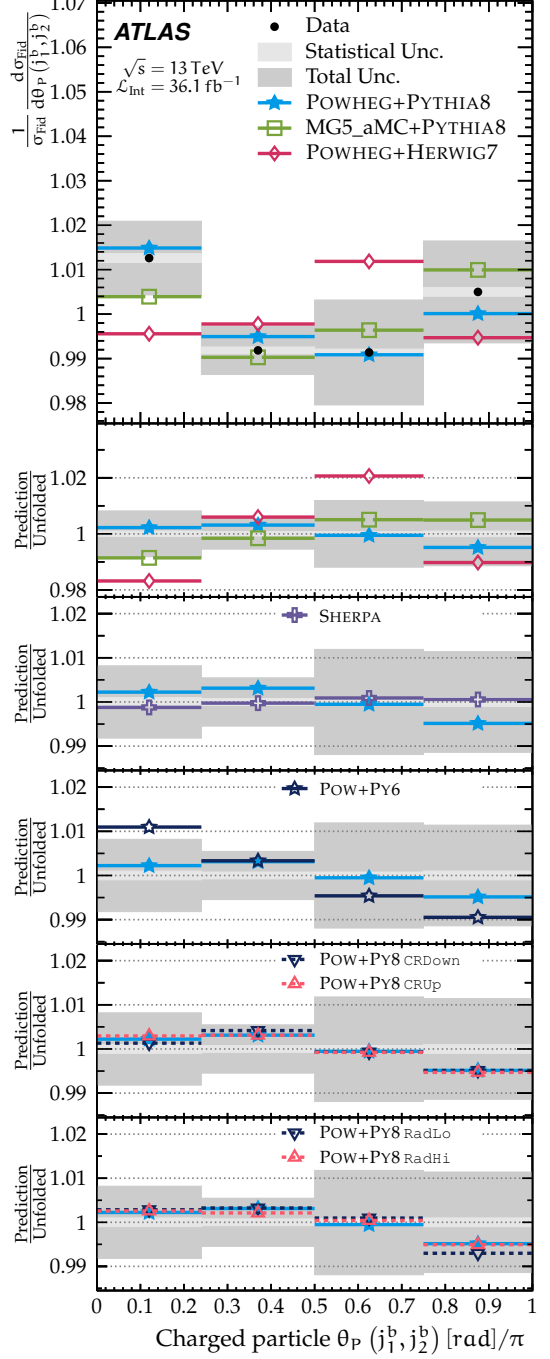


Figure 87 (1/2): Normalised fiducial differential cross-sections as a function of the (a) forward and (b) backward pull angle for the hadronically decaying W boson daughters, (c) the magnitude of the leading W daughter’s jet-pull vector, and (d) the forward di-b-jet-pull angle. The data are compared to various SM predictions as well as predictions obtained from the modelling variations of the nominal signal sample, see Section 13.2.2. The statistical uncertainties in the predictions are smaller than the marker size. The following abbreviations are used: *Pow* – POWHEG, *Py6* – PYTHIA 6, *Py8* – PYTHIA 8, *CRDown* / *CRUp* – the CR modelling variations, *RadLo* / *RadHi* – the modelling variations with reduced / enhanced radiation.



(c) $|\vec{P}(j_1^W)|$



(d) $\theta_{\mathcal{P}}(j_1^b, j_2^b)$

Figure 87 (2/2): continued

13.7.2 Comparison with Exotic Colour Flow

Figure 88 compares the unfolded distributions to the nominal SM prediction as well as the prediction obtained from the sample with exotic colour flow. Both samples are generated with POWHEG + PYTHIA 8.

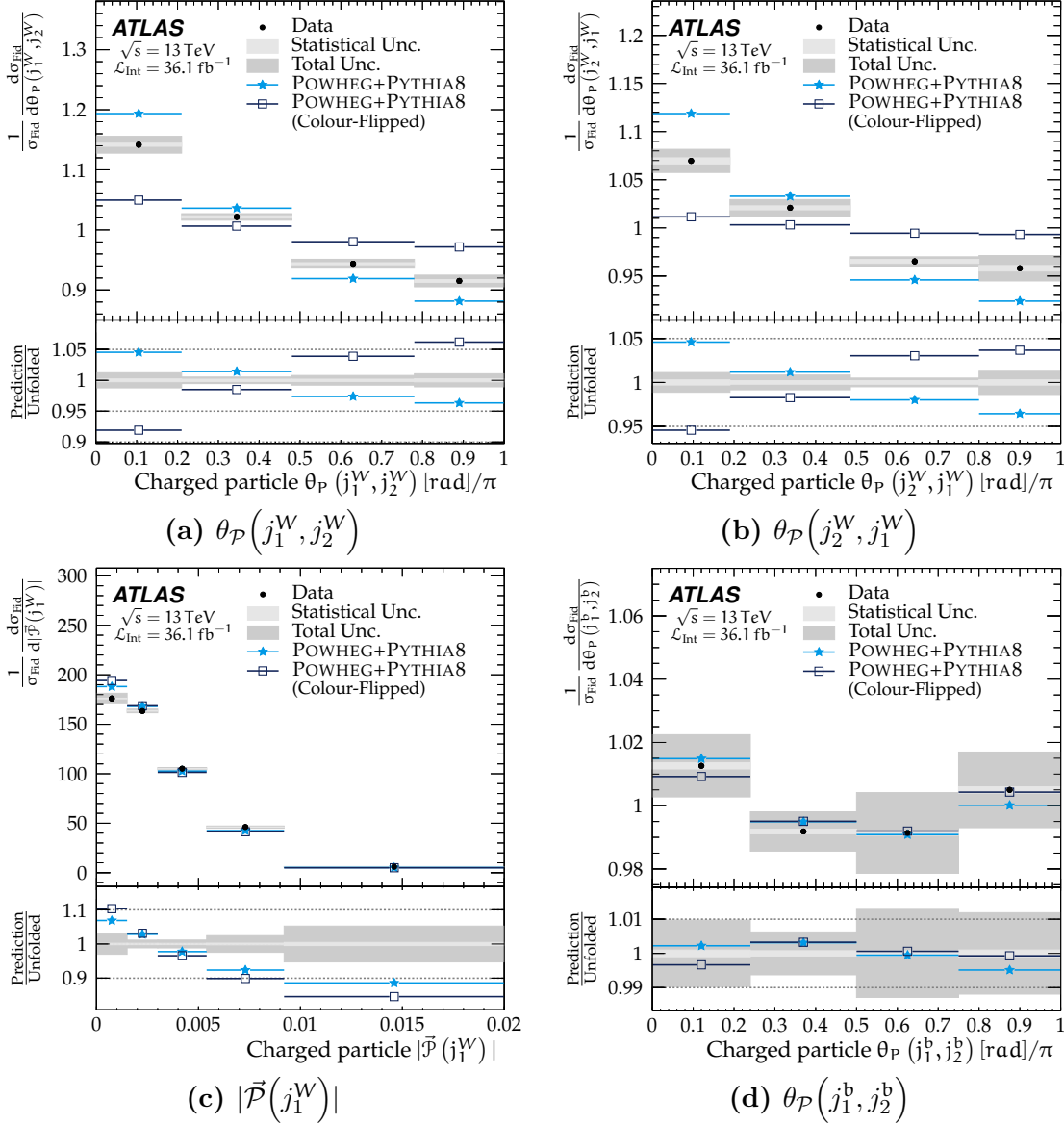


Figure 88: Normalised fiducial differential cross-sections as a function of the (a) forward and (b) backward pull angle for the hadronically decaying W boson daughters, (c) the magnitude of the leading W daughter’s jet-pull vector, and (d) the forward di-b-jet-pull angle. The data are compared to a Standard Model prediction produced with POWHEG + PYTHIA 8 as well as the model with exotic colour flow also created with POWHEG + PYTHIA 8. The uncertainty bands presented in these plots combine the baseline set of systematic uncertainties with effects due to considering the exotic colour-flow model as a source of signal modelling uncertainty. The statistical uncertainties in the predictions are smaller than the marker size.

For the purpose of comparing the unfolded data to the model with exotic colour flow, a “colour-model uncertainty” has been assigned. This uncertainty is evaluated following the same procedure that is used to evaluate the other signal modelling uncertainties, see Section 13.6.2. The alternative $t\bar{t}$ signal sample used by the

procedure is the sample generated with exotic colour flow. This “colour-model uncertainty” is similar in size to the other signal modelling uncertainties.

The data are in better agreement with the prediction obtained from the SM simulation than the prediction with exotic colour flow. However, since the overall agreement with the nominal $t\bar{t}$ sample POWHEG + PYTHIA 8 is relatively poor, the distinction is not as strong as expected from simulation. To study this further, a sample with exotic colour flow generated with POWHEG + HERWIG 7 could be useful. However, such a sample is not available and the decision to use PYTHIA when constructing the colour-flipped sample was made before studying the data.

13.7.3 Statistical Correlations

As was mentioned before, the bootstrap procedure that is used to assess the impact of the data’s statistical uncertainty can also be used to construct a global statistical correlation matrix. The global statistical correlation matrix can be constructed pre-unfolding or post-unfolding; both cases are shown in Figure 89.

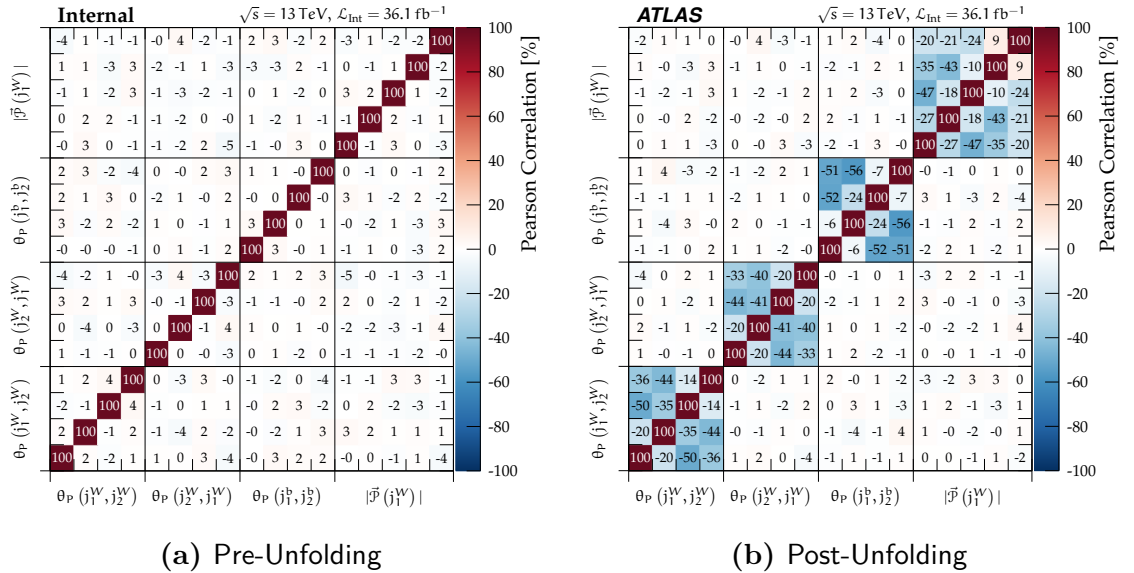


Figure 89: Global statistical correlation matrix of the four analysis observables. Shown are (a) the pre-unfolding statistical correlations which are taken from non-normalised histograms and (b) the post-unfolding statistical correlation which are taken from the normalised unfolding result.

Figure 89a shows the pre-unfolding correlations which are constructed from the non-normalised distributions of the ensemble of bootstrap samples. Correlations across different bins for the same observable are expected to be zero barring fluctuations due to the limited number of bootstrap replicas. As was discussed before, the correlations between the four observables are small. Consequently, the cross-observable correlations of the pre-unfolding distributions are small as well. Figure 89b shows the post-unfolding global correlations which are taken from the normalised distributions of the ensemble of unfolded bootstrap replicas. No meaningful correlations are observed across different observables. As expected from the normalisation, cross-correlations between bins for the same observable are almost always negative.

The two highest-valued bins of the jet-pull vector magnitude $|\vec{\mathcal{P}}(j_1^W)|$ are the only exception to this. The positive correlation likely originates from the fact that, due to the highly sloped distribution and given the relatively poor detector resolution, a fluctuation in the last bin causes tension in the unfolding which pulls the second-to-last bin in the same direction as the last bin and vice-versa.

13.7.4 Goodness of Fit Tests

The agreement of the measured distributions, i.e. the unfolded data, with the predictions obtained from MC simulation can be quantified using a χ^2 goodness-of-fit test. As was discussed previously, the unfolding procedure provides covariance matrices $\Sigma_{\text{Syst}}(s)$ for each source s of systematic uncertainty as well as a covariance matrix Σ_{Stat} which quantifies the statistical uncertainty. The full systematic covariance is obtained by summation of $\Sigma_{\text{Syst}}(s)$ over all sources s . By combining this covariance with the statistical covariance matrix, the total covariance of the measurement is constructed.

The χ^2 test statistic is calculated from the unfolded data \mathbf{D} , the model prediction \mathbf{M} , and the full covariance Σ according to

$$\chi^2 = (\mathbf{D}^T - \mathbf{M}^T) \cdot \Sigma^{-1} \cdot (\mathbf{D} - \mathbf{M}), \quad (34)$$

where \mathbf{M} and \mathbf{D} are expressed as n -vectors and Σ is the $n \times n$ covariance matrix. This calculation does not consider an uncertainty on the theoretical prediction.

As a result of the fact that the measured distributions are normalised, an additional caveat must be considered: the normalisation requirement removes one degree of freedom from the χ^2 calculation. As a result, elements of \mathbf{M} or \mathbf{D} and columns / rows of Σ are no longer independent. This must be accounted for by dropping one of the n elements of \mathbf{M} and \mathbf{D} and reducing the dimensionality of Σ from $n \times n$ to $(n - 1) \times (n - 1)$ by discarding one column and row. In symbolic form, when applying this procedure to an observable with $n = 4$ bins, Equation (34) can be written as

$$\chi^2 = \left(\begin{array}{|c|c|c|c|} \hline \color{red}{\times} & & & \\ \hline \end{array} \right) \cdot \left(\begin{array}{|c|c|c|c|} \hline \color{red}{\times} & \color{red}{\times} & \color{red}{\times} & \color{red}{\times} \\ \color{red}{\times} & & & \\ \color{red}{\times} & & & \\ \color{red}{\times} & & & \\ \hline \end{array} \right) \cdot \left(\begin{array}{|c|} \hline \color{red}{\times} \\ \hline \end{array} \right), \quad (35)$$

where the symbol $\color{red}{\times}$ marks fields of the vectors and matrix which are ignored for the calculation of χ^2 . The resulting value for χ^2 does not depend on the choice of column / row which is dropped as long as this is done consistently. Subsequently, p -values can be calculated from χ^2 and the number of degrees of freedom (NDF) which is $\text{NDF} = n - 1$. These p -values describe the probability to obtain a χ^2 value greater than or equal to the observed value.

Table 17 lists the resulting values of χ^2 , NDF, and the p -value for each of the four observables considered by the measurement. The p -values corroborate the previous findings discussed in Section 13.7.1. In particular, it can be found that predictions taken from POWHEG + HERWIG 7 provide comparatively good description of the measured data across the board while those taken from POWHEG + PYTHIA 8, the nominal $t\bar{t}$ simulation, fail to describe the data adequately for most observables.

Sample	$\theta_{\mathcal{P}}(j_1^W, j_2^W)$		$\theta_{\mathcal{P}}(j_2^W, j_1^W)$		$\theta_{\mathcal{P}}(j_1^b, j_2^b)$		$ \vec{\mathcal{P}}(j_1^W) $	
	χ^2 /NDF	p -value	χ^2 /NDF	p -value	χ^2 /NDF	p -value	χ^2 /NDF	p -value
POWHEG + PYTHIA 8	50.9 / 3	< 0.001	25.1 / 3	< 0.001	0.7 / 3	0.867	24.8 / 4	< 0.001
POWHEG + PYTHIA 6	23.2 / 3	< 0.001	8.2 / 3	0.042	4.2 / 3	0.240	21.1 / 4	< 0.001
MG5_aMC + PYTHIA 8	6.8 / 3	0.077	6.7 / 3	0.082	2.0 / 3	0.563	17.6 / 4	0.001
POWHEG + HERWIG 7	2.7 / 3	0.446	3.4 / 3	0.328	4.8 / 3	0.190	11.3 / 4	0.023
SHERPA	22.0 / 3	< 0.001	11.9 / 3	0.008	0.0 / 3	0.998	14.1 / 4	0.007
POWHEG + PYTHIA 8*	17.1 / 3	< 0.001	25.0 / 3	< 0.001	0.3 / 3	0.958	11.1 / 4	0.026
Flipped POWHEG + PYTHIA 8*	45.3 / 3	< 0.001	45.9 / 3	< 0.001	2.6 / 3	0.457	17.2 / 4	0.002

Table 17: The χ^2 and resulting p -values for the measured normalised cross-sections obtained by comparing the different predictions to the unfolded data. When comparing the data with the prediction for the exotic colour-flow model, the model itself is considered as an additional source of signal modelling uncertainty and thus added to the covariance matrix. Calculations that include this additional systematic uncertainty are marked with \star .

This procedure can be expanded to include more than one observable. The resulting χ^2 quantifies the combined agreement of the unfolded distributions for both observables with the predictions obtained from simulation. Cross-correlations are accounted for properly by including off-diagonal elements of the covariance matrix. This requires that the treatment of uncertainties is done simultaneously for all observables, thus constructing an $N \times N$ covariance matrix, where N is the sum of the number of bins for all observables. The vectors \mathbf{M} and \mathbf{D} are constructed by concatenating the vectors for different observables. Since all observables are measured as normalised distributions, the number of degrees of freedom is reduced by one for each observable considered.

The reduction affects the calculation of χ^2 , according to Equation (35), as well as NDF and the p -value derived from both. A total of four different combinations of observables is considered:

Combination A, “ W_{Had} Pull”: combines the three observables which are constructed from the jets likely to originate from the W boson. These observables are the jet-pull angles $\theta_{\mathcal{P}}(j_1^W, j_2^W)$ and $\theta_{\mathcal{P}}(j_2^W, j_1^W)$ as well as the jet-pull-vector magnitude $|\vec{\mathcal{P}}(j_1^W)|$. This combination allows to study the overall description of the colour flow of the hadronically decaying W boson.

Combination B, “All Pull Angles”: combines the three jet-pull angles. These observables are $\theta_{\mathcal{P}}(j_1^W, j_2^W)$, $\theta_{\mathcal{P}}(j_2^W, j_1^W)$, and $\theta_{\mathcal{P}}(j_1^b, j_2^b)$. The combination is sensitive to the overall modelling of jet-pull angle observables.

Combination C, “ W_{Had} Pull Angles”: combines the jet-pull angles which are constructed from the jets likely to originate from the W boson. These

observables are $\theta_{\mathcal{P}}(j_1^W, j_2^W)$ and $\theta_{\mathcal{P}}(j_2^W, j_1^W)$. While the observables are sensitive to different bits of jet substructure, they probe the same colour flow. Compared to combination **A**, this combination reduces sensitivity to modelling effects which only affect the jet-pull-vector magnitude.

Combination D, “Global”: combines all four observables into a single, global measurement.

The resulting values of χ^2 , NDF, and the p -value for each of these combinations are listed in Table 18. The p -values calculated for various combinations of observables show that there is no “one-fits-all” prediction: none of the predictions can adequately describe all four measured observables. For example, **POWHEG + HERWIG 7** describes the two jet-pull angles sensitive to the “*signal colour flow*”, both individually and in combination, quite well. However, including the jet-pull angle sensitive to the “*spurious colour flow*” in the combination results in a considerable degradation although the p -value for the single observable is about 19%. Notably, the nominal $t\bar{t}$ prediction, **POWHEG + PYTHIA 8**, agrees poorly with both individual observables and combinations thereof.

Sample	W_{Had} Pull		All Pull Angles		W_{Had} Pull Angles		Global	
	χ^2/NDF	p -value	χ^2/NDF	p -value	χ^2/NDF	p -value	χ^2/NDF	p -value
POWHEG + PYTHIA 8	92.4 / 10	< 0.001	78.6 / 9	< 0.001	64.0 / 6	< 0.001	119.4 / 13	< 0.001
POWHEG + PYTHIA 6	51.2 / 10	< 0.001	42.3 / 9	< 0.001	28.6 / 6	< 0.001	54.6 / 13	< 0.001
MG5_aMC + PYTHIA 8	34.1 / 10	< 0.001	14.5 / 9	0.104	12.0 / 6	0.062	54.7 / 13	< 0.001
POWHEG + HERWIG 7	36.8 / 10	< 0.001	40.9 / 9	< 0.001	6.3 / 6	0.396	95.2 / 13	< 0.001
SHERPA	60.0 / 10	< 0.001	27.5 / 9	0.001	26.6 / 6	< 0.001	62.8 / 13	< 0.001
POWHEG + PYTHIA 8*	90.5 / 10	< 0.001	77.9 / 9	< 0.001	62.3 / 6	< 0.001	119.4 / 13	< 0.001
Flipped POWHEG + PYTHIA 8*	660.1 / 10	< 0.001	171.6 / 9	< 0.001	164.3 / 6	< 0.001	714.7 / 13	< 0.001

Table 18: The χ^2 and resulting p -values for several combinations of the four analysis observables. The calculation is performed using the full, combined covariance matrix including cross-correlation terms between observables.

When comparing the data with the prediction for the exotic colour-flow model, the model itself is considered as an additional source of signal modelling uncertainty and thus added to the covariance matrix. Calculations which include this additional systematic are marked with \star .

14 Jet Pull and Beyond — Colour Flow in Boosted Topologies

CONTENTS	
14.1 The Jet Dipolarity	182
14.2 Particle-Level Studies	183
14.2.1 Application to Resolved Jets	183
14.2.2 Jet Dipolarity from Boosted Jets	184
14.2.3 Combining Jet Dipolarity and Jet-Pull Angle	186
14.3 Summary	187

The jet-pull angle has been introduced as an observable that is expected to be sensitive to the colour flow of two distinct jets. The measurement presented in the previous section affirms this expectation. It is also found that the jet-pull angle is capable of discriminating different colour flow scenarios, i.e. whether the two jets originate from a common colour singlet or not.

Boosted topologies, or more generally topologies which contain (two) jets with a small radial separation ΔR are particularly interesting for studying colour flow. In both cases, the proximity of the coloured partons that initiate the jets is expected to result in more easily measurable colour-connection effects.

This is illustrated by Figure 90 which compares the jet-pull angle distributions in different bins of the radial separation ΔR between the two jets used for calculation of the jet-pull angle. Compared are a simulation according to the SM with the model using exotic colour flow.¹ The difference between the two cases scales with the radial separation: it is maximal for small ΔR and essentially vanishes for large ΔR .

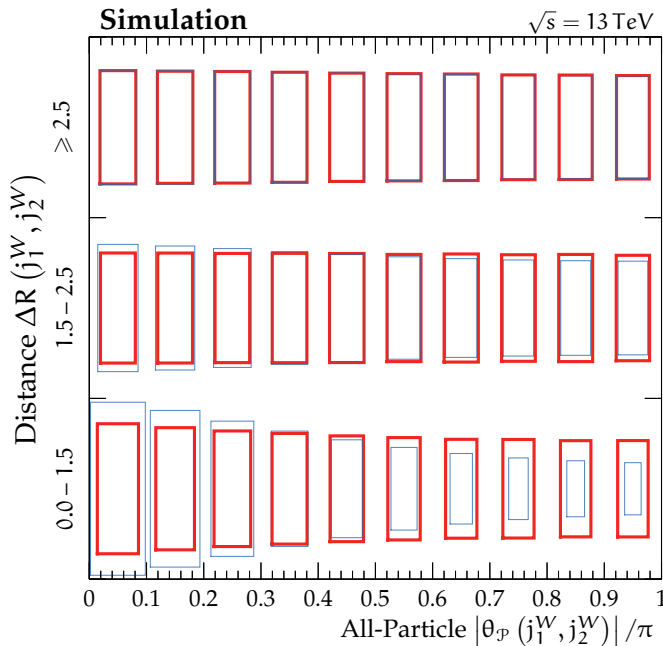


Figure 90: Comparison of the jet-pull angle distributions of the p_T -leading daughter of the hadronically decaying W boson for simulation according to the SM or the model with exotic colour flow in bins of the radial separation ΔR between the two daughters of the hadronically decaying W boson. Box size denotes bin content normalised for each ΔR bin. The blue hatched (red) boxes are constructed from simulation with colour flow according to the SM (the model with exotic colour flow).

¹ The simulation samples correspond to the nominal $t\bar{t}$ sample and the sample with exotic colour flow as discussed in Section 13.2.

However, the jet-pull angle $\theta_{\mathcal{P}}$ is not an ideal observable for studying the colour flow of two distinct jets that originate from two coloured partons. Foremost, $\theta_{\mathcal{P}}$ is only sensitive to the jet substructure of one half of the di-jet system. Hence, it is sensitive to how the enclosing di-jet system is broken into two (sub)jets. This is exacerbated in the boosted topology where the line that delineates the two (sub)jets becomes a noisy construct with considerable dependence on the particularities of the jet clustering algorithm. Furthermore, the procedure must not bias the jet constituent association towards one or the other jet.

Ideally, an observable is sensitive to the radiation from both initiating coloured partons. It should also have no or reduced sensitivity to the specifics of constructing the two (sub)jets. This can be achieved, for example, by separating the process of constructing (sub)jets entirely from the association of radiation used for calculation of the observable. In this section, a study exploring the prospects for analysing colour flow in boosted topologies of $t\bar{t}$ events is presented. The study is performed at particle level using simulated $t\bar{t}$ events.

14.1 The Jet Dipolarity

The jet dipolarity [230] is an observable designed to alleviate some limitations of the jet pull by simultaneously considering the entire radiation pattern emitted by a $X \rightarrow q\bar{q}$ decay. Calculation requires a jet \mathcal{J} and two subjet axes j_1 and j_2 . The jet \mathcal{J} defines a set of constituents $c_i \in \mathcal{J}$ and the subjet axes are just coordinates in y - ϕ space, i.e. $j_{1|2} = (y_{1|2}, \phi_{1|2})$. For each constituent $c_i = (y_i, \phi_i)$, the quantity R_i is the minimum euclidian distance in the y - ϕ space between the constituent and the line segment that runs from j_1 to j_2 . With these definitions, the jet dipolarity \mathcal{D} is defined as the p_{T} -weighted sum

$$\mathcal{D}_{\mathcal{J}}(j_1, j_2) \equiv \frac{1}{R_{12}^2} \sum_{i \in \mathcal{J}} \frac{p_{\text{T},i}}{p_{\text{T},\mathcal{J}}} R_i^2, \quad (36)$$

where $p_{\text{T},i}$ is the transverse momentum of the constituent c_i , $p_{\text{T},\mathcal{J}}$ is the total transverse momentum of the enclosing jet \mathcal{J} , and $R_{12}^2 \equiv (y_2 - y_1)^2 + (\phi_2 - \phi_1)^2$ is the squared length of the line segment from j_1 to j_2 . Figure 91 shows an illustration for calculating R_i and this roughly translates to:

- **when a constituent falls “between” j_1 and j_2 :** R_i is the shortest distance from the constituent c_i to the line segment from j_1 to j_2 :

$$R_i < \min_{j_1, j_2} \Delta R(j, c_i);$$

- **when a constituent falls elsewhere:** R_i is the radial distance from the constituent c_i to the closest subjet axis:

$$R_i = \min_{j_1, j_2} \Delta R(j, c_i).$$

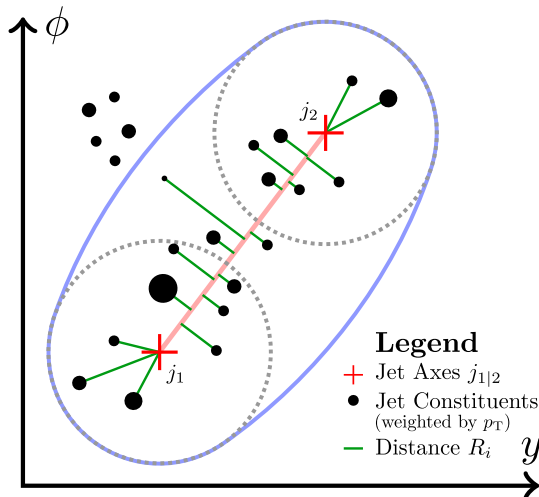


Figure 91: Schematic drawing to symbolise calculation of the distance component R_i for the jet dipolarity \mathcal{D} . Shown are the two subjet axes j_1 and j_2 (red crosses) in rapidity–azimuth space. The light-red line connecting the two axes is the line segment R_{12} . Black dots symbolise (any) jet constituents with their size weighted by their p_T . Constituents inside of the light blue ellipse are considered for calculation of the jet dipolarity. Dark green lines connecting the individual constituents to the line segment R_{12} mark the distance component R_i for each constituent.

Contributions to \mathcal{D} scale linearly in the constituent p_T but quadratically in the distance R_i . Hence, (semi)soft radiation may have considerable impact if it occurs at a sizeable distance from j_1 and j_2 — i.e. outside of the subjet cores. Radiation of this type, out-of-core and not overly soft, is the type of radiation which is expected to encode the difference between a colour-singlet and -octet state in the jet-dipolarity observable: it is expected to be small when most of the radiation enclosed by \mathcal{J} occurs in the region “between” j_1 and j_2 . Conversely, whenever a considerable amount of radiation can be found elsewhere, \mathcal{D} is expected to be larger.

While calculation of \mathcal{D} requires the coordinates j_1 and j_2 , there is no requirement on the association of the constituents c_i to those subjet axes. Consequently, j_1 and j_2 do not have to originate from traditional jet clustering (or splitting) and the constituents are not required to be logically partitioned among j_1 and j_2 .

14.2 Particle-Level Studies

The particle-level studies presented in this section use the same samples of simulated $t\bar{t}$ events that have been discussed in Section 13.2. Events are reconstructed according to the particle-level definitions discussed in Section 9.1 and analysed using a routine implemented in the Rivet framework.

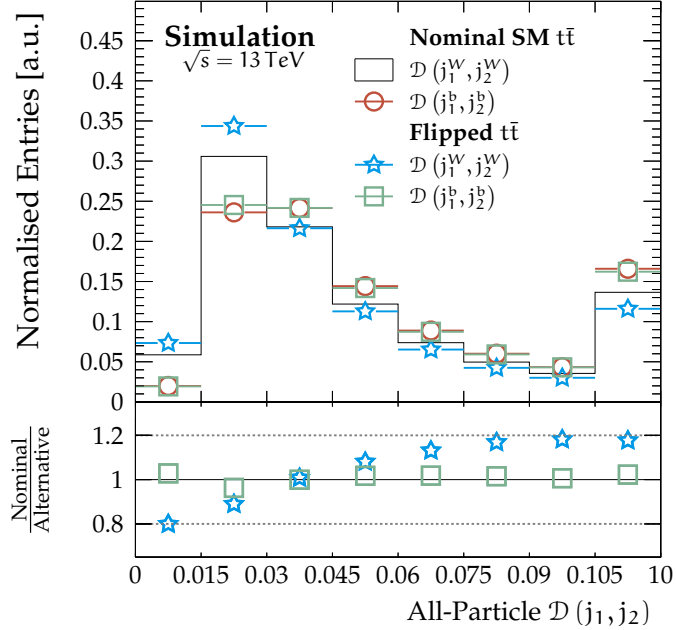
14.2.1 Application to Resolved Jets

For a naive attempt using the existing event definition, the same basic event selection that was used by the particle-level studies presented previously is applied: exactly one lepton, at least four jets, at least two b-tagged jets, and at least 20 GeV missing transverse energy. This corresponds to the so-called *resolved* scenario, where the four jets originating from the single-lepton $t\bar{t}$ topology are reconstructed explicitly and individually.

The jet dipolarity is calculated directly from pairs of jets reconstructed and identified for the resolved topology. Two pairs of jets are considered: (j_1^W, j_2^W) and (j_1^b, j_2^b) using the definitions introduced previously. The momentum vectors of the two jets

are used for the parameters j_1 and j_2 of the dipolarity and the constituents of both jets are combined to form \mathcal{J} . Consequently, radiation that falls between the two axes j_1 and j_2 but is outside of their native jet cones is not included. A requirement of $\Delta R(j_1, j_2) \leq 2$ is applied. Figure 92 compares the resulting distributions of the jet dipolarity for the two pairs of jets calculated from the nominal $t\bar{t}$ simulation with those from the simulation with exotic colour flow.

Figure 92: Comparison of the jet-dipolarity distributions using a naive approach in the resolved $t\bar{t}$ scenario. The jet dipolarity is calculated from the combined constituents of the two jets j_1 and j_2 . The jet axes required by the calculation are taken to be the jet centres of j_1 and j_2 . Note the extended upper edge of the last bin.



For simulation according to the SM, the jet dipolarity \mathcal{D} constructed from the colour-singlet jet-pairing (j_1^W, j_2^W) favours smaller values relative to that constructed from the two b -jets. This is consistent with the expected behaviour. The jet dipolarity exhibits capability to discriminate between the two pairs of jets. Separation between the jet-pairings is around or in excess of 20% in both tails of the distribution. Notably, the discriminatory power is reduced considerably if the cut on the radial separation ΔR is relaxed.

For the (j_1^b, j_2^b) jet-pairing, the simulation with exotic colour flow essentially reproduces the shape of the nominal $t\bar{t}$ simulation. Surprisingly, the jet-dipolarity distribution constructed for the colour-singlet jet-pairing from the simulation with exotic colour flow is more strongly sloped than the nominal $t\bar{t}$ simulation. This behaviour is more consistent with a colour-singlet than the *ad-hoc* colour-octet in the model with exotic colour flow.

14.2.2 Jet Dipolarity from Boosted Jets

The naive approach does not address the problem of merged jets which are likely to occur in the boosted topology. Neither does it address the issue of the ill-defined boundary between radially close subjets. This can be accounted for by considering a different type of jets. The jets considered so far are constructed with the intent of having a correspondence between individual jets and partons from the hard-scatter

topology. In the boosted topology, one may instead construct jets which correspond to combinations of these partons. The high transverse momentum of the parent particle in the boosted topology collimates the hard-scatter partons to the point that the individual shower evolutions overlap. By clustering jets with a larger radius parameter, the resulting jets deliberately contain the shower from multiple hard-scatter partons.

The alternative jet definition considered here uses a radius parameter of $R = 1.0$ with the anti- k_t jet algorithm. These jets are called *large- R jets* as opposed to the regular jets which are called *small- R jets*. Both types of jets are reconstructed independently and therefore can share constituents. Large- R jets are not considered as part of any overlap-removal procedure. A jet trimming algorithm [231] with parameters $R_{\text{Sub}} = 0.2$ and $f_{\text{Cut}} = 0.05$ is applied to the large- R jets in correspondence with the procedure used during reconstruction of detector-level jets. The large- R jets are required to satisfy $|\eta| < 2.0$ and $p_T > 175$ GeV.

The reconstruction procedure aims to find top-quark pair events in the boosted topology of the single-lepton final state where the entire decay $t \rightarrow bW(\rightarrow q\bar{q}')$ is contained within a single large- R jet. Events are preselected by requiring presence of exactly one lepton, at least one b -tagged small- R jet, a missing transverse energy in excess of 20 GeV and at least one large- R jet with $p_T > 200$ GeV and mass $m_j > 150$ GeV. This leading large- R jet is considered to be the candidate for the hadronically decaying top quark. Furthermore, one of the b -tagged small- R jets must be within $\Delta R \leq 1.0$ to the lepton.

A top-tagging requirement based on the N -subjettiness ratio τ_{32} is used to ensure that the candidate large- R jet comes from the desired topology [232, 233]. The N -subjettiness variable τ_N quantifies how well a jet can be described by N or fewer subjets. A small value of τ_N implies that radiation within a jet is mostly aligned along N subjet axes or fewer. Based on this, the ratio $\tau_{32} = \tau_3/\tau_2$ can be used to discriminate between jets that contain either a two-prong or three-prong substructure. Small values of τ_{32} are indicative of the desired three-prong structure, a cut of $\tau_{32} < 0.6$ is applied to select events.

In order to calculate the N -subjettiness, the large- R jet is broken into N subjets. For each of the events selected by the above procedure, three subjet axes are obtained from the calculation of τ_3 . Each subjet axis has associated jet constituents and is presumed to be seeded by one of the partons — b , q , \bar{q}' — from the hard-scatter decay. The jet constituents are used to identify the subjet seeded by the b -quark through the ghost-tagging method introduced previously. Events are accepted if exactly one of the subjets is likely to originate from a b -quark. The subject axes and their associated jet constituents are used as inputs to the jet-dipolarity calculation according to Equation (36).

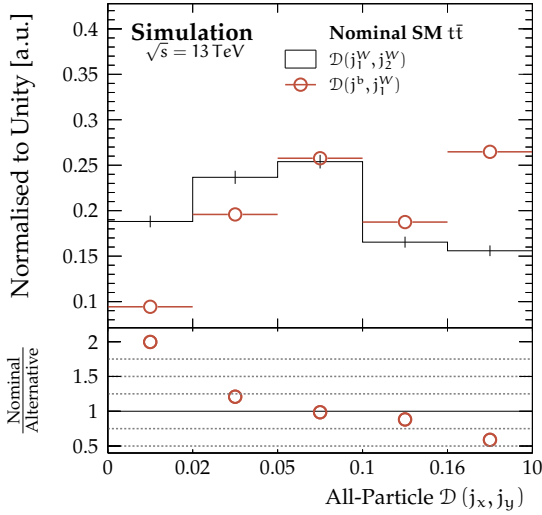


Figure 93: Comparison of normalised jet dipolarity distributions of two colour-connected (j_1^W, j_2^W) or non-colour-connected subjects (j^b, j_1^W) of large- R -jet that is a candidate for the hadronically decaying top-quark. Note that the actual bin width is highly non-uniform but is visualised using equal-width bins.

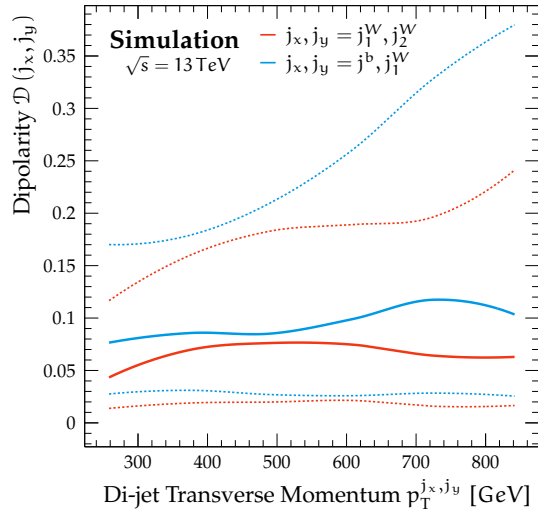


Figure 94: Jet dipolarity distributions of two colour-connected (j_1^W, j_2^W) or non-colour-connected subjects (j^b, j_1^W) of a large- R jet that is a candidate for the hadronically decaying top-quark as function of the combined di-jet transverse momentum. Thick lines denote central values, dashed lines correspond to percentiles at $\pm 1\sigma$.

Figure 93 compares the jet dipolarity calculated either from the two untagged subjects (j_1^W, j_2^W) or the b -tagged and p_T -leading untagged subject (j^b, j_1^W). As expected, the jet dipolarity favours smaller values for the two subjects likely to originate from the W boson relative to the two subjects without a colour-connection. Figure 94 compares the distribution of the jet dipolarity for both jet pairings as a function of the di-jet transverse momentum.

14.2.3 Combining Jet Dipolarity and Jet-Pull Angle

As was mentioned previously, the subjet axes j_1 and j_2 used by the calculation of the jet dipolarity \mathcal{D} do not have to correspond to real jets. In recognition of this, one may invert the purpose of the jet dipolarity: rather than fixing the subjet axes to calculate \mathcal{D} , which then encodes the colour flow information, the jet dipolarity can be minimised as function of j_1 and j_2 . After minimisation, the line segment connecting the subjet axes j_1 and j_2 is expected to be aligned with the overall shape of the radiation in y - ϕ space, assuming it is non-uniform.

This procedure constructs a jet-connection axis which itself encodes colour flow information. An observable similar to the jet-pull angle can be constructed: $\psi_{\mathcal{P}, \mathcal{D}}(j_1, j_2)$ is the angle between the jet-pull vector $\vec{\mathcal{P}}(j_1)$ and the jet-connection axis obtained from the minimisation of the jet dipolarity $\mathcal{D}(j_1, j_2)$. Figure 95 compares the regular jet-pull angle $\theta_{\mathcal{P}}$ to the new observable $\psi_{\mathcal{P}, \mathcal{D}}$, the *jet pull-dipolarity angle*, for the two untagged subjects of the large- R jet. Both observables are constructed from the same set of selected events and using the same jets.

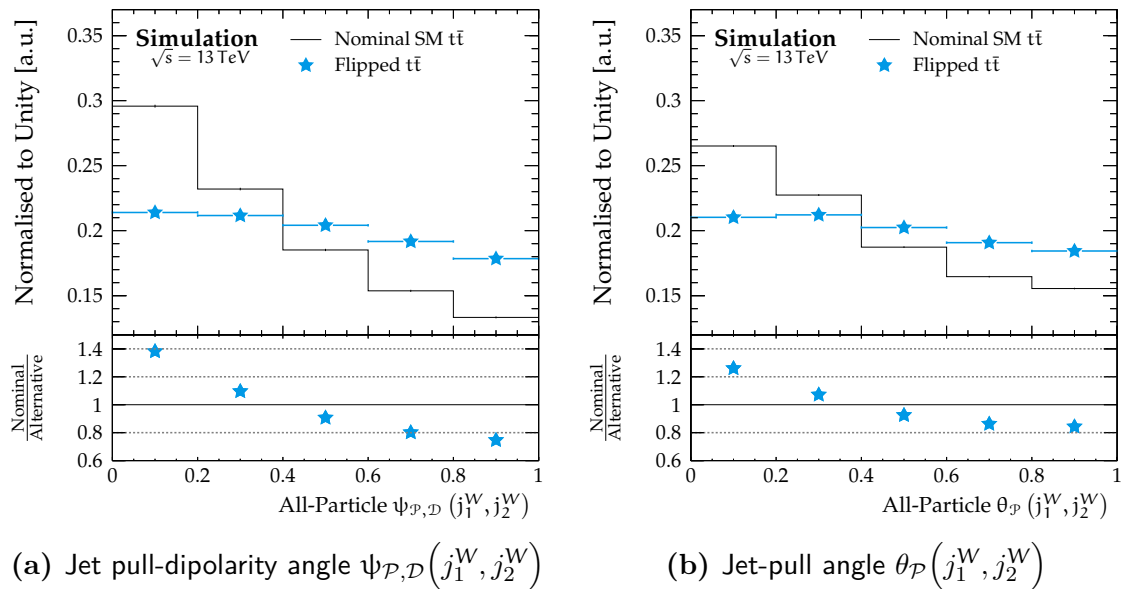


Figure 95: Comparison of colour-flow observables calculated from the nominal $t\bar{t}$ simulation with those from the $t\bar{t}$ simulation with exotic colour flow. Shown are (a) the jet pull-dipolarity angle $\psi_{\mathcal{P},\mathcal{D}}$ and (b) the jet-pull angle $\theta_{\mathcal{P}}$.

The new observable, Figure 95a, exhibits a more strongly sloped distribution than the plain jet-pull angle, Figure 95b, for the nominal $t\bar{t}$ simulation. For the simulation with exotic colour flow, the distribution remains essentially unchanged. This implies that the jet pull-dipolarity angle is more effective at discriminating the two colour flow scenarios. The efficacy of the discrimination can be further enhanced by requiring a stricter cut on τ_{32} or additional cuts on the mass of the large- R jet.

This procedure can also be applied using other subjet combinations. The observable $\psi_{\mathcal{P},\mathcal{D}}(j^b, j_1^W)$, which uses the jet-pull vector of the b -tagged subjet, shows behaviour that is more consistent with two jets without a colour connection. Calculating the same observable for the sample with exotic colour flow produces a more colour-singlet-like distribution. This matches the expectation.

14.3 Summary

A study of the prospects for analysing colour flow in boosted top-quark pair events, where the entire radiation from the hadronically decaying top quark is contained in a single jet, was presented. Merged jets, which are typical for the boosted topology, are expected to be a boon to analyses of colour flow since the QCD radiation is contained within a relatively small angular cone. A new observable, the jet dipolarity, was introduced. Unlike the jet pull, this observable is sensitive to substructure of two jets rather than just one. The jet dipolarity shows promise both in the resolved scenario, where jets correspond to individual partons, and the boosted scenario. The discriminatory power of the jet dipolarity was studied in particular with regards to identifying the $W \rightarrow q\bar{q}'$ subcomponent of a jet that contains a complete hadronically decaying top quark.

An alternative approach was investigated which uses the jet dipolarity to construct a jet-connection axis which itself encodes jet substructure by finding the axis endpoints that minimise the jet dipolarity. This jet-connection axis is then used to construct an alternative jet-pull angle. The alternative jet-pull angle exhibits a stronger sensitivity than the regular jet-pull angle constructed for the same events.

Performing a property measurement using observables sensitive to colour flow is only one half of the story. The use of colour-flow observables for discriminating between different signal hypotheses is an important motivation. Both the jet-dipolarity and the alternative jet-pull angle show promise for discriminating colour-singlet and -octet contributions within large- R jets. The crucial next step is to evaluate these capabilities within the phase space targeted by an actual measurement and using data with a detector simulation.

In the boosted topology, the event and object definitions are not as well-defined as in the resolved topology. It was found that the sensitivity of the jet dipolarity and the quantities derived from the jet-pull vector to the underlying colour flow can strongly depend on the specifics of the event definition. In particular, the definition of the top-tagged jet and how it is broken into its three subjets has a meaningful impact. As a consequence, future studies of colour flow in the boosted topology should be performed in cooperation with other property studies in this topology. In addition to the benefit of sharing resources and workforce, this implies that whichever bias is introduced by the selected top-tagging requirements is at the very least shared across the different measurements.

VI Conclusion

In this thesis, a measurement of the top-quark pair production cross-section $\sigma_{t\bar{t}}$ at a centre-of-mass energy of $\sqrt{s} = 13$ TeV was presented. The ATLAS experiment has a rich programme of top-quark physics analyses and measuring the production cross-section $\sigma_{t\bar{t}}$ is of great practical relevance to these efforts. Theoretical calculations can be used to predict $\sigma_{t\bar{t}}$ and its dependence on the centre-of-mass energy. The measurement presented here is one of the first top-quark production cross-section measurements at this centre-of-mass energy. It was performed in the single-lepton final state of the $t\bar{t}$ topology requiring either a high-momentum electron or muon. In the combined channel, a measured value of

$$\sigma_{t\bar{t}} = 817 \pm 13 \text{ (stat)} \pm 103 \text{ (syst)} \pm 88 \text{ (lumi)} \text{ pb} \quad (37)$$

is reported. This result is consistent with theoretical calculations available at NNLO+NNLL in QCD which predict $\sigma_{t\bar{t}} = 832^{+46}_{-51}$ pb. Measurements in the two sub-channels are consistent with each other as well as the combination. The ratio of the cross-section in the two channels, in which a variety of systematic uncertainties cancel, was measured as well. It is found to be consistent with the Standard Model expectation of approximately unity. The measured values are also consistent with measurements performed by ATLAS at this centre-of-mass energy in other channels as well as measurements performed by CMS [234].

A measurement of colour flow in $t\bar{t}$ events in the single-lepton final state at 13 TeV was presented. Observables derived from the jet-pull vector were constructed. These are sensitive to the colour flow of the two jets from the hadronically decaying W boson as well as the two b -jets from the top-quark decays. To remove detector effects, the measured distributions were unfolded to particle level.

The normalised unfolded distributions were compared to theoretical predictions taken from MC simulation. Furthermore, a χ^2 goodness-of-fit test statistic was used to quantify the agreement of the predictions and data. None of the predictions is found to adequately describe all measured observables. Predictions from POWHEG + HERWIG 7 are found to describe observables constructed from the daughters of the hadronically decaying W boson quite well. The observable constructed from

VI Conclusion

the two b -jets is generally described well by the predictions. It is best described by the prediction obtained from **SHERPA**. Notably, the prediction obtained from the simulation considered as “*nominal*” $t\bar{t}$ simulation, which is used to construct the detector response model needed by the unfolding, agrees poorly with data for most observables. A comparison to a prediction taken from a simulation using a model with exotic colour flow was performed and the data favours simulation according to the Standard Model. While colour flow has only subtle effects, clear differences between observables from the decay of the hadronically decaying W boson and the top-quarks are found. The measured data support the hypothesis that a colour-flow observable based on the jet-pull angle may be used as part of a signal discriminant.

The deviations observed between the measured data and some of the theoretical predictions motivate further study. It is in particular concerning that the simulation considered as “*nominal*” by **ATLAS** top-quark physics measurements, **POWHEG** + **PYTHIA 8**, produces predictions which agree poorly with the measured data. The measured data can provide a starting point for simulation tuning efforts.

A preliminary study of the prospects for measuring colour flow in the boosted topology of single-lepton $t\bar{t}$ events was presented. Variables derived from the jet-pull vector and the jet dipolarity are found to have meaningful discriminatory power for subjets within a hadronically decaying top-quark jet. A novel approach for combination of jet pull and jet dipolarity based on minimisation of the latter was presented. This observable is found to exhibit stronger sensitivity to the underlying colour flow than an observable based directly on the jet pull. The author suggests to study these observables further in the phase space of an existing analysis within the boosted topology. This would enable symbiotic exchange and sharing of resources between the two analyses.

References

- [1] C. Patrignani *et al.* *Review of Particle Physics*. [Chin. Phys. C 40.10 \(2016\)](#), p. 100001. incl. 2017 update.
- [2] M. E. Peskin and D. V. Schroeder. *An Introduction To Quantum Field Theory*. Westview Press (1995). ISBN: 0201503972.
- [3] D. Griffiths. *Introduction to Elementary Particles*. Wiley (2008). ISBN: 3527406018.
- [4] M. Thomson. *Modern Particle Physics*. Cambridge University Press (2013). ISBN: 1107034264.
- [5] Wikipedia, The Free Encyclopedia. *Standard Model* http://en.wikipedia.org/wiki/File:Standard_Model_of_Elementary_Particles.svg (visited on 02/09/2014).
- [6] P. W. Higgs. *Broken Symmetries and the Masses of Gauge Bosons*. [Phys. Rev. Lett. 13 \(16: 1964\)](#), p. 508.
- [7] F. Englert and R. Brout. *Broken Symmetry and the Mass of Gauge Vector Mesons*. [Phys. Rev. Lett. 13 \(9: 1964\)](#), p. 321.
- [8] G. S. Guralnik, C. R. Hagen and T. W. B. Kibble. *Global Conservation Laws and Massless Particles*. [Phys. Rev. Lett. 13 \(20: 1964\)](#), p. 585.
- [9] ATLAS Collaboration. *Observation of a new particle in the search for the Standard Model Higgs boson with the ATLAS detector at the LHC*. [Phys. Lett. B 716 \(2012\)](#), p. 1. arXiv: [hep-ex/1207.7214](#).
- [10] CMS Collaboration. *Observation of a new boson at a mass of 125 GeV with the CMS experiment at the LHC*. [Phys. Lett. B 716 \(2012\)](#), p. 30. arXiv: [hep-ex/1207.7235](#).
- [11] H. Fritzsch, M. Gell-Mann and H. Leutwyler. *Advantages of the color octet gluon picture*. [Phys. Lett. B 47.4 \(1973\)](#), p. 365.
- [12] D. J. Gross and F. Wilczek. *Ultraviolet Behavior of Non-Abelian Gauge Theories*. [Phys. Rev. Lett. 30 \(26: 1973\)](#), p. 1343.
- [13] H. D. Politzer. *Reliable Perturbative Results for Strong Interactions?*. [Phys. Rev. Lett. 30 \(26: 1973\)](#), p. 1346.
- [14] S. L. Glashow. *Partial-symmetries of weak interactions*. [Nucl. Phys. 22 \(4: 1961\)](#), p. 579.
- [15] A. Salam and J. Ward. *Electromagnetic and weak interactions*. [Phys. Lett. 13 \(2: 1964\)](#), p. 168.
- [16] S. Weinberg. *A Model of Leptons*. [Phys. Rev. Lett. 19 \(21: 1967\)](#), p. 1264.

- [17] N. Cabibbo. *Unitary Symmetry and Leptonic Decays*. *Phys. Rev. Lett.* **10** (12: 1963), p. 531.
- [18] M. Kobayashi and T. Maskawa. *CP-Violation in the Renormalizable Theory of Weak Interaction*. *Progr. Theor. Phys.* **49** (2: 1973), p. 652.
- [19] S. W. Herb *et al.* *Observation of a Dimuon Resonance at 9.5 GeV in 400 GeV Proton-Nucleus Collisions*. *Phys. Rev. Lett.* **39** (5: 1977), p. 252.
- [20] CDF Collaboration. *Observation of Top Quark Production in $\bar{p}p$ Collisions with the Collider Detector at Fermilab*. *Phys. Rev. Lett.* **74** (14: 1995), p. 2626. arXiv: [hep-ex/9503002](https://arxiv.org/abs/hep-ex/9503002).
- [21] DØ Collaboration. *Search for High Mass Top Quark Production in $p\bar{p}$ Collisions at $\sqrt{s} = 1.8$ TeV*. *Phys. Rev. Lett.* **74** (13: 1995), p. 2422. arXiv: [hep-ex/9411001](https://arxiv.org/abs/hep-ex/9411001).
- [22] R. P. Feynman. *The Behavior of Hadron Collisions at Extreme Energies*. In: *Special Relativity and Quantum Theory*. **33**. Fundamental Theories of Physics. Springer Netherlands (1988), p. 289.
- [23] J. D. Bjorken. *Asymptotic Sum Rules at Infinite Momentum*. *Phys. Rev.* **179** (5: 1969), p. 1547.
- [24] The Durham HepData Project. *Online PDF plotting and calculation* <http://hepdata.cedar.ac.uk/pdf/pdf3.html> (visited on 12/07/2012).
- [25] H.-L. Lai *et al.* *New parton distributions for collider physics*. *Phys. Rev. D* **82** (2010), p. 074024. arXiv: [hep-ph/1007.2241](https://arxiv.org/abs/hep-ph/1007.2241).
- [26] C. Campagnari and M. Franklin. *The discovery of the top quark*. *Rev. Mod. Phys.* **69** (1: 1997), p. 137.
- [27] ATLAS Collaboration. *Public Results — Top Quark Physics* <http://twiki.cern.ch/twiki/bin/view/AtlasPublic/TopPublicResults> (visited on 10/02/2018).
- [28] A. Quadt. *Top quark physics at hadron colliders*. *EPJ C* **48** (2006), p. 835.
- [29] I. I. Y. Bigi *et al.* *Production and Decay Properties of Ultraheavy Quarks*. *Phys. Lett. B* **181** (1986), p. 157.
- [30] L. H. Orr. *Decay versus hadronization for top quarks produced in hadron colliders*. *Phys. Rev. D* **44** (1: 1991), p. 88.
- [31] K. Kröninger, A. B. Meyer and P. Uwer. *Top-Quark Physics at the LHC*. In: *The Large Hadron Collider: Harvest of Run 1*. Ed. by T. Schörner-Sadenius. (2015), p. 259. arXiv: [hep-ex/1506.02800](https://arxiv.org/abs/hep-ex/1506.02800).
- [32] S. Catani. *Aspects of QCD, from the TeVatron to the LHC*. In: *1st Workshop on Physics at TeV Colliders*. (2000). arXiv: [hep-ph/0005233](https://arxiv.org/abs/hep-ph/0005233).
- [33] J. Stirling. *Parton Luminosity and Cross Section Plots* <http://www.hep.ph.ic.ac.uk/~wstirling/plots/plots.html> (visited on 09/02/2018).
- [34] ATLAS Collaboration. *Public Results — Standard Model Physics* <http://twiki.cern.ch/twiki/bin/view/AtlasPublic/StandardModelPublicResults> (visited on 10/01/2018).
- [35] M. Cacciari *et al.* *Top-pair production at hadron colliders with next-to-next-to-leading logarithmic soft-gluon resummation*. *Phys. Lett. B* **710** (2012), p. 612. arXiv: [hep-ph/1111.5869](https://arxiv.org/abs/hep-ph/1111.5869).

- [36] M. Beneke *et al.* *Hadronic top-quark pair production with NNLL threshold resummation.* *Nucl. Phys. B* **855** (2012), p. 695. arXiv: [hep-ph/1109.1536](#).
- [37] P. Bärnreuther, M. Czakon and A. Mitov. *Percent Level Precision Physics at the Tevatron: First Genuine NNLO QCD Corrections to $q\bar{q} \rightarrow t\bar{t} + X$.* *Phys. Rev. Lett.* **109** (2012), p. 132001. arXiv: [hep-ph/1204.5201](#).
- [38] M. Czakon and A. Mitov. *NNLO corrections to top-pair production at hadron colliders: the all-fermionic scattering channels.* *JHEP* **12** (2012), p. 054. arXiv: [hep-ph/1207.0236](#).
- [39] M. Czakon and A. Mitov. *NNLO corrections to top pair production at hadron colliders: the quark-gluon reaction.* *JHEP* **01** (2013), p. 080. arXiv: [hep-ph/1210.6832](#).
- [40] M. Czakon, P. Fiedler and A. Mitov. *Total Top-Quark Pair-Production Cross Section at Hadron Colliders Through $O(\alpha_S^4)$.* *Phys. Rev. Lett.* **110** (2013), p. 252004. arXiv: [hep-ph/1303.6254](#).
- [41] M. Czakon and A. Mitov. *Top++: A Program for the Calculation of the Top-Pair Cross-Section at Hadron Colliders.* *Comput. Phys. Commun.* **185** (2014), p. 2930. arXiv: [hep-ph/1112.5675](#).
- [42] DØ Collaboration. *Observation of Single Top-Quark Production.* *Phys. Rev. Lett.* **103** (9: 2009), p. 092001. arXiv: [hep-ex/0903.0850](#).
- [43] CDF Collaboration. *Observation of Electroweak Single Top-Quark Production.* *Phys. Rev. Lett.* **103** (9: 2009), p. 092002. arXiv: [hep-ex/0903.0885](#).
- [44] N. Kidonakis. *Next-to-next-to-leading-order collinear and soft gluon corrections for t -channel single top quark production.* *Phys. Rev. D* **83** (2011), p. 091503. arXiv: [hep-ph/1103.2792](#).
- [45] N. Kidonakis. *Top Quark Production.* In: *Helmholtz International Summer School on Physics of Heavy Quarks and Hadrons (HQ 2013)*. (2014), p. 139. arXiv: [hep-ph/1311.0283](#).
- [46] N. Kidonakis. *NNLL resummation for s -channel single top quark production.* *Phys. Rev. D* **81** (2010), p. 054028. arXiv: [hep-ph/1001.5034](#).
- [47] N. Kidonakis. *Two-loop soft anomalous dimensions for single top quark associated production with a W^- or H^- .* *Phys. Rev. D* **82** (2010), p. 054018. arXiv: [hep-ph/1005.4451](#).
- [48] R. K. Ellis, W. J. Stirling and B. R. Webber. *QCD and Collider Physics.* Cambridge: Cambridge University Press (2003). ISBN: [0521545897](#).
- [49] J. Campbell, J. Huston and F. Krauss. *The Black Book of Quantum Chromodynamics: A Primer for the LHC Era.* OUP Oxford (2017). ISBN: [0199652740](#).
- [50] Y. L. Dokshitzer *et al.* *Basics of Perturbative QCD.* Editions Frontières (1991). ISBN: [9782863321010](#).
- [51] B. R. Webber. *Color reconnection and Bose-Einstein effects.* *J. Phys. G* **24** (1998), p. 287. arXiv: [hep-ph/hep-ph/9708463](#).
- [52] T. Sjöstrand. *Colour reconnection and its effects on precise measurements at the LHC.* In: *XLIII International Symposium on Multiparticle Dynamics (ISMD13)*. (2013). arXiv: [hep-ph/1310.8073](#).
- [53] S. Argyropoulos and T. Sjöstrand. *Effects of color reconnection on $t\bar{t}$ final states at the LHC.* *JHEP* **11**, 43 (2014), p. 43. arXiv: [hep-ph/1407.6653](#).

- [54] D.-E. Boumediène. *Color reconnection phenomena in $WW \rightarrow q\bar{q}q\bar{q}$ events*. *Nucl. Phys. B — Proc. Supp.* **109.2** (2002), p. 214.
- [55] T. Sjöstrand and V. A. Khoze. *On colour rearrangement in hadronic W^+W^- events*. *Z. Phys. C* **62** (1994), p. 281. arXiv: [hep-ph/9310242](#).
- [56] L3 collaboration. *Search for colour reconnection effects in $e^+e^- \rightarrow W^+W^- \rightarrow$ hadrons through particle-flow studies at LEP*. *Phys. Lett. B* **561** (2003), p. 202. arXiv: [hep-ex/0303042](#).
- [57] J. Ellis. *The discovery of the gluon*. *Int. J. Mod. Phys. A* **29** (2014), p. 1430072. arXiv: [hep-ph/1409.4232](#).
- [58] J. Ellis, M. K. Gaillard and G. G. Ross. *Search for gluons in e^+e^- annihilation*. *Nucl. Phys. B* **111.2** (1976), p. 253.
- [59] P. Söding. *On the discovery of the gluon*. *EPJ H* **35.1** (2010), p. 3.
- [60] R. Brandelik *et al.* (TASSO Collaboration). *Evidence for planar events in e^+e^- annihilation at high energies*. *Phys. Lett. B* **86.2** (1979), p. 243.
- [61] D. P. Barber *et al.* (MARK-J Collaboration). *Discovery of Three-Jet Events and a Test of Quantum Chromodynamics at PETRA*. *Phys. Rev. Lett.* **43** (12: 1979), p. 830.
- [62] C. Berger *et al.* (PLUTO Collaboration). *Evidence for gluon bremsstrahlung in e^+e^- annihilations at high energies*. *Phys. Lett. B* **86.3** (1979), p. 418.
- [63] W. Bartel *et al.* (JADE Collaboration). *Observation of planar three-jet events in e^+e^- annihilation and evidence for gluon bremsstrahlung*. *Phys. Lett. B* **91.1** (1980), p. 142.
- [64] JADE Collaboration. *Particle distribution in 3-jet events produced by e^+e^- annihilation*. *Z. Phys. C* **21.1** (1983), p. 37.
- [65] TASSO Collaboration. *A Study of Three Jet Events in e^+e^- Annihilation Into Hadrons at 34.6 GeV Center-Of-Mass Energy*. *Z. Phys. C* **29** (1985), p. 29.
- [66] H. Aihara *et al.* *Tests of models for quark and gluon fragmentation in e^+e^- annihilation at $\sqrt{s} = 29$ GeV*. *Z. Phys. C* **28.1** (1985), p. 31.
- [67] H. Aihara *et al.* *Tests of Models for Parton Fragmentation by Means of Three-Jet Events in e^+e^- Annihilation at $\sqrt{s} = 29$ GeV*. *Phys. Rev. Lett.* **54** (4: 1985), p. 270.
- [68] TPC/Two-Gamma Collaboration. *Comparison of the Particle Flow in $q\bar{q}g$ and $q\bar{q}\gamma$ Events in e^+e^- Annihilation*. *Phys. Rev. Lett.* **57** (8: 1986), p. 945.
- [69] L3 collaboration. *Energy and particle flow in three jet and radiative two jet events from hadronic Z decays*. *Phys. Lett. B* **345** (1995), p. 74.
- [70] DELPHI collaboration. *Charged particle multiplicity in three-jet events and two-gluon systems*. *EPJ C* **44** (2005), p. 311. arXiv: [hep-ex/0510025](#).
- [71] CDF Collaboration. *Evidence for color coherence in $p\bar{p}$ collisions at $\sqrt{s} = 1.8$ TeV*. *Phys. Rev. D* **50** (1994), p. 5562.
- [72] DØ Collaboration. *Studies of Topological Distributions of the Three- and Four-Jet Events in $p\bar{p}$ Collisions at $\sqrt{s} = 1800$ GeV with the D0 Detector*. *Phys. Rev. D* **53** (1996), p. 6000. arXiv: [hep-ex/9509005](#).
- [73] DØ Collaboration. *Color coherent radiation in multijet events from $p\bar{p}$ collisions at $\sqrt{s} = 1.8$ TeV*. *Phys. Lett. B* **414** (1997), p. 419. arXiv: [hep-ex/9706012](#).

- [74] CMS Collaboration. *Probing color coherence effects in pp collisions at $\sqrt{s} = 7$ TeV.* *Eur. Phys. J. C* **74** (2014), p. 2901. arXiv: [hep-ex/1311.5815](#).
- [75] OPAL Collaboration. *Tests of models of color reconnection and a search for glueballs using gluon jets with a rapidity gap.* *EPJ C* **35** (2004), p. 293. arXiv: [hep-ex/0306021](#).
- [76] DELPHI collaboration. *Investigation of Colour Reconnection in WW events with the DELPHI detector at LEP2.* *EPJ C* **51** (2007), p. 249. arXiv: [hep-ex/0704.0597](#).
- [77] L3 collaboration. *Evidence for gluon interference in hadronic Z decays.* *Phys. Lett. B* **353.1** (1995), p. 145.
- [78] ALEPH collaboration. *Test of Colour Reconnection Models using Three-Jet Events in Hadronic Z Decays.* *EPJ C* **48** (2006), p. 685. arXiv: [hep-ex/0604042](#).
- [79] DØ Collaboration. *Evidence of color coherence effects in W + jets events from $p\bar{p}$ collisions at $\sqrt{s} = 1.8$ TeV.* *Phys. Lett. B* **464** (1999), p. 145. arXiv: [hep-ex/9908017](#).
- [80] J. Gallicchio and M. D. Schwartz. *Seeing in Color: Jet Superstructure.* *Phys. Rev. Lett.* **105** (2010), p. 022001. arXiv: [hep-ph/1001.5027](#).
- [81] J. Gallicchio et al. *Multivariate discrimination and the Higgs + W/Z search.* *JHEP* **04** (2011), p. 069. arXiv: [hep-ph/1010.3698](#).
- [82] DØ Collaboration. *Search for the standard-model Higgs boson in the $ZH \rightarrow \nu\bar{\nu}b\bar{b}$ channel in 6.2fb^{-1} of $p\bar{p}$ collisions at $\sqrt{s} = 1.96$ TeV.* *D0-6170* (2011).
- [83] CMS Collaboration. *Search for invisible decays of Higgs bosons in the vector boson fusion and associated ZH production modes.* *Eur. Phys. J. C* **74** (2014), p. 2980. arXiv: [hep-ex/1404.1344](#).
- [84] DØ Collaboration. *Measurement of color flow in $t\bar{t}$ events from $p\bar{p}$ collisions at $\sqrt{s} = 1.96$ TeV.* *Phys. Rev. D* **83** (2011), p. 092002. arXiv: [hep-ex/1101.0648](#).
- [85] ATLAS Collaboration. *Measurement of colour flow with the jet pull angle in $t\bar{t}$ events using the ATLAS detector at $\sqrt{s} = 8$ TeV.* *Phys. Lett. B* **750** (2015), p. 475. arXiv: [hep-ex/1506.05629](#).
- [86] L. Evans and P. Bryant. *LHC Machine.* *JINST* **3** (2008), S08001.
- [87] *LEP Design Report: Vol. 2. The LEP Main Ring.* *CERN-LEP-84-01* (1984).
- [88] ATLAS Collaboration. *The ATLAS Experiment at the CERN Large Hadron Collider.* *JINST* **3** (2008), S08003.
- [89] CMS Collaboration. *The CMS experiment at the CERN LHC.* *JINST* **08** (2008), S08004.
- [90] LHCb Collaboration. *The LHCb Detector at the LHC.* *JINST* **08** (2008), S08005.
- [91] ALICE Collaboration. *The ALICE experiment at the CERN LHC.* *JINST* **08** (2008), S08002.
- [92] M. Benedikt et al. *LHC Design Report. 3. The LHC injector chain.* *CERN Yellow Reports: Monographs* (2004) <https://cds.cern.ch/record/823808>.
- [93] Wikipedia, The Free Encyclopedia. *CERN* <http://en.wikipedia.org/wiki/CERN> (visited on 02/03/2015).

- [94] ATLAS Collaboration. *Public Results — Luminosity Public Results Run 2* <http://twiki.cern.ch/twiki/bin/view/AtlasPublic/LuminosityPublicResultsRun2> (visited on 31/01/2018).
- [95] J. Pequeno (ATLAS Collaboration). *Computer generated image of the whole ATLAS detector*. (2008) <http://cds.cern.ch/record/1095924>.
- [96] ATLAS Collaboration. *ATLAS Inner Detector: Technical Design Report, Vol. 1*. CERN-LHCC-97-16 (1997).
- [97] ATLAS Collaboration. *Track Reconstruction Performance of the ATLAS Inner Detector at $\sqrt{s} = 13$ TeV*. ATL-PHYS-PUB-2015-018 (2015).
- [98] ATLAS Collaboration. *ATLAS pixel detector: Technical Design Report*. CERN-LHCC-98-13 (1998).
- [99] ATLAS Collaboration. *ATLAS pixel detector electronics and sensors*. *J. Instrum.* **3** (2008), P07007.
- [100] ATLAS Collaboration. *ATLAS Insertable B-Layer Technical Design Report*. CERN-LHCC-2010-013 (2010).
- [101] ATLAS Collaboration. *ATLAS Insertable B-Layer Technical Design Report Addendum*. CERN-LHCC-2012-009 (2012). Addendum to CERN-LHCC-2010-013.
- [102] S. Parker, C. Kenney and J. Segal. *3D — A proposed new architecture for solid-state radiation detectors*. *Nucl. Instr. Meth. A* **395.3** (1997), p. 328.
- [103] C. DaVia and S. J. Watts. *The geometrical dependence of radiation hardness in planar and 3D silicon detectors*. *Nucl. Instr. Meth. A* **603.3** (2009), p. 319.
- [104] ATLAS Collaboration. *Reconstruction of primary vertices at the ATLAS experiment in Run 1 proton–proton collisions at the LHC*. *Eur. Phys. J. C* **77** (2017), p. 332. arXiv: [hep-ex/1611.10235](https://arxiv.org/abs/hep-ex/1611.10235).
- [105] ATLAS Collaboration. *Performance of the ATLAS track reconstruction algorithms in dense environments in LHC Run 2*. *Eur. Phys. J. C* **77** (2017), p. 673. arXiv: [hep-ex/1704.07983](https://arxiv.org/abs/hep-ex/1704.07983).
- [106] ATLAS Collaboration. *Muon reconstruction performance of the ATLAS detector in proton–proton collision data at $\sqrt{s} = 13$ TeV*. *Eur. Phys. J. C* **76** (2016), p. 292. arXiv: [hep-ex/1603.05598](https://arxiv.org/abs/hep-ex/1603.05598).
- [107] ATLAS Collaboration. *Early Inner Detector Tracking Performance in the 2015 Data at $\sqrt{s} = 13$ TeV*. ATL-PHYS-PUB-2015-051 (2015).
- [108] ATLAS Collaboration. *Operation and performance of the ATLAS semiconductor tracker*. *JINST* **9** (2014), P08009. arXiv: [hep-ex/1404.7473](https://arxiv.org/abs/hep-ex/1404.7473).
- [109] ATLAS Collaboration. *Performance of the ATLAS Transition Radiation Tracker in Run 1 of the LHC: tracker properties*. *JINST* **12** (2017), P05002. arXiv: [hep-ex/1702.06473](https://arxiv.org/abs/hep-ex/1702.06473).
- [110] ATLAS Collaboration. *Basic ATLAS TRT performance studies of Run 1*. ATL-INDET-PUB-2014-001 (2014).
- [111] ATLAS Collaboration. *ATLAS Liquid-Argon Calorimeter: Technical Design Report*. CERN-LHCC-96-41 (1996).
- [112] ATLAS Collaboration. *ATLAS tile calorimeter: Technical Design Report*. CERN-LHCC-96-42 (1996).

- [113] J. Pequeno (ATLAS Collaboration). *Computer Generated image of the ATLAS calorimeter*. (2008) <http://cds.cern.ch/record/1095927>.
- [114] ATLAS Collaboration. *ATLAS Muon Spectrometer: Technical Design Report*. CERN-LHCC-97-22 (1997).
- [115] J. Pequeno (ATLAS Collaboration). *Computer generated image of the ATLAS Muons subsystem*. (2008) <http://cds.cern.ch/record/1095929>.
- [116] ATLAS Collaboration. *ATLAS level-1 trigger: Technical Design Report*. CERN-LHCC-98-14 (1998).
- [117] ATLAS Collaboration. *ATLAS high-level trigger, data-acquisition and controls: Technical Design Report*. CERN-LHCC-2003-022 (2003).
- [118] A. R. Martínez (ATLAS Collaboration). *The Run-2 ATLAS Trigger System*. *J. Phys. Conf. Ser.* **762.1** (2016), p. 012003.
- [119] ATLAS Collaboration. *Performance of the ATLAS Trigger System in 2010*. *Eur. Phys. J. C* **72** (2012), p. 1849. arXiv: [hep-ex/1110.1530](https://arxiv.org/abs/hep-ex/1110.1530).
- [120] ATLAS Collaboration. *Performance of the ATLAS Trigger System in 2015*. *Eur. Phys. J. C* **77** (2017), p. 317. arXiv: [hep-ex/1611.09661](https://arxiv.org/abs/hep-ex/1611.09661).
- [121] ATLAS Collaboration. *Fast TracKer (FTK) Technical Design Report*. CERN-LHCC-2013-007 (2013).
- [122] P. L. Rocca and F. Riggi. *The upgrade programme of the major experiments at the Large Hadron Collider*. *J. Phys. Conf. Ser.* **515.1** (2014), p. 012012.
- [123] G. Apollinari *et al.* *High-Luminosity Large Hadron Collider (HL-LHC): Preliminary Design Report*. CERN Yellow Reports: Monographs (2015). arXiv: [physics.acc-ph/1705.08830](https://arxiv.org/abs/physics.acc-ph/1705.08830).
- [124] ATLAS Collaboration. *Letter of Intent for the Phase-II Upgrade of the ATLAS Experiment*. CERN-LHCC-2012-022 (2012).
- [125] ATLAS Collaboration. *ATLAS Phase-II Upgrade Scoping Document*. CERN-LHCC-2015-020 (2015).
- [126] ATLAS Collaboration. *Expected Performance of the ATLAS Inner Tracker at the High-Luminosity LHC*. ATL-PHYS-PUB-2016-025 (2016).
- [127] ATLAS Collaboration. *Expected pile-up values at the HL-LHC*. ATL-UPGRADE-PUB-2013-014 (2013).
- [128] ATLAS Collaboration. *The ATLAS Simulation Infrastructure*. *Eur. Phys. J. C* **70** (2010), p. 823. arXiv: [physics.ins-det/1005.4568](https://arxiv.org/abs/physics.ins-det/1005.4568).
- [129] S. Agostinelli *et al.* *Geant4 – A Simulation Toolkit*. *Nucl. Instr. Meth. A* **506.3** (2003), p. 250.
- [130] E. Jones, T. Oliphant, P. Peterson *et al.* *SciPy: Open source scientific tools for Python* <http://www.scipy.org/> (visited on 28/10/2017).
- [131] A. Buckley *et al.* *General-purpose event generators for LHC physics*. *Phys. Rep.* **504** (2011), p. 145. arXiv: [hep-ph/1101.2599](https://arxiv.org/abs/hep-ph/1101.2599).
- [132] S. Höche. *Introduction to parton-shower event generators*. In: *Theoretical Advanced Study Institute in Elementary Particle Physics (TASI 2014)*. (2015). arXiv: [hep-ph/1411.4085](https://arxiv.org/abs/hep-ph/1411.4085).
- [133] B. Andersson *et al.* *Parton Fragmentation and String Dynamics*. *Phys. Rep.* **97** (1983), p. 31.

- [134] B. R. Webber. *A QCD model for jet fragmentation including soft gluon interference*. *Nucl. Phys. B* **238.3** (1984), p. 492.
- [135] Z. Marshall (ATLAS Collaboration). *Simulation of Pile-up in the ATLAS Experiment*. *J. Phys. Conf. Ser.* **513.2** (2014), p. 022024.
- [136] E. Richter-Was, D. Froidevaux and L. Poggioli. *ATLFAST 2.0 a fast simulation package for ATLAS*. *ATL-PHYS-98-131* (1998).
- [137] Z. Hubacek (ATLAS Collaboration). *Upgrading the ATLAS fast calorimeter simulation*. *J. Phys. Conf. Ser.* **762.1** (2016), p. 012054.
- [138] ATLAS Collaboration. *A neural network clustering algorithm for the ATLAS silicon pixel detector*. *JINST* **9** (2014), P09009. arXiv: [hep-ex/1406.7690](https://arxiv.org/abs/hep-ex/1406.7690).
- [139] ATLAS collaboration. *ATLAS event at 13 TeV — First stable beam*. (2015) <https://cds.cern.ch/record/2022202> (visited on 01/04/2018).
- [140] ATLAS Collaboration. *Vertex Reconstruction Performance of the ATLAS Detector at $\sqrt{s} = 13$ TeV*. *ATL-PHYS-PUB-2015-026* (2015).
- [141] ATLAS Collaboration. *Public Results — Event Displays from Collision Data* <http://twiki.cern.ch/twiki/bin/view/AtlasPublic/EventDisplayRun2Collisions> (visited on 25/03/2018).
- [142] ATLAS Collaboration. *Electron efficiency measurements with the ATLAS detector using the 2015 LHC proton–proton collision data*. *ATLAS-CONF-2016-024* (2016).
- [143] ATLAS Collaboration. *Electron reconstruction and identification efficiency measurements with the ATLAS detector using the 2011 LHC proton–proton collision data*. *Eur. Phys. J. C* **74** (2014), p. 2941. arXiv: [hep-ex/1404.2240](https://arxiv.org/abs/hep-ex/1404.2240).
- [144] ATLAS Collaboration. *Electron efficiency measurements with the ATLAS detector using the 2012 LHC proton–proton collision data*. *ATLAS-CONF-2014-032* (2014).
- [145] ATLAS Collaboration. *Electron identification measurements in ATLAS using $\sqrt{s} = 13$ TeV data with 50 ns bunch spacing*. *ATL-PHYS-PUB-2015-041* (2015).
- [146] ATLAS Collaboration. *Measurement of the $t\bar{t}$ production cross-section using $e\mu$ events with b -tagged jets in pp collisions at $\sqrt{s} = 13$ TeV with the ATLAS detector*. *Phys. Lett. B* **761** (2016), p. 136. arXiv: [hep-ex/1606.02699](https://arxiv.org/abs/hep-ex/1606.02699).
- [147] ATLAS Collaboration. *Electron and photon energy calibration with the ATLAS detector using data collected in 2015 at $\sqrt{s} = 13$ TeV*. *ATL-PHYS-PUB-2016-015* (2016).
- [148] ATLAS Collaboration. *Public Results — Event Displays from Run 2 physics analyses* <http://twiki.cern.ch/twiki/bin/view/AtlasPublic/EventDisplayRun2Physics> (visited on 25/03/2018).
- [149] G. P. Salam. *Towards Jetography*. *EPJ C* **67** (2010), p. 637. arXiv: [hep-ph/0906.1833](https://arxiv.org/abs/hep-ph/0906.1833).
- [150] M. Cacciari, G. P. Salam and G. Soyez. *The Anti- $k(t)$ jet clustering algorithm*. *JHEP* **04** (2008), p. 063. arXiv: [hep-ph/0802.1189](https://arxiv.org/abs/hep-ph/0802.1189).
- [151] M. Cacciari and G. P. Salam. *Dispelling the N^3 myth for the k_t jet-finder*. *Phys. Lett. B* **641** (2006), p. 57. arXiv: [hep-ph/0512210](https://arxiv.org/abs/hep-ph/0512210).

- [152] M. Cacciari, G. P. Salam and G. Soyez. *FastJet User Manual*. **EPJ C 72 (2012)**, p. 1896. arXiv: [hep-ph/1111.6097](#).
- [153] ATLAS Collaboration. *Topological cell clustering in the ATLAS calorimeters and its performance in LHC Run 1*. **Eur. Phys. J. C 77 (2017)**, p. 490. arXiv: [hep-ex/1603.02934](#).
- [154] ATLAS Collaboration. *Properties of jets and inputs to jet reconstruction and calibration with the ATLAS detector using proton–proton collisions at $\sqrt{s} = 13$ TeV*. **ATL-PHYS-PUB-2015-036 (2015)**.
- [155] ATLAS Collaboration. *Jet energy scale measurements and their systematic uncertainties in proton–proton collisions at $\sqrt{s} = 13$ TeV with the ATLAS detector*. **Phys. Rev. D 96 (2017)**, p. 072002. arXiv: [hep-ex/1703.09665](#).
- [156] M. Cacciari, G. P. Salam and G. Soyez. *The Catchment Area of Jets*. **JHEP 04 (2008)**, p. 005. arXiv: [hep-ph/0802.1188](#).
- [157] ATLAS Collaboration. *Jet energy measurement and its systematic uncertainty in proton–proton collisions at $\sqrt{s} = 7$ TeV with the ATLAS detector*. **Eur. Phys. J. C 75 (2015)**, p. 17. arXiv: [hep-ex/1406.0076](#).
- [158] ATLAS Collaboration. *Performance of pile-up mitigation techniques for jets in pp collisions at $\sqrt{s} = 8$ TeV using the ATLAS detector*. **Eur. Phys. J. C 76 (2016)**, p. 581. arXiv: [hep-ex/1510.03823](#).
- [159] ATLAS Collaboration. *Expected performance of the ATLAS b-tagging algorithms in Run-2*. **ATL-PHYS-PUB-2015-022 (2015)**.
- [160] ATLAS Collaboration. *Commissioning of the ATLAS b-tagging algorithms using $t\bar{t}$ events in early Run 2 data*. **ATL-PHYS-PUB-2015-039 (2015)**.
- [161] ATLAS Collaboration. *Optimisation of the ATLAS b-tagging performance for the 2016 LHC Run*. **ATL-PHYS-PUB-2016-012 (2016)**.
- [162] ATLAS Collaboration. *Performance of algorithms that reconstruct missing transverse momentum in $\sqrt{s} = 8$ TeV proton–proton collisions in the ATLAS detector*. **Eur. Phys. J. C 77 (2017)**, p. 241. arXiv: [hep-ex/1609.09324](#).
- [163] ATLAS Collaboration. *Performance of missing transverse momentum reconstruction with the ATLAS detector in the first proton–proton collisions at $\sqrt{s} = 13$ TeV*. **ATL-PHYS-PUB-2015-027 (2015)**.
- [164] G. D’Agostini. *A multidimensional unfolding method based on Bayes’ theorem*. **Nucl. Instr. Meth. A 362.2 (1995)**, p. 487.
- [165] G. D’Agostini. *Improved iterative Bayesian unfolding*. (2010). arXiv: [physics.data-an/1010.0632](#).
- [166] P. Nason. *A new method for combining NLO QCD with shower Monte Carlo algorithms*. **JHEP 11 (2004)**, p. 040. arXiv: [hep-ph/0409146](#).
- [167] S. Frixione, P. Nason and C. Oleari. *Matching NLO QCD computations with Parton Shower simulations: the POWHEG method*. **JHEP 11 (2007)**, p. 070. arXiv: [hep-ph/0709.2092](#).
- [168] S. Alioli *et al.* *A general framework for implementing NLO calculations in shower Monte Carlo programs: the POWHEG BOX*. **JHEP 06 (2010)**, p. 043. arXiv: [hep-ph/1002.2581](#).
- [169] T. Sjostrand, S. Mrenna and P. Z. Skands. *A Brief Introduction to PYTHIA 8.1*. **Comput. Phys. Commun. 178 (2008)**, p. 852. arXiv: [hep-ph/0710.3820](#).

- [170] J. Alwall *et al.* *A standard format for Les Houches Event Files*. *Comput. Phys. Commun.* **176** (2006), p. 300. arXiv: [hep-ph/0609017](#).
- [171] A. Buckley *et al.* *Rivet User Manual*. (2010). arXiv: [hep-ph/1003.0694](#).
- [172] A. Rogozhnikov. *hep_ml — Machine Learning for High Energy Physics* http://arogozhnikov.github.io/hep_ml/ (visited on 07/05/2017).
- [173] O. Behnke *et al.* *Data Analysis in High Energy Physics: A Practical Guide to Statistical Methods*. Wiley (2013). ISBN: 3527410589.
- [174] ATLAS Collaboration. *Estimation of non-prompt and fake lepton backgrounds in final states with top quarks produced in proton–proton collisions at $\sqrt{s} = 8$ TeV with the ATLAS Detector*. *ATLAS-CONF-2014-058* (2014).
- [175] ATLAS Collaboration. *Measurement of the top quark pair production cross-section with ATLAS in the single lepton channel*. *Phys. Lett. B* **711** (2012), p. 244. arXiv: [hep-ex/1201.1889](#).
- [176] ATLAS Collaboration. *Measurements of normalized differential cross-sections for $t\bar{t}$ production in pp collisions at $\sqrt{s} = 7$ TeV using the ATLAS detector*. *Phys. Rev. D* **90** (2014), p. 072004. arXiv: [hep-ex/1407.0371](#).
- [177] ATLAS Collaboration. *Measurements of top-quark pair differential cross-sections in the lepton+jets channel in pp collisions at $\sqrt{s} = 13$ TeV using the ATLAS detector*. *JHEP* **11** (2017), p. 191. arXiv: [hep-ex/1708.00727](#).
- [178] ATLAS Collaboration. *Measurements of the $t\bar{t}$ production cross-section in the dilepton and lepton-plus-jets channels and of the ratio of the $t\bar{t}$ and Z boson cross-sections in pp collisions at $\sqrt{s} = 13$ TeV with the ATLAS detector*. *ATLAS-CONF-2015-049* (2015).
- [179] ATLAS Collaboration. *Comparison of Monte Carlo generator predictions from Powheg and Sherpa to ATLAS measurements of top pair production at 7 TeV*. *ATL-PHYS-PUB-2015-011* (2015).
- [180] T. Sjostrand, S. Mrenna and P. Z. Skands. *PYTHIA 6.4 Physics and Manual*. *JHEP* **05** (2006), p. 026. arXiv: [hep-ph/0603175](#).
- [181] J. Pumplin *et al.* *New generation of parton distributions with uncertainties from global QCD analysis*. *JHEP* **07** (2002), p. 012. arXiv: [hep-ph/0201195](#).
- [182] P. Z. Skands. *Tuning Monte Carlo Generators: The Perugia Tunes*. *Phys. Rev. D* **82** (2010), p. 074018. arXiv: [hep-ph/1005.3457](#).
- [183] D. J. Lange. *The EvtGen particle decay simulation package*. *Nucl. Instrum. Meth. A* **462** (2001), p. 152.
- [184] M. Bähr *et al.* *Herwig++ Physics and Manual*. *Eur. Phys. J. C* **58** (2008), p. 639. arXiv: [hep-ph/0803.0883](#).
- [185] J. Alwall *et al.* *The automated computation of tree-level and next-to-leading order differential cross sections, and their matching to parton shower simulations*. *JHEP* **07** (2014), p. 158. arXiv: [hep-ph/1405.0301](#).
- [186] T. Gleisberg *et al.* *Event generation with SHERPA 1.1*. *JHEP* **02** (2009), p. 007. arXiv: [hep-ph/0811.4622](#).
- [187] S. Schumann and F. Krauss. *A Parton shower algorithm based on Catani-Seymour dipole factorisation*. *JHEP* **03** (2008), p. 038. arXiv: [hep-ph/0709.1027](#).

- [188] S. Hoeche *et al.* *QCD matrix elements + parton showers: The NLO case.* *JHEP* **04** (2013), p. 027. arXiv: [hep-ph/1207.5030](#).
- [189] ATLAS Collaboration. *Summary of ATLAS Pythia 8 tunes.* *ATL-PHYS-PUB-2012-003* (2012).
- [190] A. D. Martin *et al.* *Parton distributions for the LHC.* *Eur. Phys. J. C* **63** (2009), p. 189. arXiv: [hep-ph/0901.0002](#).
- [191] C.-H. Kom and W. J. Stirling. *Charge asymmetry in $W + jets$ production at the LHC.* *EPJ C* **69.1** (2010), p. 67.
- [192] ATLAS Collaboration. *Luminosity determination in pp collisions at $\sqrt{s} = 8$ TeV using the ATLAS detector at the LHC.* *Eur. Phys. J. C* **76** (2016), p. 653. arXiv: [hep-ex/1608.03953](#).
- [193] ATLAS Collaboration. *Muon reconstruction performance in early $\sqrt{s} = 13$ TeV data.* *ATL-PHYS-PUB-2015-037* (2015).
- [194] ATLAS Collaboration. *Jet Calibration and Systematic Uncertainties for Jets Reconstructed in the ATLAS Detector at $\sqrt{s} = 13$ TeV.* *ATL-PHYS-PUB-2015-015* (2015).
- [195] S. Dulat *et al.* *New parton distribution functions from a global analysis of quantum chromodynamics.* *Phys. Rev. D* **93.3** (2016), p. 033006. arXiv: [hep-ph/1506.07443](#).
- [196] L. A. Harland-Lang *et al.* *Parton distributions in the LHC era: MMHT 2014 PDFs.* *Eur. Phys. J. C* **75.5** (2015), p. 204. arXiv: [hep-ph/1412.3989](#).
- [197] R. D. Ball *et al.* (NNPDF Collaboration). *Parton distributions for the LHC Run II.* *JHEP* **04** (2015), p. 040. arXiv: [hep-ph/1410.8849](#).
- [198] A. Buckley *et al.* *LHAPDF6: parton density access in the LHC precision era.* *Eur. Phys. J. C* **75** (2015), p. 132. arXiv: [hep-ph/1412.7420](#).
- [199] J. Butterworth *et al.* *PDF4LHC recommendations for LHC Run II.* *J. Phys. G* **43.2**, 023001 (2016), p. 023001. arXiv: [hep-ph/1510.03865](#).
- [200] R. D. Ball *et al.* (NNPDF Collaboration). *Parton distributions with LHC data.* *Nucl. Phys. B* **867** (2013), p. 244. arXiv: [hep-ph/1207.1303](#).
- [201] S. Frixione *et al.* *Single-top hadroproduction in association with a W boson.* *JHEP* **7**, 029 (2008), p. 029. arXiv: [hep-ph/0805.3067](#).
- [202] ATLAS Collaboration. *Measurement of W^\pm and Z Boson Production Cross Sections in pp Collisions at $\sqrt{s} = 13$ TeV with the ATLAS Detector.* *ATLAS-CONF-2015-039* (2015).
- [203] F. Berends *et al.* *On the production of a W and jets at hadron colliders.* *Nucl. Phys. B* **357.1** (1991), p. 32.
- [204] ATLAS Collaboration. *Measurement of colour flow using jet-pull observables in $t\bar{t}$ events with the ATLAS experiment at $\sqrt{s} = 13$ TeV.* *ATLAS-CONF-2017-069* (2017).
- [205] ATLAS Collaboration. *Measurement of colour flow using jet-pull observables in $t\bar{t}$ events with the ATLAS experiment at $\sqrt{s} = 13$ TeV.* (2018). Submitted to EPJ C. arXiv: [hep-ex/1805.02935](#).
- [206] ATLAS Collaboration. *ATLAS Pythia 8 tunes to 7 TeV data.* *ATL-PHYS-PUB-2014-021* (2014).

- [207] J. Bellm *et al.* *Herwig 7.0/Herwig++ 3.0 release note.* *Eur. Phys. J. C* **76.4** (2016), p. 196. arXiv: [hep-ph/1512.01178](#).
- [208] T. Sjöstrand *et al.* *An Introduction to PYTHIA 8.2.* *Comput. Phys. Commun.* **191** (2015), p. 159. arXiv: [hep-ph/1410.3012](#).
- [209] ATLAS Collaboration. *Studies on top-quark Monte Carlo modelling for Top2016.* *ATL-PHYS-PUB-2016-020* (2016).
- [210] S. Catani *et al.* *Vector boson production at hadron colliders: a fully exclusive QCD calculation at NNLO.* *Phys. Rev. Lett.* **103** (2009), p. 082001. arXiv: [hep-ph/0903.2120](#).
- [211] J. M. Campbell and R. K. Ellis. *An Update on vector boson pair production at hadron colliders.* *Phys. Rev. D* **60** (1999), p. 113006. arXiv: [hep-ph/9905386](#).
- [212] J. M. Campbell, R. K. Ellis and C. Williams. *Vector boson pair production at the LHC.* *JHEP* **07** (2011), p. 018. arXiv: [hep-ph/1105.0020](#).
- [213] J. Alwall *et al.* *The automated computation of tree-level and next-to-leading order differential cross sections, and their matching to parton shower simulations.* *JHEP* **07** (2014), p. 079. arXiv: [hep-ph/1405.0301](#).
- [214] LHC Higgs Cross Section Working Group. *Handbook of LHC Higgs Cross Sections: 4. Deciphering the Nature of the Higgs Sector.* *CERN Yellow Reports: Monographs* (2017). arXiv: [hep-ph/1610.07922](#).
- [215] ATLAS Collaboration. *Monte Carlo Generators for the Production of a W or Z/ γ^* Boson in Association with Jets at ATLAS in Run 2.* *ATL-PHYS-PUB-2016-003* (2016).
- [216] ATLAS Collaboration. *Jet reconstruction and performance using particle flow with the ATLAS Detector.* *Eur. Phys. J. C* **77** (2017), p. 466. arXiv: [hep-ex/1703.10485](#).
- [217] CMS Collaboration. *Particle-flow reconstruction and global event description with the CMS detector.* *JINST* **12** (2017), P10003. arXiv: [hep-ex/1706.04965](#).
- [218] T. Auye. *Unfolding algorithms and tests using RooUnfold.* In: *Proceedings of the PHYSTAT 2011 Workshop.* (2011), p. 313. arXiv: [physics.data-an/1105.1160](#).
- [219] ATLAS Collaboration. *Measurement of the Inelastic Proton–Proton Cross Section at $\sqrt{s} = 13$ TeV with the ATLAS Detector at the LHC.* *Phys. Rev. Lett.* **117** (2016), p. 182002. arXiv: [hep-ex/1606.02625](#).
- [220] ATLAS Collaboration. *Electron performance measurements with the ATLAS detector using the 2010 LHC proton–proton collision data.* *Eur. Phys. J. C* **72** (2012), p. 1909. arXiv: [hep-ex/1110.3174](#).
- [221] ATLAS Collaboration. *Jet energy measurement with the ATLAS detector in proton–proton collisions at $\sqrt{s} = 7$ TeV.* *Eur. Phys. J. C* **73** (2013), p. 2304. arXiv: [hep-ex/1112.6426](#).
- [222] ATLAS Collaboration. *Jet energy resolution in proton–proton collisions at $\sqrt{s} = 7$ TeV recorded in 2010 with the ATLAS detector.* *Eur. Phys. J. C* **73** (2013), p. 2306. arXiv: [hep-ex/1210.6210](#).
- [223] ATLAS Collaboration. *Single hadron response measurement and calorimeter jet energy scale uncertainty with the ATLAS detector at the LHC.* *Eur. Phys. J. C* **73** (2013), p. 2305. arXiv: [hep-ex/1203.1302](#).

- [224] ATLAS Collaboration. *Calibration of b-tagging using dileptonic top pair events in a combinatorial likelihood approach with the ATLAS experiment.* [ATLAS-CONF-2014-004](#) (2014).
- [225] ATLAS Collaboration. *Calibration of the performance of b-tagging for c and light-flavour jets in the 2012 ATLAS data.* [ATLAS-CONF-2014-046](#) (2014).
- [226] ATLAS Collaboration. *Performance of missing transverse momentum reconstruction in proton–proton collisions at $\sqrt{s} = 7$ TeV with ATLAS.* [Eur. Phys. J. C 72](#) (2012), p. 1844. arXiv: [hep-ex/1108.5602](#).
- [227] ATLAS Collaboration. *Multi-boson simulation for 13 TeV ATLAS analyses.* [ATL-PHYS-PUB-2016-002](#) (2016).
- [228] ATLAS Collaboration. *Modelling of the $t\bar{t}H$ and $t\bar{t}V$ ($V = W, Z$) processes for $\sqrt{s} = 13$ TeV ATLAS analyses.* [ATL-PHYS-PUB-2016-005](#) (2016).
- [229] B. Efron. *Bootstrap Methods: Another Look at the Jackknife.* [Ann. Statist. 7.1](#) (1979), p. 1.
- [230] A. Hook, M. Jankowiak and J. G. Wacker. *Jet dipolarity: Top Tagging with Color Flow.* [JHEP 4, 7](#) (2012), p. 7. arXiv: [hep-ph/1102.1012](#).
- [231] D. Krohn, J. Thaler and L.-T. Wang. *Jet Trimming.* [JHEP 02](#) (2010), p. 084. arXiv: [hep-ph/0912.1342](#).
- [232] J. Thaler and K. Van Tilburg. *Identifying Boosted Objects with N -subjettiness.* [JHEP 03](#) (2011), p. 015. arXiv: [hep-ph/1011.2268](#).
- [233] J. Thaler and K. Van Tilburg. *Maximizing Boosted Top Identification by Minimizing N -subjettiness.* [JHEP 02](#) (2012), p. 093. arXiv: [hep-ph/1108.2701](#).
- [234] CMS Collaboration. *Measurement of the $t\bar{t}$ production cross section using events with one lepton and at least one jet in pp collisions at $\sqrt{s} = 13$ TeV.* [JHEP 09](#) (2017), p. 051. arXiv: [hep-ex/1701.06228](#).